



Vitor Eboli Lopes Paiva

**Modern Experimental Techniques with an Emphasis on
Infrared Thermography to the Assessment of Fatigue
Components with Dents**

Tese de Doutorado

Thesis presented to the Programa de Pós-graduação em Engenharia Mecânica of PUC–Rio, in partial fulfillment of the requirements for the degree of Doutor em Ciências - Engenharia Mecânica.

Advisor: Prof. José Luiz de França Freire

Rio de Janeiro
March 2020



Vitor Eboli Lopes Paiva

**Modern Experimental Techniques with an Emphasis on
Infrared Thermography to the Assessment of Fatigue
Components with Dents**

Thesis presented to the Programa de Pós-graduação em Engenharia Mecânica of PUC-Rio in partial fulfillment of the requirements for the degree of Doutor em Ciências - Engenharia Mecânica. Approved by the Examination Committee.

Prof. José Luiz de França Freire

Advisor

Departamento de Engenharia Mecânica – PUC-Rio

Prof. Anderson Pereira

Departamento de Engenharia Mecânica – PUC-Rio

Prof. Arthur Martins Barbosa Braga

Departamento de Engenharia Mecânica - PUC-Rio

Prof. Jorge Carlos Ferreira Jorge

Centro Federal de Educação Tecnológica Celso Suckow da Fonseca

Prof. Rodolfo Luiz Martins Suanno

Universidade do Estado do Rio de Janeiro

Ana Lucia Fampa Seabra d'Almeida

Petrobras S.A.

All rights reserved.

Vitor Eboli Lopes Paiva

The author holds a degree in Mechanical Engineering and a Master degree in Engineering from the Pontifical Catholic University of Rio de Janeiro. His line of research and interest involves fracture mechanics, fatigue, infrared thermography and mechanical design.

Bibliographic data

Paiva, Vitor Eboli Lopes

Modern experimental techniques with an emphasis on infrared thermography to the assessment of fatigue components with dents / Vitor Eboli Lopes Paiva; advisor: José Luiz de França Freire. – 2020.

224f.: il. color.; 29,7 cm

Tese (doutorado)–Pontifícia Universidade Católica do Rio de Janeiro, Departamento de Engenharia Mecânica, 2020.

Inclui referências bibliográficas

1. Engenharia Mecânica – Teses. 2. Termografia infravermelha. 3. TSA. 4. Termoelasticidade. 5. Danos por Mossa. 6. Oleodutos. I. Freire, José Luiz de França. II. Pontifícia Universidade Católica do Rio de Janeiro. Departamento de Engenharia Mecânica. III. Título.

CDD: 621

To all who cheered and encouraged me to reach my goals.

Acknowledgements

Firstly, I would like to express my sincere gratitude to my advisor Prof. José Luiz de França Freire for the continuous support of my doctoral study and related research, for his patience, motivation, guidance and all the knowledge shared during my development. His guidance helped me in all the time of research and writing of this thesis.

A special thanks to Dr. Giancarlo L. González and Prof. Ronaldo D. Vieira, without whom it wouldn't be possible to perform the tests of the dented specimens.

To Alexandre and Bruno from LSFO-PUC-Rio for all help in specimens FBSG instrumentation.

To the Fotomecânica lab personnel: Dr. Julian Gonzáles, Graça, Dr. Eduardo Maneschy, Dr. Marco Guamán, Dr. Jesus L. Carvajalino, Dr. Jorge Diaz and Jorge Diniz.

To my former students Lucas Lira, Patrick Manhães, Adriano Assis, Gustavo Lemos and Romulo Etchebehere for the opportunity both to teach and to learn.

To my parents Geraldo and Maria for their example of character and life, which have always been an inspiration to me.

To my brother Fernando and sister in law Thamara for the affection and companionship.

To Joana and her family for all their love and spiritual support in writing this thesis and my life in general.

Finally, I would also like to thank all my friends, that are innumerable to be mentioned, who always supported me and encouraged me to pursue my goal.

To the CNPq for its financial support.

To project SIGITEC TCBR 409.

To Center for Pipeline Technology (CTDUT).

Abstract

Paiva, Vitor Eboli Lopes; Freire, José Luiz de França (advisor); **Modern experimental techniques with an emphasis on infrared thermography to the assessment of fatigue components with dents.** Rio de Janeiro, 2020. 224p. Tese de Doutorado - Departamento de Engenharia Mecânica, Pontifícia Universidade Católica do Rio de Janeiro.

Infrared thermography has been used as a nondestructive evaluation (NDE) technique to detect flaws in structural components, playing an important role in manufacturing inspection, in-service inspection and maintenance programs. An investigation program was launched with the objective of presenting combinations of analytical, experimental and numerical methods to predict and monitor fatigue initiation and fatigue damage progression in equipment such as pressure vessels, tanks, piping and pipelines with dents or complex-shaped anomalies. The monitoring of fatigue initiation and propagation in the actual specimens used nondestructive inspection techniques such as thermoelastic stress analysis (TSA), three-dimensional digital image correlation (3D-DIC) and fiber optic Bragg strain gages (FBSG) to determine strains at fatigue hot spots locations. Strain fields determined from the experimental measurements and from the finite element method (FEM) were combined with the fatigue Coffin-Manson strain-life equation and the Miner's fatigue damage rule to predict fatigue life (N). Results from tested 3m long tubular (with nominal dimensions: 324mm external diameter and 6.35mm wall thickness) specimens containing complex-shaped dents were reported and fully analyzed. This work confirmed that infrared rapid fatigue assessment methods are practical and efficient tools that can provide a reliable, non-destructive and faster results about the fatigue behavior of materials. Good agreement among fatigue life estimations and actual fatigue lives of complex dent shapes in pipeline specimens can only be achieved if accurate measurements or numerical determinations of the circumferential strains actuating at the dent hot-spots were coupled with suitable fatigue strain-life curves. Coupling an experimental technique

for accurately determining dent shapes to a numerical strain analysis technique will lead to good hot-spot strain estimations to be combined with the strain-life fatigue curves. The present conclusions can be applied to other structures that may present dents such as tanks and pressure vessels.

Keywords

Fatigue; Infrared Thermography; Pipeline; Dent; Assessment.

Resumo

Paiva, Vitor Eboli Lopes; Freire, José Luiz de França (orientador). **Técnicas experimentais modernas, com ênfase na termografia infravermelha para avaliação de componentes de fadiga com mossas.** Rio de Janeiro, 2020. 224p. Tese de Doutorado - Departamento de Engenharia Mecânica, Pontifícia Universidade Católica do Rio de Janeiro.

A termografia infravermelha tem sido usada como uma técnica de avaliação não destrutiva para detectar falhas nos componentes estruturais, desempenhando um papel importante nos programas de inspeção de fabricação, inspeção em serviço e manutenção. Um programa de investigação foi lançado com o objetivo de apresentar combinações de métodos analíticos, experimentais e numéricos para prever e monitorar o início da fadiga e a progressão dos danos à fadiga em equipamentos como vasos de pressão, tanques, tubulações e dutos com mossas ou anomalias complexas. O monitoramento do início e propagação da fadiga nas amostras reais utilizou técnicas de inspeção por infravermelho não destrutivo. Análise termoelástica de tensão (TSA), correlação tridimensional de imagem digital (3D-DIC) e strain gages de fibra óptica Bragg (FBSG) foram utilizados para determinar deformações em locais de fadiga em pontos críticos. Os campos de deformação determinados a partir das medições experimentais e do método de elementos finitos (MEF) foram combinados com a equação de vida-de-fadiga de Coffin-Manson e a regra de dano por fadiga de Miner para prever a vida de fadiga (N). Os resultados das amostras tubulares testadas de 3 m de comprimento contendo mossas de formato complexo foram relatados e analisados completamente. Este trabalho confirmou que os métodos infravermelhos de avaliação rápida de fadiga são ferramentas práticas e eficientes que podem fornecer resultados confiáveis, não destrutivos e rápidos acerca do comportamento à fadiga dos materiais. Uma boa concordância entre as estimativas de vida em fadiga e a vida real de mossas com geometria complexas em dutos só pode ser atingida se medições precisas ou determinações numéricas das deformações circunferenciais que atuam nos pontos

de interesse forem acopladas a curvas de fadiga deformação-vida adequadas. Acoplando uma técnica experimental para determinar com precisão a geometria das mossas com uma técnica de análise numérica de deformações fará com que sejam obtidas boas estimativas de deformação das posições críticas que serão combinadas com as curvas de fadiga baseadas na relação deformação-vida. As presentes conclusões podem ser aplicadas a outras estruturas que podem apresentar mossas, como tanques e vasos de pressão.

Palavras-Chave

Fadiga; Termografia Infravermelha; Oleodutos; Mossa; Avaliação.

Table of contents

1. Introduction	24
1.1 Infrared Thermography	24
1.2 Integrity of Pipelines	26
1.3 Literature Review About Infrared Thermography Applied to Flaw Assessment	28
1.4 Literature Review About TSA and Its Applications	30
1.5 Literature Review about Dent Assessment	32
1.5.1 Standard Approaches	32
1.5.2 Others Approaches	34
1.6 Motivation	35
1.7 Thesis Objective	38
1.8 Thesis Outline	40
2. IR Thermography	41
2.1 Active Thermography X Passive Thermography	42
2.4 Passive Thermography Applied to Experimental Mechanics	44
2.4.1 Fatigue Strength Estimation	44
2.4.1.1 Fatigue Limit: Cyclic Method	45
2.4.1.2 Fatigue Limit: Quasi – Static Method	47
2.4.1.3 Fatigue Limit: Ultra-Rapid Cyclic Method	49
2.4.1.4 Fatigue Curve Method	50
2.4.2 Thermoelastic Stress Analysis	53
2.4.2.2 Calibration	54

2.4.2.3 TSA Data Acquisition and Processing	55
2.4.2.4 TSA Data and Interpretation	57
2.2.5 Stress Separation	60
3. Material and Experimental Procedure	61
3.1 Specimens	61
3.1.1 Dent Creation Process	63
3.1.2 Reround Pressure	66
3.1.3 Dented Pipeline Specimens Profiles	68
3.2 Testing Procedure	68
3.2.1 Loading Machines	69
3.2.2 Loading Cautions	70
3.2.3 Specimen Surface Preparation	70
3.2.4 Thermal Insulation	70
3.2.5 Thermal Camera	71
3.2.6 IR Software	72
3.3 Material Behavior Assessment	73
3.3.1 Static Tensile Stress Tests	74
3.3.2 Fatigue Limit Tests Using IR: Cyclic Loading	75
3.3.3 Fatigue Limit Tests Using IR: Quasi-Static Loading	76
3.3.4 Fatigue Limit Tests Using IR: Ultra Rapid Cyclic Loading	78
3.3.5 Results: Fatigue Curves and Fatigue Limit	79
3.3.6 Results: Influence of Mean Stress on the Fatigue Limit	82
3.3.7 TSA Calibration for Low Carbon Steel	83
3.4 Complementary Experimental Techniques	85
3.4.1 Digital Image Correlation (DIC)	85
3.4.2 Fiber Bragg Strain Gauges (FBSG)	88

4. Fatigue Assessment of Dented Specimens	91
4.1 Fatigue Life Approaches	91
4.1.1 API 579-1/ASME FFS-1 - 2016 Part 12 Standard	92
4.1.2 PDAM – Pipeline Defect Assessment Manual	93
4.1.3 Mean Stress Method	95
4.1.4 Coffin-Manson Method	97
4.1.4.1 Analytical Methods to Calculate the Strain Amplitude	97
4.1.4.1.1 Calculation of Strain Range Using the Hysteresis Loop Curve (Alternative Method 1)	98
4.1.4.1.2 Calculation of Strain Range Using the Stabilized Curve of The Elastic-Perfectly Plastic Material (Alternative Method 2)	98
4.1.5 API 579-1/ASME FFS-1 - 2016 Part 14 Standard	99
4.1.5.1 Level 2 Method A - Assessment Using Elastic Stress Analysis and Equivalent Stresses	100
4.1.5.2 Level 2 Method B - Assessment Using Elastic-Plastic Stress Analysis and Equivalent Strain	101
4.1.5.3 ASME Fatigue Curve	102
4.2 Finite Element Models	103
4.2.1 First Type of Finite Element Model	104
4.2.1.1 Model Geometry	104
4.2.1.2 Model Parameters and Configuration	106
4.2.2 Second Type of Finite Element Model	108
4.2.2.1 Model Geometry	108
4.2.2.2 Model Parameters and Configuration	109
5. Results and Discussions	111
5.1 Experimental Campaign	111

5.2 Finite Element Results	113
5.2.1 First Model	113
5.2.1.1 Numerical Creation of the Dents	113
5.2.1.2 Numerical Rerounding of the Created Dents	116
5.2.1.3 Snap Thru	117
5.2.1.4 Final Dent Shape Before the Cyclic Loading	120
5.2.1.5 Numerical Cyclic Behavior of the Dented Specimens	121
5.2.1.6 History of Deformation at the Critical Points	124
5.2.2 Second Finite Element Model	127
5.3 Actual Test Results	128
5.3.1 Cyclic Pressure Application	128
5.3.2 DIC and Finite Element Test Results	129
5.3.3 Fiber Bragg Strain Gauges (FBSG) Results	138
5.3.4 Thermoelastic Stress (TSA) Results	142
5.3.5 Stress and Strain Concentration Factors Results	148
5.3.6 TSA Fatigue Crack Monitoring	149
5.4 Fatigue monitoring using IR thermography	152
5.4.1 Assessment of fatigue hot spots by temperature measurements when the specimen is loaded in quasi-static conditions	153
5.4.2 TSA Monitoring Tool Algorithm to Detect Fatigue Crack Initiation	156
5.5 Fatigue life estimation	162
5.5.1 API-579 Part 12 and PDAM Approaches	162
5.5.2 Mean Stress Approach	165
5.5.3 Strain-Life (Coffin- Manson) Approaches	168
5.5.4 API-579 Part 14 or ASME Sec VIII div. 2 Part 5 Approaches	170
5.5.5 Comparison Between All Approaches	173

5.5.6 Dent 3 Fatigue Assessment	175
6. Conclusions and Future Work	177
6.1 Conclusions	177
6.2 Recommendation for Future Works	183
7. References	185
Appendix A.	198
A.1 IR Thermography Physical Principles	198
A.1.1 Radiation in IR Thermography Applications	200
A.2 IR Sensors	202
Appendix B.	203
Appendix C.	208
Appendix D.	211
Appendix E.	215
Appendix F.	217

List of Figures

Figure 1.1: Maximum temperature rises above ambient during cyclic test [18]...	28
Figure 1.2: Timeline of some important steps in the development of TSA [65]...	32
Figure 2.1: Active pulsed thermography applied to detection of defects in anticorrosive coating: a) visual condition; b) inspected condition [103].	42
Figure 2.2: Schematic setup for active transmissive thermography.	43
Figure 2.3: Different used of passive thermography: a) Detecting of electrical flaw; b) Stress measurement - TSA; c) Medical application; d) Inspection of plane fuselage.	44
Figure 2.4: Phases of the thermal behavior of ΔT vs. N curve for a hot spot in the specimen surface during typical fatigue tests, adapted from [26].	45
Figure 2.5: Stepped loading procedure for the determination of the fatigue limit.	46
Figure 2.6: ΔT_i vs. $\Delta \sigma_i$ curve for various incremental load steps and determination of the fatigue limit (intercept of the two straight lines) [64].	47
Figure 2.7: Stress-strain and temperature curve.	48
Figure 2.8: Schematic of the application of the ultra-rapid method using a dog bone specimen.	50
Figure 2.9: Parameter ϕ (hatching area) for different stress levels ($\sigma_1 > \sigma_2 > \sigma_3 > \sigma_4 > \sigma_5$).	52
Figure 2.10: Evolution of the thermoelastic response signal from the camera over the test duration when a static load is applied.	55
Figure 2.11: Schematic thermoelastic analysis setup, [111].	56
Figure 2.12: Form of thermoelastic data during cyclic test: a) the intensity of the reference signal and the thermoelastic response (S^*) vs. time, and the phase relationship (θ) between them; b) the resulting thermoelastic vector in polar	

coordinate (R and θ) and in cartesian coordinates (X and Y), adapted from [47].	57
Figure 2.13: Thermoelastic response of a plate containing a central hole: a) X data; b) Y data; c) R data; d) θ data.....	59
Figure 2.14: Thermoelastic response of a Key-hole specimen: a) X data; b) Y data; c) R data; d) θ data.....	60
Figure 3.1: Dog bone specimen geometry.....	62
Figure 3.2: a) The nine pipe specimens after the indentation process; b) the concrete grafts used to minimize the volume of water during the pressurizing tests.	62
Figure 3.3: Steps of the dent creation process.	64
Figure 3.4: Indentation force vs. displacement curves.	65
Figure 3.5: Dent creation process: a) the specimen is placed in the saddle and align with the indenter; b) the indenter is displaced in order to produce an initial dent; c) the indenter is gradually withdrawn; d) the final shape of the initial dent; e) the profile of the dent is measured with a caliper; f) the plain longitudinal dent obtain after rerounding.	65
Figure 3.6: a) Dent 1 rerounding test; b) dent 1 final shape; c) dent 2 rerounding test; d) dent 2 final shape.	67
Figure 3.7: Dented specimens profiles before rerounding.	68
Figure 3.8: Dented specimens profiles after rerounding.	68
Figure 3.9: Test machines used in this work.	69
Figure 3.10: Thermal insulation used: a) wooden box; b) cloth.....	71
Figure 3.11: FLIR camera A655sc.	71
Figure 3.12: DeltaTherm 2 signal processing model [122].	73
Figure 3.13: Stress-strain curve of the API 5L Gr. B [123].	74
Figure 3.14: Specimen 6 cyclic IR method results: a) ΔT vs. N curve for various stress amplitudes $\Delta\sigma_i$, with the determination of each ΔT_i ; b) ΔT_i vs. $\Delta\sigma_i$ curve for various incremental load steps and determination of the fatigue limit.....	76
Figure 3.15: Specimen 5 quasi-static IR method result.....	77

Figure 3.16: Specimen 6 stress-strain curves used for the quasi-static method. ...	78
Figure 3.17: Specimen 6 ultra-rapid method results for the load steps above the fatigue limit.	79
Figure 3.18: Fatigue SN curves for stress ratios measured using IR assessment methods, traditional method and analytically calculated.....	80
Figure 3.19: Comparison between all fatigue SN curves for different stress ratios using R=-1 ratio ($\sigma_m=0$).....	80
Figure 3.20: Alternate stress vs. mean stress for Gerber, Goodman and IR data.....	82
Figure 3.21: Alternate stress vs. mean stress for Gerber, Goodman and IR average data.	83
Figure 3.22: Test specimens utilized in the gain calibration.	84
Figure 3.23: a) TSA response (S^*) map; (b) Arbitrarily line chosen in the highest tensile section of the specimen TS1.	84
Figure 3.24: TSA gain calibration.	85
Figure 3.25: A pair of imagens used in the analysis of DIC-3D using two cameras.	86
Figure 3.26: a) Basic physical principal of the DIC; b) Procedure of the calculation of the strain.	87
Figure 3.27: a) Dented pipe specimen Dent 6 black painted for the thermographic analysis and with small white dots to allow for digital image correlation analysis; b) Performing spatial calibration.	88
Figure 3.28: Specimen Dent 5 FBSGs positioned at the circumferential direction.	89
Figure 3.29: FBSG position in each of the studied specimens.....	90
Figure 4.1: Material with a perfect elastic-plastic behavior.	99
Figure 4.2: Fatigue data for carbon alloy steel [129].	103
Figure 4.3: Finite element model geometry with $\frac{1}{4}$ of symmetry.	105
Figure 4.4: Indenter dimensions.	105

Figure 4.5: Pipe specimen dimensions.	105
Figure 4.6: Saddle dimensions.	105
Figure 4.7: API 5L Gr. B true stress vs. strain curve utilized in the model obtain from the curve presented in Figure 3.13.....	106
Figure 4.8: Mesh used in the first type of finite element models.	107
Figure 4.9: Dent 6 longitudinal profiles measured with a caliper and with DIC.	109
Figure 4.10: Geometry of the second type of finite element model with applied boundary conditions: a) Dent 6; b) Dent 3.	109
Figure 4.11: Meshes used in the second type of finite element models: a) Dent 6; b) Dent 3.	110
Figure 5.1: Experimental arrangement for testing the dented pipeline specimens.	111
Figure 5.2: Numerical and experimental result curves of force vs. displacement during the indentation process.....	114
Figure 5.3: Numerical and experimental profiles of Dent 3 and Dent 6 after the creation of the initial dent.....	115
Figure 5.4: Dent 3 and Dent 6 models sectioned views: a) longitudinal; b) transversal.....	116
Figure 5.5: Snap thru: a) load-displacement buckling curve of spherical shell structures; b) schematic representation of a thin shell.....	118
Figure 5.6: Numerical and experimental profiles of Dent 3 and Dent 6 after the rerounding operation.....	120
Figure 5.7: Sectioned views: a) Dent 6 longitudinal; b) Dent 6 transversal; c) Dent 3 longitudinal; b) Dent 3 transversal.	121
Figure 5.8: Dent 3: a) Circumferential strain variation in all nodes over the last pressure cycle; b) Critical node location.	122
Figure 5.9: Dent 6: a) circumferential strain variation in all nodes over the last pressure cycle; b) Critical node locations.....	123

Figure 5.10: Stress- strain curves for the critical nodes of the models.....	123
Figure 5.11: Dent 3 node 1870 circumferential strain history.....	125
Figure 5.12: Dent 6 node 1847 circumferential strain history.....	125
Figure 5.13: Dent 3 circumferential strain history over the cycles of internal pressure for the most critical node.....	126
Figure 5.14: Dent 6 circumferential strain history over the cycles of internal pressure for the most critical node.....	127
Figure 5.15: Pressure load along the specimen life test: a) Dent 3; b) Dent 6.	129
Figure 5.16: Dent geometry after rerounding determined from 3D-DIC measurements: a) Dent 3; b) Dent 6.	130
Figure 5.17: Comparison between the longitudinal profiles measured with the DIC, the caliper and simulated with the first type of finite element model: a) Dent 3; b) Dent 6.	130
Figure 5.18: Circumferential strain measured by DIC: a) 3D view of Dent 3; b) Superior 2D view of Dent 3; c) 3D view of Dent 6; d) Superior 2D view of Dent 6.	132
Figure 5.19: 2D view of the depth of the specimens: a) Dent 3; b) Dent 6.	133
Figure 5.20: History of circumferential and longitudinal strains along the first stage of pressurization at the most stressed point of the dent.	134
Figure 5.21: Evolution of circumferential strain at points P0 and P1 of Dent 6 measured by DIC during the first two preliminary cycles and the first 100 cycles of the second block of pressurization.....	136
Figure 5.22: Distribution of circumferential strains on the outer surface (top view) of the models using the second type of FEM: a) Dent 3; b) Dent 6.	136
Figure 5.23: Circumferential and longitudinal strains measured by DIC and calculated by FE at the last cycle of the first load sequence for point P0 of Dent 3.	137

Figure 5.24: Circumferential and longitudinal strains measured by DIC and calculated by FE at the last cycle of the first load sequence for points P0 and P1 of Dent 6.	138
Figure 5.25: Schematic arrangement of the FBSGs, their positions measured by DIC and the comparison of the experimental and numerical results for the first pressurization block of Dent 3.....	139
Figure 5.26: Schematic arrangement of the FBSGs, their positions measured by the DIC and the comparison of the experimental and numerical results for the first pressurization block of Dent 6.....	140
Figure 5.27: Dent 3 history of strains measured by the FBSGs during the second block of pressurization.....	141
Figure 5.28: Dent 6 history of strains measured by the FBSGs during the second block of pressurization.....	141
Figure 5.29: TSA output: a) Dent 3 specimen magnitude; b) Dent 3 specimen phase angle; c) Dent 6 specimen magnitude; d) Dent 6 specimen phase angle.	143
Figure 5.30: TSA output (magnitude and phase angle) and the first invariant stress response: a) Dent 3 specimen; b) Dent 6 specimen.....	145
Figure 5.31: TSA, DIC and FE results plotted for points located at the meridional symmetric line: a) Dent 3 specimen; b) Dent 6 specimen.....	146
Figure 5.32: TSA magnitude around 1000 cycles of all tested dent specimens..	147
Figure 5.33: Graphic comparison between the stress concentration factor obtained with the different techniques presented in Table 10.....	149
Figure 5.34: Dent 3 TSA magnitude of the dented area taken at specific number of cycles showing crack development (after 3909 cycles) and through crack (after 21393 cycles).	150
Figure 5.35: Dent 6 TSA magnitude of the dented area taken at specific number of cycles showing crack development (after 4000 cycles) and through crack (after 6500 cycles).	151

Figure 5.36: TSA magnitude (converted in sum of principal stress ranges) measurements along the symmetry line inside the dent area showing the influence of crack propagation during the number of cycles.	152
Figure 5.37: Pre-selected interest positions for both specimen geometry.	153
Figure 5.38: Quasi-static IR method applied to Dent 6 point E.	154
Figure 5.39: Quasi-static IR method applied to all Dent 6 points.	155
Figure 5.40: TSA monitoring tool algorithm.	157
Figure 5.41: Dent 6 specimen TSA data for 1000 and 6500 cycles analyzed using the TSA monitoring algorithm proposed.	158
Figure 5.42: Dent 3 TSA crack monitoring.	159
Figure 5.43: Dent 6 TSA crack monitoring.	160
Figure 5.44: Dent 7 TSA crack monitoring.	161
Figure 5.45: API-579 Part 12 and PDAM fatigue curves for the longitudinal plain dent geometry plotted against the measured life of the specimens.	164
Figure 5.46: API-579 and PDAM fatigue curves for the humped dent geometry plotted against the measured life of the specimens.	164
Figure 5.47: Mean Stress fatigue curves for the longitudinal plain dent geometry plotted against the measured life of the specimens.	166
Figure 5.48: Mean Stress fatigue curves for the humped dent geometry plotted against the measured life of the specimens.	166
Figure 5.49: Comparison of the SN approaches for the longitudinal plain dent.	167
Figure 5.50: Comparison of the SN approaches for the longitudinal plain dent geometry.	167
Figure 5.51: Coffin-Manson fatigue curves all dent geometries plotted against the measured life of the specimens.	170
Figure 5.52: Comparison between the ASME SN carbon steel best-fit curve with an ϵN approach.	171

Figure 5.53: Coffin-Manson and the ASME fatigue curves plotted against the estimated life using the API 579-1/ASME FFS-1 - 2016 Part 14 methods A and B [66].	172
Figure 5.54: Dent 6 specimen results applying API 579-1/ASME FFS-1 - 2016 Part 14 [66] and different finite element models.	173
Figure 5.55: Comparison of all methodologies results with the actual fatigue life.....	174
Figure 5.56: Circumferential strain amplitudes calculated from the relationship between pressure and strain given by the DIC curve of Figure 5.23.....	176
Figure 5.57: Fatigue damage accumulation calculated from strain-cycle history presented in Figure 5.55.	176
Figure 5.58: Fatigue damage accumulation calculated from strain-cycle history determined from the relation between applied pressure and strains calculated from finite elements given in Figure 5.22.	176

Tables

Table 1: Pipeline incidents and percentage of occurrence [12].....	27
Table 2: Dent depths before and after the rerounding	67
Table 3: Types of IR tests that each specimen was subjected to.	74
Table 4: Material Properties (API 5L Gr. B) [62].	75
Table 5: Measured IR results for each specimen.....	81
Table 6: Average fatigue limit for each type of test.	81
Table 7: Average fatigue limit for each load ratio R and its standard deviation.	81
Table 8: Dented specimens pressure loads, cycles to failure and crack position.	112
Table 9: Stress and strain concentration factors at the critical nodes of the FE models.....	124
Table 10: Stress and strain concentration factors.	148
Table 11: Measured IR response for each dented specimen.	156
Table 12: Minimum and maximum pressures, the calculated alternate stress used in both methods and the ratio H/D for each dented specimen.	163
Table 13: Stresses used in the fatigue analysis.....	165
Table 14: Strains used in the fatigue analysis.....	169
Table 15: Alternate stress calculate with API 579-1/ASME FFS-1 - 2016 Part 14 and with FEM.	171
Table 16: Estimated life and the actual life of the specimens.	174
Table 17: Specimen Dent 3 pressure-loading history.....	175

1. Introduction

The consequences of structural failure are often catastrophic. Lessons learned from decades of experience, including some high profile accidents, have led to the development of rules and standards dedicated to managing the integrity risk associated with different types of flaws present in components and structures. The importance of structural integrity failures can be addressed from the viewpoint of its effect on the costs, estimated to be at least one hundred billions of dollars per year [1].

The increasing concern for safety and sustainability requires the development of risk management programs to mitigate and fully comprehend the mechanisms of damage associated with integrity failure. The appearance of small cracks in steel components is almost unavoidable, whether due to manufacturing processes, external damage, and continuous operation, not necessarily causing an imminent risk of failure, but surely impairing its functionality, accelerating its degradation and diminishing its service life.

In this context, fatigue emerges as one of most important and dangerous type of damage mechanism that leads to failure, being the object of study for more than a century. Bridges, buildings, airplanes, ships, pipes and pressure vessels - which are large, critical, and expensive structures – are often subjected to variable load amplitudes that may initiate and propagate fatigue cracks, which must be detected, located and dimensioned while in the safe range.

1.1 Infrared Thermography

The use of infrared (IR) thermography as a nondestructive evaluation (NDE) technique to analyze flaws is not new, being used in large scale to evaluate the delamination of composite polymer materials [2-4], crack inspection [5-9] and

estimation of remaining strength of components [5-10], playing an important role in manufacturing inspection and maintenance programs.

IR thermography for non-destructive testing and evaluation aims at the detection of surface or subsurface features (i.e. defects, anomalies, etc.).

In general, IR thermography measures temperature differences (ΔT) that occur at surface points of the investigated component during the inspection activity or during its continuous monitoring.

IR thermography is divided into two basic approaches: passive and active. The passive approach is used to investigate the surface of components that are at temperatures different from the ambient. In the case of the active approach, an external stimulus source (e.g. optical flash lamps, heat lamps, hot or cold air guns, etc.) is used to induce significant thermal contrasts, given that the objective is to detect defects.

Moreover, another very useful passive IR method is the thermoelastic stress analysis (TSA), having great applicability to structural assessment. TSA is a full-field noncontact technique which determines the elastic strain distribution actuating on the surface of interest during the component operation. TSA may have its sensitivity similar to that of strain gauges.

The main advantage of IR thermography over other techniques is that large surface areas can be rapidly analyzed without need of their destruction during testing, resulting in major savings not only in time, but also in terms of operational cost. In addition, there are some advantages of IR thermography over the other non-destructive techniques. The IR camera is risk-free, as it does not emit any radiation; it only records the IR radiation emitted from the material that is under assessment. Besides that, IR thermography is a global or full-field technique, whereas most of the other methods are either point or line methods.

1.2 Integrity of Pipelines

Pipelines present themselves as one of the most important and critical relevant structures for the modern society, because of the role they play under severe operation conditions during their lifetime. Pipelines represent the main way to transport liquid or gaseous products between two places. For certain volumes and distances, the transportation of fuel products by pipeline, when compared to other transport modes, is generally presented as a more advantageous, reliable and safe economic alternative, [11].

In transportation of oils and gases, structural failure concerns to the loss of containment, that is, the release of the product transported through the pipe. Releases of a product transported by such pipelines may affect surrounding populations, properties and the environment, resulting in injury or death as well as material damage to property and to the environment.

The reliable operation of a pipeline is dependent on maintaining the structural integrity of the system. Defects, that could compromise the safety, can be introduced into the pipeline at any point throughout its life cycle, that is, during the pipe manufacturing process, construction and operation.

Therefore, the study of its structural integrity deserves special attention, since mechanical damages can cause safety and environmental disasters as well as operational setbacks. Within the different types of pipeline damage, dents can be described as one of the most dangerous and hazardous for the welfare of the structures. According to the Office of Pipeline Safety of the United States linked to the Department of Transportation (DOT), between 2006 and 2010 14% of the incidents with pipelines were caused by ducts that contained dents [12]. Dents are generated from the impact of external elements such as construction equipment and rocks during the phases of construction and operation of the pipeline. A dent can be described as an inward plastic deformation on the cylindrical surface of the pipe, which produces a macroscopic change in its wall curvature and consequent modification of its stress state.

Cyclic internal pressure loading in a dented pipe is a potential danger to its structural integrity as a consequence of the stress concentrators and deformations

present in the dent region. The combined cyclic loading and stress concentrations can lead to fatigue cracks and consequently the failure of the pipe before reaching its service life [13].

Some occurrences of pipe failure associated with fatigue are shown in Table 1 [12], dent incidents are associated with external interference and fall under the category of excavation damage. It is observed that a large number of incidents started from external interference, and this high incidence of failures justifies the investigation program proposed in this work.

Table 1: Pipeline incidents and percentage of occurrence [12].

Pipeline/ Defect type	Material failure (%)	Incorrect operation (%)	Excavation damage (%)	Corrosion (%)	Geotechnical failure (%)	Vandalism (%)	Other (%)
Oil	36	10	14	24	6	3	7
Gas	31	4	14	20	6	9	16

Hence, the study of the influence of dents, which represents 14% of total pipeline incidents, on the reliability of structures is extremely relevant, e.g. [14], since their failure and loss of containment can cause severe damages. Thus, predicting, monitoring and detecting fatigue flaw in pipelines caused by the existence of dents have been of paramount importance¹.

In this thesis, IR thermography was applied as a non-destructive testing and quantitative evaluation technique together with other modern experimental techniques, such as: digital image correlation (DIC) and fiber Bragg strain gauges (FBSG), to predict and monitor fatigue initiation and fatigue damage progression in real scale 3m long pipeline specimens (with nominal dimensions: 324mm external diameter and 6.35mm wall thickness) made of API 5L Gr. B steel, containing complex-shaped dents. The results obtained with the experimental techniques were also coupled with finite element method (FEM) simulations to fully assess the dented specimen behavior.

¹ By extension, to piping and pressure vessels with dents.

1.3

Literature Review About Infrared Thermography Applied to Flaw Assessment

The first applicability of an IR sensor was in Britain for aircraft detection, in 1929. The first kind of thermographic cameras developed were IR line scanners used for military purposes. Over the years the use of IR cameras became more widespread, being used for detection and assessment of defects. Barenblatt et al. [15] was one of the precursors in this kind of the study, proposing a theory which correlated appreciable temperature rise in the tip of a crack.

This assumption was confirmed by Attermo et al. [16], who used an AGA thermosetting camera to test several specimens made of three types of polymer and austenitic stainless steel.

Through the evolution of thermal cameras technology, new findings could be achieved. Charles et al. [17] used IR thermography to scan and visualize the surface temperature field on steel and on fiberglass-epoxy composite samples during fatigue tests, being able to predict the probable location of the critical fatigue damage well before any damage could be visible in the form of a crack.

Through the use of the IR scanning to map temperature fields it was possible to determinate stress concentration sites in cyclically loaded materials, and to establish a method to determine the fatigue strength [18,19], Figure 1.1. Different measurement methods to study the dissipation of energy in a solid subjected to cyclic fatigue until failure were conducted [20].

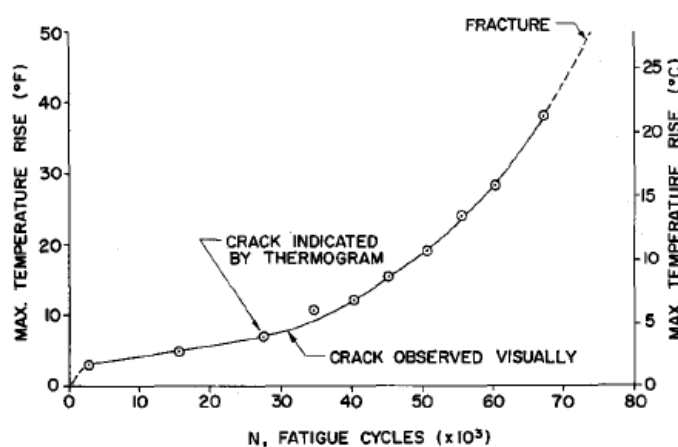


Figure 1.1: Maximum temperature rises above ambient during cyclic test [18].

Continuing this line of research, Catalbino et al. [21] and Geraci et al. [22] used IR thermography to investigate surface temperature variations during fatigue tests. They observed that only for loads above the fatigue limit the specimen presented a considerable increase in temperature. Moreover, they located the critical spot where the sample would break after some cycles if subjected to a cyclic load superior to the fatigue limit.

Based on these observations a new method for the rapid determination of fatigue limit was proposed and tested by Risitano and coworkers [22-26]. In their method, they plotted the measured temperature of a critical point against the applied cyclic stress range and related the fatigue limit with the instant where the slope of the temperature curve changed. This method significantly reduces the testing costs by decreasing the quantity of required specimens and by decreasing the testing time. In general, only three specimens are needed in practical applications to determine accurately the fatigue limit.

Blarasin et al. [27] used the method proposed by Curti et al. [24] to direct test a mechanical component (a rod). Similarly, Loung et al. [28-31] proposed a method to determine the fatigue based on the evaluation of the change of slope of the temperature response. However, this methodology is less conservative than the one proposed by La Rosa and Rititano et al. [23].

On the same line of analysis Fargione et al. [32] proposed a methodology to obtain the fatigue curve of the tested material based on the method of Risitano et al. [26]. Results shown a correlation between the energy supplied per unit volume and the fatigue resistance of the materials tested and established a direct and rapid correlation between the damage until failure with the energy dissipated during the cyclic loading.

Some innovations in the methods of determining the fatigue limit using cyclic loads were proposed. As an example, a new iteration to estimate the fatigue limit more accurately was proposed by Cura et al. [33] as an improvement of the methodology presented by [28-31].

More recently, a new and fast method to determine the fatigue limit using IR thermography was proposed by Risitano and coworkers [34-38]. It analyzes the thermal variation in quasi-static uniaxial tensile tests.

1.4

Literature Review About TSA and Its Applications

Thermoelastic Stress Analysis (TSA) is a technique based in the thermoelastic effect that is built on the linear relationship between the temperature change in a solid and the change in the sum of principal stresses for an isotropic material. Through the measurement of the stress field it is possible determine stress concentrations, predict and monitor the evolution and behavior of cracks and macro discontinuities

TSA is a relatively young experimental technique. It emerged in the 80's as a consequence of advances in instrumentation and equipment such as the SPATE 8000 [39]. In the last 20 years it has developed extensively as a consequence of major progress in the field of high-resolution IR detectors [40].

Earlier works date from the 19th century. Weber et al. [41] observed that when a vibrating wire receives an increase in tension, it experiences a change of temperature. Although not been able to determine neither the stress field nor quantify the temperature variation, this paper set the basis of the thermoelastic effect. Later on, Willian Thomson, the Lord Kelvin, established the theoretical foundation of the thermoelastic effect, but despite some mathematical advancement in refining the theory it was only in 1967 that Belgen et al. [42, 43] conducted the first non-contacting experiment in a cantilever beam.

TSA has been used as a non-destructive testing technique to determine the damage parameters for predicting the remaining life of structural components as can be seen in Bakis et al. [44, 45], Sakagami et al. [5-10], and Lesniak and Boyce [46].

Among the applications, thermoelasticity has been widely used for fracture mechanics studies, determining stress intensity factors (SIF) and crack growth rate, requiring high stress sensitivity and spatial resolution because of the localized stress gradients [47].

The combined use of thermoelasticity and other numerical and experimental approaches to separate principal stresses in a variety of elasticity problems [48] and in order to calculate SIF's and J-integral for cracks has been proposed by innumerous researches.

Stanley and Chan et al. [49] used the first two terms of the Westergaard's stress function to fit the thermoelastic data near a crack under opening modes I and II.

Stanley and Dulieu-Smith [50] shown that the isopachic contour in the crack tip region looked like a cardioid shape. Lesniak et al. [51] used Airy stress functions to fit the data using the least squares method (LSM). Lin et al. [52] developed a hybrid method based on equilibrium, compatibility and the J-integral. They used far-field thermoelastic data to determine the stress intensity factor.

Tomlinson et al. [53] used a multipoint-over-deterministic method (MPODM) along with on Muskhelishvili's stress field equations to describe the crack tip stress field. Díaz et al. [54, 55] proposed a TSA methodology for finding the crack tip location, and then fitting the data using a non-linear approach to determine SIF's of propagating cracks. Tomlinson and Olden [56] presented a broad review on the use of TSA in fracture mechanics and fatigue cracks.

Vieira et al. [57] used a hybrid approach to calculate the SIF and to predict crack growth rate in polycarbonate specimens using TSA and temperature measurements.

Paiva et al. [58] carried out an experimental calibration of the thermoelastic constant for low carbon steel specimens using a FLIR A655sc camera, relating the measured temperature with the TSA response signal. After that, superficial stress distributions of chain links were measured with TSA and compared with FE results. Paiva et al. [59-64] conduct an investigation program to assess pipeline specimens containing dent defects using IR thermography. In these cases, the component behavior was evaluated, and the material properties were quantified using the thermal response.

Figure 1.2, below, presents the evolution of TSA over the year, from discovery to the present day.

200 Years of Thermoelasticity

Data from "Thermoelastic Stress Analysis" Harwood and Cummings, 1991

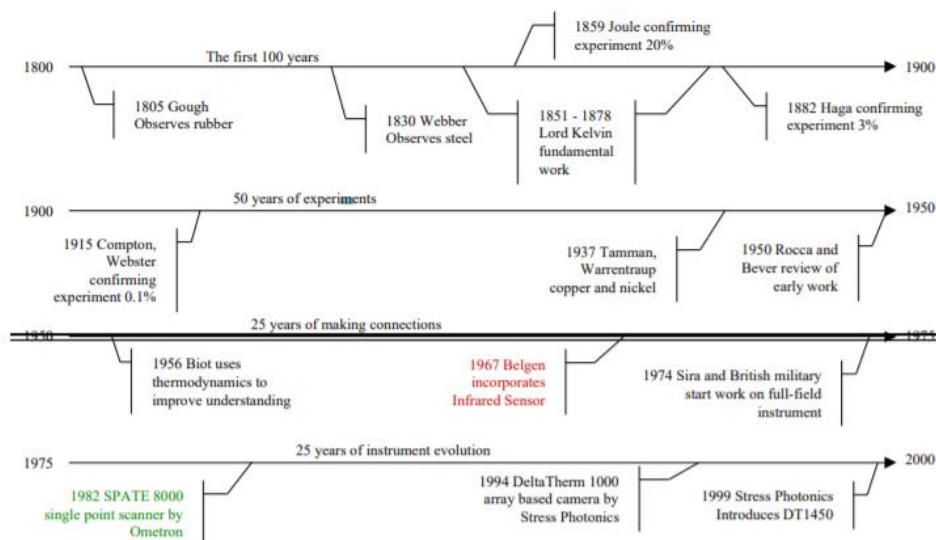


Figure 1.2: Timeline of some important steps in the development of TSA [65].

1.5 Literature Review about Dent Assessment

There are several approaches available in the literature to assess dent flaws. Depth criteria are the most frequently used in the industry for their ease of application. Various studies using different methodologies related to dents in pressurized pipelines were undertaken to understand and assess the severity of such flaws.

1.5.1 Standard Approaches

The standards API 579-1/ASME FFS-1 - 2016 Part 12 [66] proposes an approach considering membrane tensions and resistance factors. A different criterion proposed by ASME B31.8-2016 Appendix R standard [67] combines both depth and deformation.

In this way, similarly to the ASME B31.8-2016 [68], which is applied to gas pipelines, the standard the ASME B31.4-2016 [67] evaluates the dents effects in oil pipes.

The API 1156-1999 standard [69] is based on an experimental study to assess the static and cyclic behavior of pipe specimens with dents. It considers a number of variables, such as: dent depth, indenter type, pipe diameter, pipe wall thickness, smooth and sharp dents, constrained and unconstrained condition, stress concentrations, proximity of the dent to corrosion flaws, welds, and the effect of hydrostatic rerounding.

The European Pipeline Research Group (EPRG) first developed an empirical model [70] for predicting the fatigue life of a smooth dent. Based both on dent maximum depth and on the maximum operation stress the model calculates the fatigue life of a pipe modified by the stress concentration due to the dent using the fatigue strength-fatigue life (SN) curves for submerged arc welded pipes given in the DIN 2413 standard [71].

After a review [72], it was proposed a semi-empirical method for predicting the fatigue life of dented specimens, which was still based on the SN curves of DIN 2413 standard [71] using a dimensional stress concentration factor (K_t) as a function of the remaining depth of the dent. Besides modifying the way of calculating the stress concentration factors, the review also included the topic of dents combined with gouges.

The pipeline defect assessment manual, also known as PDAM [73], is a guideline that presents the best practices to assess several types of failure in pipelines. It is based upon an extensive literature review. This guide evaluates constraint and unconstraint dents based on the relation between the depth and the pipe diameter and recommends methods to predict the burst pressures of dents (plain and with other forms of damage) in piping subject to internal pressure. It is based on the first methodology developed by the EPRG and provides less conservative fatigue life results compared to those provided by the general procedures of BS 7910 [74] and API-579 [66] standards.

The fatigue life prediction methodologies are based on different criteria and were validated by experimental and numerical data. A large amount of the approaches utilizes finite element method (FEM) to estimate the stress and strain distributions along the pipe wall and around the dent region, relating them to the applied internal pressure. The damage accumulation and failure approaches utilized

in the various methods include stress-life (SN), strain-life (ϵN) and fracture mechanics approaches.

Due to the wide availability and variety of stress-life curves available in both open literature and in the various international standards and regulations, the stress-life method is the most used one. Some examples of using stress-life based methods can be seen at Fowler, et al. [75], Alexander et al. [76] and Rosenfeld et al. [77, 78]. The dent fatigue assessment method proposed by the API 579-1/ASME FFS-1 - 2016 Part 12 [66] is based on stress-life methodology proposed by the revised EPRG method [72].

Part 14 of the API 579 standard [66] presents level 1 and level 2 general methods that can be applied to fatigue assessment of dents. These methods are also presented in ASME Sec VIII div. 2 [79], which provides a number of criteria for verifying the need of a fatigue analysis, and if this is necessary, two more approaches for calculating alternate stresses: the elastic and the elastic-plastic approaches. The elastic approach, uses a penalty factor due to the existence of possible plastic deformations. The elastic-plastic approach uses the strain-life or ϵN method.

1.5.2 Others Approaches

Pinheiro et al. [80] performed experimental fatigue tests out on small scale pipes containing dents produced by a semispherical indenter. By means of a numerical model using finite element analysis (FEA), two equations were adjusted to calculate the stress concentration factor of dents in pipes with axial restrains. In continuity with this line, Pinheiro et al. [81, 82] updated the equations previously obtained, and proposed an equation based only on the dent depth. Cunha et al. [83] used the Gerber parabola to consider the effect of the mean stress on the SN curve, estimating K_t for longitudinal plain dents.

In 2007, Ávila [84] utilized the SN method to predict the fatigue life of small scale pipe specimens. The mean and alternate stress components were calculated using the FEM and three load conditions were applied.

Silva et al. [85], evaluated the fatigue life of pipes containing unconstrained spherical dents. The SN methodology was used and the effect of the mean stress, calculated by the FEA, was taken into account by a Gerber curve. The results were validated by experimental data available in the literature [86].

Other approaches focused on the development of strain fields after the formation of a dent [87-89]. Strain distributions in pipe walls have two major components; longitudinal and circumferential strains. Each of these can be split into bending and membrane components. The bending component of the strain changes linearly from the inner to the outer surface [90].

In-line inspection tools can provide accurate data from which the dent shape can be obtained and combined with the use of FEA to evaluate the dent strain distribution.

Noronha et. al. [91] examined equations presented at ASME B31.8 standard [67] and proposed corrections to them. A procedure based on a fourth order B-spline curves, that interpolate the dent contour obtained from the data extracted by in-line inspection tools, was also presented.

Paiva et al. [59, 60, 61, 92, 93] studied the behavior of re-rounded dents using a strain-life approach. These references conducted an experimental investigation using DIC coupled with FEA to determine the actual dent shape and strain distributions over the deformed regions.

1.6 Motivation

There are numerous approaches available in literature that address the assessment of fatigue damage, especially in pipelines with dent defects. Managing safety is expensive. As a result, there is a need for methodologies that can provide an analysis criteria which can be used as a tool to incorporate reliability in the component performance.

Some problems related to localization of hot spots and determining stress and strain concentrations arise when evaluating, predicting and monitoring the fatigue flaw behavior during the operation of a structural component. Experimental and

numerical methods are two important ways to help solving those problems in order to assess the fatigue life of structures.

Experimental methods such as DIC, strain gauging (electric resistance) and FBSG are techniques that are well developed and widely applied in assessing strain concentrations.

FEA, in which many analysis methodologies are based on, becomes a much more viable approach in structural life prediction. Of course, knowledge of the hot spot geometrical shape and material behavior must be granted for an accurate assessment.

Conventional methodologies for measurement and determination of the material fatigue properties are often a laborious task, involving the realization of numerous tests. In spite of that, they are extremely necessary in order to truly comprehend the functionality of the material.

IR thermography emerges as a viable nondestructive real-time alternative to provide wide information about the behavior of structures, measuring the full stress field distribution, monitoring the development of a fatigue crack and helping the fast determination of the fatigue behavior of the specimen material. With relation to the material behavior, IR thermography can be used to determine the fatigue limit and the fatigue curve of the component material in a much more fast and easy way.

Moreover, TSA is a relatively simple experimental technique for surface stress measurement, especially in terms of the required surface preparation. TSA yields the change in the sum of the principal surface stresses during a loading event, and is particularly well suited to the study of components undergoing cyclic fatigue or vibration testing.

Regarding pipeline suffering from fatigue failure occasioned by the combination of dents and cyclic internal pressure, some problems in the current analysis methodologies can be listed below:

- The majority of works focus on the stress-life analysis, disregarding the effects of plastic behavior in the flaw affected region.

- Some methodologies that use the strain based criteria do not deal with the problem of the previous strain history related to the component fabrication and the dent creation process.
- There are not studies that fully investigate the combined effect of different parameters such as dent depth, dent shape, and the influence of internal pressure on modifying the dent shape and consequently the strain distributions along the cyclic loading processes.
- One of the main challenges in assessing dents is to fully determine the format of the dent. Although general shapes such as plain, spherical and transversal are widely studied, unique shapes with miscellaneous forms, that are more similar to the actual shapes found in the field, are not covered by the available literature. Most times, only the maximum depth is taken into account, disregarding the global format of the dent
- The acceptancy criteria are generally based on the dent depth; there is no approach for pipes containing dents with high deformation levels, e.g. depth to diameter ratios above 7%.
- The availability of reliable dent shape data is difficult to be determined by in line inspection tools. Generally, the only information provided is the maximum dent depth and the location of the defect in the line. Unless an excavation is performed, the geometry, diametral position and the constraint conditions of the dent remain unknown.
- Measurement of stresses at the hot spots have been only done by electric strain gauges [82, 94]. As a consequence, the fully stress/strain fields at the dent and around it remains unknown due the punctuality of the gauge measurement. Moreover, the measurements depend on the position in which the strain gauges are placed. Thus, if the positioning is not adequate, in a region of high deformation, the measurement will not represent the real critical strain state.
- There is few availed information about the acceptance of pipes containing re-rounded dents. The final shape of the dent depends on the pressure applied in the re-rounding.

1.7 Thesis Objective

Real time fatigue assessment is an arduous task. Often, locating the initial damage is impractical, due to the functionality of the structure and to the applicability of the select evaluating method. Therefore, fast and reliable crack detection and crack propagation monitoring by means of some automatic procedure is highly needed to replace slow and subjective inspections. Most of the experimental techniques traditionally used, e. g. electrical resistance strain gauges, in fatigue analysis provide local information about the analyzed component, making it difficult to specify the exact time instant and position of initiation of a fatigue crack.

Although different assessment techniques are employed and, when possible, synergic combined in this work, a special attention will be given to the thermographic techniques (IR thermography and TSA), because they are less known and widespread in the literature.

IR thermography provides surface data that can be used to assess both the mechanical and fatigue behavior of complex-shaped components without the need of contact and with lower computational cost, determining the critical hot spots susceptible to failure, helping to determine material properties and tracking the growth of a developed flaw.

As a result, this thesis aimed establishing a methodology to determine the fatigue damage behavior of full-scale dented pipeline specimens subjected to cyclic pressure loading. The specimens were made of 3 meter long API 5L Gr. B steel, with 12.75" (323mm) outside diameter and 1/4" (6.35mm) thickness. A combination of modern experimental and numerical techniques was used such as IR, DIC, FBSG and FEM.

The objectives can be summarized as follows:

- To use the IR thermography as a fast and efficient alternative to measure the fatigue properties of the specimens material: the fatigue limit and its SN curve.

- To simulate using FEA the process of creation of a plain longitudinal dent with final depth after re-rounding of about 15%, with emphasis on obtaining the forces and displacement necessary to carry out the indentation process and the re-rounding pressure needed.
- To measure the strain fields of the whole dented region using the DIC technique during the realization of a series of preliminary cyclic loads.
- To measure and monitor the strain at specific locations using FBSG during the realization of the fatigue test.
- To provide the dented region shape measured by the DIC technique as an input to a FEA for simulating the stress-strain behavior of each individual specimen accurately.
- To use the TSA to measure the stress during the realization of the fatigue test and monitor the development of fatigue crack at the hot spots.
- To compare results of strain fields or determined using the experimental and numerical techniques.
- To perform an evaluation of the fatigue life based on traditional SN approaches present in the literature.
- To perform an evaluation of the fatigue life based on the strains measured and calculated by the experimental, analytical and numerical techniques using the Coffin-Manson strain-life equation and Miner's fatigue damage rule.
- To propose an approach to assess fatigue damage of components with complex-shaped dents using standard SN methods available in literature and strain-based methodologies.

1.8 Thesis Outline

This thesis is divided in six chapters. The first is the introduction and presents the objectives. The second has the relevant theoretical background needed to develop the work. The third one presents an investigation about the material behavior and the utilized experimental procedures. The fourth describes the analysis methodologies and how the methods were employed, especially how the combination of different techniques can be of major importance for ensuring structural health. The fifth chapter reports findings on fatigue flaw assessment and discusses such results. Finally, the sixth chapter draws conclusions and suggests future works.

2. IR Thermography

IR thermography is an experimental technique that allows the thermal mapping of a body or a region through the use of a thermal camera, in order to distinguish areas with different temperatures. It is a technique that allows artificial visualization of light within the IR spectrum. It is within the group of techniques known as full-field, real-time and non-contact, having wide range of application in research as well as in different fields of industry, such as nondestructive testing, condition monitoring, and predictive maintenance [95-100].

Most equipment failure modes, whether electrical, mechanical and process, are signaled by a significant rise in operating temperature before failure occurs. IR thermography can detect heat patterns in the IR wave length spectrum that are not visible to the naked eye. These heat patterns can identify the deterioration of the component before the catastrophic failure.

The non-contact nature of IR thermography technique makes it ideal for a wide range of applications where components is in motion, at elevated temperatures, the contact is dangerous, it is difficult to reach, impossible to shut off and could be contaminated.

Unlike early thermal cameras that were large, very expensive, difficult to use, slow to acquire data, and offered poor image resolution, competition in the segment of thermal cameras has recently led to the introduction of low-cost models at a price level of only several thousand dollars. The technology has evolved to produce compact, ergonomic cameras that are easy and fast to use, are much more affordable and provide high resolution images, which has opened new application fields for IR thermography.

The physical principles of IR thermography and its particularities are presented in Appendix A.

2.1

Active Thermography X Passive Thermography

Active thermography is an imaging technique for non-destructive material testing. There are situations where no natural temperature differences are present or, if present, they may not be sufficiently strong enough, or the component may be too thick for an identification of structural discontinuities below the surface. In these cases, the heat flow induced by an excitation source in the studied object, which can be done with a transmissive or a reflective setup, is influenced by interior material layers and defects. These inhomogeneities can be captured on the object surface by IR cameras during the heating or cooling processes [101].

Active thermography works detecting passive defects. This type of defect has this denomination because it has the same temperature of the structure in its ambient operating condition. Therefore, an external excitation is required to induce a temperature contrast between the defective region and the region without defect [102]. The additional application of different evaluation algorithms improves the signal-to-noise-ratio, which allows for detection of small defects. Figure 2.1 shows an example of pulsed active thermography applied in detection of defects in anticorrosive coatings:

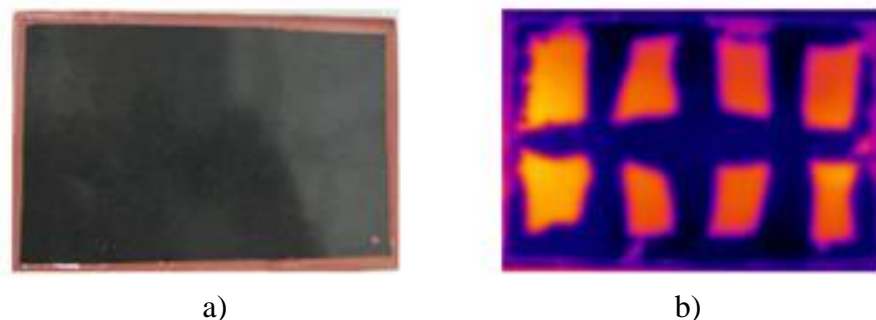


Figure 2.1: Active pulsed thermography applied to detection of defects in anticorrosive coating: a) visual condition; b) inspected condition [103].

Active thermography can be classified into: Pulsed, Pulsed Phase, Step Heating, Locked, Pulsed Eddy Current Thermography and Vibro-thermography, each of them with their specific characteristics related to the type of thermal excitation used and temperature data obtained in the sequence of thermograms [104].

Figure 2.2, presents a schematic setup for active transmissive thermography:

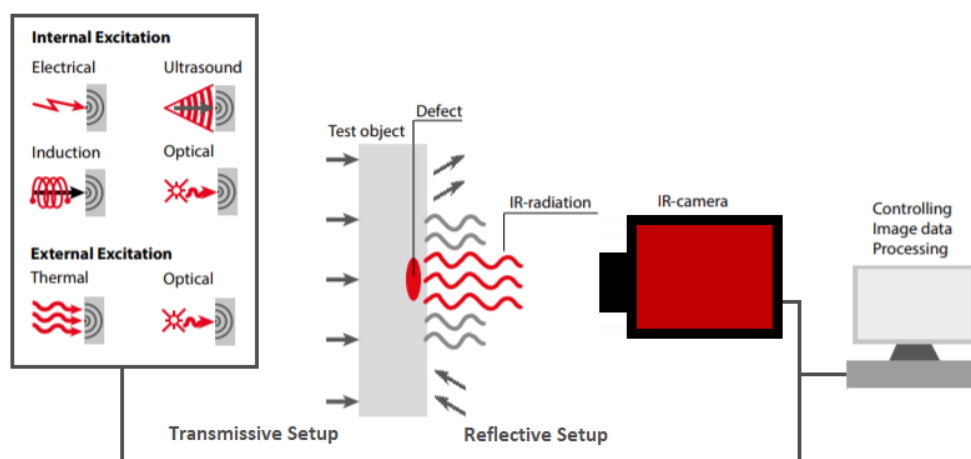


Figure 2.2: Schematic setup for active transmissive thermography.

On the other hand, in some applications of IR thermography, the investigation is done passively, which means that the camera observes a scene and detects the thermal radiation emitted from the objects. Because of the thermal radiation from the surroundings, a thermal contrast in an image is only observed if temperature gradients exist. This method is called passive since the existing temperature distribution of the object is analyzed without imposing an additional heat flow to the object.

Passive thermography techniques are based on the fact that all bodies experiencing some kind of deformation have a change of its internal temperature related to the deformation level that they are submitted. Temperature changes when loading is applied, tension causing cooling, compression causing heating. In zones of stress concentrations these effects are more pronounced. In metals, e.g. steel and aluminum, these changes are of the order of thousandths of Celsius degrees for small elastic strains, while for plastic deformations changes may reach several Celsius degrees. These thermal variations, characterized by significant heat generation, enable detection and estimation of plastic zone propagation, crack propagation and the final fracture.

Passive thermography has many applications in different fields; non-destructive inspections, military, medical and experimental mechanics. Figure 2.3 shows different examples of the use of passive thermography.

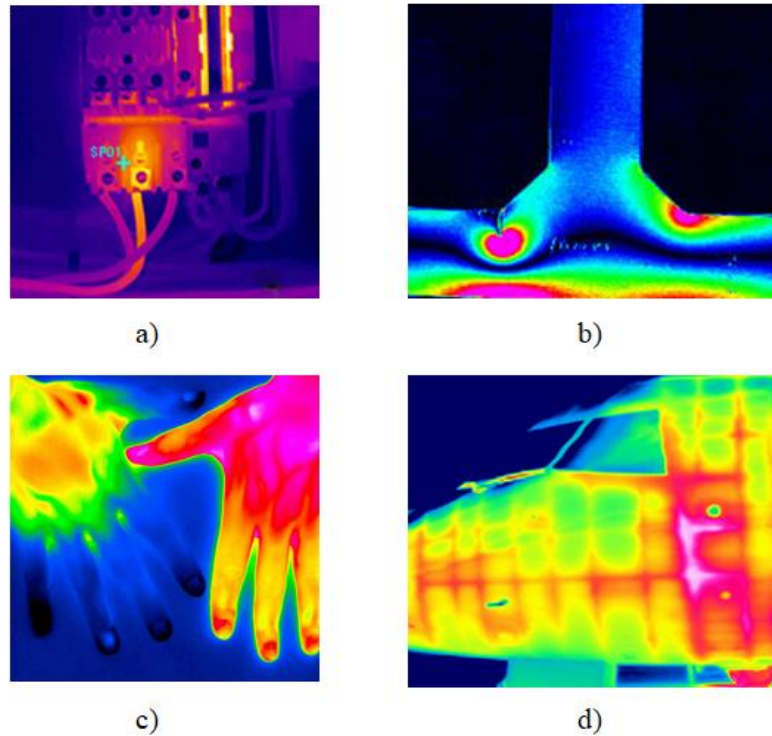


Figure 2.3: Different used of passive thermography: a) Detecting of electrical flaw; b) Stress measurement - TSA; c) Medical application; d) Inspection of plane fuselage.

2.4 Passive Thermography Applied to Experimental Mechanics

Among applications, the use of passive thermography to study experimental mechanics problems has grown over the last decades and has become an increasingly versatile approach. Two applications, fatigue strength estimation and thermoelasticity, are presented herein this section.

2.4.1 Fatigue Strength Estimation

The use of IR thermography methods in fatigue characterization consists on the measurement of the temperature rise on the external surface of the tested specimen during load application in order to identify a singular transition from a conservative and non-damaging state of energy to a dissipative and damaging one [24-38].

Fatigue damage is an energy dissipation process that is accompanied by some temperature variation. IR thermography procedures to measure and estimate the fatigue properties of the materials, such as the fatigue limit and the SN curve, have become fast and accurate alternatives. In comparison with traditional methodologies, IR thermography presents itself as a faster and less expensive alternative, needing few specimens, usually only three, and less testing time to provide accurate estimations. It has been reported variations of about $\pm 15\%$ between the thermographic methods and the traditional ones [26].

2.4.1.1

Fatigue Limit: Cyclic Method

According to the methodology proposed by La Rosa and Risitano et al. [26] and by Loung et al. [28-31], when the specimen is cyclic loaded below the fatigue limit, its temperature varies very slightly due to the thermoelastic effect. Alternated stress amplitudes ($\Delta\sigma_i = \sigma_{ai}$) above the fatigue limit the temperature induce significant temperature variations. The temperature variation according to a given reference, ΔT , may be classified along the test inside three phases.

Figure 2.4 presents the temperature variation with the number of cycles N for the test where the stress amplitude, $\Delta\sigma_i$, was made constant. It increases during the first part of the test (Phase 1), then remain stable for a while (Phase 2). If the load is above the fatigue limit, it finally and rapidly increases prior to failure at a life of N_f cycles (Phase 3), as shown.

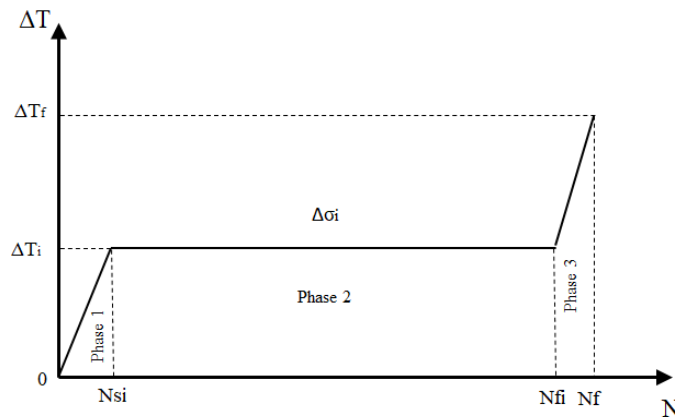


Figure 2.4: Phases of the thermal behavior of ΔT vs. N curve for a hot spot in the specimen surface during typical fatigue tests, adapted from [26].

Although several specimens subjected to constant and different values of $\Delta\sigma_i$ can be used to generate curves, such as presented in the Figure 2.4, a procedure using only one specimen can be used to achieve the same objective.

The one specimen test procedure requires a sequential of constant stress range increments to be applied in a stair case pattern, during a pre-established number of cycles. The fatigue limit can be evaluated considering the heating rate ($\Delta T/\Delta N$) or the stabilized temperature increment ΔT_i , reached for each stress level, $\Delta\sigma_i$, Figure 2.5.

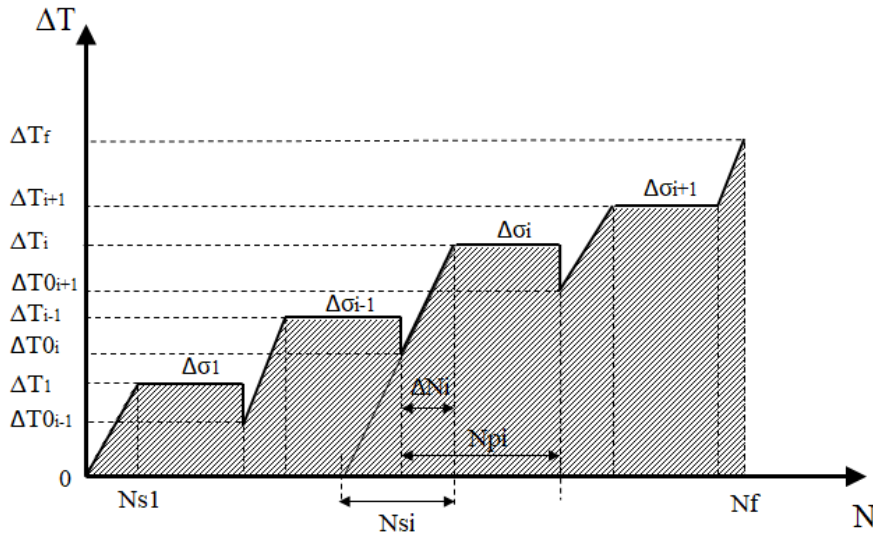


Figure 2.5: Stepped loading procedure for the determination of the fatigue limit.

Through the analysis of the temperature response curve under incremental cyclic step loading the fatigue limit can be evaluated by plotting the stabilization temperature increment (ΔT_i) vs. the stress range ($\Delta\sigma_i$), as presented in Figure 2.6. Although very similar, the methodologies proposed by La Rosa and Risitano et al. [26] and by Loung et al. [28] are slightly different. The Risitano method is more conservative using the intersection of a single regression line, which fits the data above the fatigue limit, and the horizontal axes (stress range). Loung method uses two linear regression lines to approximate the thermal data and determine graphically the fatigue limit. The basic principle is that the data above the fatigue limit produces damage dissipating a considerable amount of energy in the form of heat, and the data below do not affect the welfare of the material. Figure 2.6, shows an example of determination of the fatigue limit using the two methods:

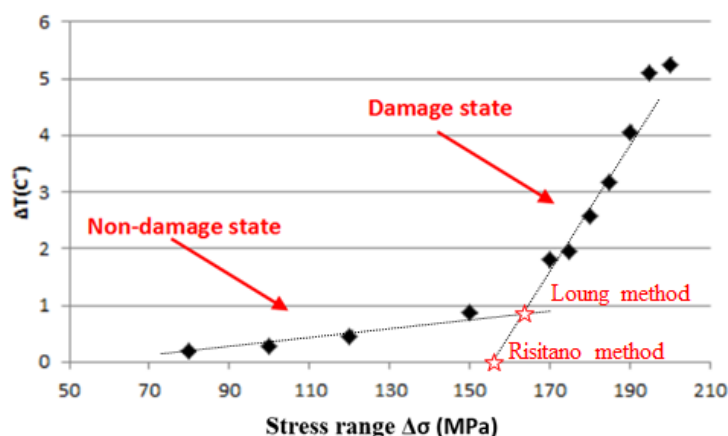


Figure 2.6: ΔT_i vs. $\Delta \sigma_i$ curve for various incremental load steps and determination of the fatigue limit (intercept of the two straight lines) [64].

2.4.1.2

Fatigue Limit: Quasi – Static Method

As stated by the theory formulated by Risitano et al. [35-38], energy dissipation caused by the application of a loading is an indication of damage. Starting from this premise, any load above the fatigue limit, whether static or cyclical, can cause the initiation of a flaw and has a thermal response.

Fatigue happens for loads capable to induce local plasticity in the material. The determination of the change of the behavior from a non-damage to a damage state involves the determination of the change of temperature correspondent to the initiation of first plastic local deformation [38].

When a material experiences a quasi-static load not all its crystals reach their elastic limit at the same time due to several non-homogeneities (crystal orientation, microstructural defects, dislocations, grain size and heterogeneity, etc.). Consequently, while some material points present elastic deformation, other points present plastic deformation. The temperature behavior can be subdivided into four stages, Figure 2.7:

Stage I - The load is so small that all the material points inside its crystal grains are elastically stressed.

Stage II - The load is such that most crystals grains deform elastically, but some small regions of them present plastic and elastic deformation together. As the

elastic part is majoritarian, when the sample is unloaded it regain its original shape. Macroscopically, the material body seems to have behaved perfectly elastic.

Stage III - The load is such that some crystals deform elastically together with others that present plastic deformation. When unloaded the material body does not regain its original shape presenting measurable permanent deformation.

Stage IV - The load has reached levels where the plastic deformation is such that most material points are plastically deformed. When the load ceases the permanent deformation becomes apparent.

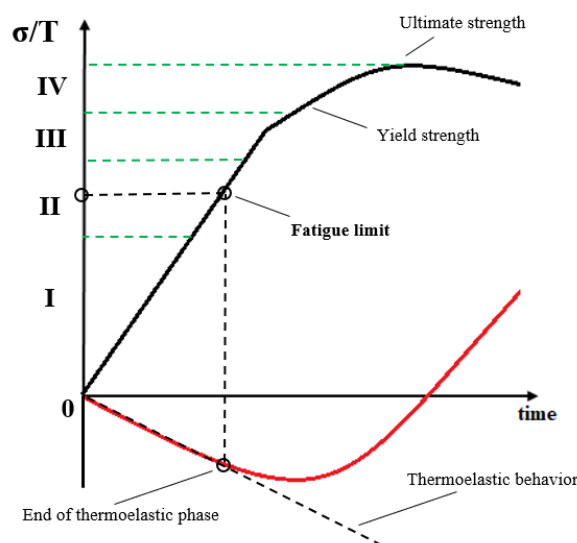


Figure 2.7: Stress-strain and temperature curve.

In some apparently perfect metals, Stage I is very limited. The internal stresses between the zones deformed elastically and plastically give rise to an 'after-elastic' effect in polycrystalline metals. This effect is linked to elastic hysteresis.

Fatigue failures occur at points where the local stress is higher than the local material strength, being able to induce plastic deformation. This phenomenon happens due to the presence of microstructural stress heterogeneity where some sites of higher stresses coincide with sites of microstructural defects that decrease the material strength. During a static tensile test, the micro-plasticization process occurs in Stage II, Figure 2.7.

The material thermal behavior during a tensile static test has two distinguish phases; in the first phase, in which all crystals are deformed in an elastic field (stage I, Figure 2.7), the stress-strain relation is linear in the macroscopic and microscopic

sizes. In the second phase, not all crystals are elastic deformed, and some are already plastically deformed (zone II, Figure 2.7). Although in this phase a macroscopic view of the stress-strain curve is a straight line, the temperature curve undergoes a change of slope characterized by the accumulation of plastic damage in the material.

In the first phase, the behavior of the material follows the thermo-elasticity theory. In the second phase this behavior becomes non-proportional.

For the quasi-static method, the fatigue limit is defined by the stress corresponding to the first noticeable deviation of the slope of the temperature curve that occurs in the uniaxial tension test, in which plastic local conditions are reached and generate a considerable volume of plastically damaged material that is detectable by using IR thermography. This slope deviation point is related with the fully alternate fatigue strength, valid for the stress ratio $R = \sigma_{min}/\sigma_{max} = -1$ [35-38].

2.4.1.3 Fatigue Limit: Ultra-Rapid Cyclic Method

Similar to the cyclic method, the ultra-rapid cyclic method uses cyclic loads to determine the fatigue limit based on the change of the thermal response of the material. The great innovation is the need of only one alternated load amplitude, instead of the stair case pattern previously required. This test, besides being much less expensive, is also much faster.

The principle of the test is to use a specimen whose geometry makes possible the existence of sections or points presenting different stress ranges, like a hole or a variable cross-section. The method requires the application of a single cyclic load above the fatigue limit for the most stressed sections, in order to produce a stress gradient along the specimen.

The load must be such that the critical section of the specimen is at a high stress state, above the fatigue limit, while some portions remain beneath it. One of the advantages is the application to components that have variable geometry and consequently stress gradients, being able to measure the fatigue limit during its own operation without much effort.

Figure 2.8 presents a schematic of the application of the ultra-rapid method:

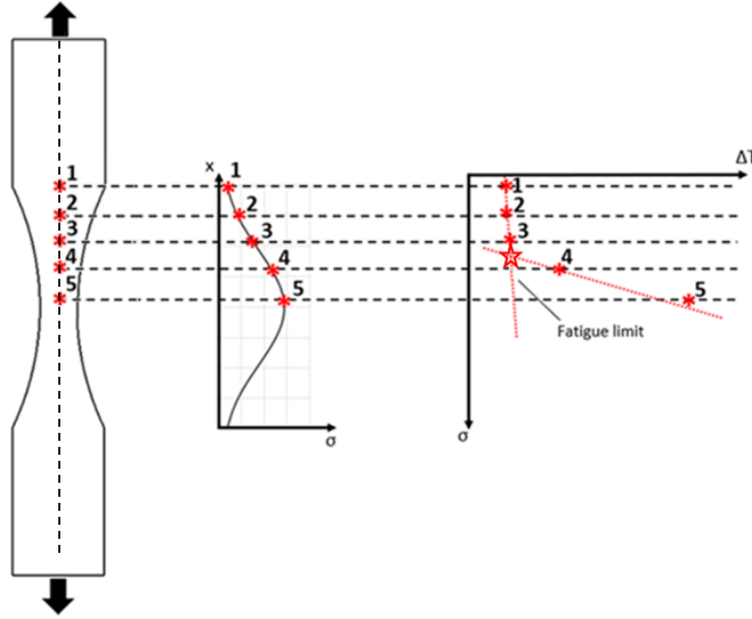


Figure 2.8: Schematic of the application of the ultra-rapid method using a dog bone specimen.

A similar extension applicable to a quasi-static test is currently under development.

2.4.1.4 Fatigue Curve Method

Extending the cyclic methodology used to determine the fatigue limit [35-38], Fargione et al. [32] proposed a method to determine the fatigue life SN curve of the material using IR thermography.

The concept behind the method is the correlation of the plastic deformation energy (E_c) with the material fatigue failure, which can be described according to Eq. (10):

$$E_c = \int_0^{N_f} E_p dN \quad (10)$$

where, E_c is the amount of micro-plastic deformation energy to failure per unit volume, a material property, N_f is the number of cycles to failure and E_p is the energy due to yielding per unit volume per cycle.

Using the energy balance to correlate the work done at the system (E_w) with the stored energy (E_i) and the energy converted into heat (Q), Eq. (11) is obtained:

$$E_w = E_i + Q \quad (11)$$

Assuming that the stored energy is small compared to the energy converted in heat (under 100K, implicating small loading frequencies), and using the assumption that E_w is proportional to E_p for small variations of temperature:

$$E_c = \int_0^{T_f} dQ \quad (12)$$

The energy dissipated in the form of heat, Q , from the specimen to the environment can be considered proportional to the temperature difference ΔT . Because of that, a parameter called ϕ , which is the integral of the ΔT vs. N curve, shown in Figure 2.5, is assumed constant for given test conditions, such as the specimen geometry and material, loading frequency and environment.

$$\phi = \int_0^{N_f} \Delta T dN \quad (13)$$

This critical value corresponds to fatigue failure and it is associated to the total area under the curve of Figure 2.4 (for one constant stress amplitude level), or the total dashed area in Figure 2.5 (for several stress amplitude levels). The ϕ value can be used together with values of ΔT_i , ΔT_{0i} , ΔN_i measured at stress amplitude levels $\Delta \sigma_i$ for a single specimen, as depicted in Figure 2.5 and modeled by Eq. (14) and Eq. (15), to yield the whole fatigue SN curve.

$$\phi = \Delta T_i \left(N_{fi} - \frac{\Delta N_{si}}{2} \right) \quad (14)$$

$$N_{si} = \frac{\Delta N_i \Delta T_i}{\Delta T_i - \Delta T_{0i}} \quad (15)$$

The parameter ϕ is material dependent. It varies with each test condition, depending basically on the applied load. Theoretically, there exists a ϕ for each material and test conditions. It could be measured with just one test; if the material hot spot point is taken to failure it would only require integrating the ΔT vs. N curve, like the one shown in Figure 2.5. In spite of that, the most advisable is the measurement of each ϕ for each test at its own realization conditions.

Figure 2.9 shows that the parameter ϕ should be the same for each different stress level, the area representing ϕ being the same tests under cyclic stress ranges σ_1 to σ_5 .

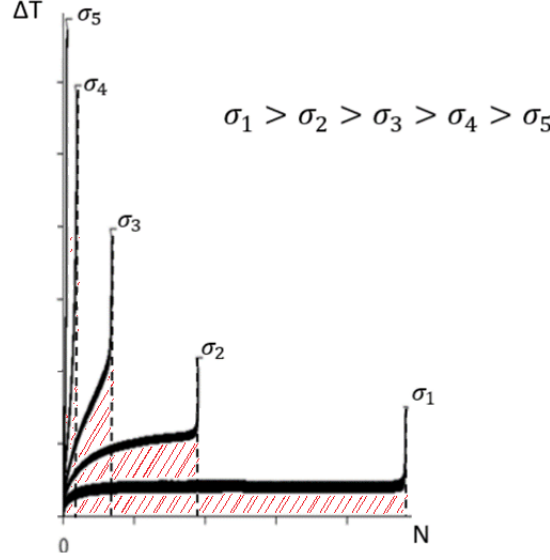


Figure 2.9: Parameter ϕ (hatching area) for different stress levels ($\sigma_1 > \sigma_2 > \sigma_3 > \sigma_4 > \sigma_5$).

Using the plot of Figure 2.5 it can be shown that the SN curve can be found. Each data point of the SN curve is formed by the pair $(N_{fi}, \Delta\sigma_i)$, where N_{fi} is calculated from Eq. (14), that is derived with the help of Figure 2.5 and the assumption that phase 3, depicted in Figure 2.4, is small and can be neglected. The value of N_{si} is determined from Eq. (15) with the help of Figure 2.5.

A partial damage value D_i results from the partial integrated value ϕ_i resulting from the application of each stress amplitude $\Delta\sigma_i$. The value ϕ_i is calculated considering the number of cycles applied at each stress level, N_{pi} . The denominator of Eq. (16) represents the total thermal energy amount released during the duration of the test, it also can be described as the area under the curve ΔT vs. N considering the interval N_{pi} . The partial damage value of Eq. (16) assumes that the Miner's linear damage accumulation rule is valid.

$$D_i = \frac{\phi_i}{\phi} = \frac{\left(\frac{\Delta T_i + \Delta T_{oi}}{2}\right) \Delta N_i + \Delta T_i (N_{fi} - \Delta N_{si})}{\sum_1^f \phi_f} \quad (16)$$

Some researchers using the procedure described above have measured the SN curve for different load ratios and different types of material, like: carbon steel, aluminum alloys, polycarbonate and brass [62,63,64, 101].

2.4.2 Thermoelastic Stress Analysis

Thermoelastic stress analysis (TSA) was an emerging technique around the 80's [39,47,48,49]. From the last two decades it has been used successfully for the evaluation and validation of design concepts and applications to fracture mechanics, damage detection, fatigue monitoring and residual stress analysis [47, 105].

The TSA technique is based on the thermoelastic effect, which states the relationship between a reversible conversion of mechanical into thermal energy, since the temperature variation will reverse when the load is withdrawn. However, this energy conversion is reversible only if the elastic range of the material is not exceeded and there is no significant transport of heat between material points during loading and unloading of the structure [106].

Maps of surface stress are obtained in real time by measuring the temperature changes induced by time varying stress/strain distributions. Under adiabatic and reversible conditions, a cyclically loaded structure experiences in-phase temperature variations that, for isotropic materials, are proportional to the change in the sum of the principal stresses.

It is known that, when the temperature of a gas decreases if it expands and similarly, when the gas is compressed the temperature increases. The same phenomenon occurs with solid materials, although the temperature changes associated with elastic deformations are very small, on the order of 0.001°C.

The physical principles of TSA are presented in Appendix B. Under plane-stress isotropic conditions, the TSA stress equation can be written as:

$$S^* = K(\Delta\sigma_1 + \Delta\sigma_2) \quad (17)$$

where S^* is the signal output from the thermal sensor and K is the thermomechanical coefficient.

2.4.2.2 Calibration

Typical TSA applications require calibration of the temperature change of the thermoelastic signal S^* in terms of elastic stress or strain. The calibration procedure may take different forms [107-110]. One concept is based on the relationship between the specimen material properties and measurement system characteristics.

The other approach compares the measured thermoelastic response signal with either a theoretical solution or some independent determined state of stress. Although methods described herein emphasize a classical thermoelastic response, material nonlinearities and nonadiabatic factors are taken into consideration.

The theoretical calibration technique relates the predicted sample digital output signal provided by the thermal camera, with the change in the appropriate linear combination of stresses. This approximation measures the thermomechanical coefficients K for each type of material, based on the thermoelastic and physical theory of IR thermographic detection. As such it involves knowledge of the mechanical and thermal properties of the material being analyzed, camera and lock-in analyzer sensitivities and various signal attenuation factors.

This procedure can be hard to perform, once it requires an accurate knowledge of many individual factors, whose values may be difficult to specify. This procedure could be useful to determine the traditional thermoelastic relationship, Eq. (17), or when material nonlinearities and mean stresses need to be considered.

Thermomechanical coefficient values are reliably and easily determined by experimental calibration of specimens using the same material, paint layer, loading frequency, and ambient conditions of the real test structure.

The calibration procedure employs a geometry and loading conditions where the stress state is theoretically known, which is sometimes confirmed by using strain gauges. For the cases of specimens with stress gradients, strain gauges can be placed at regions of uniform stress and their output, converted in stress, compared to the thermoelastic response S^* .

As the name of the technique itself suggests, TSA is applied only to the elastic interval, until the end of the thermoelastic phase. After that, the analysis of the results becomes qualitative. As the yield strength is theoretically defined as the point with 0.2% of permanent deformation or sometimes 0.5% of total strain, its thermal response is not proportional at so high strain levels. Figure 2.10, below, is similar to Figure 2.7, showing the evolution of the thermoelastic response signal from the camera over the time. The relationship between the thermomechanical coefficients, K , and the response signal S^* is only valid in the linear interval, until the end of the thermoelastic phase.

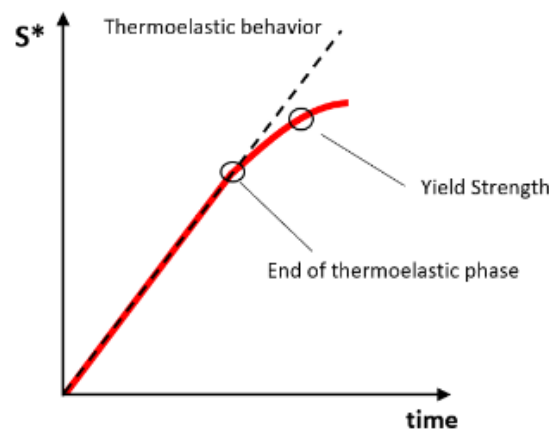


Figure 2.10: Evolution of the thermoelastic response signal from the camera over the test duration when a static load is applied.

2.4.2.3 TSA Data Acquisition and Processing

The main component of a thermoelastic analysis setup, Figure 2.11, is the IR sensor, which is capable of measuring the small temperature variations associated with the thermoelastic effect. The IR sensor acts as a transducer converting incident radiant energy into an electrical signal.

In addition, the experimental setup requires a testing machine capable of performing cyclic loading on the test specimen, a load cell to input the desired loads, a lock-in analyzer and a computer for video display and postprocessing data. More information about the experimental configurations used in this thesis will be given in Chapter 3.

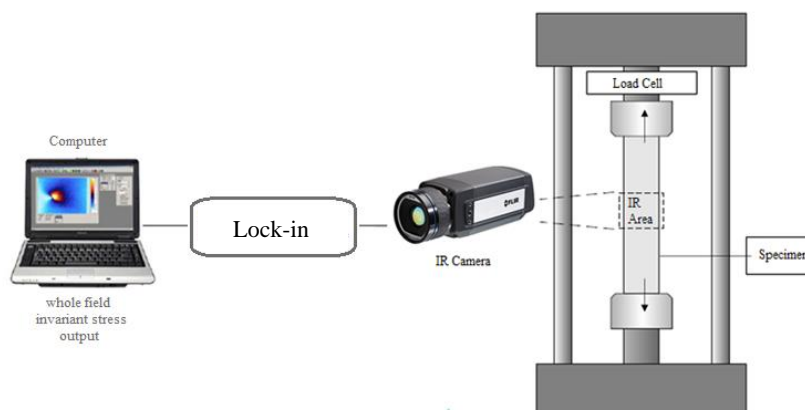


Figure 2.11: Schematic thermoelastic analysis setup, [111].

A lock-in analyzer is employed as the signal processing unit that extracts the thermoelastic information from an extremely noisy detector output signal, being described in a simplified manner as a series-connected signal mixer and a low-pass filter [112].

Lock-in analyzers used in thermoelastic systems generally separate the detector output into two components; one in-phase and other 90° out of phase with respect to the reference signal. The adiabatic structural response is expected to be in phase with the reference load frequency. If heat generation occurs in regions of high stress gradients, or if the loading frequency is insufficient for an adiabatic response, a phase shift from the reference frequency will occur and will be apparent as an out of phase detector signal [47].

There are two types of lock-in, one synchronizes load measurements with temperature through a connection between the loading machine and the thermocamera, the other synchronizes measurements on the body itself through a reference window using a specific software.

This thesis was carried out using the software DeltaTherm 2, a commercial TSA software that provides thermoelastic data in real time, which has been developed by Stress Photonics Inc. More information will be given in Chapter 3. The main advantage of this software, when compared to the typical TSA approach described above, is the way the lock-in process is performed. The software turns the lock-in into an automatic process and setting up a TSA test becomes a simple task.

2.4.2.4 TSA Data and Interpretation

Eq. (17) relates the change in temperature to the change in the invariant stress state. In practice this typically implies correlating the IR signal with some form of signal that is representative of the applied load. The latter is commonly called the reference signal and, while it can be out of phase with the observed IR response, it is critical that its form varies in the same manner as the loading.

Limitations are often imposed on the reference signal form by the hardware used during the measurements, since the correlation process can be sensitive to the presence of noise. In this way, it is preferable to use the cleanest available source of reference signal, like the output from load transducers, surface strain gauges, or proximity probes. In this work, the reference signal was used within a window of interest, for this it is necessary that it be robust in relation to the noise of temperature measurement.

Independent of the setup used to capture the thermoelastic data, the data always contain both magnitude and phase information from the correlation between IR response and cyclic loading. This information can be presented as a vector in either polar or cartesian coordinate system. Figure 2.12 illustrates the polar representation, where the magnitude of the thermoelastic response is the length of the vector R and θ is the angular coordinate, which is the phase difference between the reference signal and observed IR response.

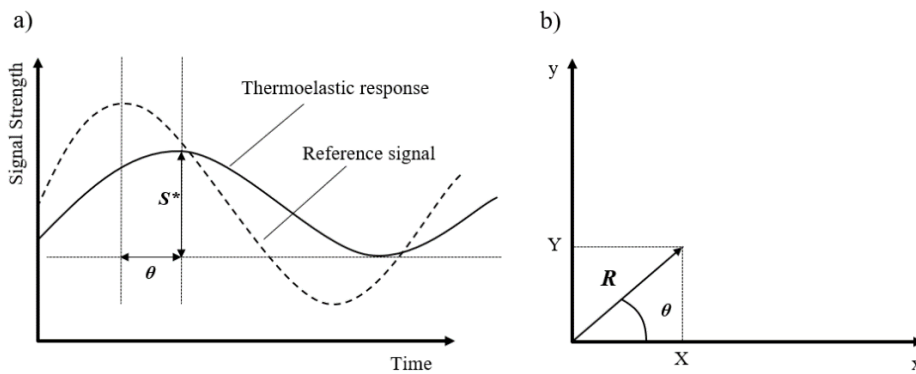


Figure 2.12: Form of thermoelastic data during cyclic test: a) the intensity of the reference signal and the thermoelastic response (S^*) vs. time, and the phase relationship (θ) between them; b) the resulting thermoelastic vector in polar coordinate (R and θ) and in cartesian coordinates (X and Y), adapted from [47].

The cartesian representation has the advantage of presenting in a single diagram both the stress distribution and the relative tension/compression state. If the reference signal is out of phase with the IR response this will produce an apparent shift in the recorded thermoelastic data. This effect can also be generated by a global offset in the system. Such a phase shift causes a constant nonzero value to be superimposed on the entire data and can be correlated typically by applying a constant vector throughout the data map. The constant vector is deduced from data captured under conditions of zero loading amplitude.

The signal to noise ratio of the thermoelastic signal is not only dependent on the magnitude of the stress change event, or the sensitivity of the IR imaging system, but also on the quantity of information used in the correlation process.

The correlation process is essentially a noise filter in which the thermoelastic information is extracted and IR and electric noises are rejected. Consequently, the greater the quantity of IR data that can be compared to the reference signal, the greater the success of this noise filter procedure. Therefore, most correlation processes yield better data as more IR data flows through them so that the ratio of signal to noise improves with time.

Although all effort to reduce the noise prevenient from different sources it is inevitably to mitigate it all. Some cases are suitable for the application of filters, such as, low stress distributions. On the other hand, cases with severe stress gradients, like; crack or notch tips, tend to be distorted by the application of filter, and there is loss of information.

The heat loss by conduction (non-adiabatic condition) only becomes a problem in case of high thermal gradients. For example, a small aluminum structure would be a case of special attention to the adiabatic assumption. The loss of convective heat or significant radiation is not common [65].

The adiabatic assumption is satisfied continuously and "rapidly" by increasing the load of the structure. This is often done with a constant amplitude load, but variable amplitude or transient load may be sufficient to make the measurement.

Figure 2.13, show the thermoelastic response of a plate in uniaxial tension with a central hole. The X data shows a large positive response along the horizontal hole centerline (relative tension) and smaller negative response along the vertical centerline (relative compression). The Y data shows an approximately null field. R data is similar to X data, except on the hole perimeter, since the value of R is absolute. The θ data, which is mostly in phase with the tensile regions of the plate and is 180° out of phase with compressive areas.

Figure 2.14, show the thermoelastic response of a SAE Key-hole specimen, The X data shows a large positive response near the stress concentration and proportional negative response at the back of the specimen. The Y data shows an inverse proportion of the X data. R data is similar to X data, except on the stress concentration, since the value of R is absolute. The θ data, show the transition from positive to compressive areas.

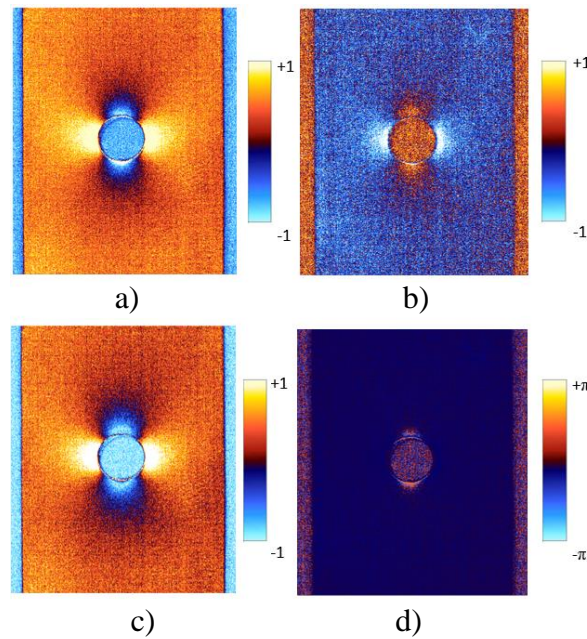


Figure 2.13: Thermoelastic response of a plate containing a central hole: a) X data; b) Y data; c) R data; d) θ data.

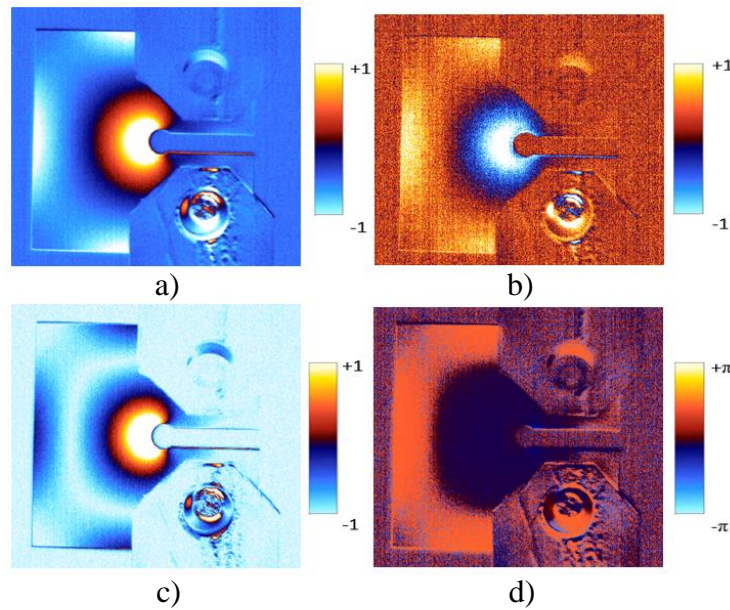


Figure 2.14: Thermoelastic response of a Key-hole specimen: a) X data; b) Y data; c) R data; d) θ data.

2.2.5 Stress Separation

As all techniques have their disadvantages, the TSA has some limitations regarding stress separation and its use to points very close to the boundary of the specimen. Although it is a very powerful tool for experimental mechanics in many fields of study, some difficulties are presented, like; the correct use of the measure information (the first stress invariant, $(\Delta\sigma_1 + \Delta\sigma_2)$) [47].

TSA has been frequently used to measure the stress fields in complicated geometries and around discontinuities, coupled with stress functions, numerical and other experimental methods to separate the principal stresses [113-116]. In complex components, where the stress field has a maximum away from a border, stress separation techniques must be used.

Most of the developed stress separation methods assume isotropic material behavior, adiabatic, reversible thermodynamic, and therefore employ cyclic mechanical loading. Another limitation is the linear elastic plane stress assumption; there are few three-dimensional stress separation formulation and experimental results are available in the literature [117-119].

3.

Material and Experimental Procedure

This work aims to evaluate the behavior of components containing dents using modern experimental and numerical techniques, however a special focus was given to thermographic techniques due to little dissemination in the literature.

Herein all the experimental campaign that was carried out during the development of this thesis will be detailed and discussed. This chapter presents the specimens types, their dimensions and preparation, testing procedures, loading machines, analysis software and thermal sensor, assessment of material properties using the techniques presented in Chapter 2 and the other experimental techniques, such as Digital Image Correlation (DIC) and fiber Bragg strain gauges (FBSG), that were also used in the analyzes.

3.1

Specimens

Two types of specimens were used in this work. The first one is the dog bone specimen, Figure 3.1, also known as the constant radius tensile specimen, which presents a stress gradient along its length due to the continuous variation of the cross-sectional area.

This specimen, Figure 3.1, was adapted from ASTM E 466-07 - Standard Practice for Conducting Force Controlled Constant Amplitude Axial Fatigue Tests of Metallic Materials [120]. The specimens were cut from a 12.75" diameter and 1/4" thick tube. After the specimens were cut and flatted in a press, they were milled to a uniform thickness of 5 mm.

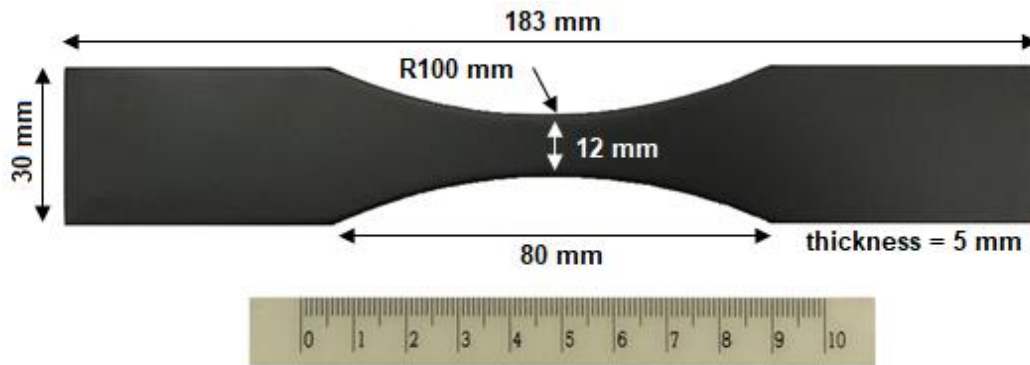


Figure 3.1: Dog bone specimen geometry.

The second type of specimen was the 3 meter long pipe made of API 5L Gr. B steel, with 12.75" (323.85mm) outside diameter (OD) and 1/4" (6.35mm) thickness. A total of nine pipe specimens were used and each one of them contained an artificially created dent. The final dent shape depended on a number of factors, like: format of the indenter, maximum indentation depth, material and rerounding pressure.

The specimen's raw material originally came in pipes with 12 meter long, which were cut and sectioned into smaller 3 m long parts. Figure 3.2a shows the nine pipe specimens after the indentation process waiting for the head cap to be welded to continue the generation of the desired dent shape, Figure 3.2b shows the concrete grafts used to minimize the volume of water inside the specimens during the cyclic pressurizing tests.



Figure 3.2: a) The nine pipe specimens after the indentation process; b) the concrete grafts used to minimize the volume of water during the pressurizing tests.

3.1.1 Dent Creation Process

The dent creation process begins with the selection of the final shape of the dent. The format chosen was the one with longitudinal shape without gouge, also known as plain longitudinal dent, where the length of the dent is greater than the width.

The sequence of the dent generation process consisted of five consecutive steps, which are outlined in Figure 3.3. The Step 1 corresponds to the initial specimen positioned in the limit condition prior to the indenter contact. The pipe specimen was placed in a steel saddle, whose function was to ensure the alignment between the specimen and the indenter during the deformation process. The indenter was positioned right above the center of the pipe, without any contact.

During Step 2, the indenter was displaced to contact and press the pipe in order to produce a dent with a maximum depth of approximately 157 mm ($\approx 48\%$ of the outside diameter) after the removal of the load. This value considers the elastic return of the material after the unloading. Therefore, the maximum depth during the indentation was a few millimeters greater. The force to produce this indenter displacement was approximately 480 kN as shown in Figure 3.4. All this information was obtained from a previous study that used the finite element method to find the relation between the indenter shape, the maximum indentation depth, the material behavior, the re-rounding pressure and the dent final shape after re-rounding. More details about this study are given in Chapter 4 and in Appendix B.

In Step 3, the indenter is gradually withdrawn, allowing the recovery of the elastic fraction of deformation. Thus, the depth of the dent decreased to a certain value ($\approx 48\%$ of the OD), characterizing its permanent shape. At the end of this step, the specimen was removed from the saddle.

At the beginning of Step 4, concrete grafts to minimize the free internal volume were placed inside the pipe and head caps (containing an inlet to allow filling the specimens with water) were welded to the specimen. The pipe was filled with water and it was applied a hydrostatic internal pressure, the re-rounding pressure. This pressure induced a recuperation of the dent maximum depth, leaving the dent with a final depth of approximately 14% of its OD.

The value of the re-rounding pressure varied from specimen to specimen. According to the finite element analysis, a pressure equal to 7.0 MPa should be enough to obtain the desired final dent shape and depth of the plain longitudinal dent. However, some problems occurred during this step. Due to the behavior of the material associated with the dent shape and applied pressure load, three dented specimens suffered snap thru buckling² at their prefabricated dents, at re-rounded pressures lower than 7.0 MPa. This lower pressure was around 6.6 MPa. The snap thru phenomenon causes the appearance of a hump in the central portion of the dent, modifying the intended shape. It was opted not to deform again the specimens that suffered the snap thru and to work with them in this condition, since it is an intrinsic state of this denting process. Because of this, five specimens were rerounded with a lower pressure, 6.5 MPa, to avoid the occurrence of the snap thru event. Comparison between the shapes of the re-rounded dents obtained with and without snap-thru will be shown later.

In Step 5 the internal hydrostatic pressure is removed, and the specimens are ready to be fatigue tested with predefined loading pressures.

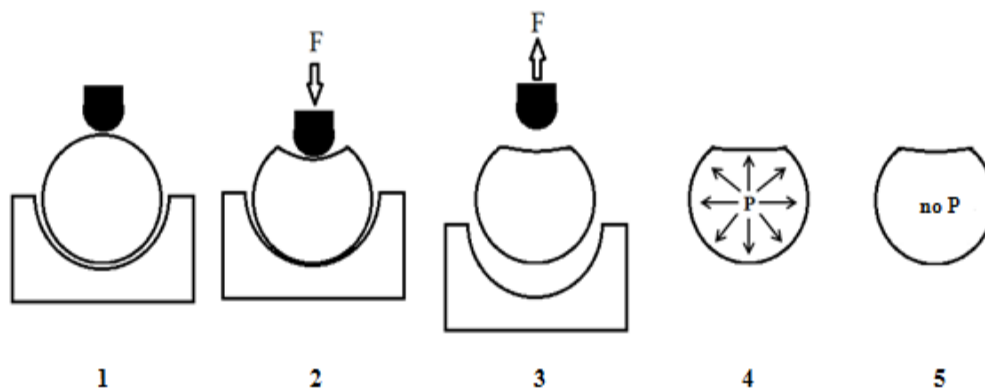


Figure 3.3: Steps of the dent creation process.

² The snap thru buckling is a shell buckling phenomenon, where the system passes from an equilibrium state to a non-adjacent equilibrium configuration. This problem will be addressed in section 5.2.1.3.

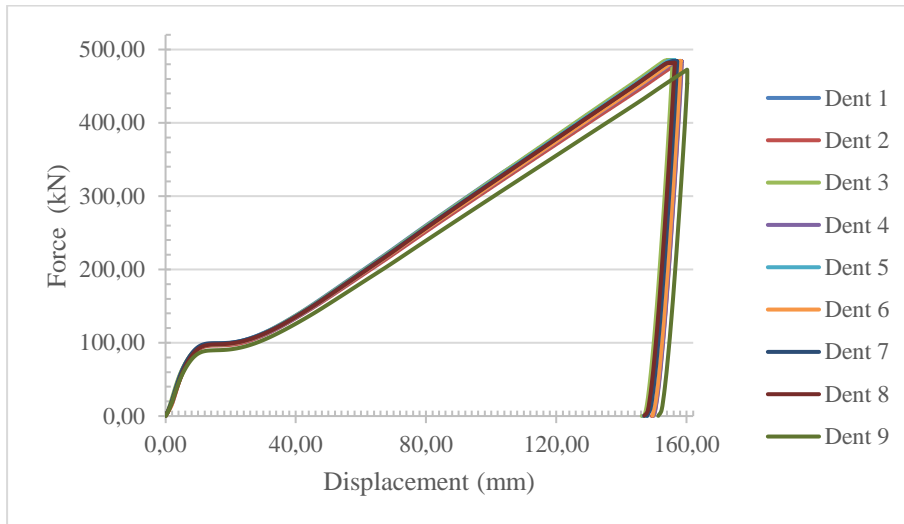


Figure 3.4: Indentation force vs. displacement curves.

Figure 3.5 shows the stages of the dent creation. All the specimens have similar dents after the indentation process, Figure 3.5d. Although, the final shape may vary due to the occurrence of the snap thru, the dent shown at Figure 3.5f have the plain longitudinal shape desired.

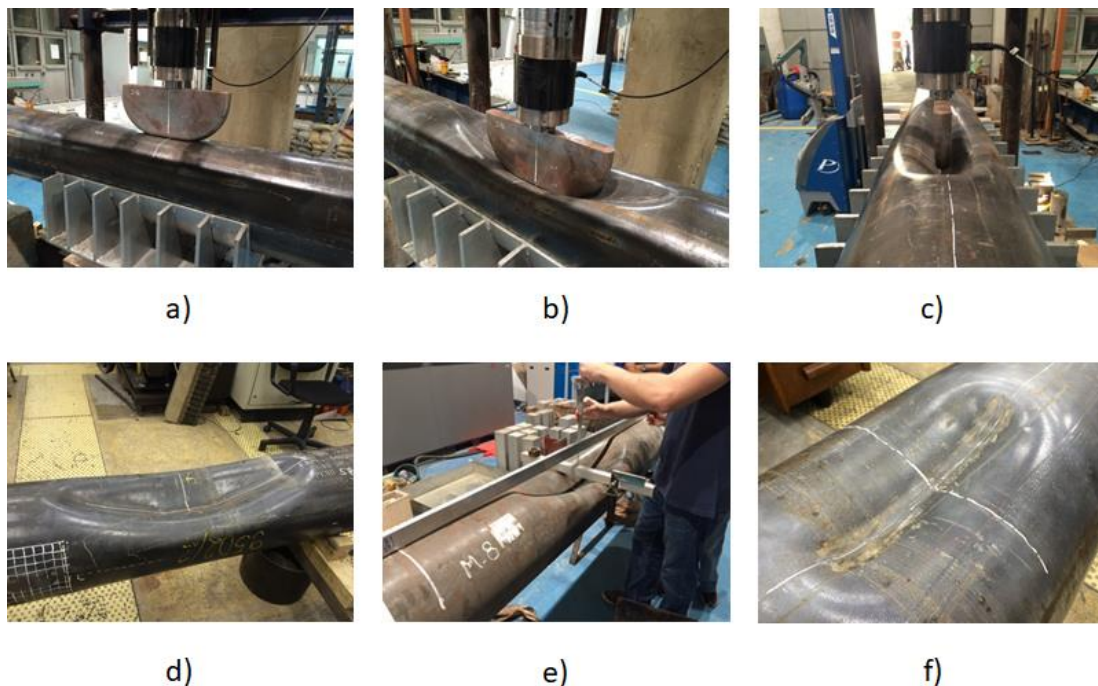


Figure 3.5: Dent creation process: a) the specimen is placed in the saddle and align with the indenter; b) the indenter is displaced in order to produce an initial dent; c) the indenter is gradually withdrawn; d) the final shape of the initial dent; e) the profile of the dent is measured with a caliper; f) the plain longitudinal dent obtain after rerounding.

3.1.2 Reround Pressure

Any dent that is unrestrained is able to be reround under the influence of increasing internal pressure in the pipe, and recover a percentage of its initial depth as a result of this single cycle of pressure-induced re-rounding [69]. Some ductility and, consequently, fatigue life are consumed in the process of forming and re-rounding the dent [121].

As the pipe specimens were tested for fatigue and knowing that the initial dent with depth of 48% of OD would not be accepted in any case of study, it was defined that the initial dent depth should be recovered to a more admissible value. The chosen depth was 14% of the OD, and it would be obtained through a rerounding procedure.

The specimens were re-rounded by hydrostatic internal pressure loading using a pneumatic driven hydraulic pump with a maximum capacity of 70 MPa. The re-rounding pressure was previously anticipated from the numerical study that will be presented in Chapter 4, and it was equal to a percentage of the specified minimum yield strength (SMYS). Initially, the pressure that would form the 14% OD dent was calculated to be equal to 7.0 MPa (a pressure capable of inducing a nominal circumferential stress equal to 73% of the pipe material SMYS).

However, three specimens experienced the snap thru buckling phenomenon during re-rounding, presenting the formation of a hump in the central portion of the dent. To maintain the desired dent shape, the re-rounding pressure was reduced to 6.5 MPa (68% of SMYS) to avoid the occurrence of the snap thru phenomenon for the other five out nine specimens (the first re-rounded specimen did not present snap-thru although reaching the initial desired pressure of 7.0 MPa).

Table 2 presents the depths of the specimens before and after the re-rounding, showing the occurrence of the snap thru and the new adopted re-round pressure.

Table 2: Dent depths before and after the rerounding

Dented pipe specimen	Central depth before rerounding (mm)	Central depth before rerounding (% OD)	Rerounding pressure (MPa)	Central depth after rerounding (mm)	Central depth after rerounding (% OD)	Snap thru pressure (MPa)	Hump
Dent 1	154.0	48	7.0	40.0	12	-	No
Dent 2	155.5	48	7.0	1.5	0	6.6	Yes
Dent 3	157.5	49	7.0	13.0	4	6.9	Yes
Dent 4	157.5	49	7.0	10.0	3	6.9	Yes
Dent 5	156.0	48	6.5	50.0	15	-	No
Dent 6	156.5	48	6.5	51.0	16	-	No
Dent 7	155.5	48	6.5	49.0	15	-	No
Dent 8	155.0	48	6.5	50.5	16	-	No
Dent 9	160.0	49	6.5	48.0	15	-	No

Figure 3.6 shows the performance of the rerounding test for dented specimens 1 and 2, and their final shape after rerounding. As it can be seen, Dent 2 exhibits the occurrence of the snap thru, characterized by the development of a hump.

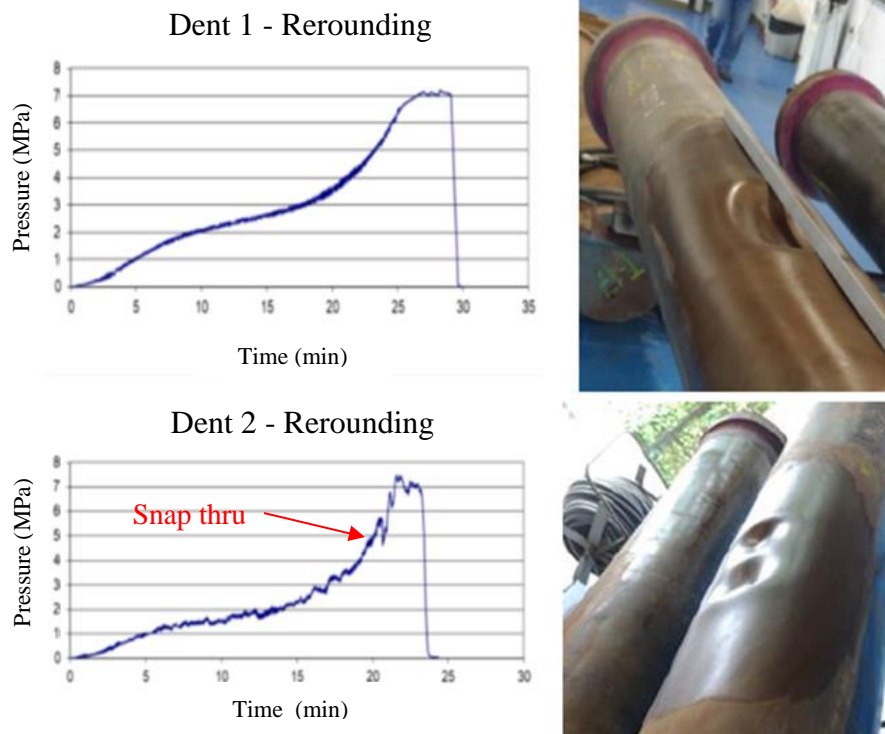


Figure 3.6: a) Dent 1 rerounding test; b) dent 1 final shape;
c) dent 2 rerounding test; d) dent 2 final shape.

3.1.3 Dented Pipeline Specimens Profiles

Figure 3.7 and Figure 3.8 present the longitudinal and transversal profiles, along symmetry lines that pass through the center of the dents.

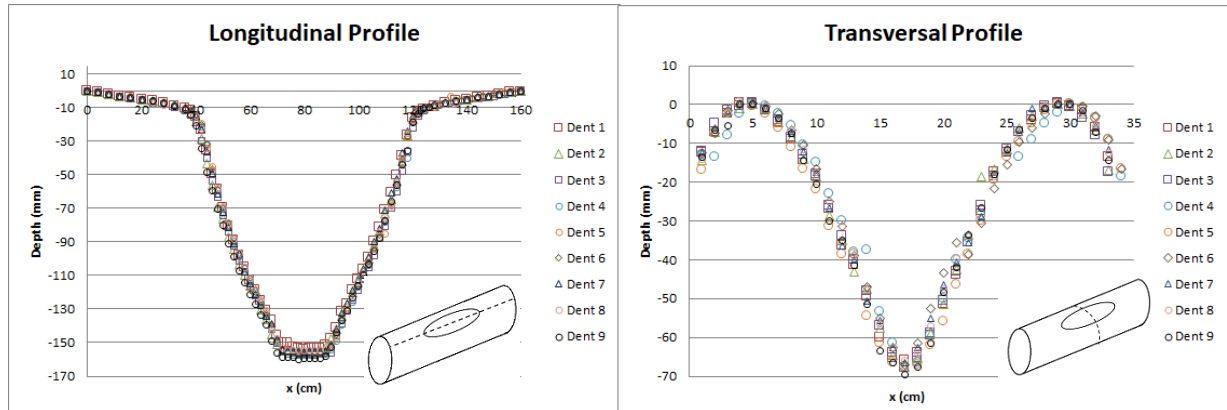


Figure 3.7: Dented specimens profiles before rerounding.

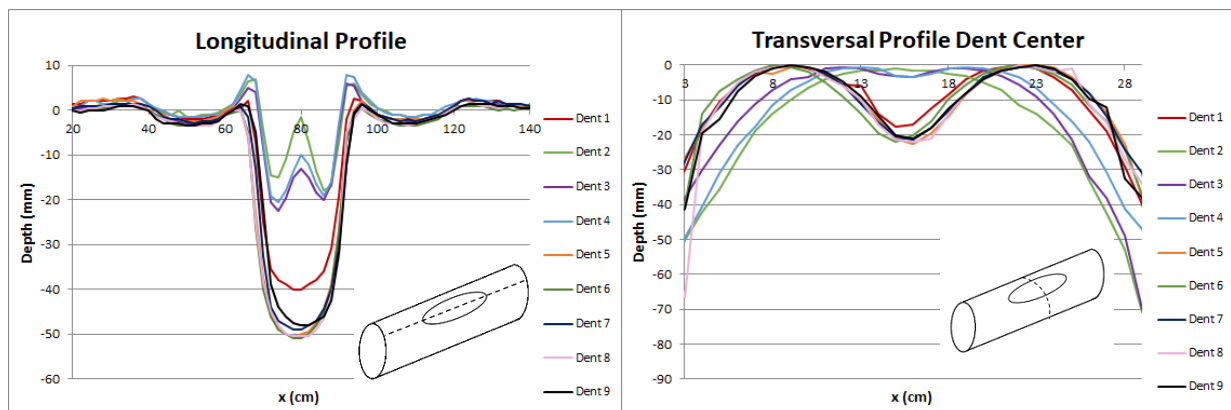


Figure 3.8: Dented specimens profiles after rerounding.

3.2 Testing Procedure

This section summarizes the experimental procedures and cautions that were taken throughout all performed experiments.

3.2.1 Loading Machines

Different loading machines were used in this work to assess the static and dynamic behavior of the specimens. Three servo-hydraulic fatigue testing machines (Figure 3.9a-c), one being adapted to apply cyclic pressure loads (Figure 3.9c), and another tensile tester machine (Figure 3.9d).

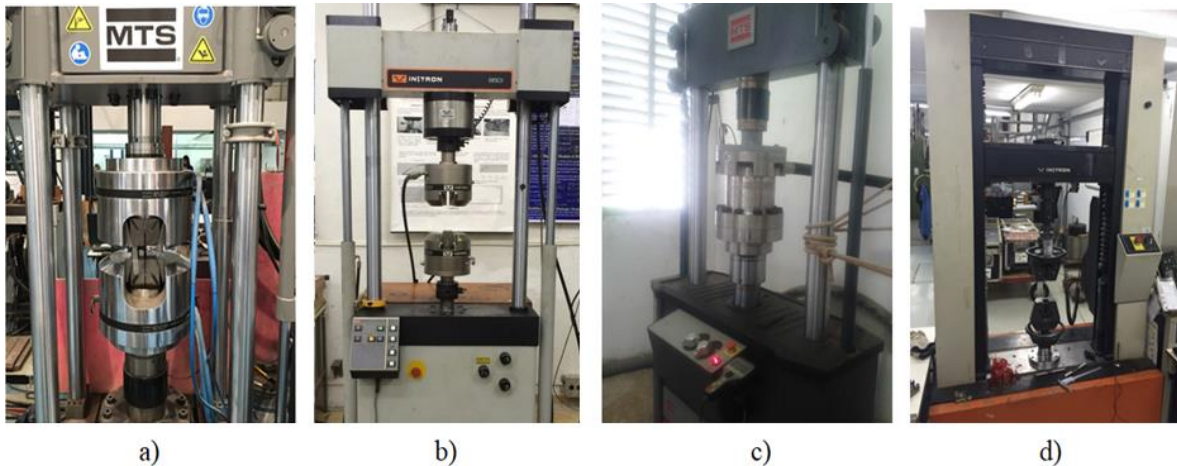


Figure 3.9: Test machines used in this work.

The MTS 311.31 machine, Figure 3.9a, with load capacity of 1000 kN, and the INSTRON 8501 machine, Figure 3.9b, with load capacity of 100kN, were used to test the dog bone specimens at different loading ratios ($R = \text{min load}/\text{max load}$).

The MTS machine, Figure 3.9c has a load capacity of 500kN. A system was adapted to it to allow the application of cyclic internal pressure to the pipeline specimens. A cylinder-piston arrangement was designed and constructed, being coupled to the hydraulic actuator of the machine. The system is filled with water, so it is possible to vary the internal pressure in the pipe specimens by moving the actuator inside the cylinder. The pressure reading of the system was carried out by means of a pressure sensor installed in the hydraulic circuit. The pressure sensor used was the Gefran TPS-7-V-B35D-T, that could measure a pressure range from 0 up to 350 bar.

The INSTRON 5500R machine, Figure 3.9d, was used in the static tests that utilized the dog bone specimens.

3.2.2 Loading Cautions

Before the realization of the fatigue test the dented specimens were filled with water and all air trapped was removed from the interior of the pipes to avoid cavitation and facilitate the load control of the system. During the process of filling the pipes with water, the concrete grafts, which were used to minimize the volume of water, were immerse in water for several hours to eliminate any air bubble.

3.2.3 Specimen Surface Preparation

The preparation of specimens for thermographic analysis is described by Charles et al., [17]. All specimens were sanded to clean the analysis surfaces and to eliminate superficial corrosion. Following that, the specimens were painted with a thin layer of opaque black paint to increase their emissivity, as shown at Figure 3.1, making it close to the value of a black body along their whole surfaces.

The black paint layer provides a uniform surface emissivity. This preparation is necessary for metallic materials because they tend to have low and quite variable emissivity. Matte black aerosol commercial paint is suitable for application to surfaces and usually have emissivity of 0.9 [47]. The present tests used the *Suvinil* spray brand.

3.2.4 Thermal Insulation

To avoid the contamination of the tests by unwanted IR radiation, whose sources can be generated by passing people, environment lighting, operation of other equipment, among others, and to reduce the errors associated with the measurements, the specimens were isolated during the tests. The insulation has the role of ensuring the maintenance of an environment steady state during a certain period of time, since a change in the thermal response of the tested material is expected. Sometimes a wood box or a cloth cover was used to isolate the test from external radiation, Figure 3.10.

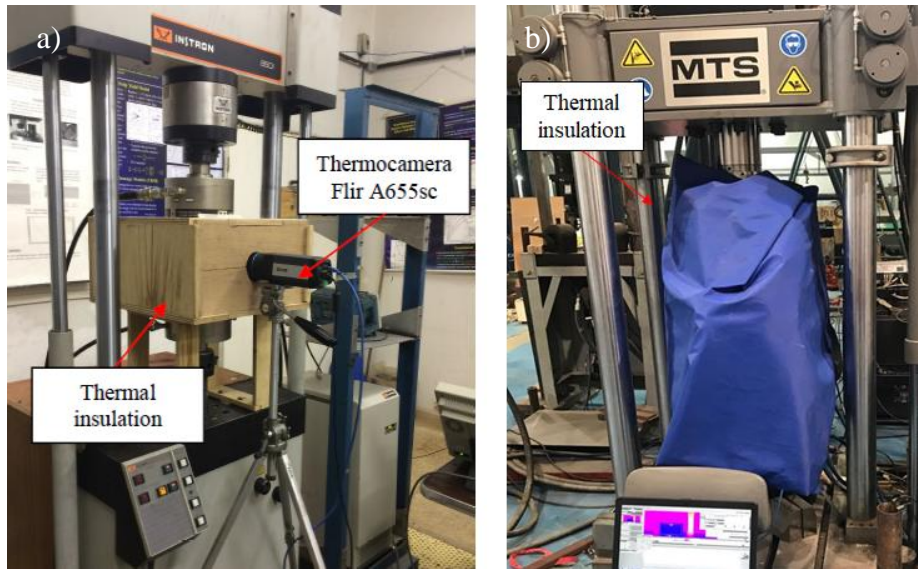


Figure 3.10: Thermal insulation used: a) wooden box; b) cloth.

3.2.5 Thermal Camera

During each fatigue test, the surface temperature of the specimens was recorded in real time by a microbolometer thermocamera FLIR A655sc, Figure 3.11, which has a focal plane array (FPA) of 640 by 480 pixels of 17 microns each, data acquisition frequency of 50Hz on full frame configuration up to 200Hz for a quarter frame and spectral range from 7.5 to 14 μ m. It can be used in two different temperature ranges (-40 to 150°C and 100 to 650°C) with a 30mK sensitivity in both of them.



Figure 3.11: FLIR camera A655sc [100].

3.2.6 IR Software

Two measurement and analysis software packages were used coupled with the thermocamera herein used, they present different applicability and focus at different aspects of the measured temperature; one works with the measured raw temperature and the other works with the temperature post processed into stress signal.

The ResearchIR [100] software is designed for efficiency and productivity, providing camera control, highspeed data recording, image analysis, data sharing, post-processing of fast thermal events and generation of time-temperature plots from live images or recorded sequences. The software connects directly to the FLIR camera to acquire “raw” thermal snapshots or movie files. In addition the software includes facility to set-up advanced start/stop recording conditions, including start times, end times, and the number of frames to acquire, analyze data with an unlimited number of analysis functions, rapidly organize files, take a closer look at images with zoom and pan controls and set-up multiple user-configurable tabs for live images, recorded images or plotting.

The TSA analysis software package was developed by Stress Photonics Inc. and includes the DeltaTherm 2, for acquisition, processing and archiving of IR images, and the DeltaVision, for presentation, and reporting.

DeltaTherm 2 collects the IR microbolometer camera output that records radiation emitted from the surface of an object undergoing periodic loading, producing a near-live full-field stress image. The high-speed digital electronics correlate stress induced temperature changes for immediate video presentation of stress patterns.

The software uses an algorithm to obtain simultaneously time, amplitude and phase of a sinusoidal signal, turning the lock-in into an automatic process. It uses a bypass of the load signal requirement to allow the selection of a reference region on the sensor image. The phase information from this region is used as the load signal [122]. The software signal processing can be illustrated by the diagram in Figure 3.12.

DeltaVision software is designed to do final processing and presentation of TSA data. Batch processing and reporting modes are available from within the software.

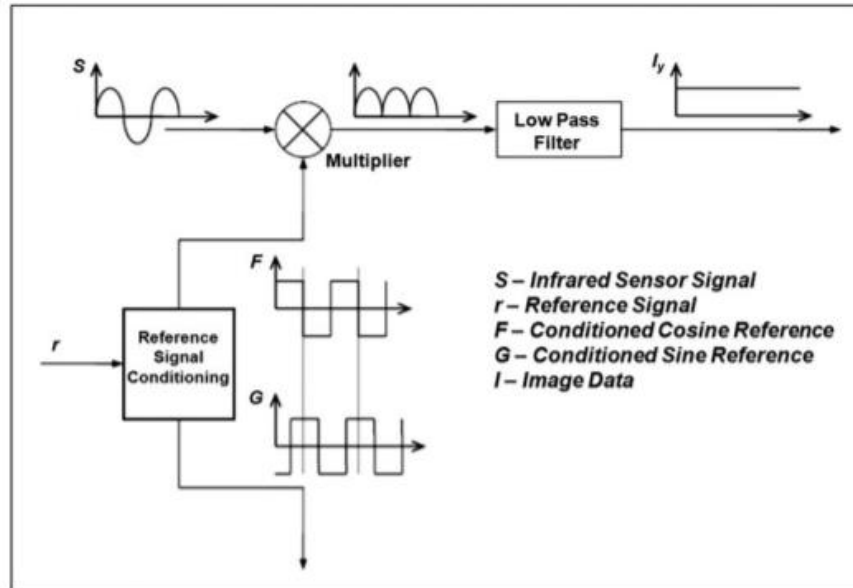


Figure 3.12: DeltaTherm 2 signal processing model [122].

3.3 Material Behavior Assessment

All the specimens tested in this work were made of steel API 5L Gr. B, very common in the pipeline industry. This section summarizes the results of the investigation that was conducted to fully assess the material behavior and the static as well as the cyclic loading conditions there were used. Preliminary static uniaxial tensile test results [123] are commented in section 3.3.1. In this Thesis, a total of 11 dog bone specimens were tested under quasi-static and cyclic loads applying the methodologies presented at section 2.4.1. Fatigue uniaxial test details and results related to each of the 11 specimens tested are presented in sections 3.3.2 to 3.3.4 and are summarized in Tables 3 and 5. It should be noted that some of these specimens were subjected to more than one type of rapid fatigue evaluation tests as presented in Table 3.

Table 3: Types of IR tests that each specimen was subjected to.

Dog bone specimen	Type of IR test performed		
	Quasi-static	Cyclic	Ultra-rapid
1	-	X	X
2	-	X	X
3	-	X	X
4	-	X	X
5	X	-	-
6	X	X	X
7	X	X	X
8	X	X	X
9	X	-	-
10	X	-	-
11	X	-	-

3.3.1 Static Tensile Stress Tests

A preliminary work [123] tested 54 tensile specimens, that were machined from the API 5L Gr. B raw 12m long pipes according to API 5L / ISO 3183 – 2008 standard [124]. Figure 3.13 presents the characteristic stress-strain curve of the material, corresponding to the measured curve of one of the specimens for a monotonic test.

Table 4 shows the measured mechanical properties and the chemical composition of the material.

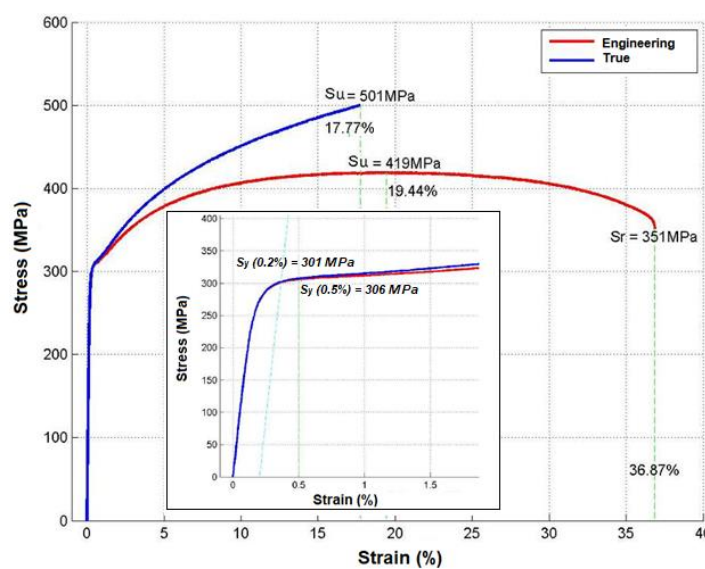


Figure 3.13: Stress-strain curve of the API 5L Gr. B [123].

Table 4: Material Properties (API 5L Gr. B) [62].

Actual chemical composition	0.13C, 0.54Mn, 0.01Si and low P, S
Specified minimum yield strength, SMYS, [11]	245 MPa
Specified minimum ultimate strength, SMUS, [11]	415 MPa
Yield Strength S_y (average of 54 specimens, 0.5% total strain)	316 MPa
Engineering ultimate strength (average of 54 specimens)	420 MPa
True ultimate strength S_u (average of 54 specimens)	500 MPa
Maximum strain at fracture ϵ_f	0.36
Young modulus (average of 54 specimens), E	182 GPa

3.3.2

Fatigue Limit Tests Using IR: Cyclic Loading

Figure 3.14 depicts the determination of the fatigue limit by applying the cyclic IR method to a dog bone specimen called Specimen 6. As presented in Table 3, this specimen had its fatigue $R = -1$ previously determined using the quasi-static method. These results are presented in section 3.3.5.

In what concerns the cyclic loading method, the temperature variation with number of cycles and with applied stress amplitude for specimen 6 are presented respectively in Figure 3.14a and Figure 3.14b. These plots show that the temperature undergoes a significant increase when it is submitted to elevated stress levels, above the fatigue limit. Figure 3.14a shows that temperature stabilizes around 3000 cycles for each stress level, completing the transition from phase 1 to phase 2, as shown in Figure 2.4. Figure 3.14a shows that, after reaching temperature stabilization, the cyclic loading is kept for approximately 6000 cycles until the test stress level is changed. This way the specimen is consecutively loaded until it finally reaches its failure (phase 3 in Figure 2.5).

Figure 3.14b shows the stabilized temperatures, ΔT_i , obtained from Figure 3.14a, plotted against their corresponding amplitude stress levels, $\Delta \sigma_i$. According to the cyclic IR method and the approach proposed by Loung [28], the fatigue limit, S_L , can be determined graphically by the intersection of two regression lines based on the data below and above the fatigue limit, as illustrated. When the specimen is subjected to a stress amplitude above the fatigue limit, its temperature increases significantly, and damage begins to accumulate at one or more critical hotspots until

the formation and propagation of a crack leads to the specimen failure. Figure 3.14b shows that the fatigue limit, S_L is equal to 149 MPa as determined for Specimen 6 under the load ratio $R(\sigma_{min}/\sigma_{max}) = 0.1$. This value is a little less conservative compared to the one using the Risitano approach presented in [26].

Hence, all the cyclic IR tests conducted in this work used the Loung methodology to determine the fatigue limit, this is due to the level of conservatism imposed to the analysis by the Risitano approach. Values for all other specimens tested using the cyclic IR method under other loading ratios R are given in Table 5.

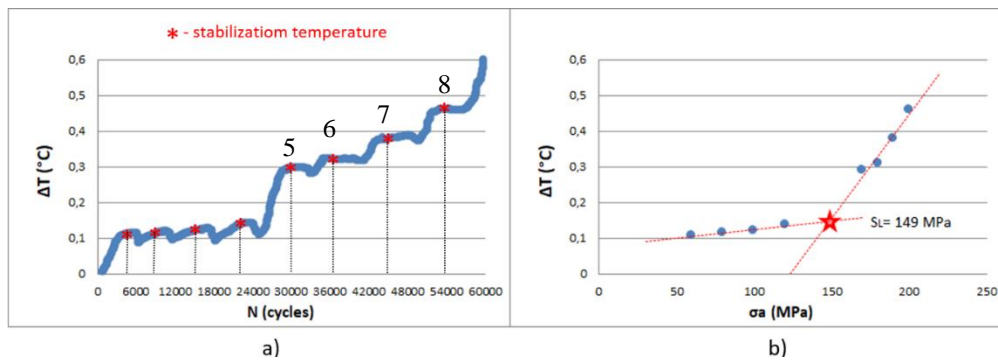


Figure 3.14: Specimen 6 cyclic IR method results: a) ΔT vs. N curve for various stress amplitudes $\Delta\sigma_i$, with the determination of each ΔT_i ; b) ΔT_i vs. $\Delta\sigma_i$ curve for various incremental load steps and determination of the fatigue limit.

3.3.3 Fatigue Limit Tests Using IR: Quasi-Static Loading

Figure 3.15 shows the quasi-static IR method for the determination of the full alternated uniaxial fatigue limit of a dog bone specimen called Specimen 5. The method is based on the first deviation of the slope of the temperature curve along the time that occurs in the uniaxial tension test. This slope deviation point is related with the fully alternate fatigue strength, valid for $R = -1$. The inflection in the curve corresponds to the nucleation of several sites of micro-damage in the area being analyzed. This value was found to be $S_{L,R=-1} = 253$ MPa.

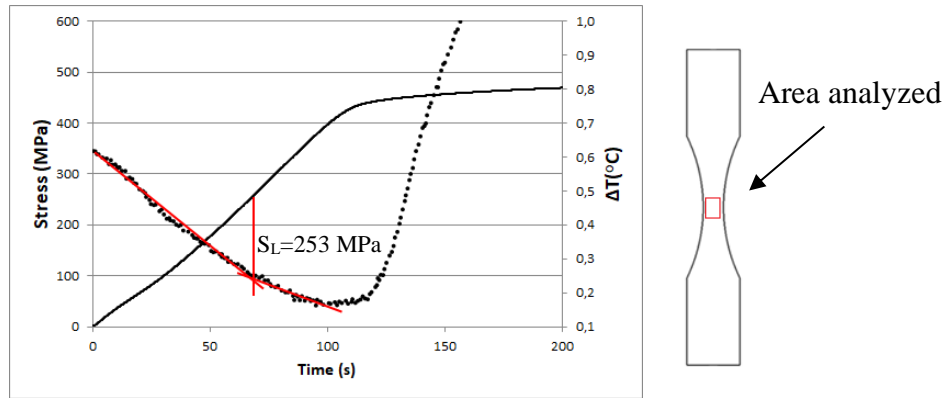


Figure 3.15: Specimen 5 quasi-static IR method result.

The test of Specimen 5 consisted of taking the specimen to failure during the uniaxial load test.

In order to analyze the influence of accumulated plasticity a test procedure was adopted for some of the specimens (numbered 6 to 11) that were tested using the quasi-static IR method. These specimens were loaded and unloaded five times until a certain level of plastic deformation was reached. In each of these quasi-static tests, the quasi-static method was applied. After those quasi-static tests, the specimens were tested under cyclic load condition using the Loung approach.

The sequence of quasi-static test procedure mentioned in the above paragraph consisted of loading and unloading the specimens three consecutive times until reaching 1% of permanent deformation, then one more full cycle until reaching 3% of permanent deformation and one last full cycle until reaching 5%. After these cycles and final unloading the specimens were cyclic tested using the methodology described in section 3.3.2. During each quasi-static loading cycle the fatigue limit was measured using the quasi-static methodology. Figure 3.16 presents the stress-strain curves of Specimen 6, which was also tested using the cyclic method mentioned in section 3.2.2.. Results for specimen 6 and other specimens (numbered 7 to 11) that were also tested using this stepped quasi-static loading procedure (1 to 5 steps) are given in Table 5.

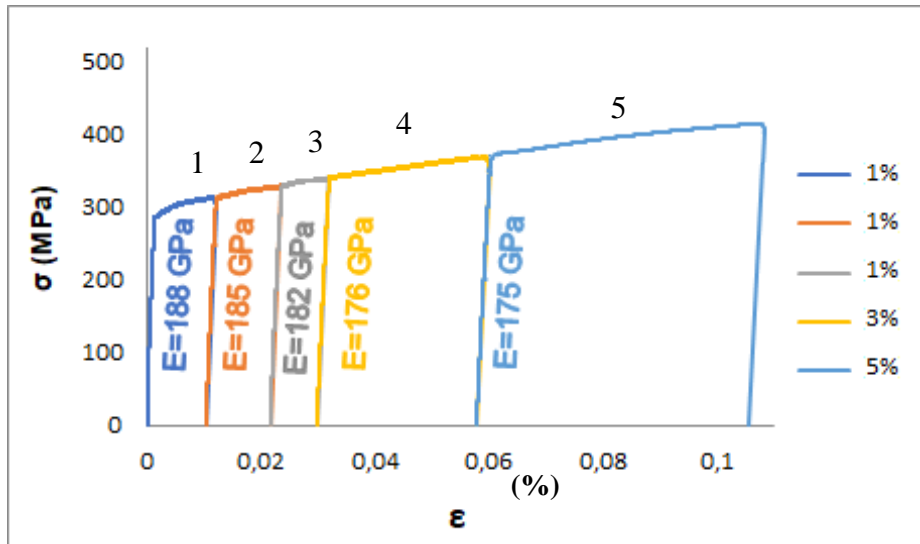


Figure 3.16: Specimen 6 stress-strain curves used for the quasi-static method.

3.3.4

Fatigue Limit Tests Using IR: Ultra Rapid Cyclic Loading

Figures 3.17a to 3.17d show the temperature distribution along a meridional line drawn in the middle of Specimen 6 during cyclic load steps 5 to 8 (steps with stresses above the fatigue limit, that are enumerated in Figure 3.14a). The stress amplitude at each load step at the center of the specimen (critical region) range from 170 to 200 MPa. At each load level it is possible to determine not only the fatigue strength for the same load ratio of the cyclic IR method ($R=0.1$), but also the transition from a non-damage state to a damage one along the specimen length. This procedure was presented in Figure 2.8.

It should be noted that the specimens numbered 1 to 4 and 6 to 8 were submitted to the ultra-rapid tests, as depicted in Tables 3 and 5.

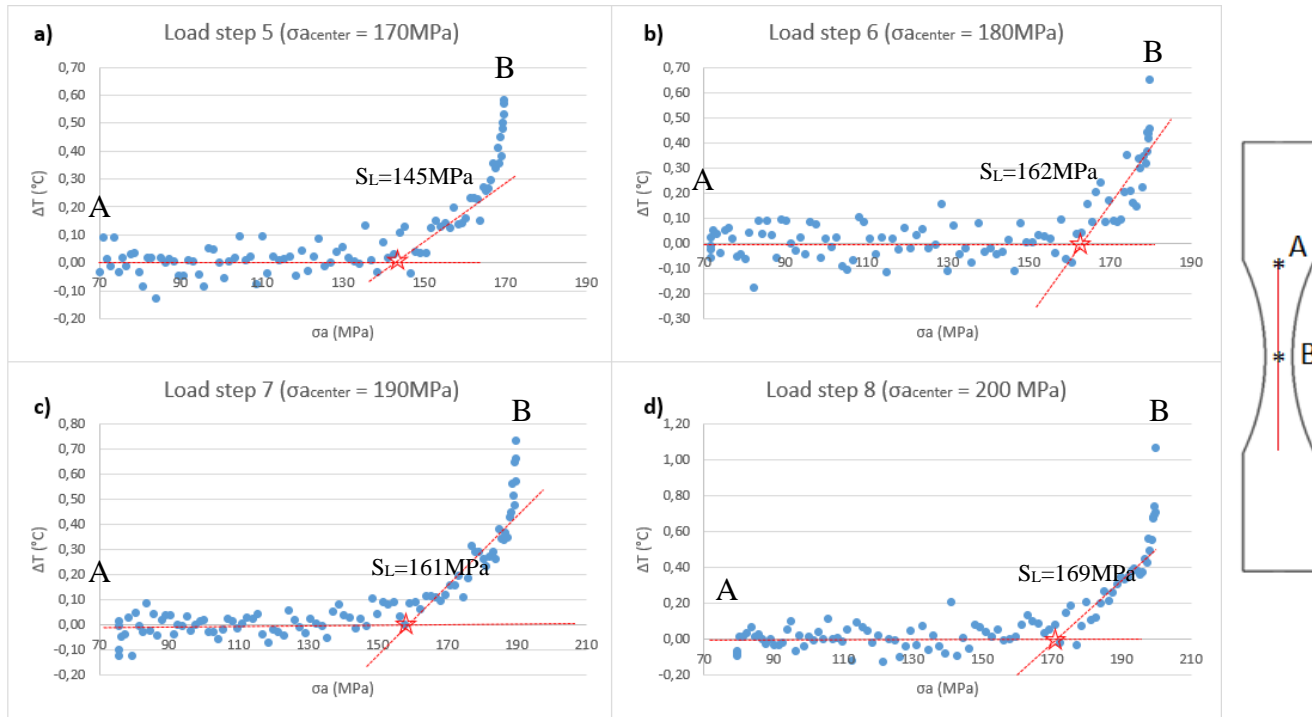


Figure 3.17: Specimen 6 ultra-rapid method results for the load steps above the fatigue limit.

3.3.5 Results: Fatigue Curves and Fatigue Limit

Having determined the values of ϕ as presented in Eq. (12), the SN fatigue curve can be constructed using the process outlined in the section 2.4.1.4. The SN fatigue curves for each stress ratio R calculated in this way are presented in Figure 3.18. The calculated curves encompass data fitted to the interval 10^3 to 10^6 cycles. Traditional push-pull fatigue tests were also performed using the ratio $R = 0.025$ [125]. An empirical curve for $R = -1$, with stress amplitudes for the analyzed interval (10^3 to 10^6) equal to $0.5Su$ and $0.9Su$, respectively is also plotted in Figure 3.18. Table 5 presents the fatigue results for all tested specimens using the rapid assessment methods. Table 6 and 7 provide additional information about the IR results measured.

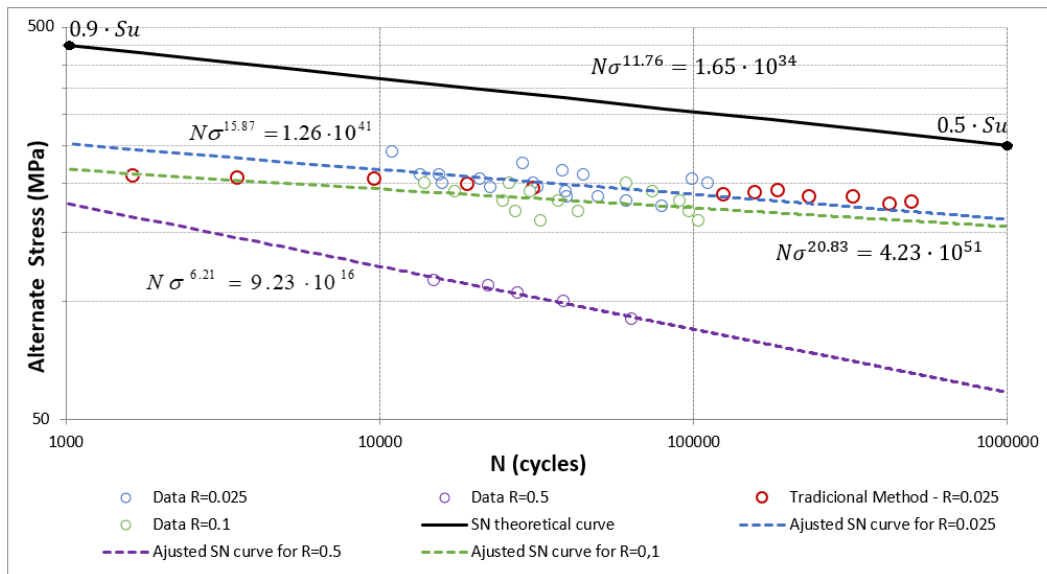


Figure 3.18: Fatigue SN curves for stress ratios measured using IR assessment methods, traditional method and analytically calculated.

Figure 3.19 compares all the SN curves presented in Figure 3.18, for that all curves were transposed to $R=-1$ ratio ($\sigma_m=0$). To relate the alternate stress with the mean stress it was used the adjusted exponents, m being equal to 1.40 and n equal to 1, which will be shown later in the Figure 3.21, section 3.3.6.

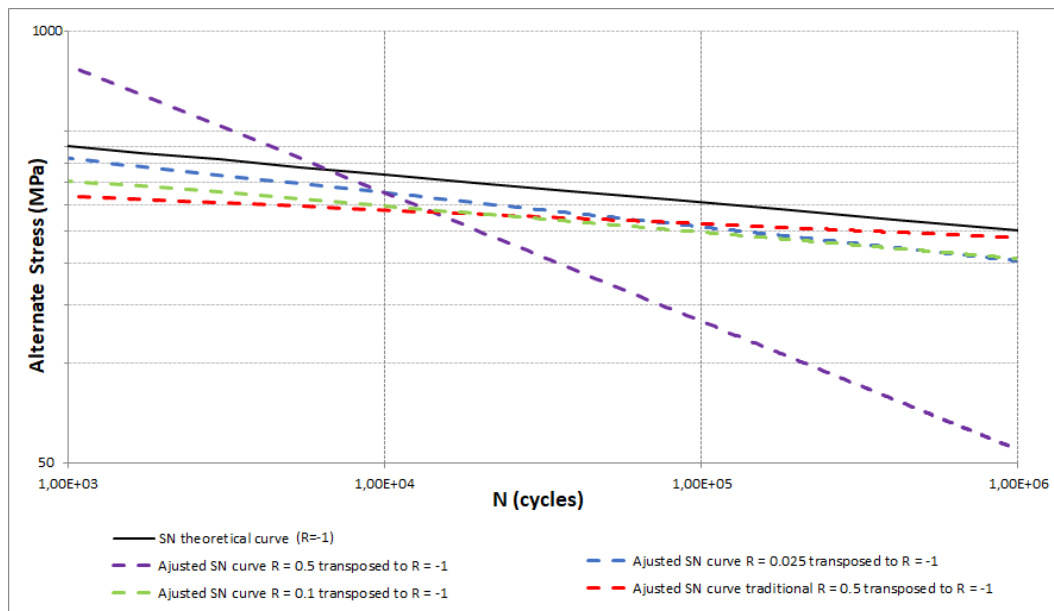


Figure 3.19: Comparison between all fatigue SN curves for different stress ratios using $R=-1$ ratio ($\sigma_m=0$).

Table 5: Measured IR results for each specimen.

Dog bone specimen	f (Hz) / stroke rate (mm/min)	Cyclic test				Quasi-Static test ($R=-1$) - S_L (MPa)						Ultra-Rapid test (number of load steps above fatigue limit ³)
		R	S_L (MPa)	ϕ (°C.cycles)	D (Eq. (14))	1%	1%	1%	3%	5%	Till failure	
1	15 / -	0.025	169	1.53×10^5	0.98	-	-	-	-	-	-	181 (3)
2	15 / -	0.025	184	9.2×10^4	0.97	-	-	-	-	-	-	179 (4)
3	5 / -	0.025	196	5.2×10^5	0.95	-	-	-	-	-	-	190 (3)
4	15 / -	0.5	86	3.0×10^4	0.96	-	-	-	-	-	-	88 (3)
5	- / 1	-	-	-	-	-	-	-	-	-	253	-
6	2 / 1	0.1	149	3.5×10^4	0.93	243	253	259	225	246	-	159 (4)
7	10 / 1	0.1	157	2.7×10^4	1.09	269	241	227	218	242	-	165 (3)
8	15 / 1	0.1	165	2.8×10^4	1.04	241	200	151	258	268	-	153 (2)
9	- / 1	-	-	-	-	250	239	242	259	266	-	-
10	- / 1	-	-	-	-	246	265	266	269	249	-	-
11	- / 1	-	-	-	-	262	270	252	251	228	-	-

Table 6: Average fatigue limit for each type of test.

Test type	R	Average S_L (MPa)	Standard deviation (MPa)
Cyclic	0.025	183	11
	0.5	86	0
	0.1	157	7
Static	-1	245	23
Ultra-Rapid	0.025	184	5
	0.5	88	0
	0.1	159	5

Table 7: Average fatigue limit for each load ratio R and its standard deviation.

R	Average S_L (MPa)	Standard deviation (MPa)
0.025	183	8
0.5	87	1
0.1	158	6
-1	245	24

³ The number of load steps with a stress amplitude superior to the measured fatigue limit using the IR cyclic method that also could be used to perform of the ultra-rapid cyclic method analysis.

3.3.6

Results: Influence of Mean Stress on the Fatigue Limit

Based on the fatigue limits presented in Table 5 for each applied IR method and R , data points S_N , which represent the fatigue strength at N cycles, formed by pairs of alternate stress amplitude values (σa) and mean stress (σm) were calculated and plotted in Figure 3.20. The resulting data was adjusted by a fitting equation presented in Eq. (18), the adjusting exponent m being equal to 1.40 and n equal to 1. The m exponent falls between the exponents given by the so-called Goodman and Gerber curves, respectively equal to 1 and 2 [126,127].

$$\left(\frac{\sigma a}{S_N}\right)^n + \left(\frac{\sigma m}{S_U}\right)^m = 1 \quad (18)$$

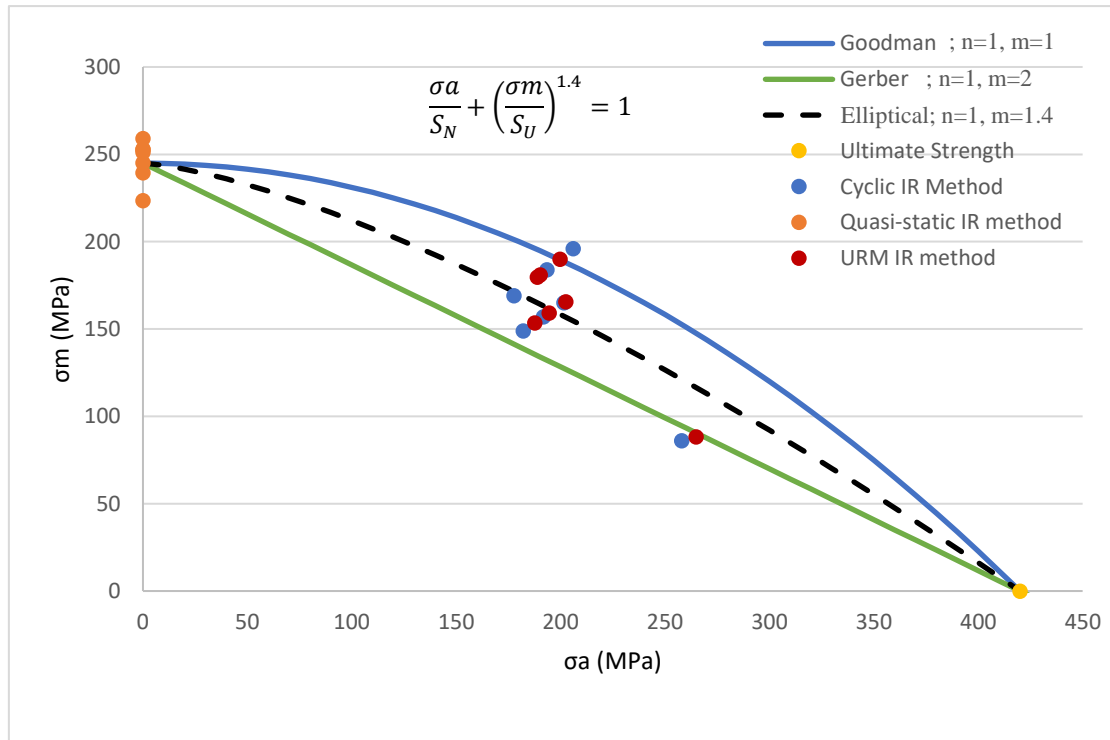


Figure 3.20: Alternate stress vs. mean stress for Gerber, Goodman and IR data.

Considering the data presented in Table 7, data points formed by the average values for each R were plotted in Figure 3.21.

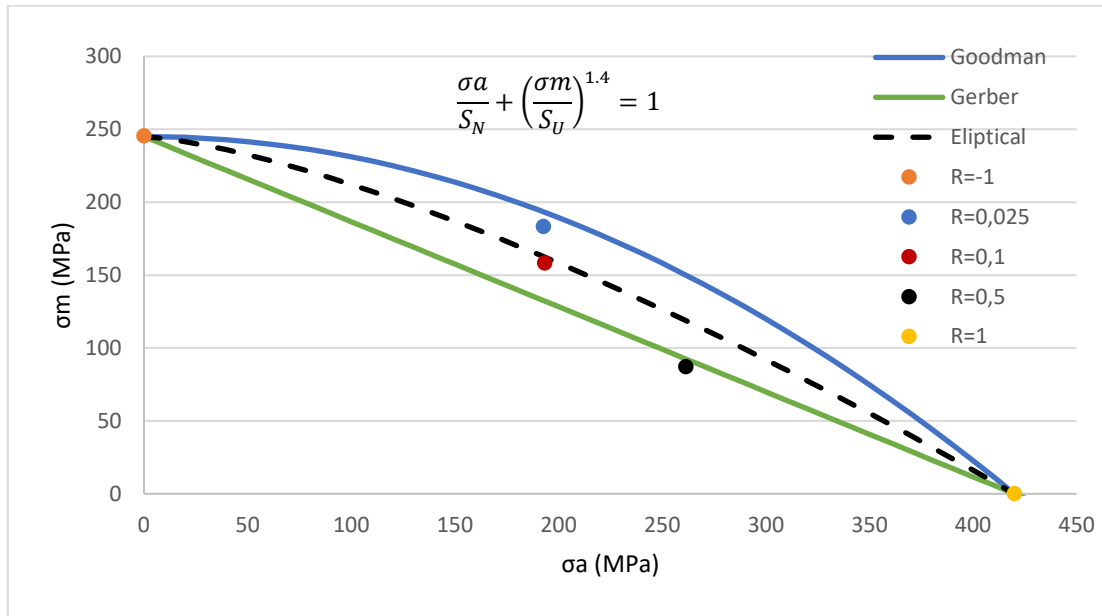


Figure 3.21: Alternate stress vs. mean stress for Gerber, Goodman and IR average data.

3.3.7 TSA Calibration for Low Carbon Steel

Typical TSA applications require knowing the relation between the temperature variations and the camera response signal, S^* . In order to correlate the cyclic stress range with temperature it is necessary to quantify the gain from the thermoelastic signal, so a calibration process between the mechanical properties of the specimen and the characteristics of the measurement system was conducted. For this purpose, several tests were performed on specimens with known stress states ($\Delta\sigma_1 + \Delta\sigma_2$). Considering single uniaxial tests specimen, $\Delta\sigma_1 = \Delta P/A$ and $\Delta\sigma_2 = 0$, where ΔP is the applied load range and A is the cross section being analyzed.

The gain values are usually determined more easily and reliably by experiments using the same material, an opaque black paint thin layer, a constant loading frequency and ambient conditions. The tests were carried out by applying a known unidirectional load and measuring the response of the camera.

The camera signal calibration employed five different specimens as presented in Figure 3.22. TS1 specimen and TS2 specimen were dog bone specimens taken

from a API 5L Gr. B pipe with a thickness of 6.35 mm, the TS3 specimen was removed from a 10 mm thick AISI 1212 steel pipe, TS4 specimen was taken from an AISI 1006 2mm thick steel plate and the TS5 specimen was machined from a SAE 1020 steel plate, in cylindrical format, according to ASTM E606M-12, with transversal section diameter equal to 8.5 mm.

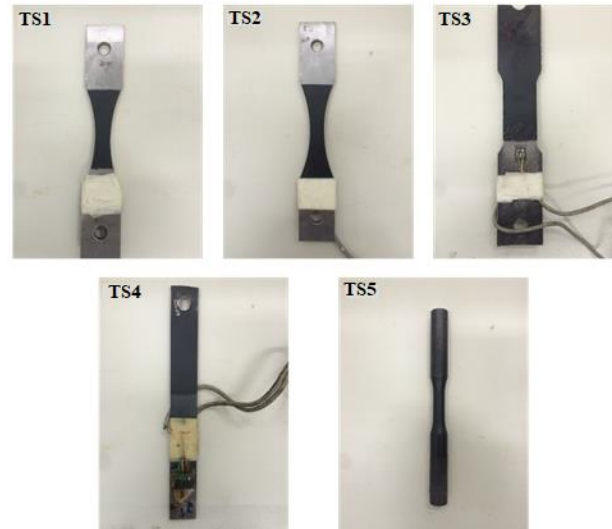


Figure 3.22: Test specimens utilized in the gain calibration.

Figure 3.23a shows the measured response map of TSA calibration sample TS1, while Figure 3.23b shows the response of the arbitrarily line chosen in the highest tensile stress cross-section of the specimen. The response scale is in camera units (*Cam Units*), which corresponds to the emissivity of the specimen in focus captured by the camera.

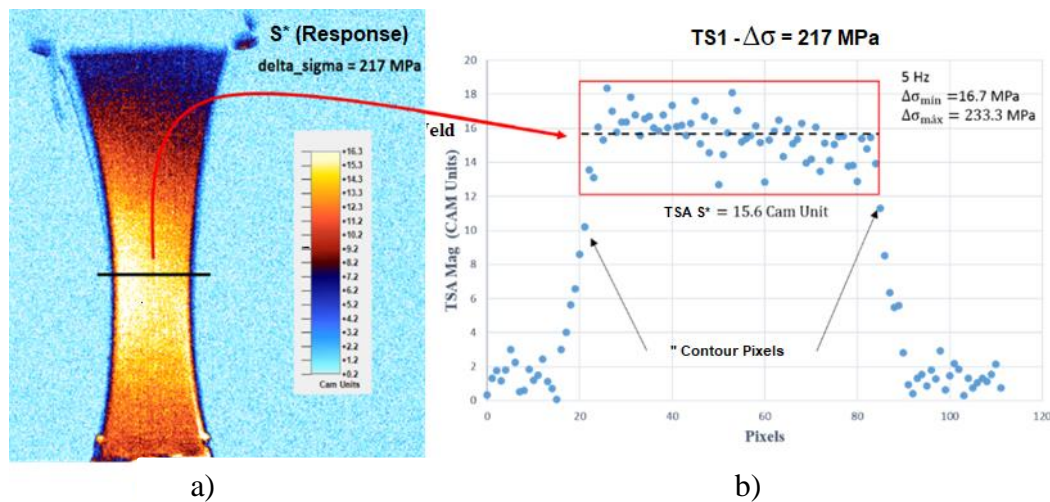


Figure 3.23: a) TSA response (S^*) map; (b) Arbitrarily line chosen in the highest tensile section of the specimen TS1.

Figure 3.24 shows the values of the TSA response of all test specimens used. The trend line is linear, compatible with the characteristic of the expected elastic mechanical behavior of the low carbon steels employed in the calibration tests.

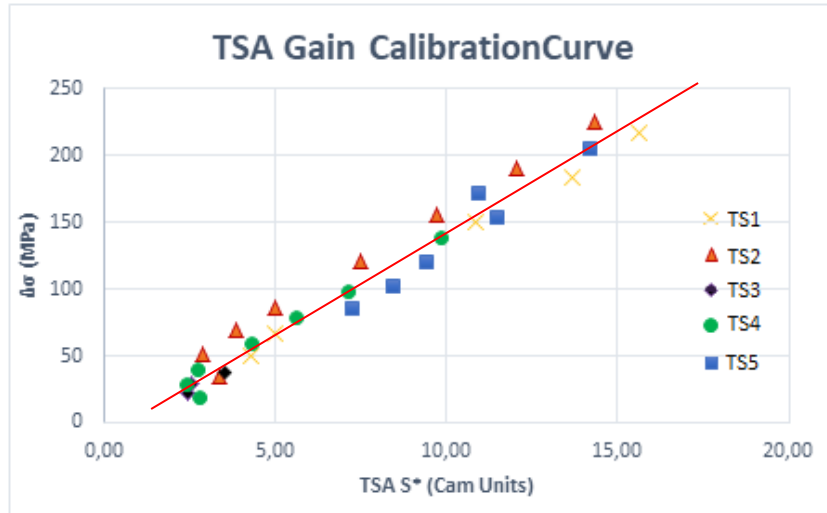


Figure 3.24: TSA gain calibration.

The experimental data adjusted curve is given by Eq. (19), it is valid for the particular IR camera and for the low carbon steel materials used.

$$\Delta\sigma = 15.027 \cdot S^* - 6.8752 \quad (19)$$

3.4 Complementary Experimental Techniques

This section describes the additional experimental techniques that were also used to assess the pipeline specimens during the realization of the tests, showing its principles and the experimental methodology employed.

3.4.1 Digital Image Correlation (DIC)

Digital Image Correlation is a non-contact optical-numerical technique widely used in experimental mechanics to obtain displacement fields of generated on the surface of a structural component when subjected to a given load. DIC uses one (DIC-2D) or more (DIC-3D) cameras to account for in-plane displacements (DIC-2D) and in and out-of-plane displacements (DIC-3D).

This technique is based on the comparison of two images, Figure 3.25, of the surface under observation, one obtained before the deformation (reference image) and the other in the deformed state (deformed image).

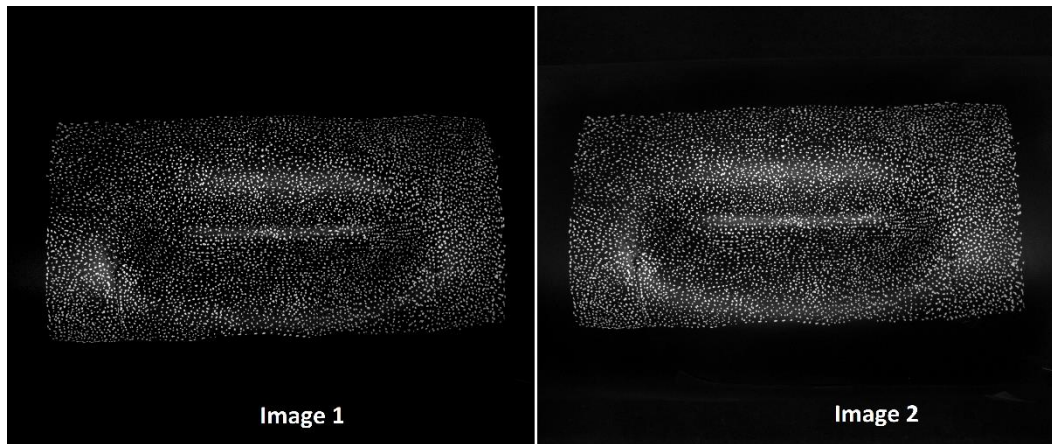


Figure 3.25: A pair of imagens used in the analysis of DIC-3D using two cameras.

The correlation process uses a numerical algorithm that tracks small elements in the images after the application of the load, called subsets or correlation windows, previously defined in the reference image. The tracking is performed through a correlation function, and the degree of similarity between subsets is determined by the maximum correlation value. To perform this process efficiently, the material must have a high contrast random pattern on its surface [128]. By tracking each subset, its displacement is defined as shown in Figure 3.26a, where u and v are the shifts along the x and y directions, respectively. In addition to the size of the subsets, another parameter defined by the analyst is the size of the step with which the algorithm performs the correlation process.

The deformation components are calculated by the displacement field differentiation. As this step is done independently for each subset, noisy data can be easily introduced and amplified in the differentiation. Thus, a process of data smoothing is commonly used in the calculation of the deformation. For this, the data are organized into small groups determined by the parameter known as strain window, also defined by the user, as shown in Figure 3.26b.

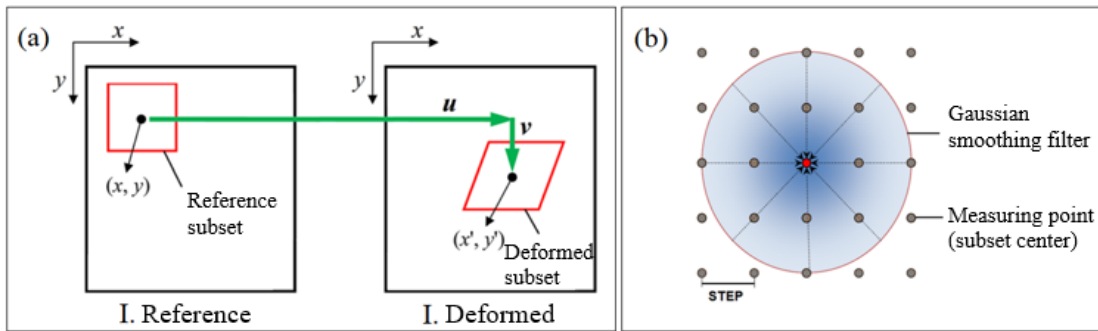


Figure 3.26: a) Basic physical principal of the DIC; b) Procedure of the calculation of the strain.

Like any other experimental technique, the DIC requires some cautions, such as: preparing the sample, organizing the equipment (cameras, light source, and computer controller), and calibrating the experiment.

The sample should be clean to minimize external interference. Then, the speckles are added over a white coating with speckles size in accordance with spatial resolution and lens magnification.

As rule of thumb, speckles should about 3 to 4 pixels in size. They can be applied with airbrush, with a standard spray aerosol, a regular brush, off the shelf stickers, or rubber stamped. Nonetheless the method, the pattern should non-repetitive and exhibit a high contrast. Because the cameras are usually black and white, those colors are recommended for the speckles. The cameras are usually monochromatic and with a high resolution. The light source should be in accordance with the camera's minimum exposure time. Finally, the computer controller triggers cameras, synchronizes the testing matching to record analog signals.

A spatial calibration is required to provide a field of view from known coordinates. This is achieved by placing grids of known separation in front of the cameras, recording them and processing them to create such envelope. The calibration includes intrinsic parameter (focal length, aspect ratio, and sensor center) as well as extrinsic parameters (such as relative linear and angular position between cameras). The latter will change in case the cameras are moved during the experiment.

Figure 3.27a shows a black coating with white speckles used for DIC of specimen Dent 6. The choice of black paint was made based on the paint emissivity for IR thermography. Figure 3.27b presents the calibration plate being used to perform calibration.

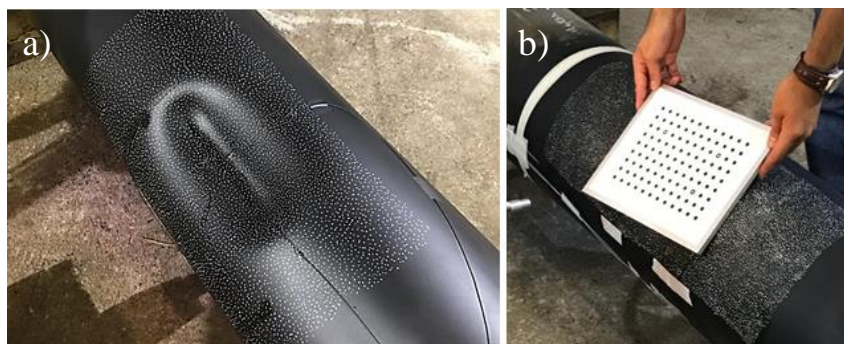


Figure 3.27: a) Dented pipe specimen Dent 6 black painted for the thermographic analysis and with small white dots to allow for digital image correlation analysis; b) Performing spatial calibration.

For the evaluation of behavior of the dented specimens the software VIC-Snap and VIC-3D from Correlated Solutions Inc. were employed respectively for image acquisition and image analysis.

The stereoscopic system consisted of two 5MP cameras (Point Grey GRAS-50S5M) including high magnification lenses (Tamron AF28-200mm F/3.8-5.6). DIC data analysis used the correlation algorithm NSSD (normalized sum of squared differences), a subset size of 35×35 pixels, a grid step of 8 pixels, a strain window of 15 displacement points and a pixel size about $200 \mu\text{m}$.

3.4.2 Fiber Bragg Strain Gauges (FBSG)

Not so recently, FBSG have achieved increased attractiveness and market acceptance, providing unique advantages in comparison to traditional sensors for certain applications.

To start the measurement the sensor must be bonded to the surface of interest just like any other strain gauge. The FBSG are sensitive to two physical quantities, deformation and temperature. Displacement and temperature gradients induce a stretching of the sensor, causing a change in the grating period and consequently a

change in the wavelength of the reflected light. Cases with considerable thermal variations require a thermal compensation to isolate the corresponding portions of the deformation from the temperature.

Regarding the assessment of the dented specimens, from the results obtained with the DIC, the fiber optics were placed as close as possible to the critical positions and most of them oriented in the circumferential direction. Figure 3.28 show the FBSG used in specimen Dent 5. Figure 3.29 shows schematically the disposition of the FBSG in specimen Dent 5 and also on each of the other studied dented specimens.

The fiber optics used in the strain measurements contained two Bragg grating sensors per fiber provided by FBGS – Fiber Bragg Grating Sensors, with gage length size of 8 mm, each grating having distinct wavelengths (1514 nm and 1524 nm), which allowed multiplexing the strain signal. The strain measurement was performed with an interrogator for optical extensometry Micron Optics model SI-255, which has 16 channels and can acquire the signal up to 1kHz.

The optical fiber employed had 20% reflectivity and a 0.1 nm spectral bandwidth with an ORMOCER coating.

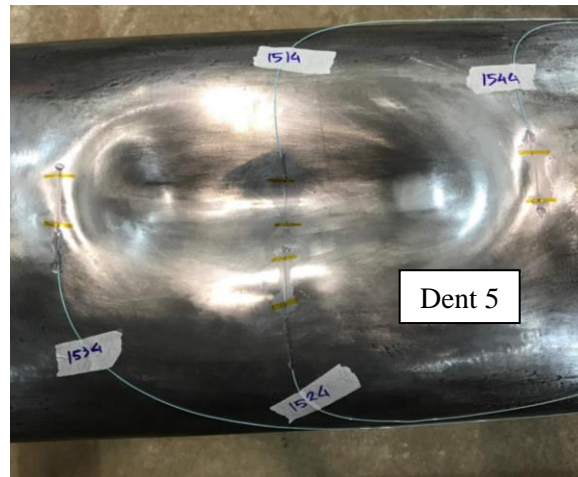


Figure 3.28: Specimen Dent 5 FBSGs positioned at the circumferential direction.

The conversion of wavelength variation to deformation is performed by Eq. (20):

$$\varepsilon = \frac{1}{k} \left(\frac{\Delta\lambda}{\lambda_0} \right) \cdot 10^6 \text{ } [\mu\varepsilon] \quad (20)$$

where λ is the wavelength, λ_0 is the initial wavelength and k is the gauge factor, being equal to 0.79.

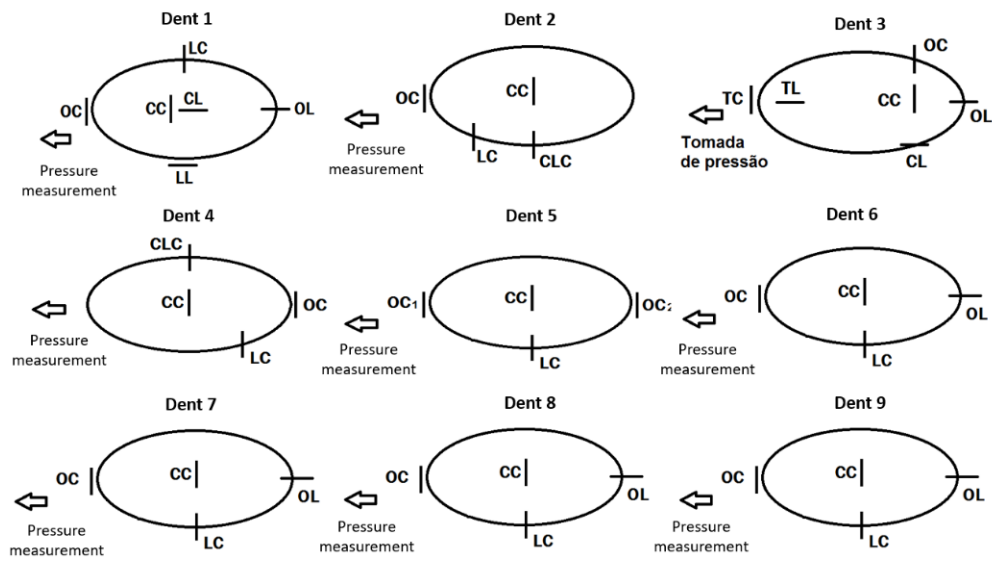


Figure 3.29: FBSG position in each of the studied specimens.

4. Fatigue Assessment of Dented Specimens

Cyclic internal pressure loading of a dented pipeline is a potential danger to its structural integrity due to the stress concentrators and deformations that can cause initiation and growth of fatigue cracks, leading the pipe to fail before reaching its service life [126]. There are several approaches available in the literature to assess fatigue of dents. The depth criteria is one of the most frequently used in the industry for their ease of application. Three approaches based on the API 579-1/ASME FFS-1 - 2016 Part 12 and Part 14 [66], and on the PDAM [73] will be discussed in this chapter.

Previous works, proposed and discussed by Ávila et al. [84] and Silva et al. [85, 86], successfully utilized the SN method coupled with finite element method to predict fatigue life of pipe specimens subject to dents. Based on that, an initial approach accounted the use of the SN methodology coupled with the finite element technique to study the plain dent pipe specimen presented in this work. As will be seen in the development of this chapter this assumption will be later improved to a strain-life approach.

Besides the mean stress approach proposed by Silva et al. [85, 86], this chapter also discusses a more realistic approach based on the ϵN that used the Coffin-Manson equation. This latter approach uses the actual hot spot strains measurements as well as strains obtained from two numerical models of dents, which were developed using the finite element method.

4.1 Fatigue Life Approaches

Initially, neglecting the fact that the maximum depth of the dented specimens analyzed in this thesis would be not accepted by a static level 1 rejection criteria and based on the experience gathered from the literature [66], a stress-life fatigue methodology was adopted to assess the behavior of the dented specimens.

A vast majority of analysis employs the SN method, which is a more conservative approach of the dent phenomenon.

Going further, using the techniques of experimental mechanics coupled with the finite element method and considering that the dented specimens analyzed presented high levels of deformation, a more efficient approach was applied by employing the Coffin-Manson strain-life methodology and the Miner's fatigue damage rule.

4.1.1

API 579-1/ASME FFS-1 - 2016 Part 12 Standard

The standard API 579-1/ASME FFS-1 - 2016 Part 12 Level 2 [66] presents an assessment procedure for pressurized components containing dents, gouges, or dent-gouge combinations resulting from mechanical damage. The Level 1 criterion accepts the dent if the ratio dent depth to pipe diameter is less than 7% (or 10% for restrained dents), and if the component is not in cyclic service or subjected to less than 150 cycles. Otherwise, if more than 150 cycles are applied a Level 2 analysis is required.

In Level 2 assessment a SN fatigue analysis is provided. Some requirements must be met to use the procedure; the pipe diameter should be between 168 mm and 1050 mm, the uniform thickness away from the damage should be between 5 mm and 19 mm and the depth of the dent must not exceed 7% of pipe diameter. If Level 2 is not satisfied, a Level 3 assessment can be performed.

The Level 2 assessment considers the membrane stress along with stress concentration factors and does not consider reliability factors. The stress component used is the nominal circumferential and the parameters of the fatigue curve, Eq. (21), are defined in Eqs. (22) to (29).

$$N = 562.2 \left[\frac{Su}{2\sigma_A K_d K_g} \right]^{5.26} \quad (21)$$

$$\sigma_A = \sigma_a \left[1 - \left(\frac{\sigma_{m,max}^c - \sigma_a}{Su} \right)^2 \right]^{-1} \quad (22)$$

$$\sigma_a = \frac{\sigma_{m,max}^c - \sigma_{m,min}^c}{2} \quad (23)$$

$$K_d = 1 + C_s \sqrt{\frac{t_c}{D_o} (d_{d0} \cdot C_{ul})^{1.5}} \quad (24)$$

$$C_s = 2.0 \quad (\text{for smooth dents, } r_d \geq 5t_c) \quad (25)$$

$$C_s = 1.0 \quad (\text{for sharp dents, } r_d < 5t_c) \quad (26)$$

$$K_g = 1.0 \quad (\text{for dent without gouges}^4) \quad (27)$$

$$C_{ul} = 1.0 \quad (\text{data in millimeters}) \quad (28)$$

$$C_{ul} = 25.4 \quad (\text{data in inches}) \quad (29)$$

The pipe nominal circumferential stress respectively to the maximum and minimum pressures correspond to $\sigma_{m,max}^C$ and $\sigma_{m,min}^C$. The dent depth in the unpressurized condition is d_{d0} , the pipe wall thickness considering the effects of corrosion is t_c and S_u is the minimum specified ultimate tensile strength.

The stress concentration caused by the dent is taken into consideration by the term K_d , which is dimensional and a function of the dent and the pipe geometry.

The technical basis and validation of the assessment procedures in Part 12 for dents is provided by the revised methodology developed by the EPRG [72].

4.1.2 PDAM – Pipeline Defect Assessment Manual

The PDAM presents a model to assess the fatigue life of the plain dent using an SN curve for a longitudinal submerged arc welding pipe according to the DIN 2413 [71], modified for the stress concentration due to the dent.

The methodology is based on the dent shape, primarily on its depth, and on the pipe dimensions. The method does not include a stochastic analysis; however, safety factors are already embedded in its formulation. The stress concentration factor is given as a function of the remaining depth after the relief of the rerounding pressure. The fatigue life of an unconstrained plain dent is given by:

⁴ For dents with gouges - $K_g = 1 + 9(d_g/t_c)$, in this work this type of flaw was not considered.

$$N = 1000 \left[\frac{(Su-50)}{2\sigma_A K_s} \right]^{4.292} \quad (30)$$

where

$$2\sigma_A = Su[B(4 + B^2)^{0.5} - B^2] \quad (31)$$

$$B = \frac{\frac{\sigma_a}{Su}}{\left[1 - \frac{\sigma_a(1+R)}{Su(1-R)} \right]^{0.5}} \quad (32)$$

$$R = \frac{\sigma_{min}}{\sigma_{max}} \quad (33)$$

$$K_s = 2.871\sqrt{K_d} \quad (34)$$

$$K_d = H_o \frac{t}{D} \quad (35)$$

$$H_o = 1.43H_r \quad (36)$$

A more conservative approach, called herein PDAM_95, uses a one tail confidence level of 95 percent. This equates to reducing the predicted fatigue life calculated by Eq. (30) by a factor of 13.3.

$$N_{PDAM_95} = \frac{N}{13.3} \quad (37)$$

The pipe nominal circumferential stress respectively to the maximum and minimum pressures correspond to σ_{max} and σ_{min} . H_o and H_r are the dent depth at zero pressure and at pressurized conditions, respectively. The pipe geometry is described by the minimum wall thickness, t , and by the nominal pipe diameter, D . σ_a is the alternate stress and σ_A is the equivalent alternate stress, which is taken into consideration by an elliptic relation that uses the term B . The term Su is the minimum specified ultimate tensile strength.

The stress concentrated around the dented region is quantified by the term K_s , which is not dimensionless, being dependent of the dent and the pipe geometry. The method is expressed in SI units and modifications are required if a different system of units is used.

This methodology is based on the first empirical method developed by the EPRG [70] for predicting the fatigue life of an unconstrained plain dent.

4.1.3 Mean Stress Method

This fatigue method was proposed by Silva et al. [85,86]. It uses the solution of the stress problem solved for each mesh node by a FEM and then is applied in a Wohler curve, where the mean and alternating von Mises equivalent stresses resulting from each cyclic pressure loading are determined after the rerounding process. The influence of the mean stress is taken into account using the Gerber parabola.

The dent width and length play an important role in the distribution of strains and stresses. The stress concentrations associated with the dent format can deteriorate the performance as well as the fatigue life of pipe. The stress concentration factor (K_t) was calculated using Eq. (38):

$$K_t = \frac{\Delta\sigma_{VMmax}}{\Delta\sigma_{VMnom}} \quad (38)$$

where $\Delta\sigma_{VMmax}$ is the maximum variation of the von Mises equivalent stress and $\Delta\sigma_{VMnom}$ is the variation of the nominal von Mises equivalent stress corresponding to the internal pressure applied.

The equivalent alternate stress is calculated by the von Mises using Eq. (39), the variation of its value in each pressure cycle.

$$\sigma_{VM}^a = \frac{1}{\sqrt{2}} [(\sigma_c^a - \sigma_l^a)^2 + (\sigma_c^a - \sigma_r^a)^2 + (\sigma_l^a - \sigma_r^a)^2 + 6(\tau_{cl}^{a^2} + \tau_{lr}^{a^2} + \tau_{cr}^{a^2})]^{0.5} \quad (39)$$

Similarly, the equivalent mean stress can be calculated using Eq. (40), the variation of its value in each pressure cycle.

$$\sigma_{VM}^m = \frac{1}{\sqrt{2}} [(\sigma_c^m - \sigma_l^m)^2 + (\sigma_c^m - \sigma_r^m)^2 + (\sigma_l^m - \sigma_r^m)^2 + 6(\tau_{cl}^{m^2} + \tau_{lr}^{m^2} + \tau_{cr}^{m^2})]^{0.5} \quad (40)$$

where

$$\sigma_i^x = \left(\frac{\sigma_i^{x_{end}} \pm \sigma_i^{x_{beginning}}}{2} \right), \quad i = c, l \text{ and } r; \quad x = a (-) \text{ and } m (+). \quad (41)$$

$$\tau_{ij}^x = \left(\frac{\tau_{ij}^{x_{end}} \pm \tau_{ij}^{x_{beginning}}}{2} \right), \quad i \neq j = c, l \text{ and } r; \quad x = a (-) \text{ and } m (+). \quad (42)$$

From the geometry of the dent, it can be assumed that $\sigma_r^a = \tau_{cr}^a = \tau_{lr}^a = \sigma_r^m =$

$$\tau_{cr}^m = \tau_{lr}^m = 0.$$

The SN fatigue curve is presented in Eq. (43), and its parameters are defined in Eqs. (44) to (47) from reference [127]. The influence of the mean stress is considered by using Gerber's parabola.

$$N = C \left[\frac{\sigma_a}{1 - \left(\frac{\sigma_m}{S_u} \right)^2} \right]^{-B} \quad (43)$$

where

$$B = \frac{\log(10^6/10^3)}{\log(S_f/S_e)} \quad (44)$$

$$C = 10^6 S_e^B \quad (45)$$

The fatigue limit can be measured like previously shown in Chapter 3 or can be calculated from the value of the tensile strength (S_u) according to Eq. (46) and modified by the factors of finishing (k_a - cold rolled), size (k_b), and loading (k_c) [126, 127].

$$S_e = 0.5 \cdot S_u \cdot k_a \cdot k_b \cdot k_c \cdot K_t^{-1} \quad (46)$$

The fatigue strength at 10^3 cycles (S_f) is determined by Eq. (47)⁵.

$$S_f = 0.76 \cdot S_u \quad (47)$$

Other values of S_f can be used depending on the material being used, for example:

$$S_f = 0.9 \cdot S_u \quad (48)$$

$$S_f = 1 \cdot S_y \quad (49)$$

where S_y is the yield strength of the material.

⁵ The effect of K_t can also be used to multiply the corresponding nominal acting stress. In this case, the calculus of S_e should use $K_t=1$. The effect of the notch sensitivity, q , as proposed by Peterson [127] may be used and then $K_f=1+q(K_t-1)$ should be used instead of K_t . If the effect of K_t or K_f can also influence the value of S_f , in this case, equations (47) to (49) would be calculated as $S_f = X(1/K_t)$.

4.1.4 Coffin-Manson Method

As the results will later show, because of the high level of deformation caused by the dent a more robust and precise analysis methodology is required. The Coffin-Manson method is a strain-life approach where the relationship between the strain range and the corresponding initiation life of a crack is done taking into consideration the elastic and plastic portions of the deformations. For very short lives, the Coffin-Manson curve tends to its plastic part, as the elastic deformations are negligible in front of them. Though, for very long lives, the curve tends to its elastic part, which is nothing more than a material adopted SN approach

The fatigue damage initiation prediction is accomplished by using Coffin-Manson model, Eq. (50), to determine life as a function of some equivalent strain amplitude ε_a ($\mu\epsilon$). As results for the strain measurements will show clearly, the circumferential strain actuating at the dent hot spots were used to in the life predictions. In the present case, the universal fatigue exponents 0.12 and 0.6 as proposed by Manson [111] were used. Values of S_u , E and ε_f are shown in Table 4.

$$\varepsilon_a = \left(3.5 \frac{S_u - \sigma_m}{E} (N)^{-0.12} + \varepsilon_f^{0.6} (N)^{-0.6} \right) \frac{10^6}{2} \quad (50)$$

4.1.4.1 Analytical Methods to Calculate the Strain Amplitude

The finite element method was used to estimate the strain developed in the specimens with dents subjected to internal pressure, as it will be shown in section 4.2. Moreover, other two analytical formulations for the strain range prediction will be presented in this section.

4.1.4.1.1

Calculation of Strain Range Using the Hysteresis Loop Curve (Alternative Method 1)

The relation between stress and strain is given by the monotonic stress-strain curve, often represented by the Ramberg-Osgood⁶ equation, Eq. (51), which proposes that the total strain can be divided in an elastic and a plastic portion.

$$\Delta\varepsilon = \frac{\Delta\sigma}{E} + 2 \left(\frac{\Delta\sigma}{2K_c} \right)^{\frac{1}{n_c}} \quad (51)$$

The strain amplitude can also be described by the linear rule, Eq. (52).

$$\Delta\varepsilon = \frac{P_{Neuber}}{\Delta\sigma} \quad (52)$$

The influence of the elastic stress concentration K_t can be evaluated following Eq. (53) given by the so called Neuber's product P_{Neuber} [126].

$$P_{Neuber} = K_t^2 \cdot \frac{\Delta\sigma_{nom}^2}{E} \quad (53)$$

The strain and stress ranges can be calculated by solving the equation system composed by Eqs. (51) and (52).

4.1.4.1.2

Calculation of Strain Range Using the Stabilized Curve of The Elastic-Perfectly Plastic Material (Alternative Method 2)

Assuming a material with perfectly elastic-plastic behavior, as shown by Figure 4.1, the strain range can be calculated by Eq. (54).

$$\Delta\varepsilon = \frac{K_t^2 \cdot \Delta\sigma_{nom}^2}{E \cdot \Delta\sigma} \quad (54)$$

$$\Delta\sigma = \min [K_t \cdot \Delta\sigma_{nom}; 2S_{flow}] \quad ^7 \quad (55)$$

⁶ The coefficients of the Ramberg-Osgood model for the studied API-5L Gr. B steel were estimated from the measured stress-strain curve, Figure 3.13, as $K_c = 663$ MPa and $n_c = 0.145$.

⁷ S_{flow} can be assumed equal to S_y , $\frac{S_u + S_y}{2}$ or $1.2S_y$

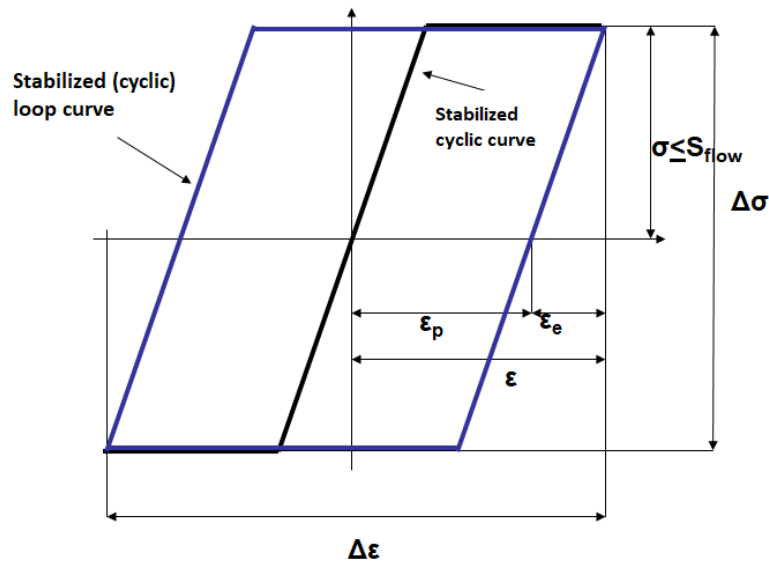


Figure 4.1: Material with a perfect elastic-plastic behavior.

4.1.5 API 579-1/ASME FFS-1 - 2016 Part 14 Standard

The API 579-1/ASME FFS-1 - 2016 Part 14 Level 2 [66] presents a fatigue damage evaluation similar to the one presented in the ASME Sec VIII div. 2 Part 5 [79]. The analysis methods for fatigue and the associated fatigue curves are presented in two forms: fatigue analysis method and curves that are based on smooth bar test specimens, and fatigue analysis method and curves that are based on test specimens that contains welds.

At Level 2 assessment, in which the present fatigue analyses are performed, three methods for fatigue evaluation are provided. Methods A and B that use an approach focused on elastic stresses and elastic-plastic deformations, respectively. Method C, which analyses weld details, will not be considered in this work because of the absence of relevant welds near or at the dented regions of the studied specimens.

4.1.5.1

Level 2 Method A - Assessment Using Elastic Stress Analysis and Equivalent Stresses

In Method A the effective total equivalent stress amplitude is used to evaluate the fatigue damage for results obtained from a linear elastic stress analysis. The controlling stresses for the fatigue evaluation are the primary plus secondary plus peak equivalent stress amplitudes. These are defined as one-half of the primary plus secondary plus peak stress equivalent stress ranges, $(P_L + P_b + Q + F)$, calculated for each cycle in the loading history. P_L , P_b , Q and F represent the membrane, bending, secondary and peak stress, respectively.

The membrane component is the stress resulting from the load application. When the wall offers resistance to bending, bending stresses occur in addition to membrane stresses. Secondary stress is produced by a relenting load (self-limiting). Peak stresses are the additional stresses due to stress intensification in highly localized areas. They apply to both sustained loads and self-limiting loads. There are no significant distortions associated with peak stresses [79].

The primary plus secondary plus peak stress equivalent stress range is the equivalent stress, derived from the highest value across the thickness of a section, of the combination of all primary, secondary, and peak stresses produced by specified operating pressures and other mechanical loads and by general and local thermal effects and including the effects of gross and local structural discontinuities. In the dents analysis all thermal effects were neglected.

After determining the loading history and obtaining the stress tensor at the start and end of the k^{th} cycle counted at the critical spot of the dent, the fatigue analysis procedure is defined in Eqs. (56) to (62).

$$\Delta\sigma_{ij,k} = \max^{load}\sigma_{ij,k} - \min^{load}\sigma_{ij,k} \quad (56)$$

$$\Delta S_{P,k} = \frac{1}{\sqrt{2}} \left[(\Delta\sigma_{11,k} - \Delta\sigma_{22,k})^2 + (\Delta\sigma_{11,k} - \Delta\sigma_{33,k})^2 + (\Delta\sigma_{22,k} - \Delta\sigma_{33,k})^2 + 6(\Delta\sigma_{12,k}^2 + \Delta\sigma_{13,k}^2 + \Delta\sigma_{23,k}^2) \right]^{0.5} \quad (57)$$

$$S_{alt,k} = \frac{K_{e,k} \cdot \Delta S_{P,k}}{2} \quad (58)$$

$$K_{e,k} = 1.0 \quad (\text{for } S_{n,k} \leq S_{PS}) \quad (59)$$

$$K_{e,k} = 1.0 + \frac{(1-n)}{n(m-1)} \left(\frac{\Delta S_{n,k}}{S_{PS}} - 1 \right) \quad (\text{for } S_{PS} \leq \Delta S_{n,k} \leq mS_{PS}) \quad (60)$$

$$K_{e,k} = \frac{1}{n} \quad (\text{for } \Delta S_{n,k} \geq mS_{PS}) \quad (61)$$

$$S_{PS} = \min[S_u, \max[3S_m, 2S_y]] \quad (\text{for } \Delta S_{n,k} \geq mS_{PS}) \quad (62)$$

where, for the k^{th} cycle, $\sigma_{ij,k}$ is the stress tensor at the location under evaluation at time, $\Delta S_{P,k}$ is the range of primary plus secondary plus peak equivalent stress, $S_{alt,k}$ is the alternating equivalent stress, $K_{e,k}$ is the fatigue penalty factor, S_{PS} is the allowable limit on the primary plus secondary stress range, $\Delta S_{n,k}$ is the primary plus secondary equivalent stress range, S_m is the material maximum allowable stress⁸, n is the fatigue crack-growth exponent and m is the time-dependent crack-growth coefficient⁹.

The permissible number of cycles is based on smooth bar test results that will be shown later at section 4.1.5.3.

4.1.5.2

Level 2 Method B - Assessment Using Elastic-Plastic Stress Analysis and Equivalent Strain

In Method B, an effective strain range is used to evaluate the fatigue damage based on the results from an elastic-plastic stress analysis. This analysis is performed for the complete loading time history using a cyclic plasticity algorithm with kinematic hardening¹⁰. The effective strain range is calculated using the equation shown below for the k^{th} cycle identified using a multiaxial cycle counting procedure.

After determining the loading history and obtaining the strain tensor at the start and end of the k^{th} cycle counted, the fatigue analysis procedure is defined in Eqs. (63) to (68).

⁸ For the API-5L Gr. B steel $S_m = 147$ MPa [79]

⁹ For carbon steel $n = 0.2$ and $m = 3.0$ [66].

¹⁰ Herein, the analysis was performed using the results of linear elastic FEM (second type of finite element model).

$$\Delta e_{ij,k} = \max load e_{ij,k} - \min load e_{ij,k} \quad (63)$$

$$\Delta p_{ij,k} = \max load p_{ij,k} - \min load p_{ij,k} \quad (64)$$

$$\Delta \varepsilon_{peq,k} = \frac{\sqrt{2}}{3} \left[(\Delta p_{11,k} - \Delta p_{22,k})^2 + (\Delta p_{11,k} - \Delta p_{33,k})^2 + (\Delta p_{22,k} - \Delta p_{33,k})^2 + 6(\Delta p_{12,k}^2 + \Delta p_{13,k}^2 + \Delta p_{23,k}^2) \right]^{0.5} \quad (65)$$

$$\Delta \varepsilon_{e,k} = \frac{1}{\sqrt{2}(1+\nu)} \left[(\Delta e_{11,k} - \Delta e_{22,k})^2 + (\Delta e_{11,k} - \Delta e_{33,k})^2 + (\Delta e_{22,k} - \Delta e_{33,k})^2 + 6(\Delta e_{12,k}^2 + \Delta e_{13,k}^2 + \Delta e_{23,k}^2) \right]^{0.5} \quad (66)$$

$$\Delta \varepsilon_{eff,k} = \Delta \varepsilon_{e,k} + \Delta \varepsilon_{peq,k} \quad (67)$$

$$S_{alt,k} = \frac{E_{ya,k} \cdot \Delta \varepsilon_{eff,k}}{2} \quad (68)$$

where $e_{ij,k}$ is the elastic strain tensor at the location under evaluation at time for the k_{th} cycle, $p_{ij,k}$ is the plastic strain tensor at the location under evaluation at time for the k_{th} cycle, $\Delta \varepsilon_{eff,k}$ is the effective strain range for the k_{th} cycle, $S_{alt,k}$ is the alternating equivalent stress for the k_{th} cycle.

The permissible number of cycles is based on smooth bar test results that will be shown later at section 4.1.5.3.

4.1.5.3 ASME Fatigue Curve

Figure 4.2 shows the fatigue data that was used to construct the original ASME Sec VIII div. 2 Part 5 [79] on which the API 579-1/ASME FFS-1 - 2016 Part 14 Level 2 [66] was based. The solid line is the best-fit failure curve for zero mean stress and is described by Eq. (69). Knowing the value of the stress amplitude, the number of cycles to failure can be obtained.

$$S = \frac{E}{4\sqrt{N}} \ln \frac{100}{100-RA} + S_e \quad (69)$$

where E is the elastic modulus (psi), N the number of cycles to failure, S the stress amplitude (psi), S_e the fatigue or endurance limit (psi) and RA the reduction in area in the tensile test (%).

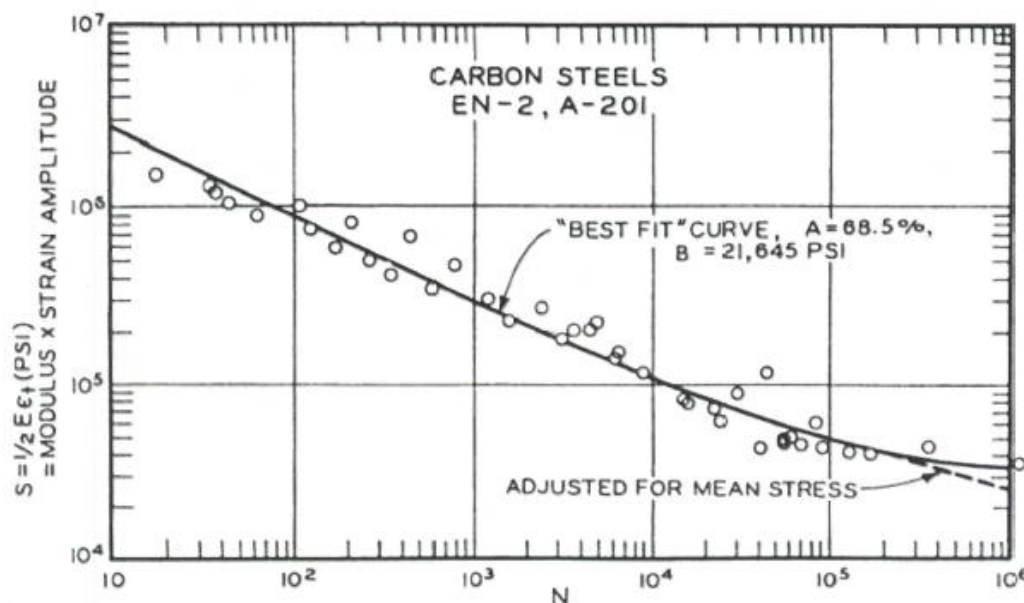


Figure 4.2: Fatigue data for carbon alloy steel [129].

4.2 Finite Element Models

The finite element modeling begins with the discretization of the specific geometry in a finite number of elements, so that each element individually satisfies the equilibrium conditions and, among themselves, the geometric compatibility conditions of the continuous.

The shape of the dent depends greatly not only on the final indentation depth, but also on the format of the indenter. As previously mentioned, a preliminary study was conducted where several different indenters were modeled, totalizing 16 different formats, having been 2 actually manufactured and tested, to simulate attempts to generate the desired plain dent shape. This study can be found at Appendix C.

Herein, the two types of finite element models that were developed using a commercial software package ANSYS v15.0 to simulate the dented specimens under cyclic internal pressure are presented. The first model type focuses on the dent creation process, simulating the entire initial indentation and spring back processes, the later rerounding operation and the first cycles of cyclic pressure loading. This type of model considered the geometric, material and contact nonlinearities during the simulation of the indentation and later the pipeline cyclic operation.

On the other hand, the second type of model is much simpler. It combines the “exact” dent shape measured by the DIC technique with the quasi-cylindrical portion of the non-deformed pipe to build the model geometry. It uses a material with a linear elastic behavior. This type of model focuses only on the pipeline cyclic operation process.

4.2.1 First Type of Finite Element Model

The different dent geometries worked in this thesis, a total of nine dented pipeline specimen, can be summarized into two distinguished shapes; one with plain format, corresponding to specimen Dent 6, where the length of the dent is greater than the width, and one with a hump in the central portion of the dent, corresponding to specimen Dent 3, where the snap thru buckling occurred.

In this way, two models were developed as similar as possible to reality employing the true-stress-true strain curve of Figure 3.13, with the aim of simulating the process of obtaining the dents geometry, one for the plain format and one for the buckled format.

4.2.1.1 Model Geometry

Both models used the same geometry, Figure 4.3, which has $\frac{1}{4}$ of symmetry with restrictions to the displacements in the faces of symmetry ($ux = 0$ in the free faces at yz plane and $uz = 0$ in free faces at the xy plane).

The head cap was not simulated, instead a pressure equal to the longitudinal force exerted by the head was applied in the free end of the pipe.

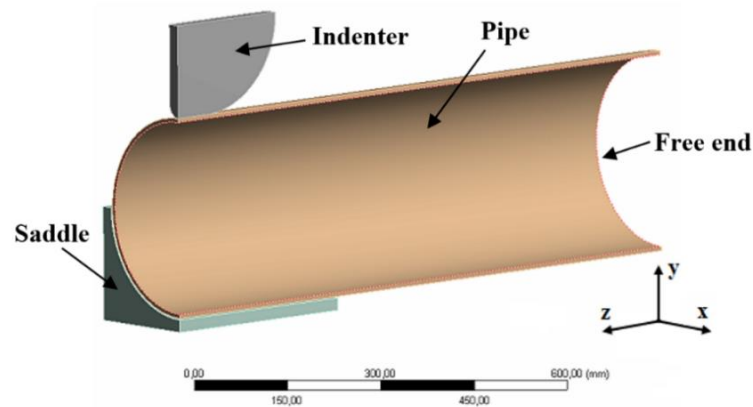


Figure 4.3: Finite element model geometry with $\frac{1}{4}$ of symmetry.

Figures 4.4 to 4.6 show the geometry of the indenter, the pipe specimen and the saddle, respectively.

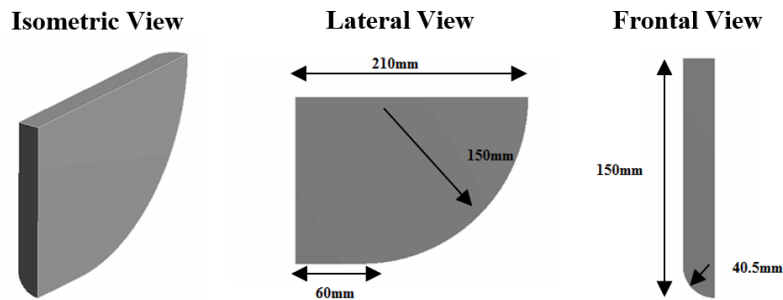


Figure 4.4: Indenter dimensions.

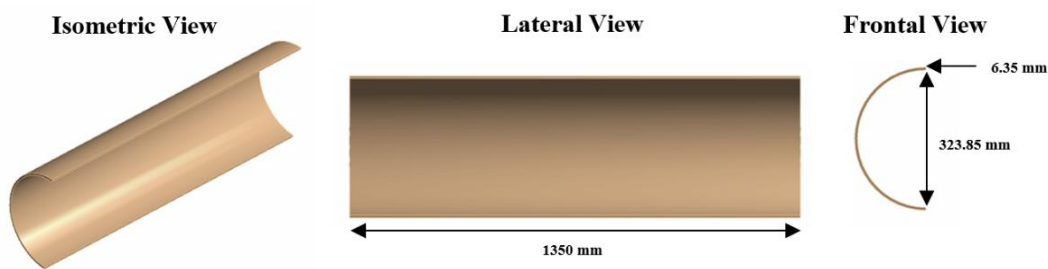


Figure 4.5: Pipe specimen dimensions.

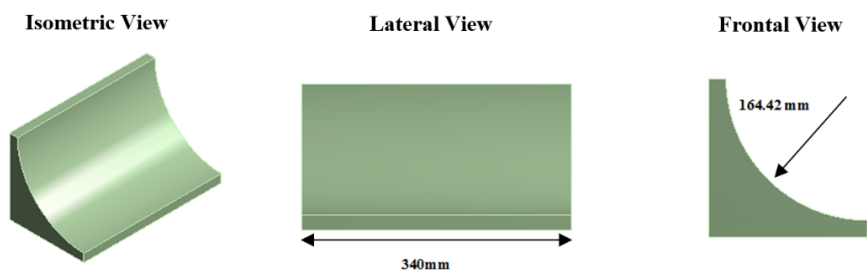


Figure 4.6: Saddle dimensions.

4.2.1.2 Model Parameters and Configuration

The numerical models for the determination of the geometry of the dents caused by a longitudinal cylindrical indenter was based on a three-dimensional model (3D). The 3D modeling allows quantifying the influence of parameters such as: the length of the dent, the depth of the dent and the size of the saddle; these parameters cannot be fully quantified in a 2D modeling.

It was assumed the material of both the indenter and saddle would have a linear elastic behavior, suffering no deformation during the analysis. The pipe specimen, in its turn, was simulated with elastic-plastic behavior, being used the multilinear isotropic hardening configuration. Figure 4.7 shows the true stress vs. strain curve of Figure 3.13 that was imputed in the software for the simulations.

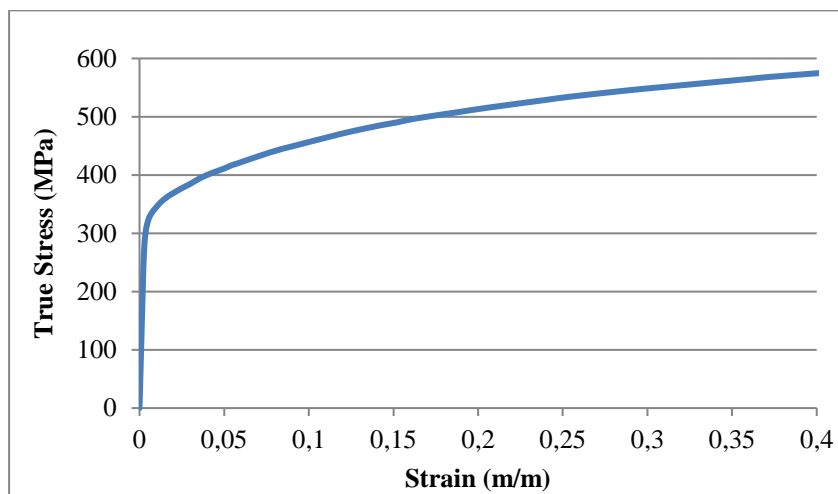


Figure 4.7: API 5L Gr. B true stress vs. strain curve utilized in the model obtain from the curve presented in Figure 3.13.

The models mesh consisted of 3923 elements, being constituted by the elements SOLID186, CONTA174 and TARGE170, and a total of 26885 nodes, Figure 4.8. the solid element SOLID186 with eight nodes and with prismatic and tetrahedral variant, which has better performance when used in regular meshes, was chosen for the pipe simulation [130]. The main feature of this solid element is its ability to withstand large deformations together with plasticity and large displacements.

The contact surfaces of the indenter and the saddle were modeled using the rigid contact element TARGE170. This element is used to represent "target" surfaces for the respective contact elements of the other body.

The contact area in the pipe was modeled using the element CONTA174. This type of element is located on the surface of solid elements (SOLID186) of the pipe, having the same geometric characteristics of the solid face to which it is connected. The contact will occur when the element located on the surface penetrates a "target" surface formed by TARGE170 type elements.

The type of contact between the pipe and the indenter and between the pipe and the saddle was defined as frictionless. This condition allows the surfaces in contact to slide over each other freely and the contact passes to open and close according to the loading, without taking into consideration a coefficient of friction.

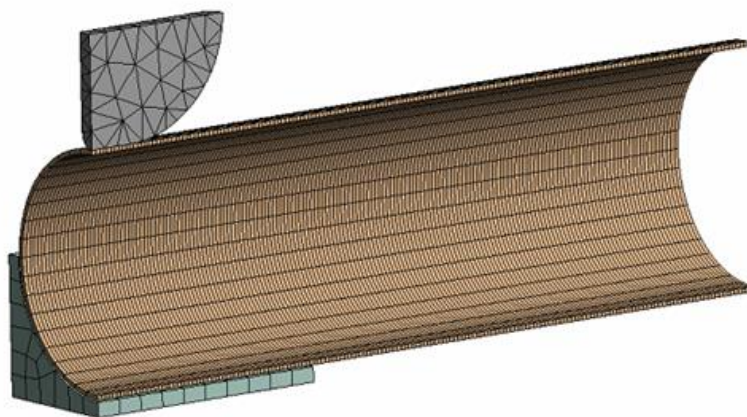


Figure 4.8: Mesh used in the first type of finite element models.

The algorithm used to formulate the contacts was the Augmented Lagrange, which is similar to the penalties method (standard software method), in which a problem with constraints is replaced by a series of problems with no constraints, [131]. The purpose of the increase is to reduce the sensitivity to contact stiffness, to ensure compatibility to the contact interface. The Augmented Lagrange method should produce a lower penetration between the contact surfaces than in the pure penalty method.

The numerical analysis of the process of creation of the dents has the purpose of modeling the behavior of the material and the pipe during the indentation, elastic recovery and rerounding. The behavior of the material and the pipe obeys the changes in the stiffness of the structure with the increments of the force.

The non-linearity of a structure can be due to several reasons that fall into four categories: geometric non-linearity; large deformations and large displacements; material non-linearity (plasticity); changes of status (contact).

The shape changes of the elements must be considered, so the “Large Deflection” condition of the software has been activated in order to allow the pipe to perceive large deformations and large changes of shape. Rigid body effects are also taken into account using the Weak Springs condition.

Due to the nonlinearities present in the models, the convergence of the solution is difficult, and it is not possible to perform the simulation in a single step. In this way the simulations were divided into 46 steps and each step was divided into a different number of sub-steps with multiple sub-step interactions until convergence was reached.

4.2.2 Second Type of Finite Element Model

The second type of model uses a more direct approach of the internal pressure cyclic loading analysis. The results obtained with the first type of model show that after reaching the final shape of the dents, when the samples are cyclically pressurized, they show a linear elastic behavior. The last steps show that there is a linear behavior between strain and the applied cyclic pressure. Therefore, a more simplified and less expensive analysis can be performed.

4.2.2.1 Model Geometry

Instead of using the geometry obtained from the end of the first type of numerical models, this simpler FE model used the exact dents geometries determined by the DIC analysis. The DIC dent shape data were converted into a CAD solid, and later on into a finite element mesh. For example, Figure 4.9 displays the comparison between the longitudinal profiles measured along a meridional line that passes through the center of the pipe specimen Dent 6 using a caliper and the DIC.

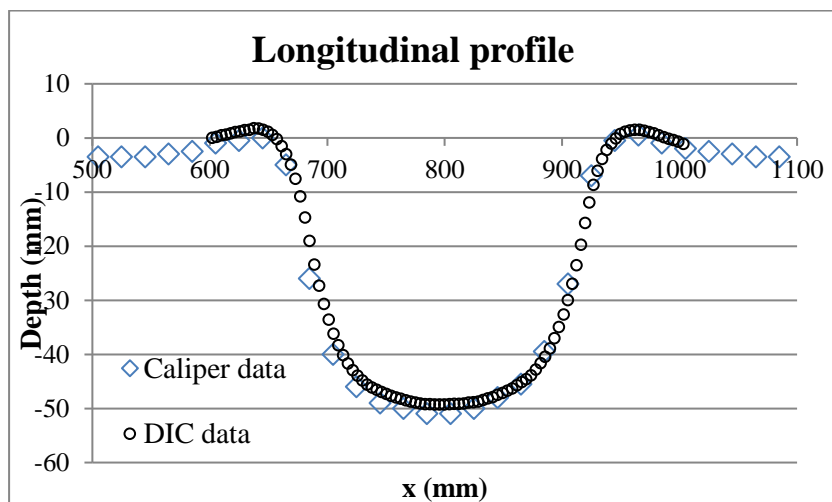


Figure 4.9: Dent 6 longitudinal profiles measured with a caliper and with DIC.

All models used $\frac{1}{2}$ of symmetry with restrictions to the displacements in the faces of symmetry ($u_x = 0$ in the free faces at yz plane and $u_z = 0$ in free faces at the xy plane).

Figure 4.10 shows the geometries of the second type of finite element model analysis of specimens Dent 6 and Dent 3 with the applied boundary conditions.

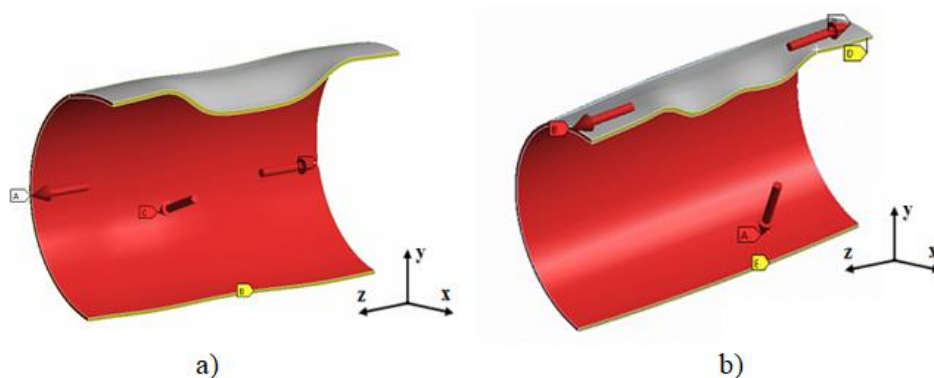


Figure 4.10: Geometry of the second type of finite element model with applied boundary conditions: a) Dent 6; b) Dent 3.

4.2.2.2 Model Parameters and Configuration

Different from the first type of model results, due to the absence of nonlinearities and the linear relation between strain and the applied load, the simulations of the dents models were much less time consuming when assuming a linear elastic behavior of the pipe material. The convergence of the solutions was not a problem and the analyses were performed in a single time step.

Appropriate boundary conditions were applied together with the rest of the quasi-cylindrical portion of the non-deformed pipe to build the models. As only the central portion of the specimens were simulated, pressure loads proportion to the acting internal pressure were applied at both ends to reproduce the head caps behavior.

Figure 4.11 shows the meshes of models Dent 6 and Dent 3 with respectively 88701 elements and 449184 nodes, and 79500 elements and 402893 nodes.

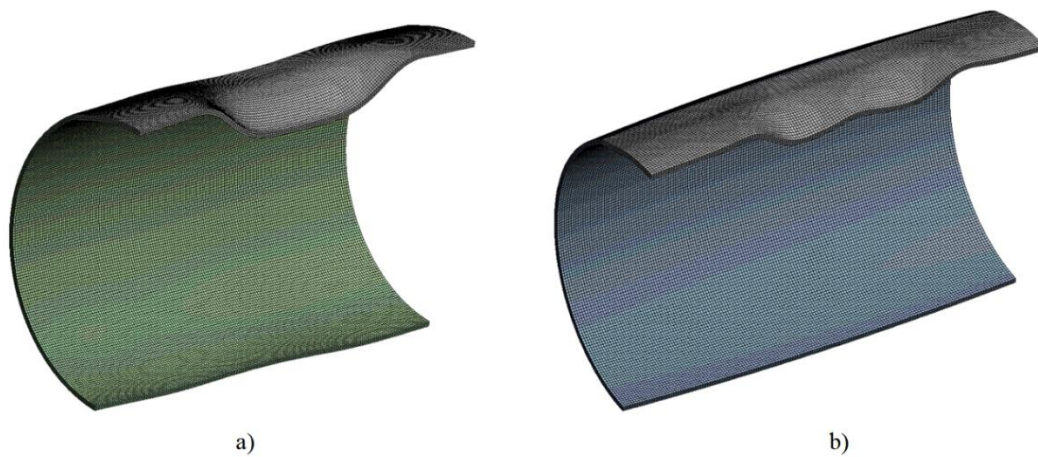


Figure 4.11: Meshes used in the second type of finite element models: a) Dent 6; b) Dent 3.

5. Results and Discussions

The dented specimens were tested as close as possible under the actual field operation conditions and selected cyclic internal pressure loading ranges were applied to each specimen in order to assess the fatigue behavior of each dent.

5.1 Experimental Campaign

The specimens were connected to a hydraulic system, with a cyclic test load machine (Figure 3.9c), and the experimental tests were carried out in a laboratory prepared for the tests in the facilities of CTDUT (Center of Technology in Pipelines). Assessment experimental and numerical techniques, such as DIC, IR thermography, TSA, FBSG and finite element, were employed to monitor and evaluate the fatigue behavior of the specimens, as it can be seen in the experimental arrangement of Figure 5.1, which shows the pipeline testing bunker of CTDUT.

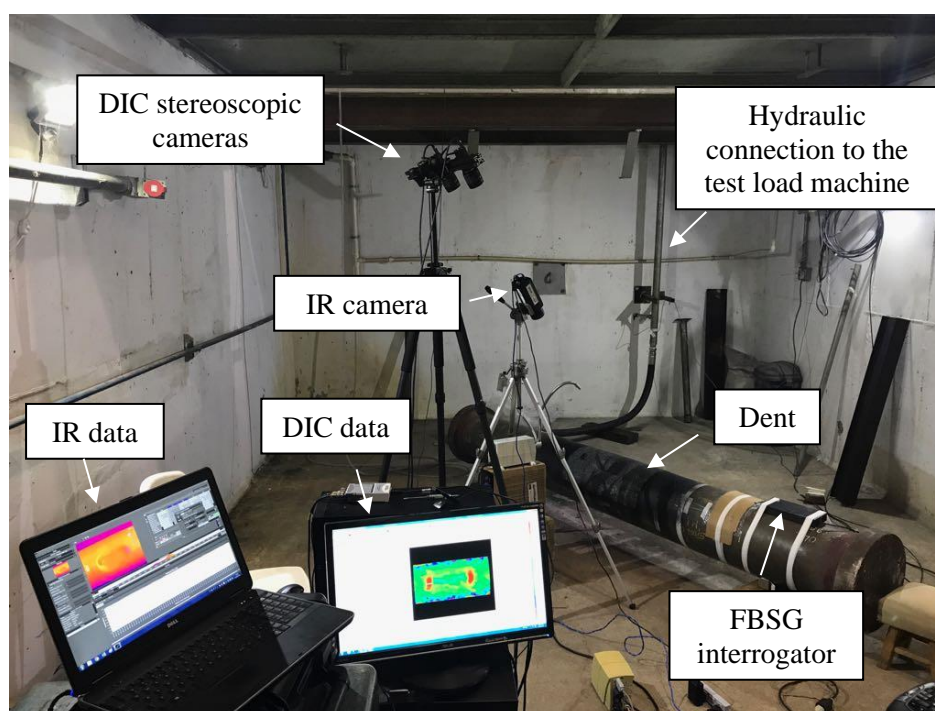
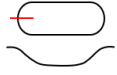
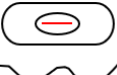
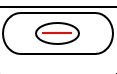
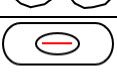



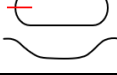
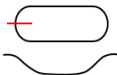


Figure 5.1: Experimental arrangement for testing the dented pipeline specimens.

During the performance of the tests, each specimen was subjected to a series of loads. Initially, preliminary two or three cycles of internal pressure, varying from 0.2 to 4.2 or 6.2 MPa were performed in order to obtain the mechanical behavior of the dented region. In these low frequency tests, the DIC, FBSGs and IR techniques were used. Since rerounding occurs at a higher pressure (6.5 and 7.0 MPa) than the one of the preliminary pressure cycles, the later had the function of stabilizing the material behavior, ensuring that it would work in the elastic regime. After these preliminary cycles each specimen was subjected to its own internal pressure cyclic load as presented in Table 8. This table also presents the number of cycles that each specimen survived until reaching fatigue failure (loss of containment of pressurized water) and the position where the first through wall crack occurred.

Table 8: Dented specimens pressure loads, cycles to failure and crack position.

Specimen	Order of testing	Pressure range (MPa)	Min-max pressure (MPa)	Number of cycles to failure ($\times 10^3$)	Crack position
Dent 1	2°	4.0	0.4-4.4	38.3	
Dent 2	3°	6.0	0.3-6.3	8.12	
Dent 3	1°	- ¹¹	-	22.2	
Dent 4	4°	4.0	0.2-4.2	2.1	
Dent 5	5°	3.0	0.2-3.2	220	
Dent 6	6°	6.0	0.2-6.2	6.5	
Dent 7	8°	4.0	2.2-6.2	34.4	
Dent 8	9°	3.0	3.3-6.3	53.3	
Dent 9	7°	4.0	0.2-4.2	38.9	

¹¹ Specimen Dent 3 loading history will be address in section 5.5.6

5.2 Finite Element Results

5.2.1 First Model

The first type of finite element models aimed to simulate entirely the process of creating the plain longitudinal dents, including in that the partial dent reroundment caused by the application of internal pressure and, moreover, the full field stress distributions that results from application of cyclic internal pressure. The first model is also capable of simulating the buckling or snap thru behavior of a dent when a central internal pressure is applied to the pipe with a dent. As examples, this section presents the case of specimens called Dent 3 and Dent 6, the snap thru phenomenon occurring for the first one.

Using this simulation process, it was possible to determine the indenter shape, the curve force *vs.* displacement to produce the initial dents, the effect of the rerounding pressure application and the strains caused by cyclic loading. Another very important result was the prediction of the mechanical behavior of the specimens, determining the critical positions, and the strains acting on these points.

5.2.1.1 Numerical Creation of the Dents

The actual test procedure for the creation of the dent began with the alignment of the tubular specimen on the support saddle with the indenter, so the simulations started from instant in the actual test.

When the dent is forced against the pipe wall (the pipe being without internal pressure), the reaction to the indentation is provided by the pipe wall. The seams welds were located diametrically opposite to the application of the force.

Figure 5.2 shows results numerical and actual results determined for the displacement of the indenter *vs.* the actual actuating force for the generation of the initial dents.

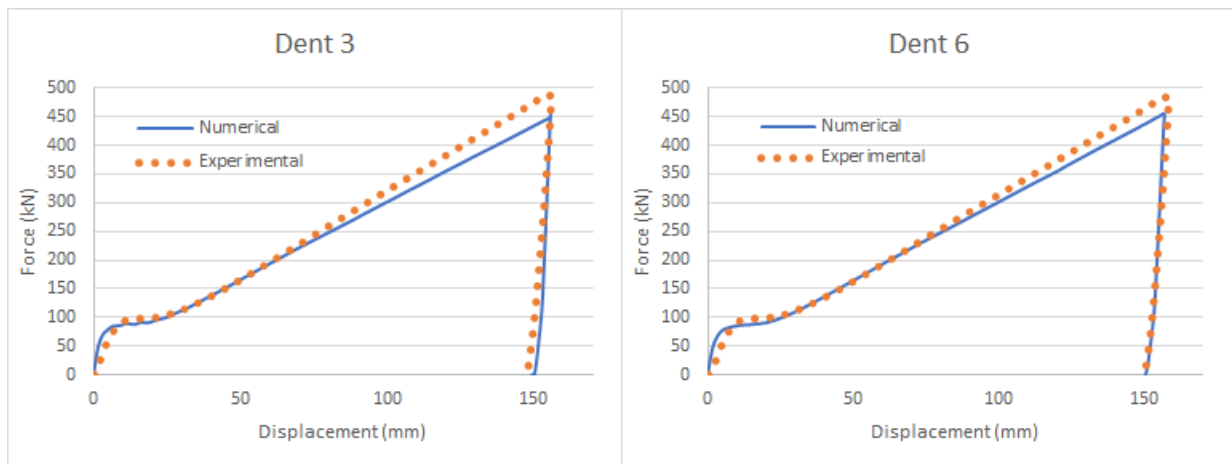


Figure 5.2: Numerical and experimental result curves of force vs. displacement during the indentation process.

After achieving the desired indentation displacement, the indenter was withdrawn and the elastic portion of the initial imposed deformation occurred. This phenomenon is known as springback. The actual tests specimens were then removed from the saddle. These steps comprehended the creation of the initial dent, which was designed to reach an initial depth of about 48% of the outer diameter of the pipe.

Thereafter, the longitudinal and transversal dent profiles were measured using a caliper. As the dent is the most important region of the specimens, the profiles were acquired along meridional lines that passed through the center of the dents in both circumferential and longitudinal directions. Figure 5.3 displays the comparison among the experimentally measured longitudinal and transversal profiles and the ones simulated by the of finite element models. At this point, the process of creating Dent 3 and Dent 6 presented very similar behavior.

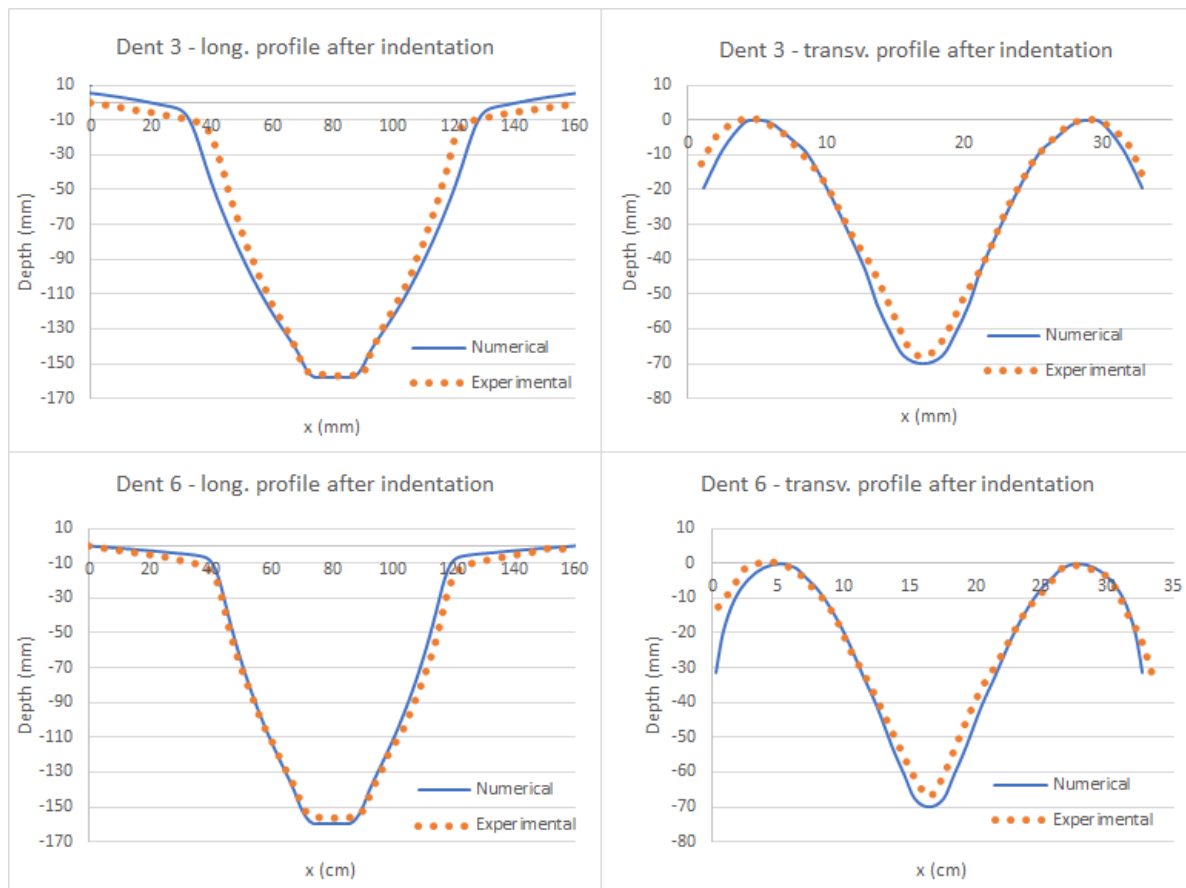


Figure 5.3: Numerical and experimental profiles of Dent 3 and Dent 6 after the creation of the initial dent.

It also can be noticed good agreement between the numerical and experimental results. It has to be considered that some small deviation occurred that can be credited to the behavior of the material inputted in the finite element software. It was used an average uniaxial stress-strain curve (Figure 4.7) that resulted from 54 tensile tests performed [123]. Some small errors are also associated with the measurements using the caliper, especially at the edges of specimens.

Figure 5.4 presents longitudinal and transversal views of the simulated models. At this point it can be said that both models presented very close shapes.

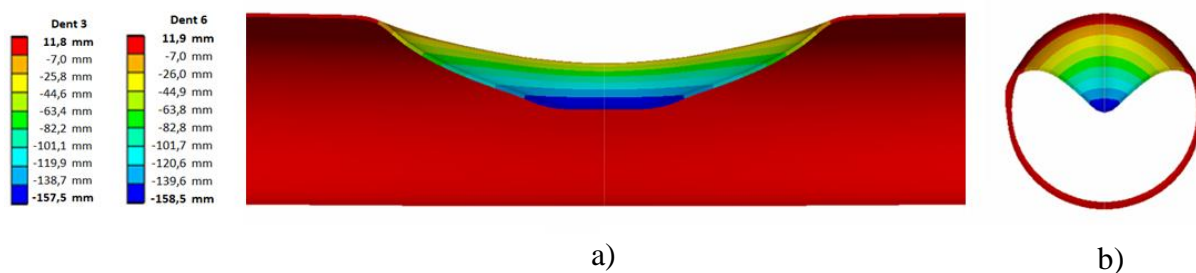


Figure 5.4: Dent 3 and Dent 6 models sectioned views: a) longitudinal;
b) transversal.

5.2.1.2

Numerical Rerounding of the Created Dents

In what concerns the actual experiments, concrete grafts to reduce the internal volume of the pipe were introduced in the specimens. After that, plane head caps were welded to the ends of the pipes. The specimens were filled with water and hydrostatic pressure was applied to perform the rerounding tests.

The rerounding test phase had the objective of making the dents to achieve a final desired dent format. Initially, the pressure that would form the 14% OD plain dent was numerically calculated to be, using the finite element model, equal to 7.0 MPa (the application of this internal pressure causes a circumferential stress equal to 73% SMYS of the API 5L Gr. B material) using the indenter shape presented in Figure 4.4. The dented specimens were rerounded in the order that they were numbered, starting with Dent 1 and finishing with Dent 9. Dent 1 was the first one to be rerounded with a pressure of 7.0 MPa. A plain dent format was obtained with maximum depth of 12% of the outer diameter. Performing the rerounding of specimens Dent 2, Dent 3 and Dent 4 with a pressure of 7.0 MPa caused snap thru buckling at pressures below equal to 6.6 MPa, 6.9 MPa and 6.9 MPa, respectively. Because of that, the maximum rerounding pressure was decreased to a safer level in order to maintain the desired geometry, without the occurrence of snap thru buckling.

The new rerounding pressure adopted was equals to 6.5 MPa. For this reason, the specimens Dent 3, that presented snap thru and was rerounded with 7.0 MPa, and Dent 6, without snap thru and rerounded at a maximum pressure of 6.5 MPa, were selected as exemplary specimens to be analyzed in this section.

5.2.1.3 Snap Thru

The snap thru buckling phenomenon pose some of the most difficult problems in nonlinear structural analysis [132]. It is essentially a geometric nonlinear problem of instability of the structure resisting the acting load.

Stability of systems including structures and piping systems is one of the major requirements for maintaining the functionality. In simple terms, stability of a system implies that the system can maintain an existing state without major deviations from that state. The lack of stability (i.e., the instability) may result in a change of the functionality of the system, which are not necessarily desired. The structural systems including pipelines may undergo certain deformations and change of stiffness that would reduce their strength and serviceability. [133].

Elastic structures could lose their stability a number of ways. Modes of instability depend on the properties of the system itself, its environment, applied forces and boundary conditions. Systems in static equilibrium may become statically and dynamically unstable. For structural systems, three types of instability may be identified, being the limit equilibrium instability or snap-through buckling the one of interest in this work.

Similar to what occurs in slender rods and thin plates, thin walled shell structures such as the dented pipeline specimens are prone to snap thru buckling, being extremely sensitive to imperfections, which can be caused or be present in geometry, loading conditions and material behavior.

The loss of stability through the so-called limitation of equilibrium and occurrence of snap thru is characteristic of structures which carry the transverse loading by compressive axial forces. These cases present bifurcation points. The load-deformation curve is continuous and consists of a single curve with no branches. The curve has some stationary maximum and minimum points; the critical load corresponds to one of these maximal points.

In the snap through buckling the system passes from an equilibrium state to a non-adjacent equilibrium configuration. Figure 5.5 schematically shows the snap through type of instability of an elastic system. The branch OA of the load-deformation curve describes the predominantly linear behavior of the arch.

At the stationary point A, corresponding to a maximum applied force, the system "jumps" from a deformed state, marked by point A, to another deformation state much further away from its neighboring deformed configurations, point B. The final buckled format is a reverse shape of the original shell and some of the energy released is dissipated as noise to the environment [134].

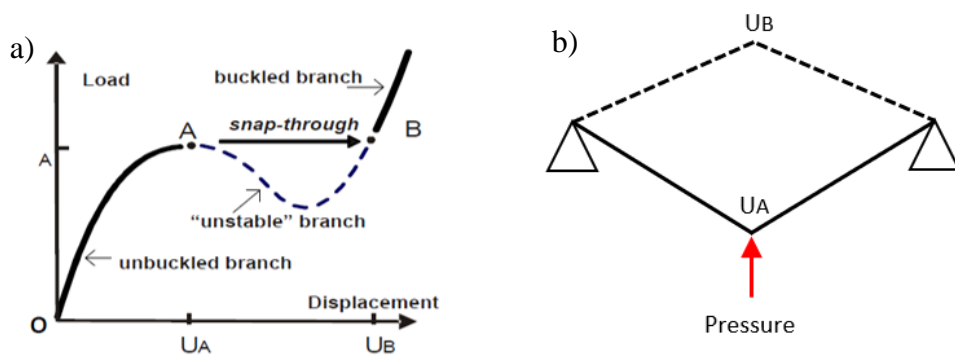


Figure 5.5: Snap thru: a) load-displacement buckling curve of spherical shell structures; b) schematic representation of a thin shell.

Regarding the dented specimens that experienced the snap thru phenomenon in the present tests, all of them were rerounded to a maximum pressure of 7.0 MPa. Snap thru and its humped geometry occurred below 7.0 MPa, at slightly lower different pressure levels (Dent 2 (6.6MPa); Dent 2 (6.9MPa); Dent 4 (6.9MPa)). The snap thru was present at the numerical simulations, but at different values. For Dent 3, the snap thru occurred at a much higher pressure, 8.73 MPa. Several factors contributed to the lower values of the pressures that caused the snap thru in the actual specimens as compared to numerically calculated values.

In general, thin shells prone to buckling are sensitive to imperfections. Imperfections can reduce the buckling load of a thin shell drastically compared to that of the perfect shell. Geometrical imperfections and loading imperfections, which influence the buckling load, are defined as deviations from perfect shape and perfect loading distributions, respectively. The ratio of nonlinear buckling loads of

imperfect and perfect structures, the so-called knock-down factor, defines the sensitivity to imperfections [135].

Imperfections can be added to the numerical model, a “perfect” material is used to construct the pipe specimen, which is free from metallurgical imperfections and microscopic flaws. The load is also considered to be applied in a constant rate, independent of any pressure drop in the hydraulic system. The condition of geometry symmetry was also employed, stating that the dent shape can be assumed proportional.

In reality, any of these conditions represent the actual rerounding operation and the real specimens, although the trying to be as close as possible to the real setup. The material curve used in the simulations (Figure 4.7) represents the average curve obtained from the 54 tensile tests that were conducted in the beginning of this investigation. Therefore, some dispersion of the measured properties and consequently some variation between real and estimated mechanical behavior can be expected. Some difference can already be seen at the comparison of the numerical and experimental profiles of the initial dents shown at Figure 5.3.

Besides that, material at the critical buckling area or central portion of the tested or simulated dent undergoes enormous deformations, something around 130000 $\mu\epsilon$, during the indentation step, which will be shown later. Associated with this, the material has a ratcheting behavior, which is not considered in the numerical plasticity model used (multilinear isotropic hardening), what ends up contributing to a divergence between the actual behavior and the simulated one. For better results a more robust plasticity model can be applied.

Another source of imperfection is the way loading/pressurizing operation is performed during the reround. When using a pneumatic driven hydraulic pump, the pressure does not increase linearly and smoothly, as shown by Figure 3.6c. Instead, it rises in steps that are proportional to the compressed air strokes that are fed into the pump mechanism. These pressure strikes contribute to increased sensitivity turning the dent more susceptible to snap thru buckling.

At last, the dented models were considered with a perfect geometry. Furthermore, $\frac{1}{4}$ of symmetry was also utilized, implying that all the opposite parts of the dents were geometric similar, which was not necessarily true.

All those factors contributed to reducing the pressure at which snap thru buckling occurred, showing that the real rerounding process was extremely sensitive to geometric, loading and material imperfections.

5.2.1.4 Final Dent Shape Before the Cyclic Loading

Figure 5.6 exhibits the comparison among the experimentally measured longitudinal and transversal profiles and the ones simulated by the finite element models of specimens Dent 3 and Dent 6 after rerounding.

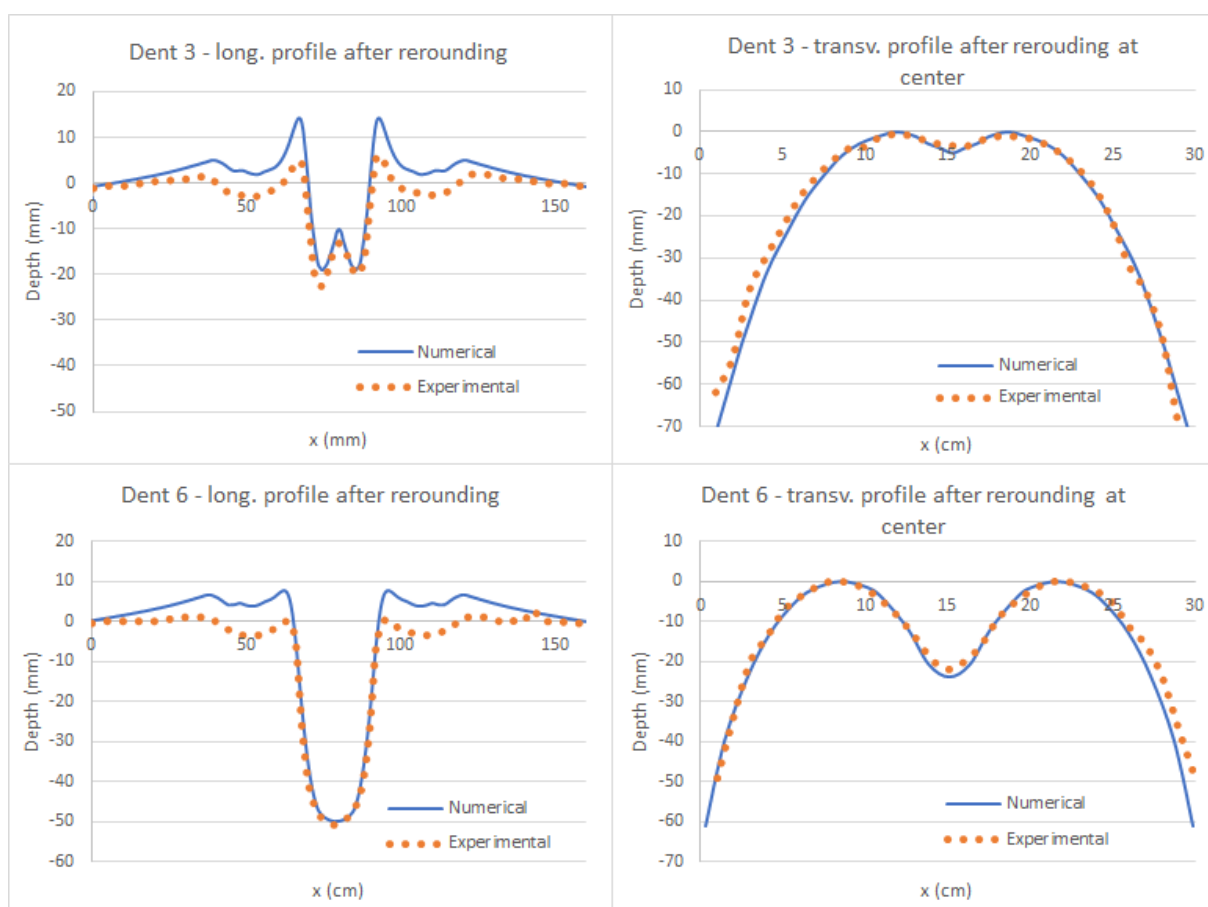


Figure 5.6: Numerical and experimental profiles of Dent 3 and Dent 6 after the rerounding operation.

Through the analysis of the profiles presented above, the depth at the center in the numerical and experimental approaches are very similar in both models. Some discrepancy between the measured shape of the dents and the simulated ones can be observed, especially in the border regions of the dents.

Figure 5.7 presents the sectioned longitudinal and transversal views of the numerical models after rerounding. It can be seen that some portions near the final dents are found at a positive height, taking into consideration the zero reference that was considered in the initial measurements.

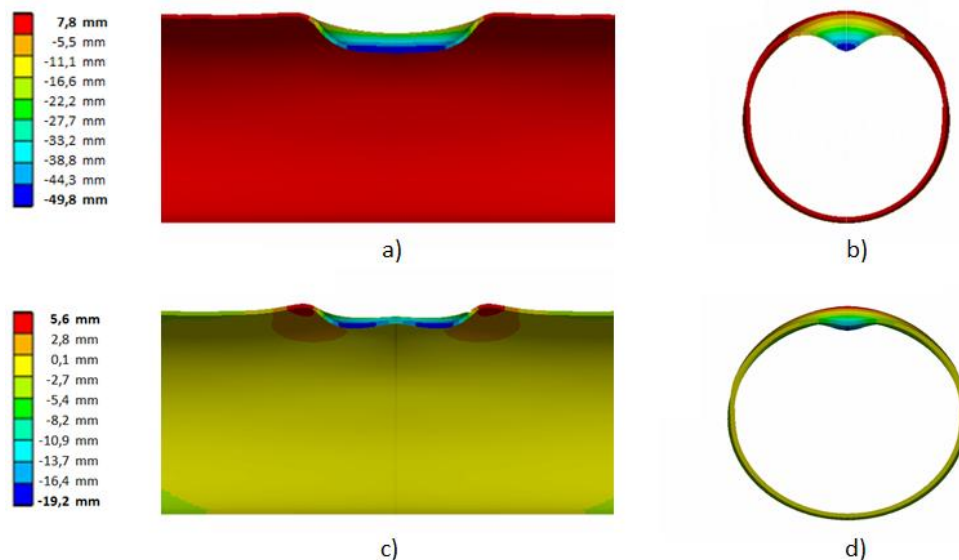


Figure 5.7: Sectioned views: a) Dent 6 longitudinal; b) Dent 6 transversal; c) Dent 3 longitudinal; b) Dent 3 transversal.

5.2.1.5 Numerical Cyclic Behavior of the Dented Specimens

The differences between the real specimen shapes and the simulated specimen model also entail a change in the mechanical behavior of the specimens, even if small. During the cyclic pressurization, at the dented area, the specimens pulsate like a lung and try to recover the pipe original shape by reducing the dent depth.

The critical regions are those that when the dent is most loaded. They will be the first to experience a shape change (high deformation) causing the specimen to return to a condition as similar as possible to its initial geometry. In Dent 3 the center, already buckled, is the portion that carry larges stresses, while in Dent 6 the portions in its edge are the most stressed.

After the rerounding process, the actual and the numerical models were tested cyclically with internal pressure varying from 0.2 to 6.2 MPa and 0 to 6.0 MPa,

respectively, for at least two cycles (specimen Dent 6) and three (specimen Dent 3). The actual cyclic maximum pressure applied was 6.2 MPa, to avoid any possible snap thru during the continuous fatigue loading process.

Analyzing the circumferential strain variation during the last pressurization cycle of both numerical models the most loaded critical positions were determined as presented in Figure 5.8 and Figure 5.9.

As it will be presented in Figures 5.11 and Figure 5.12, two or three cycles of internal pressure ranging from 0 to 6.0 MPa were enough for the strains in the hot spot of the dents to reach a repeatable linear behavior with varying pressure. Figures 5.8 and 5.9 present the circumferential strain ranges ($\Delta\epsilon_c$) in all model nodes along the last cycle of pressurization and the location of the critical node in the pipe specimen.

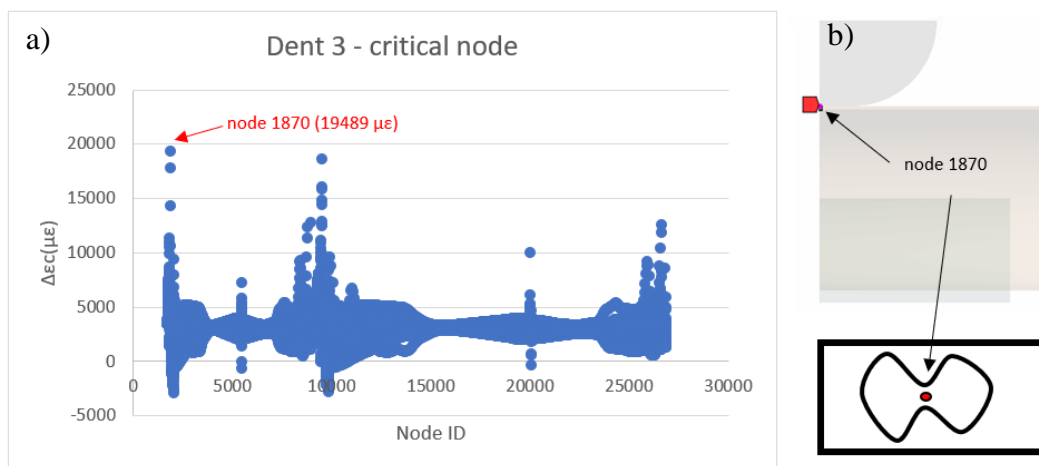


Figure 5.8: Dent 3: a) Circumferential strain variation in all nodes over the last pressure cycle; b) Critical node location.

As previously mentioned, the Dent 3 critical spot is located on the surface at the center of the dent, what is corroborated by the crack position shown by Table 8. The most loaded node number 1870 experienced a circumferential strain range of about 19489 $\mu\epsilon$.

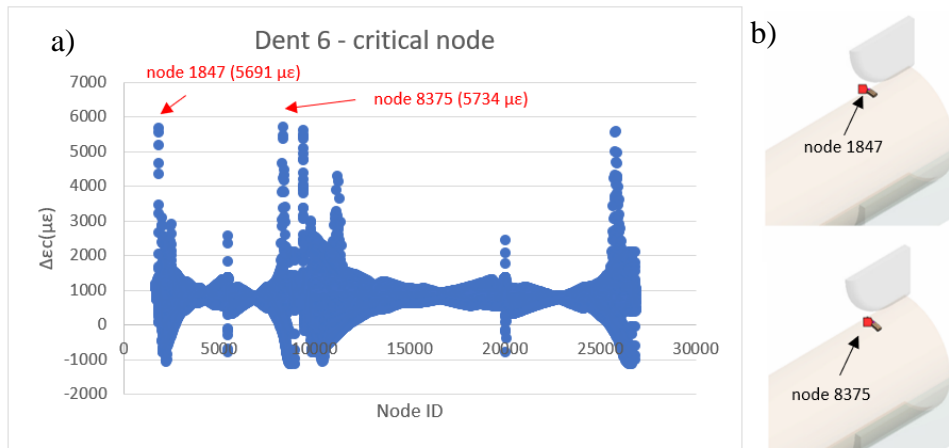


Figure 5.9: Dent 6: a) circumferential strain variation in all nodes over the last pressure cycle; b) Critical node locations.

The numerical model of Dent 6 shows that the critical position in the model is located on the surface at the edge of the dent. Nodes number 1847 ($\Delta\epsilon_c = 5691 \mu\epsilon$) and 8375 ($\Delta\epsilon_c = 5734 \mu\epsilon$) are the two most loaded ones, the only difference is that node 8375 located slightly away from the center while node 1847 is in the center. Although node 8375 exhibits a bit higher deformation level, in the actual test specimen there is a competition between positions for the failure. Based on this fact and on the crack position shown in Table 8, node 1847 was assumed to be the most critical one.

The numerical stress- strain curves for the critical nodes of the models are presented in Figure 5.10, it can be seen that an elastic cyclic range appears at these points.

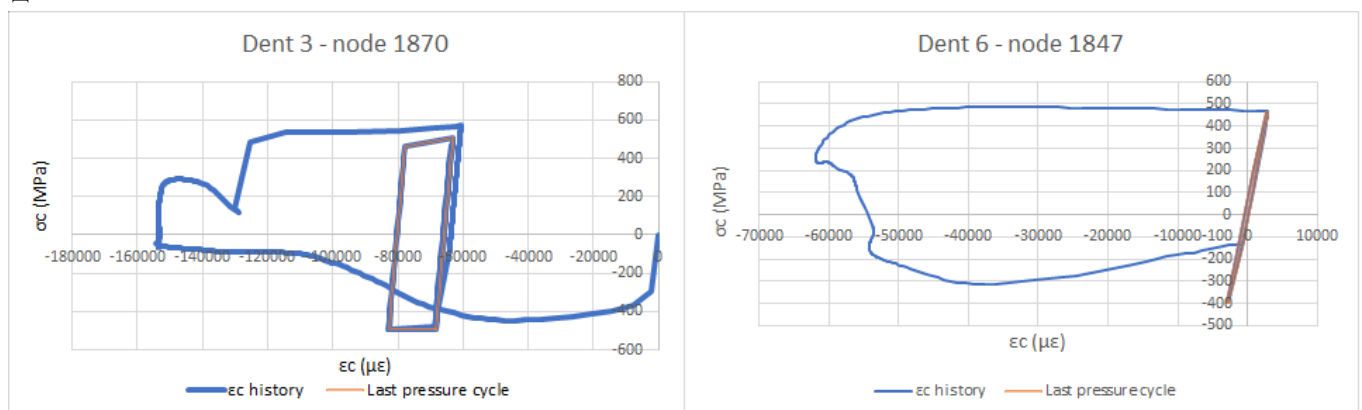


Figure 5.10: Stress- strain curves for the critical nodes of the models.

From these results, circumferential stress concentration factors ($K_{\sigma c}$) and circumferential strain concentration factors ($K_{\epsilon c}$) can be calculated with relation to the nominal circumferential stress and strain acting in the critical points of the specimens using Eq. (70) and Eq. (71):

$$K_{t_{\sigma c}} = \frac{\Delta \sigma c \max}{\Delta \sigma c \text{ nom}} \quad (70)$$

$$K_{t_{\epsilon c}} = \frac{\Delta \epsilon c \max}{\Delta \epsilon c \text{ nom}} \quad (71)$$

A value of elastic stress concentration factor (circumferential strain) for these points can be evaluated following Eq. (72) given by Neuber's rule [127].

$$K_{t_{elastic}}^2 = K_{t_{\sigma c}} \cdot K_{t_{\epsilon c}} \quad (72)$$

Table 9 present the summary of the results of the stress and strain concentration at the critical nodes of the FE models (Dent 3 – node 1870 and Dent 6 – node 1847) generated by the presence of the dents, using Eqs. (70) to (71) during the last cycle of the first block of pressurization.

Table 9: Stress and strain concentration factors at the critical nodes of the FE models.

Specimen/ Critical node	$\Delta \sigma c \text{ nom}$ (MPa)	$\Delta \epsilon c \text{ nom}$ ($\mu\epsilon$)	$\Delta \sigma c \max$ (MPa)	$\Delta \epsilon c \max$ ($\mu\epsilon$)	$K_{t_{\sigma c}}$	$K_{t_{\epsilon c}}$	$K_{t_{elastic}}$
Dent 3/1870	153	840	957	19489	6.25	23.20	12.04
Dent 6/1847	153	840	857	5691	5.60	6.77	6.15

5.2.1.6 History of Deformation at the Critical Points

By analyzing the history of deformation of the critical nodes in both Dent 3 and Dent 6 models it is possible to obtain a glance about the pressure-strain behavior during each of the stages to which they are submitted.

Figures 5.11 and 5.12 show de circumferential strain variation over the time for the most critical nodes. For Dent 3, the hot spot assessed was the node 1870, located on the pipe specimen surface at the center. For Dent 6, the hot spot assessed was the node 1847, located on the pipe specimen surface at the edge of the dent region. Whereas they undergo to practically the same stages, differing only in

indentation depth and rerounding pressure, the strain levels are a direct response to the node location and to the dent final format after rerounding.

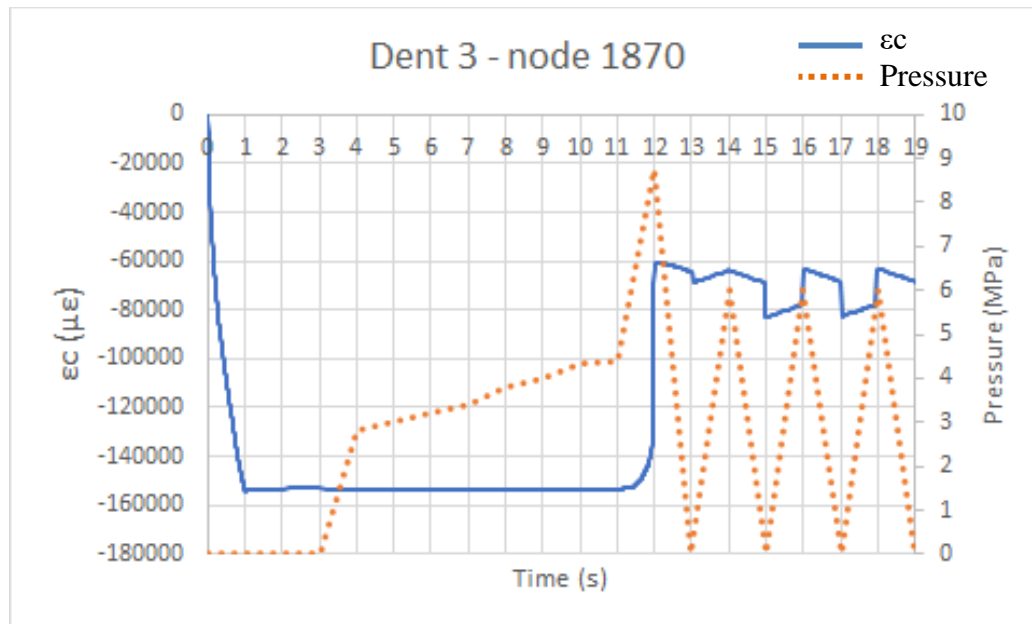


Figure 5.11: Dent 3 node 1870 circumferential strain history.

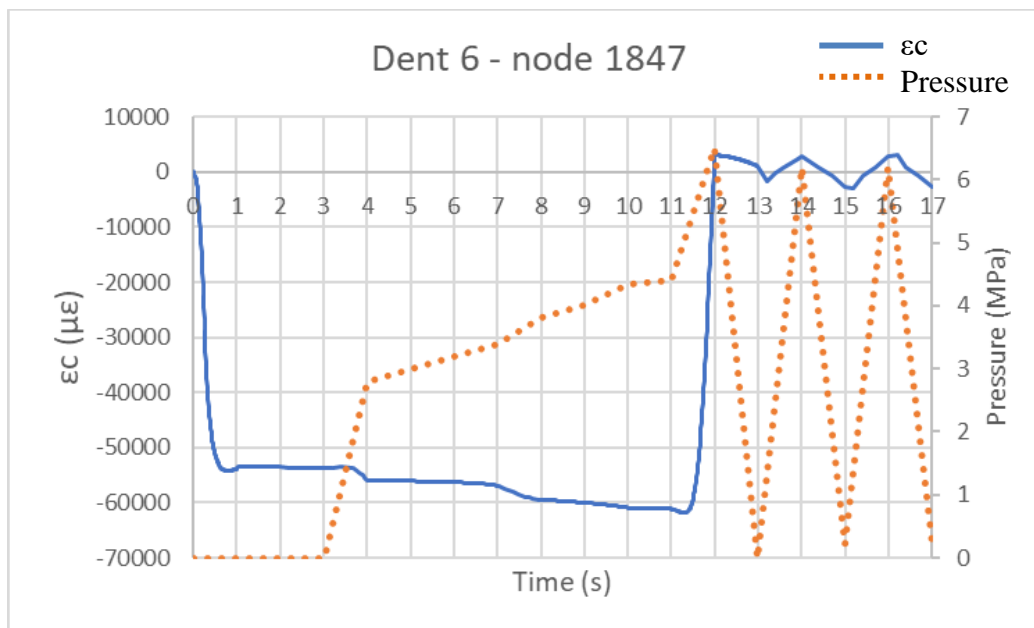


Figure 5.12: Dent 6 node 1847 circumferential strain history.

Analyzing Figures 5.11 and Figure 5.12, the indentation process is represented by the first time-step defined from 0 to 1s. Punch unloading occurs along time-steps defined from 1 to 4s. The rerounding of the initial dent occurs due to the application of internal pressure to a maximum of 8.73 MPa (Dent 3) and 6.5 MPa (Dent 6) (time-steps defined from 4 to 12s). Depressurization occurs at time-steps defined from 12 to 13s. Dent shapes similar to those presented in Figure 5.7 result after decreasing the internal pressure to zero are obtained (time 13s). Finally, three (Dent 3) and two (Dent 6) cycles of internal pressure ranging from 0 to 6.0 MPa (time steps defined from 13 to 19s (Dent 3) and 13 to 17s (Dent 6) were applied.

Figures 5.13 and 5.14 present the circumferential strain history over the cycles of internal pressure for the most critical nodes of specimen Dent 3 and Dent 6, respectively.

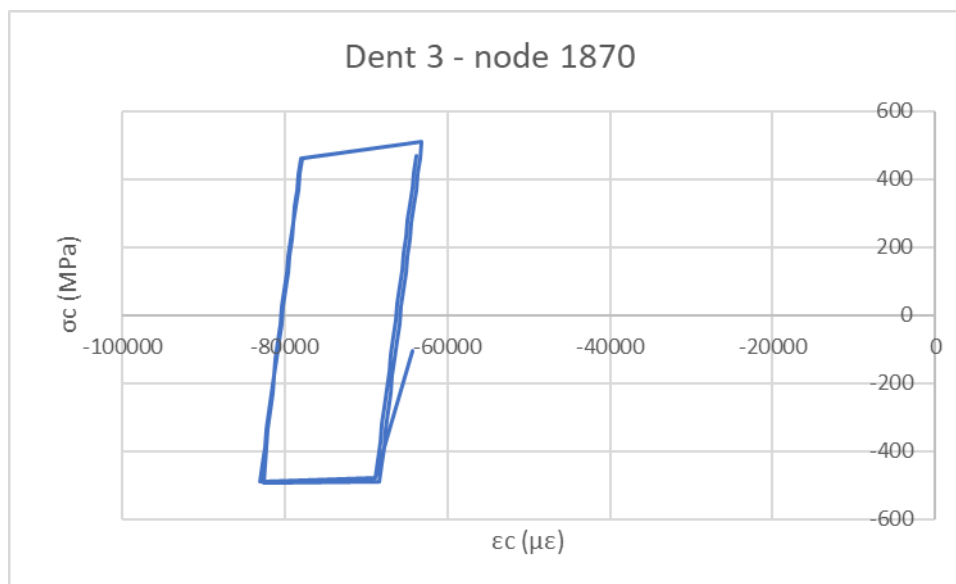


Figure 5.13: Dent 3 circumferential strain history over the cycles of internal pressure for the most critical node.

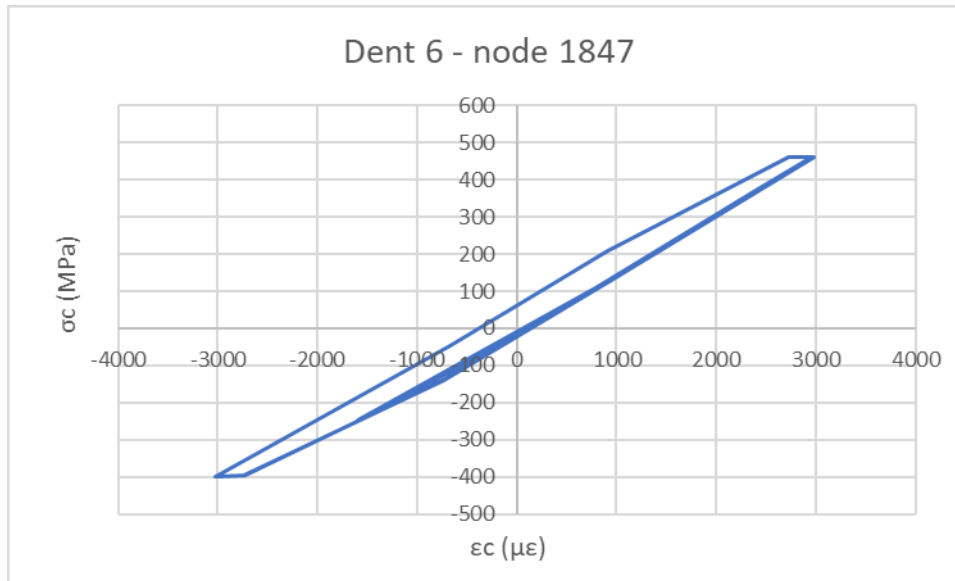


Figure 5.14: Dent 6 circumferential strain history over the cycles of internal pressure for the most critical node.

A similar case of plasticity problem was studied in Appendix D, a plate containing a hole and with the same material studied here, the steel API-5L Gr. B.

5.2.2 Second Finite Element Model

The analysis of the time steps defined from 13 to 19s (Dent 3) and 13 to 17s (Dent 6) shows that the variation of the circumferential strain after of the execution of first cycle (0 to 6.0 MPa) corresponds to a linear elastic behavior.

Therefore, the second FE model was developed using the elastic part of the stress-strain curve of Figure 3.13.

The second finite element analysis combined the “exact” dent shape measured by the DIC technique, as commented in 4.2.2.1, with the quasi-cylindrical portion of the non-deformed pipe to build the new models.

5.3 Actual Test Results

A detailed analysis of each actual dented specimen behavior was performed in this section.

5.3.1 Cyclic Pressure Application

Cyclic pressure was applied in two cyclic blocks using as water pressure inductor the hydraulic system connected to the servo-hydraulic testing machine (Figure 3.9c).

The first block consisted of two or three preliminary cycles that were performed to investigate the dented region behavior with pressure varying from 0.2 to a maximum of 4.2 or 6.2 MPa depending on the specimen. The actual test pressure frequency in this block was low, about 0.05 Hz so that DIC data recording could be accomplished (about 100 data point per cycle). The low loading rate was also required in order to enable the IR thermographic camera to record the required amount of data for the quasi-static analysis in an ideal time rate, this one performed during the pressure increase part of the first loading cycle.

The second block of cycles was carried out subjecting each dented specimen to the pressure range presented at Table 8. Test frequency was 1.0 Hz and the second block endured up to the appearance of the first through wall crack and consequent loss of containment. Starting from the second test (Dent1) to the final test (Dent 8), all tests suffered constant cyclic pressure ranges as presented in Table 8, excepted for Dent 3, the first specimen to be tested, for which the second block of pressure loading had multiple loading ranges, as presented Figure 5.15a and Table 15.

Figure 5.15 shows the pressure applied over the time during the tests of Dent 3 and Dent 6. Dent 3 presented several cycles at different pressure ranges loading rates, Figure 5.15a. Dent 6 test and the others dent specimens (except Dent 3) presented constant pressure ranges as shown in Figure 5.15b.

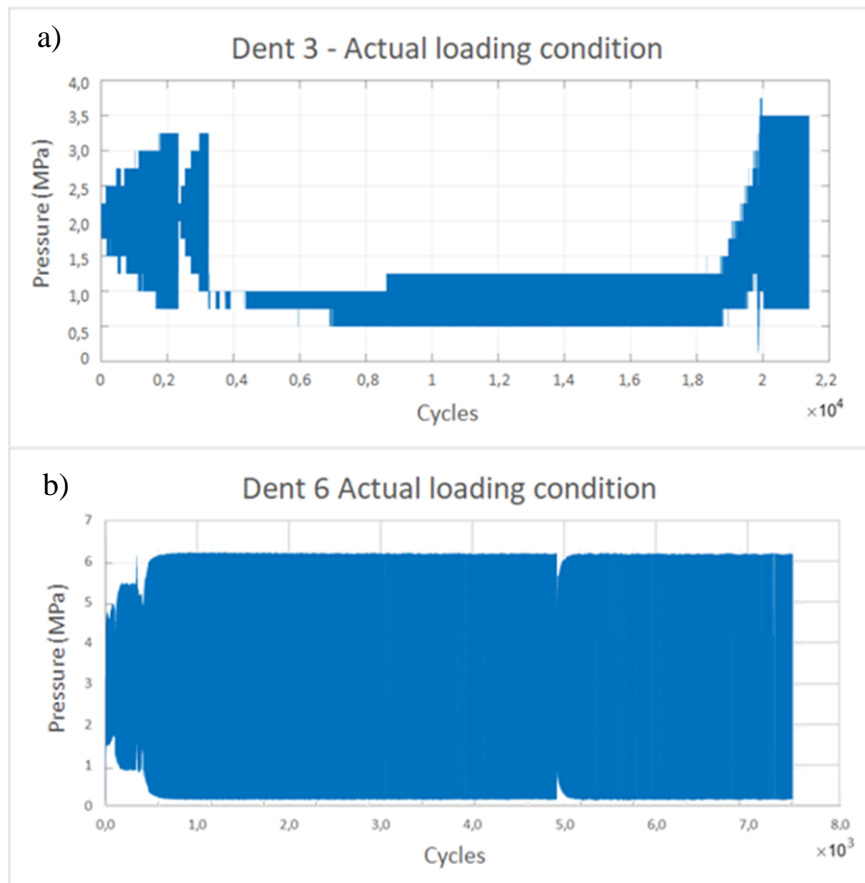


Figure 5.15: Pressure load along the specimen life test:

a) Dent 3; b) Dent 6.

5.3.2 DIC and Finite Element Test Results

The full field dent shape determined using the 3D-DIC technique and inputted as the exact dent geometry at the second type of finite element model (sections 4.2.2.1 and 5.2.2) are presented in Figure 5.16 for dented specimens Dent 3 and Dent 6. The measured shapes accurately reproduce the actual shape of the samples, which is corroborated by measurements using a caliper and presented in Figure 5.17.

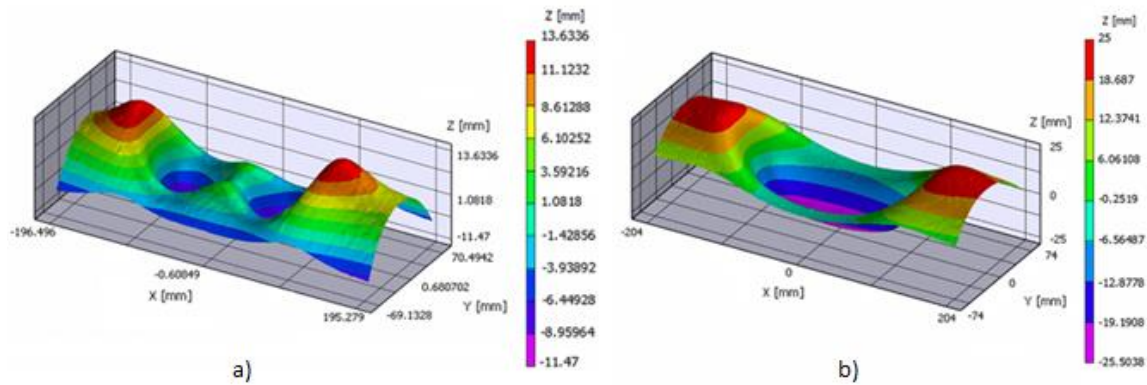


Figure 5.16: Dent geometry after rerounding determined from 3D-DIC measurements: a) Dent 3; b) Dent 6.

Figure 5.17 compares the measurements made along a meridional longitudinal line, that goes through the middle of the specimens, using the DIC, the caliper and the results from the first type of finite element, where the profile of the dent was entirely simulated from the beginning (dent creation) to the application of the cyclic load (section 5.2.1.6). It can be noticed that DIC can accurately scan the shape of the dent. The complete numerical model approaches the exact dent shape with reasonable accuracy, the difference been accounted by the same reasons explained in section 5.2.1.3.

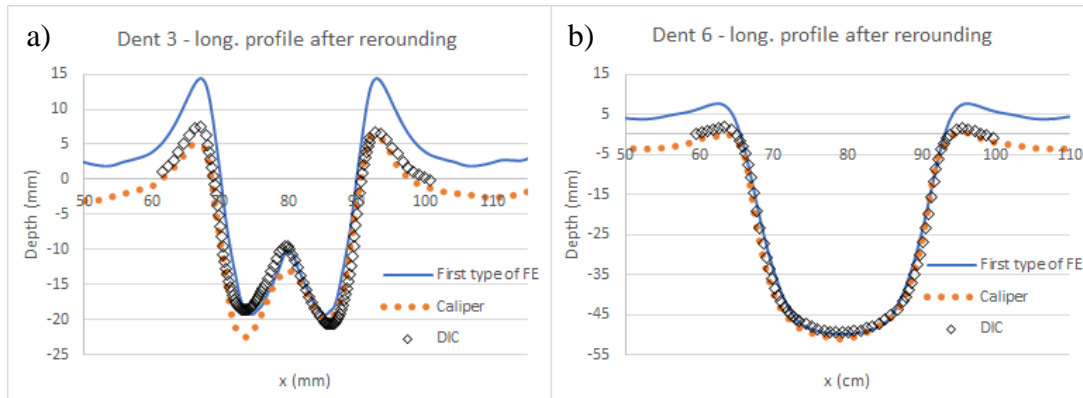


Figure 5.17: Comparison between the longitudinal profiles measured with the DIC, the caliper and simulated with the first type of finite element model: a) Dent 3; b) Dent 6.

At the actual first block of pressurization two or three cycles of internal pressure (0.2 to 4.2 or 6.2 MPa) were applied at a low frequency (0.1 Hz) for DIC and IR data recording. These first block had two distinct purposes: to provide essential information about the dent behavior (to allow experimental and numerical

displacements and strains results to be compared) and to induce certain level of plastic deformation, that stabilized their behavior in a linear elastic regime or in a fixed and representative hysteresis stress-strain loop.

The initial indentation process and rerounding lead plastic deformation as it is shown by time-steps 4 to 12s in the Figures 5.11 and 5.12. After that, any loading below the rerounding pressure would expect to cause an elastic response. However, this will not be true if the stress concentration is high, causing elastic-plastic stress-strain loops. Analyzing Figures 5.11 and 5.12, time-steps 12 to 17s that encompass the rerounding depressurization, the first and the second preliminary pressure cycles, only after the performance of the first cycle the circumferential strain starts to behave linearly with pressure, but that may not be true when the local point stress-strain is analyzed.

As expected from the results of the first type of model, each specimen when it is pressurized, the dent region pulsates with a tendency to return the pipe to the undeformed initial condition. At the buckled dents the center is the most critical spot and in the others dents, the regions near the edge are the most stressed positions.

Besides dent shapes, among the variety of data that the DIC technique can provide, the circumferential strain may be one of the most relevant, being representative of the general behavior of the specimens under pressure loading. Figure 5.18 provides a valuable insight about the loaded dent behavior, showing the distribution of circumferential strains along a buckled dent specimen (Dent 3) and along a longitudinal plain dent specimen (Dent 6). Figure 5.18 presented the 3D and 2D projection results over the dented area measured at the maximum pressure condition (6.2 MPa). These results correspond to the last preliminary cycle of the first pressure block, with emphasis on stress or strain concentration positions.

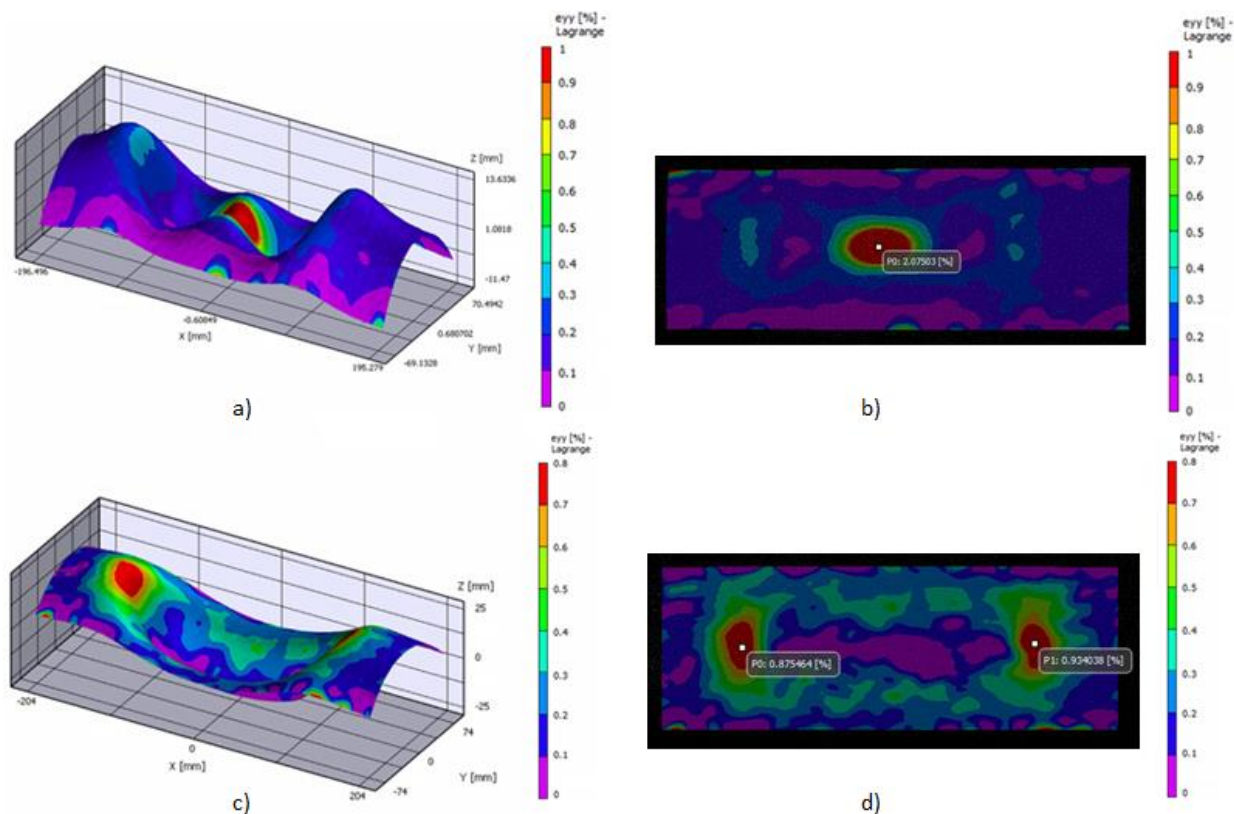


Figure 5.18: Circumferential strain measured by DIC: a) 3D view of Dent 3; b) Superior 2D view of Dent 3; c) 3D view of Dent 6; d) Superior 2D view of Dent 6.

The regions of strain concentration can be seen clearly at the hot spot points of Figure 5.18, located at the hump region at Dent 3 and at the edges of the dent at Dent 6. These positions of highest strains (hot spots) are the potential places for the development of a fatigue crack. Since the maximum strain at Dent 3 is much higher than the one at Dent 6 for the same pressure range, it can be said that the buckled geometry is much more critical from the point of view of fatigue failure.

Figure 5.19, below, exhibits the depth profiles of Dent 3 and Dent 6, being highlighted the hot spot positions in both specimens identified in Figure 5.18.

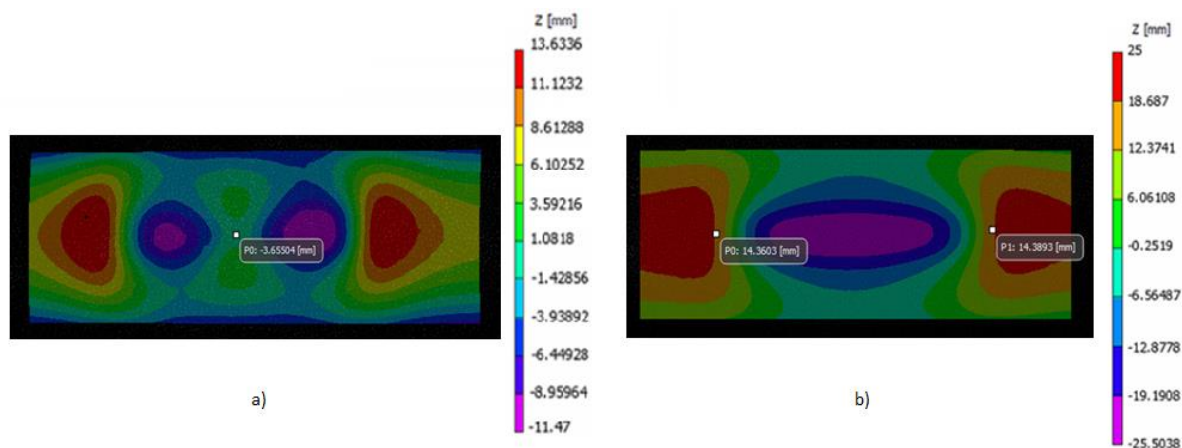


Figure 5.19: 2D view of the depth of the specimens: a) Dent 3; b) Dent 6.

Although all the specimens are made of the same material, API-5L Gr. B steel, and have similar shapes (but no identical), when loaded to the same level of pressure they display distinct behaviors. This is due to three factors; to the slight variations in shape between the specimens that induce high differences in the strain values at the specimen's hot spots, to the dispersion of mechanical properties in each specimen and to the ratcheting¹² behavior of the material, the first one cited being the most important in the present case.

Figure 5.20 shows the history of circumferential and longitudinal strains along the first block of pressurization at the most strained point. It can be seen that, after each pressurization cycle ratcheting accumulated progressively plastic deformation¹³, not predicted by the developed numerical models.

¹² Ratcheting is a behavior in which plastic deformation accumulates due to cyclic stress [62]. It is a progressive, incremental inelastic deformation characterized by a shift of the stress-strain hysteresis loop along the strain axis.

¹³ Although out of scope of this investigation, this phenomenon happened more accentually for specimens Dent 6, Dent 7, Dent 8 and Dent 9.

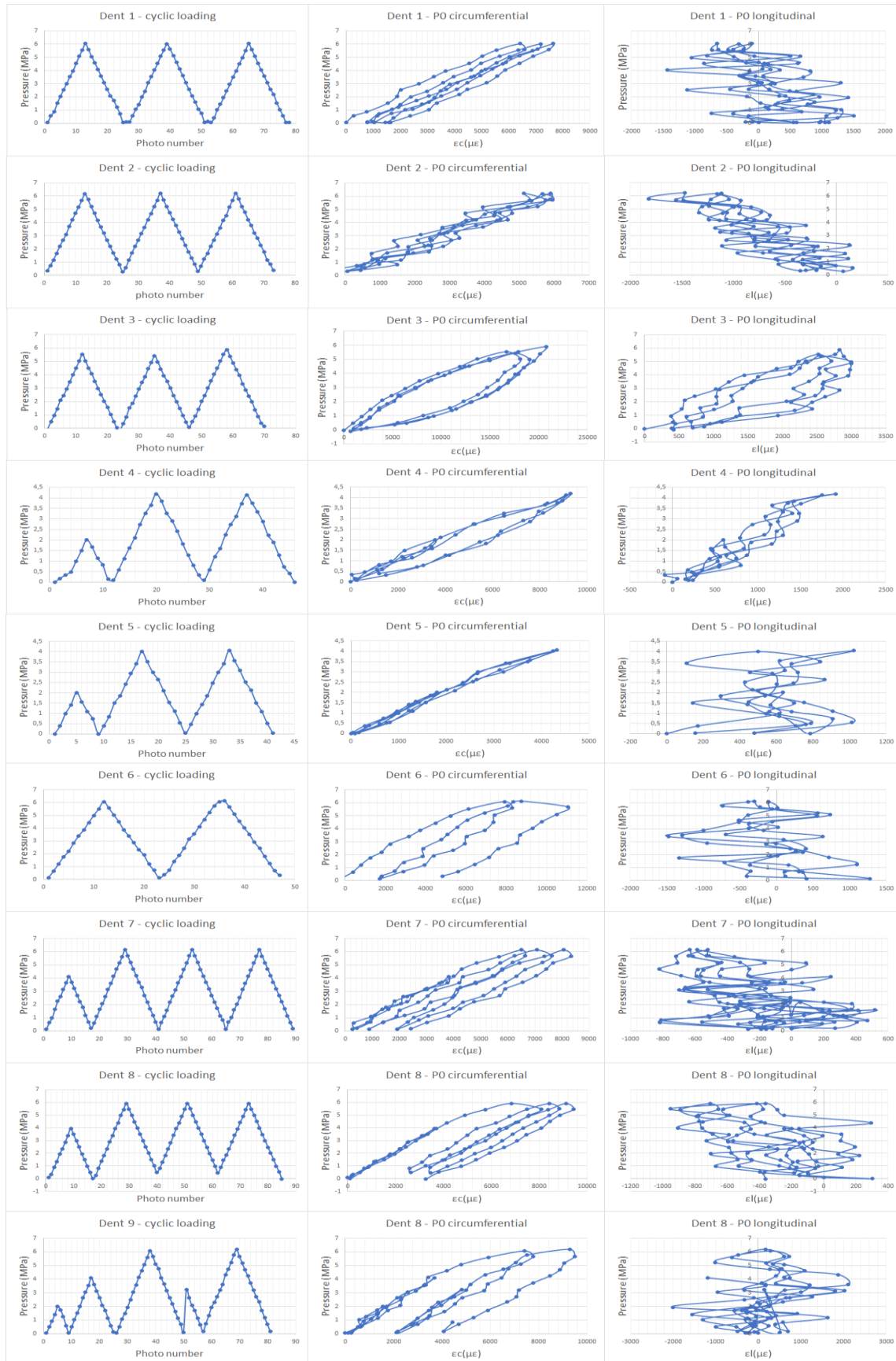


Figure 5.20: History of circumferential and longitudinal strains along the first stage of pressurization at the most stressed point of the dent.

During the pressurization cycles the specimens undergo to large deformation at the hot spots, especially in the circumferential direction. Therefore, considering $\Delta\epsilon_c \gg \Delta\epsilon_l$, the strain range $\Delta\epsilon_c$ was assumed to be representative of the specimen's fatigue behavior. Besides, in most cases the longitudinal strain shown compressive magnitudes.

The snap thru buckled specimens presented the highest levels of deformations. Dent 3 presented strain ranges in the order of 19000 $\mu\epsilon$. The average strain range of the non-buckled specimen was 6000 $\mu\epsilon$ at the last pressurization cycle.

From the area profile determined by DIC the second type of finite element model was created. It used the exact dent contour measured by the DIC experiments, and therefore was expected a much better correspondence between the numerical and the experimental analysis. The only input for the finite element models, besides the boundary conditions were the shell profiles, being necessary to set up the thickness of each model, which was done considering the absence of defects and a standard thickness of 6.35 mm.

Because of the ratcheting behavior of the material, the results of the second type of finite element models are only valid when compared to the results from the last pressurization cycle of the first block of pressure loading. After the preliminary pressurization cycles the accumulation of plastic deformation decreased to a certain level where it could be disregarded, especially when the pressure of the second pressurization stage was considerably lower than that of the first one. In these cases, the material stayed in a stabilized condition, behaving elastically, as shown by Figure 5.21. This figure presents the evolution of circumferential strain at points P0 and P1 of Dent 6 measured by DIC during the first two preliminary cycles and after some cycles of the second block of pressurization.

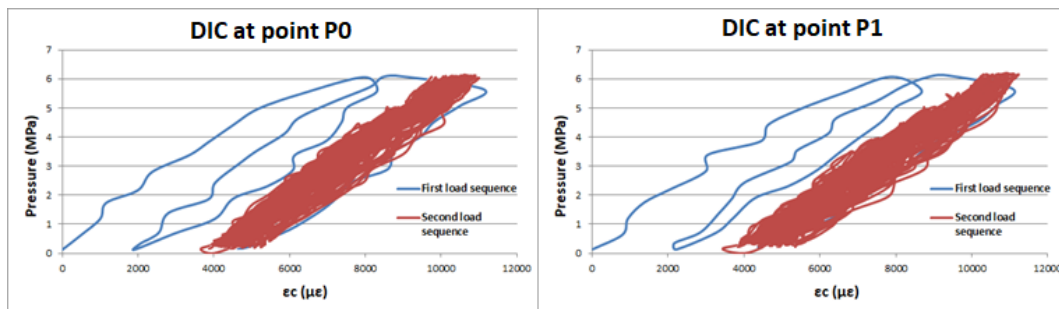


Figure 5.21: Evolution of circumferential strain at points P0 and P1 of Dent 6 measured by DIC during the first two preliminary cycles and the first 100 cycles of the second block of pressurization.

The second type of numerical models was assumed with linear elastic behavior having $\frac{1}{2}$ of symmetry, providing information not only on the specimens' surface, but also through their thickness. This is a valuable information for determining where the fatigue crack is expected to begin, i. e., whether it begins at the outer or inner surface of the dent. Figure 5.22 presents the distribution of the circumferential strains on the outer surface over the whole model of specimens Dent 3 and Dent 6, highlighting the critical spots and considering the plastic deformation accumulated over the first cycles of the first block of pressurization using the second type of FEM.

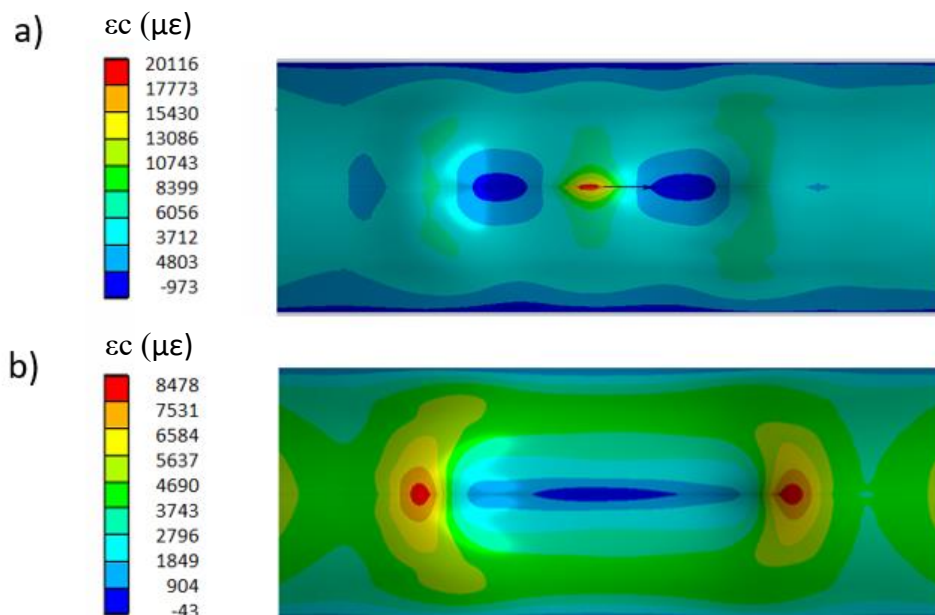


Figure 5.22: Distribution of circumferential strains on the outer surface (top view) of the models using the second type of FEM: a) Dent 3; b) Dent 6.

It can be seen that the highest strain concentration spot is indeed located on the outer surface of the specimens for both types of geometries, justifying the expectation that the fatigue cracking would start from the outside surface¹⁴. As the exact shape of the dent was used, the finite element results were very similar to the DIC measurements.

It was found a good agreement between displacement and strain results measured by the DIC and determined from the second FE model for the positions located at the hot spots, also known as points P0 and P1, as well as the results obtained using these two techniques compared to those of FBSG¹⁵ at other positions of interest.

Figures 5.23 and 5.24 compare the circumferential and longitudinal strains measured by DIC during the last cycle of the first load sequence with the linear elastic finite element results of the second type of model determined for positions P0 and P1 in Dent 3 and Dent 6, respectively.

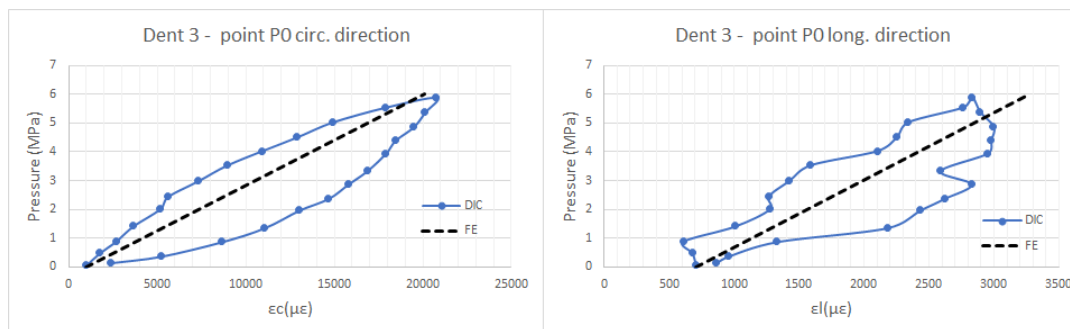


Figure 5.23: Circumferential and longitudinal strains measured by DIC and calculated by FE at the last cycle of the first load sequence for point P0 of Dent 3.

Based on the elastic behavior of the dent presented by Figure 5.13 and Table 9, although $\Delta\epsilon_c$ is very large, the elastic $\Delta\epsilon_c$ predicted by the FE can be used in the analysis as an approximation without any major problems.

¹⁴ Fractography examining the dented specimens after being cyclic tested confirmed this hypothesis.

¹⁵ Results determined with FBSG will be commented in section 5.3.3.

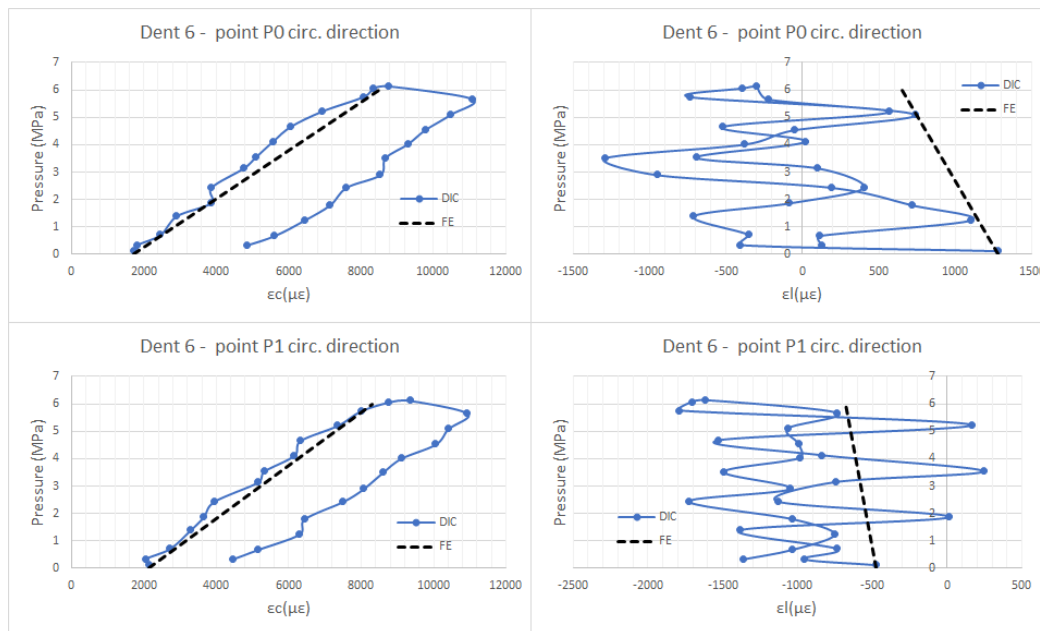


Figure 5.24: Circumferential and longitudinal strains measured by DIC and calculated by FE at the last cycle of the first load sequence for points P0 and P1 of Dent 6.

In order to compare the strains obtained with the DIC technique and the FE models over the last cycle of pressurization of the first pressure block it is necessary to take into account the plastic deformation accumulated by all previous pressurization cycles. As mentioned, the deformation in the circumferential direction is much more relevant than the one in the longitudinal direction. The circumferential strains reached high values at the critical spots, around 21000 $\mu\epsilon$ and 8500 $\mu\epsilon$ for Dent 3 and Dent 6, respectively. Meanwhile, at the longitudinal direction it was obtained in average 2500 $\mu\epsilon$ for Dent 3 and -600 $\mu\epsilon$ for Dent 6.

5.3.3 Fiber Bragg Strain Gauges (FBSG) Results

The FBSG were used to obtain the maximum and representative results about each specimen around the dent areas during the cyclic loading operation. It is important to emphasize that the DIC is either unused or underused at the second pressurization block due to the size of the results files and mainly because of the acquisition frequency required by the system. Thus, the fiber optic strain gauges were very useful to monitor the specimens during the second cycling block.

Figures 5.25 and 5.26 show the schematic arrangement of the FBSGs, their positions measured by DIC and the comparison of the experimental and numerical results for the first pressurization block of Dent 3 and Dent 6 specimens, respectively.

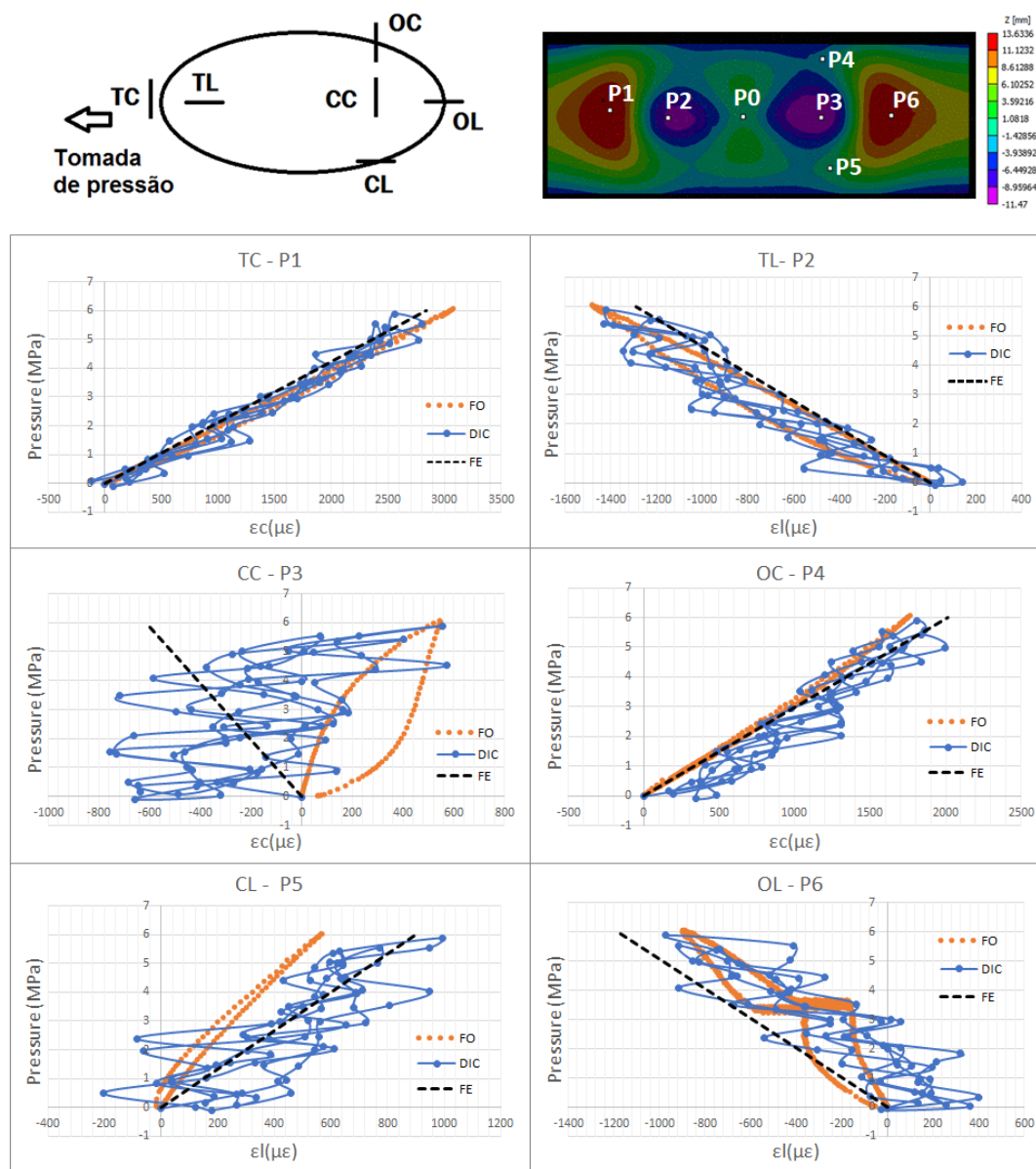


Figure 5.25: Schematic arrangement of the FBSGs, their positions measured by DIC and the comparison of the experimental and numerical results for the first pressurization block of Dent 3.

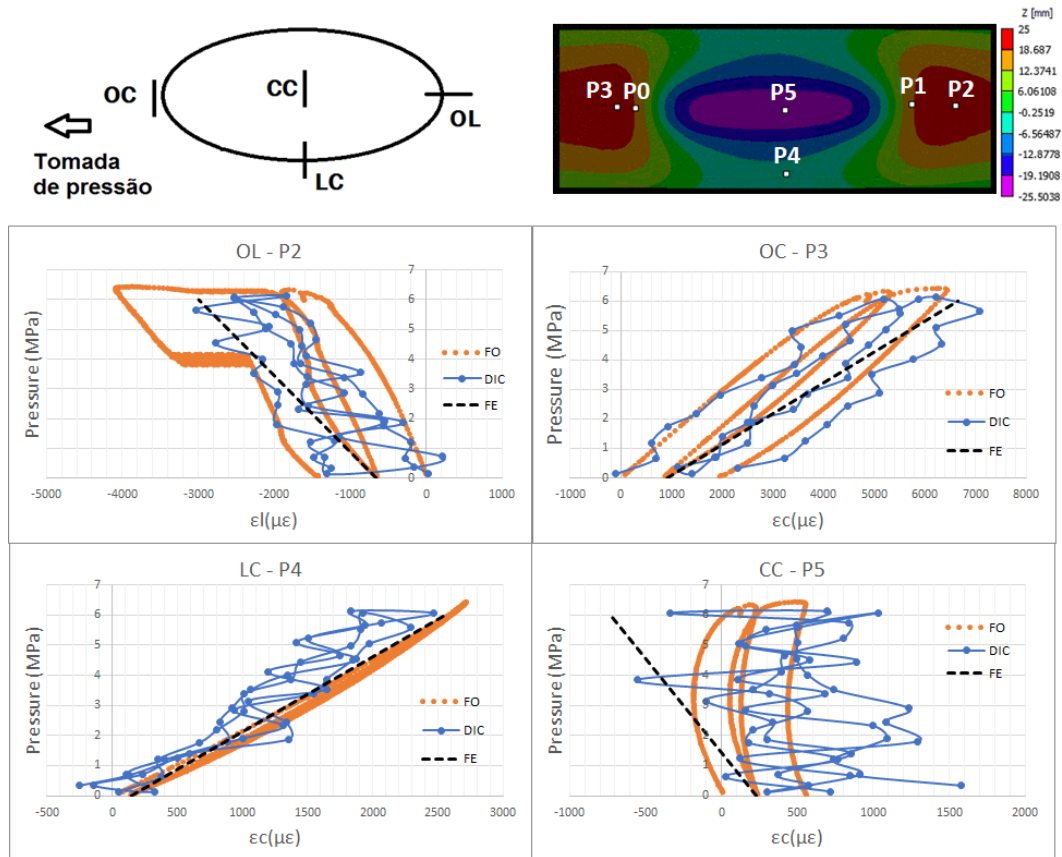


Figure 5.26: Schematic arrangement of the FBSGs, their positions measured by the DIC and the comparison of the experimental and numerical results for the first pressurization block of Dent 6.

The results using the different techniques applied to both specimens, showing good agreement and highlighted the advantages of coupling two or more techniques. Although FBSG is the most expensive technique, it presented considerable advantages considering the monitoring of specimens during the second pressurization block, providing real-time measurements and information along the full test duration.

Analyzing the strains distributions of Dent 3, Figure 5.25, it can be observed that the deformations inside the depressions around the hump are relatively small and the circumferential strain at the edges are considerable, but not as large as compared to those acting at the hump region. At this stage of the investigation, a fiber optic strain gauge was not programmed to be placed over the humps. In this case, FE and DIC helped determining the maximum strains that were located at the humped areas.

Regarding Dent 6, Figure 5.26, the deformation at the center of the dent shown to be small, the edges of the dent presenting much more significant strains, especially in the circumferential direction.

The FBSGs were used as a monitoring tool during the second block of pressurization, providing knowledge about the status of the specimens along the full time of realization of the tests. Figures 5.27 and 5.28, Dent 3 and Dent 6, show the history of strains measured by the FBSGs while the cyclic tests were performed. The positions of the gauges are presented in Figures 5.25 and 5.26.

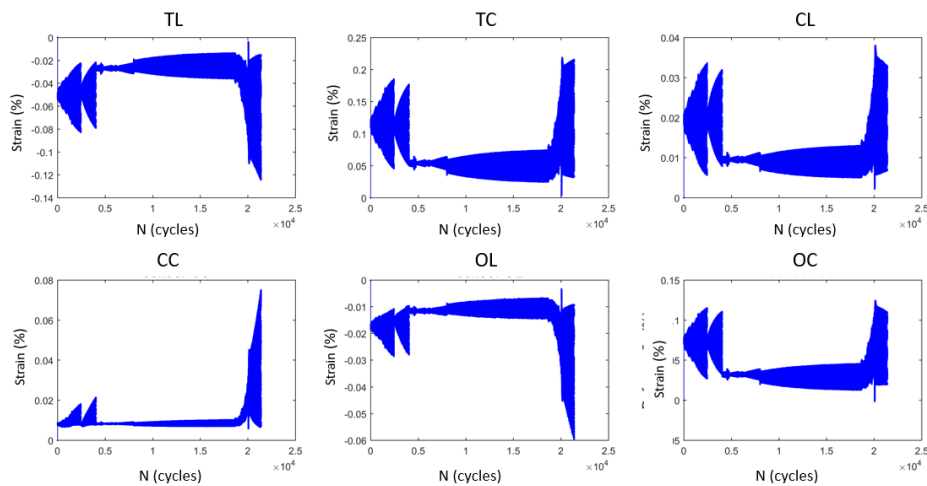


Figure 5.27: Dent 3 history of strains measured by the FBSGs during the second block of pressurization.

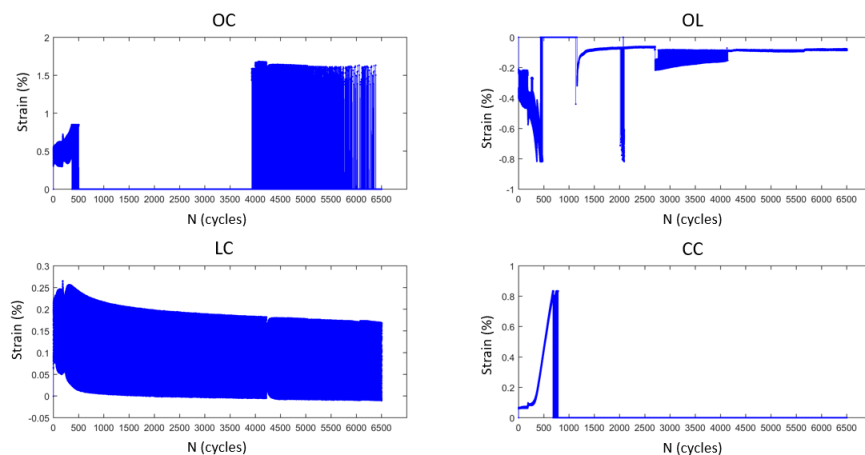


Figure 5.28: Dent 6 history of strains measured by the FBSGs during the second block of pressurization.

The levels of strains recorded along the duration of the second block of pressurization of the test of the Dent 3 specimen confirmed the behavior that was measured during the first block of pressurization. Sensor TC located at the far edge of one of the dimples shown the highest tensile strains along with sensor OC, both placed at the circumferential direction, although the largest strains are present in the center of the hump (point P0).

With regard to the test of specimen Dent 6, the LC sensor located at the circumferential direction was the one that measured the highest tensile strain. The other sensors experienced some recording problems starting around 500 cycles.

One of the disadvantages observed in the use of FBSG was the finding of the hot spot location a priori, i. e., before any numerical or DIC analysis has been done. The DIC technique was very useful to help locating high strain areas, even when there were not strain gauges placed to it.

In some cases, the high strain in the hot spots of the dents damage the gauges during the measurement, as it can be seen in Figure 5.28 sensor CC.

5.3.4 Thermoelastic Stress (TSA) Results

The TSA output (proportional to the principal elastic stress invariant range) is presented in Figure 5.29. The TSA images were taken when the pressure ranges were 1.5 MPa (Dent 3) and 6.0 MPa (Dent 6) and were gathered after 1000 pressurizing cycles of the second block of pressurization. It has to be noted that, for some locations and at this pressure ranges, some plasticity occurred, and therefore the TSA results obtained at these locations must be interpreted as qualitative results.

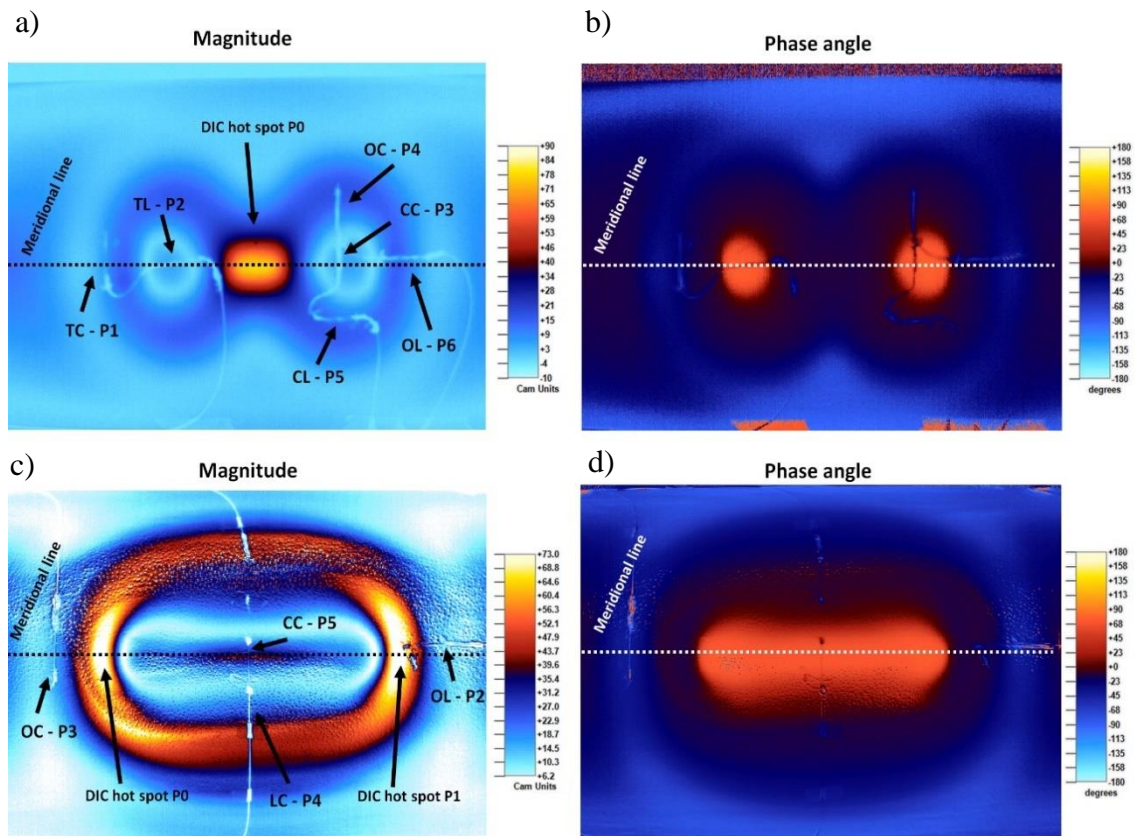


Figure 5.29: TSA output: a) Dent 3 specimen magnitude; b) Dent 3 specimen phase angle; c) Dent 6 specimen magnitude; d) Dent 6 specimen phase angle.

Figure 5.29a, for Dent 3 specimen, shows the critical hot-spot at the center of the image as well as (caused by different temperatures) the uniaxial fiber optic strain gage locations, three of them measuring circumferential strains and three measuring longitudinal strains at reasonably symmetrical points.

In the same way, for Dent 6 specimen TSA results, Figure 5.29c, shows the critical hot-spot at the edges of the dent and the fiber optic strain gage locations, one of them measuring circumferential strain and another measuring longitudinal strain at reasonably symmetrical points. The two circumferential FBSG at the center of the dent measured low stresses levels when compared to the hot spot positions.

While TSA is in essence a linear elastic technique, some plasticity occurs in and around the hot spot positions even if a double flow stress magnitude is expected and considered. Besides, the TSA signal is composed of a magnitude proportional to the temperature variation caused by the thermoelastic effect, and a phase angle, which is related to the signal of the actuating stresses. Vieira et al. [101] studied fatigue crack propagation on a SAE keyhole specimen made of polycarbonate,

finding a phase angle modulus equal to 45° to differentiate the magnitude signal (tension or compression). This value was found based on the specimen geometry and expected behavior.

In the present work, techniques such as DIC and FE were used to help determine the phase in which the magnitude signal change occurs. This range varied from 20° to 45° depending on the case analyzed.

The relation between the TSA magnitude signal (cam units provided by the camera) and the principal stress state (MPa) was made using a linear calibration relationship established by Eq. (17), where low carbon steel tensile specimens were tested at different stress ranges. It is important to note that this relationship was obtained for uniaxial test specimens made from the same type of steel (low carbon steel).

Figure 5.30 shows the plot of the TSA magnitude (measured in camera units), the phase angle and the first invariant stress response along the meridional line that passes through the center of each dent, as shown by Figure 5.29. These TSA results were collected in 1000 cycles of loading. Part of the noise in the signal may have origin in the pattern of white dots applied on the surface of the specimen applied to facilitate the use of the DIC technique.

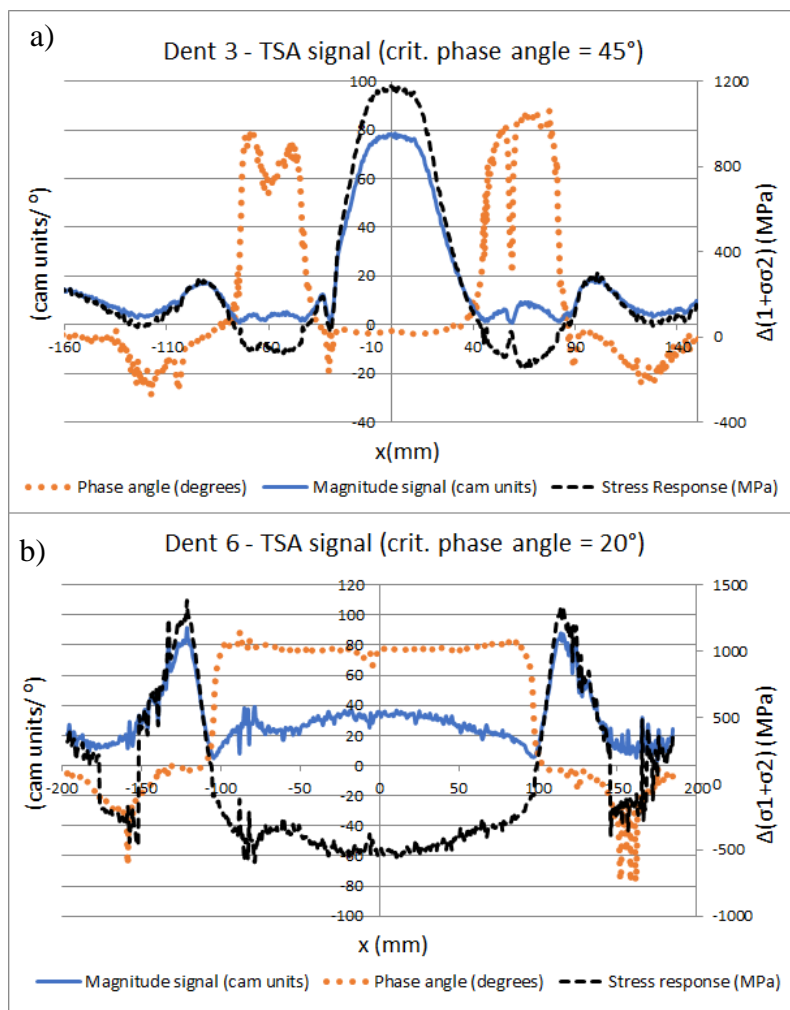


Figure 5.30: TSA output (magnitude and phase angle) and the first invariant stress response: a) Dent 3 specimen; b) Dent 6 specimen.

At the regions of low stress, the center of the two depressions of Dent 3 specimen and the center of Dent 6 specimen, the phase angle was around 90° signaling the change in magnitude signal. The hot spots positions for both specimens exhibited a phase angle around 0° , showing that the response signals in these areas were in phase.

The value of the critical phase angle modulus for the response signal inversion was obtained comparing the TSA results to the other employed techniques. It was found that for Dent 3 specimen the critical phase angle was equal to 45° and for Dent 6 specimen was 20° .

Taking into consideration the meridional line that passes through the center of each dent, as shown in Figure 5.29, DIC, TSA and linear elastic FE (second type of finite element model) results were assessed along it. These results are plotted in Figure 5.31, in terms of the sum of the principal stress for the pressure range equal to 1.5 MPa (Dent 3 specimen) and to 6.0 MPa (Dent 6 specimen), used in the second block of pressure. Although, some discrepancy exists, results shown very good comparison among the TSA, the DIC and FE results.

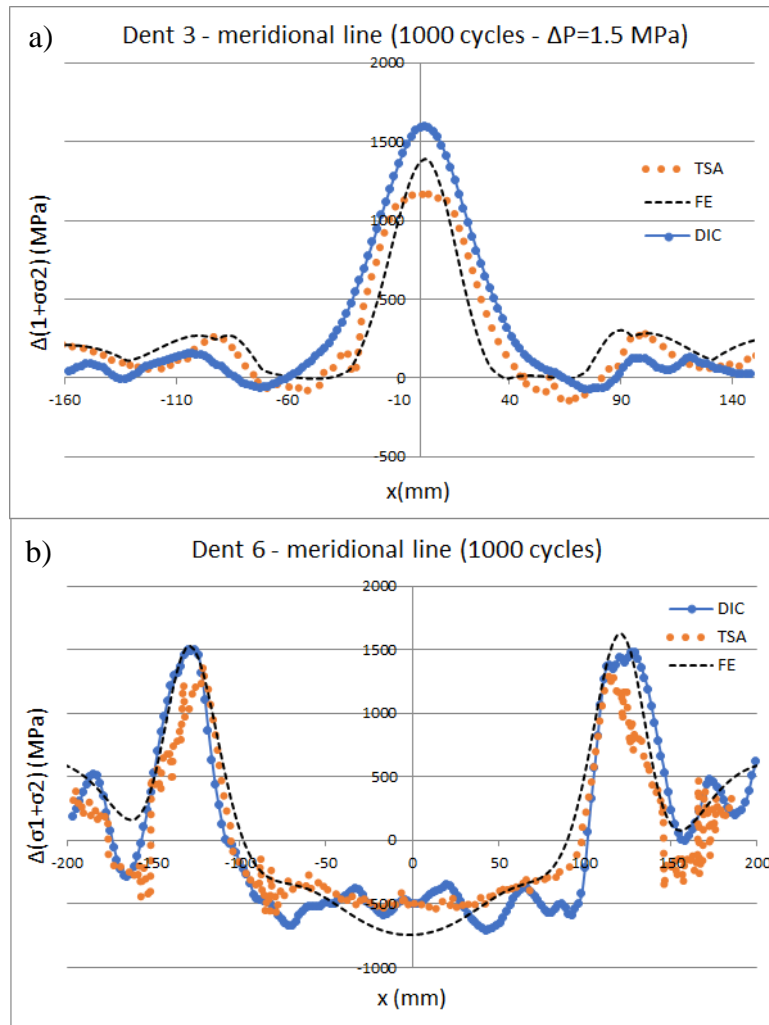


Figure 5.31: TSA, DIC and FE results plotted for points located at the meridional symmetric line: a) Dent 3 specimen; b) Dent 6 specimen.

Figure 5.32 shows the TSA magnitude signal of all tested dented specimens around 1000 cycles. Although the TSA magnitude signal response are different at each specimen, due to the difference of the applied pressure ranges, the distribution of TSA magnitude is very similar when comparing the behavior of specimens with similar geometry (with or without snap-thru).

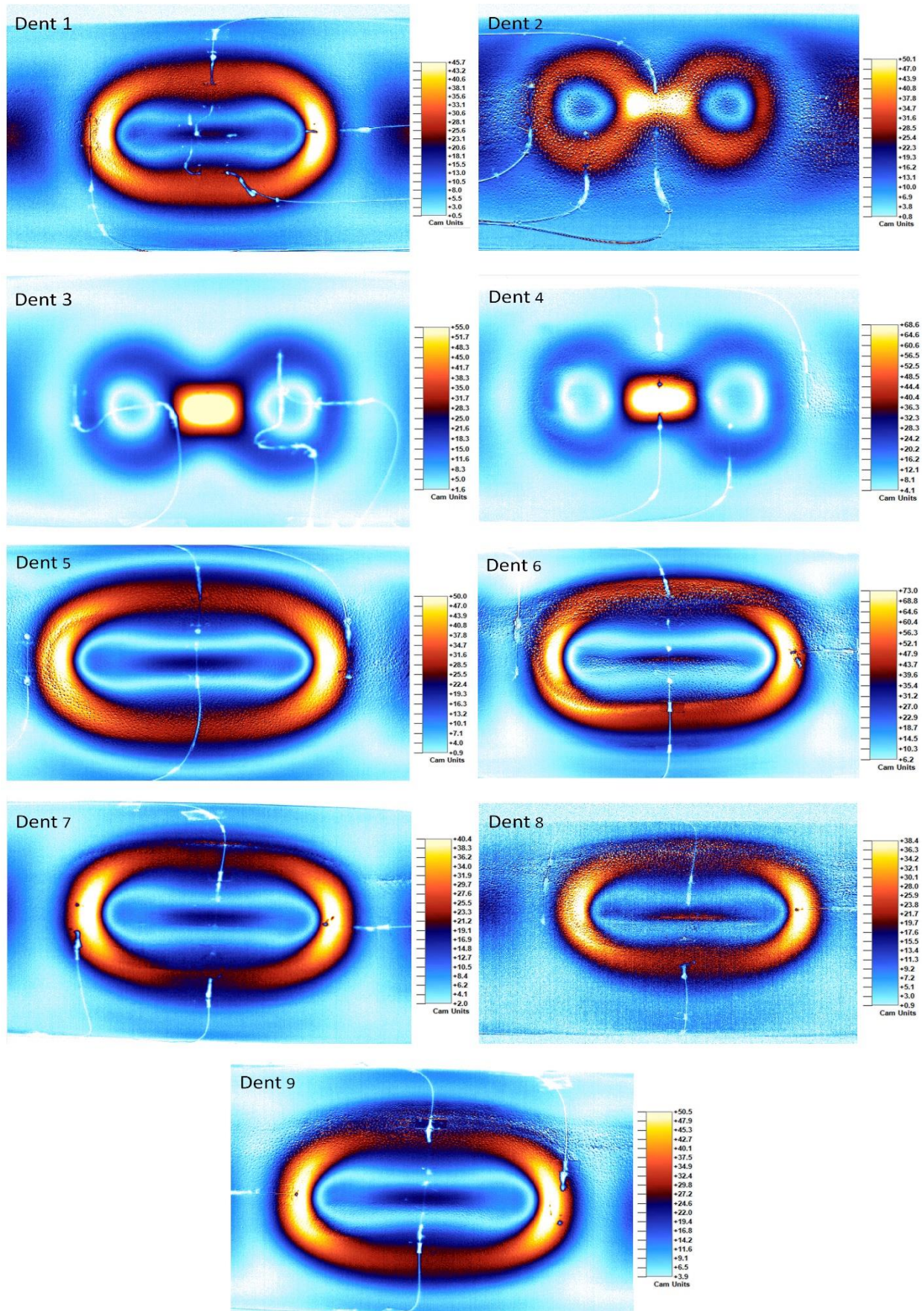


Figure 5.32: TSA magnitude around 1000 cycles of all tested dent specimens.

5.3.5 Stress and Strain Concentration Factors Results

The values of stress/strain concentration generated by the dent biaxial strain/stress state in the pipe specimens measured and estimated with the experimental and numerical techniques are shown in Table 10.

Table 10: Stress and strain concentration factors¹⁷.

Specimen	TSA	FEM					DIC					FBSG
	$K_{\sigma_1+\sigma_2}$	$K_{\sigma c}$	$K_{\varepsilon c}$	$K_{\sigma c \cdot \varepsilon c}$	$K_{\sigma VM}$	$K_{\sigma_1+\sigma_2}$	$K_{\sigma c}$	$K_{\varepsilon c}$	$K_{\sigma c \cdot \varepsilon c}$	$K_{\sigma VM}$	$K_{\sigma_1+\sigma_2}$	$K_{\varepsilon c}$
Dent 1	5.42	7.77	8.83	8.32	8.50	5.78	7.51	8.67	8.11	8.42	5.31	6.35
Dent 2	4.35	6.85	7.73	7.31	7.43	5.19	6.97	8.15	7.58	7.97	4.75	5.84
Dent 3	21.37	26.01	26.77	26.39	26.13	24.58	26.67	27.66	27.17	26.86	24.79	- ¹⁶
Dent 4	10.43	18.33	18.25	18.29	18.33	18.49	18.39	18.70	18.54	18.42	17.80	15.05
Dent 5	7.15	7.68	9.13	8.44	9.03	4.93	8.71	8.98	8.85	8.76	8.20	4.99
Dent 6	5.98	8.58	9.45	9.02	9.04	6.94	8.01	9.28	8.67	9.02	5.62	6.52
Dent 7	5.43	8.11	9.27	8.71	8.95	5.92	7.82	8.59	8.21	8.21	6.37	7.15
Dent 8	6.17	7.35	8.48	7.93	8.22	5.22	7.71	8.48	8.10	8.11	6.27	3.88
Dent 9	5.68	8.79	9.99	9.41	9.63	6.52	9.55	9.94	9.75	9.64	8.80	7.72

The values measured with FBSG are a little smaller compared to the ones measured with FE and DIC. This is caused by the positioning of the fiber Bragg sensors in the specimens, which were located near but not exactly at the points of higher strain concentration.

$K_{\sigma c \cdot \varepsilon c}$ in this case is the quadratic average calculated using the values $K_{\sigma c}$ and $K_{\varepsilon c}$ and corresponds to the elastic stress concentration factor K_t .

Figure 5.33 shows a graphic comparison between the stress concentration factor obtained with the different techniques presented in Table 10.

¹⁶ As the FBSG sensor was not positioned at the maximum strain spot, Figure 3.27, the strain concentration could not be determined.

¹⁷ The calculation log is shown in Appendix E.

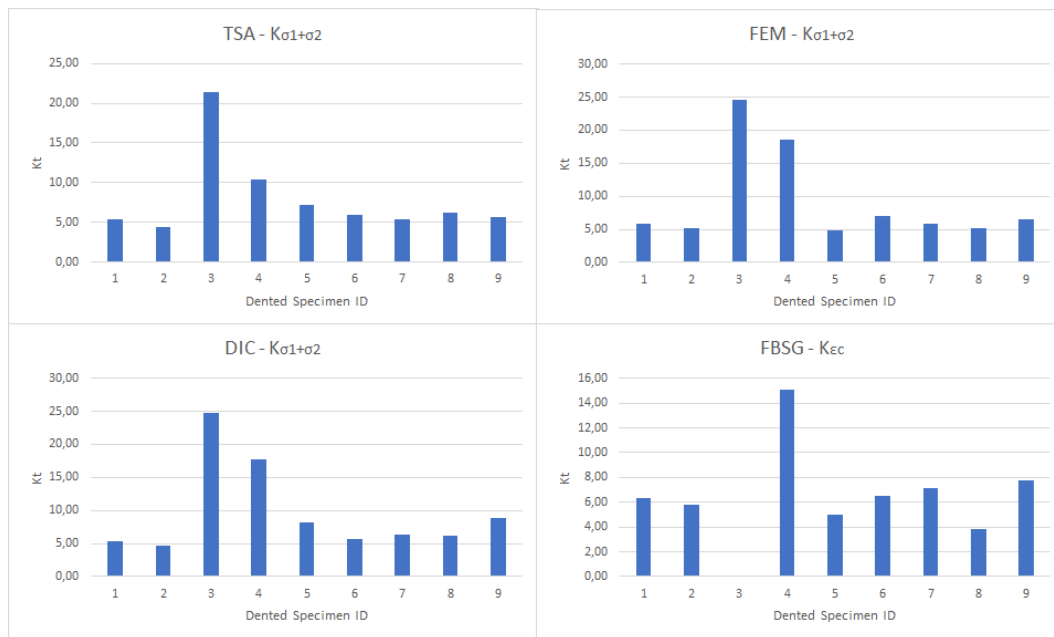


Figure 5.33: Graphic comparison between the stress concentration factor obtained with the different techniques presented in Table 10.

5.3.6 TSA Fatigue Crack Monitoring

This section shows that TSA, besides providing information on the stress state of a cyclic loaded sample, can also be used as a fatigue monitoring tool, supplying real time information about the specimen damage condition. Due to the nature of the technique, it can be used to locate and monitor the development of a fatigue crack. Taking Dent 3 specimen as an example, Figure 5.34 shows that after 1000 cycles of loading no crack could be noticed. However, from 3000 cycles onwards, a decrease in the stress level in the center of the specimen can be observed, symbolizing the initiation and start of propagation of a fatigue crack. In the subsequent images it is clear the growth of a crack in the highest stress region.

The birth and evolution of fatigue crack is accompanied by a local stress relief, which is perceived as the decrease in the stress level compared to an earlier stage. Large cracks can be easily spotted, while small ones need several cycles until can be detected. If the crack is already present in the specimen or the measurement begins after its development, it can be identified by the stress concentration originated at its tips and the stress relief at the crack surfaces.

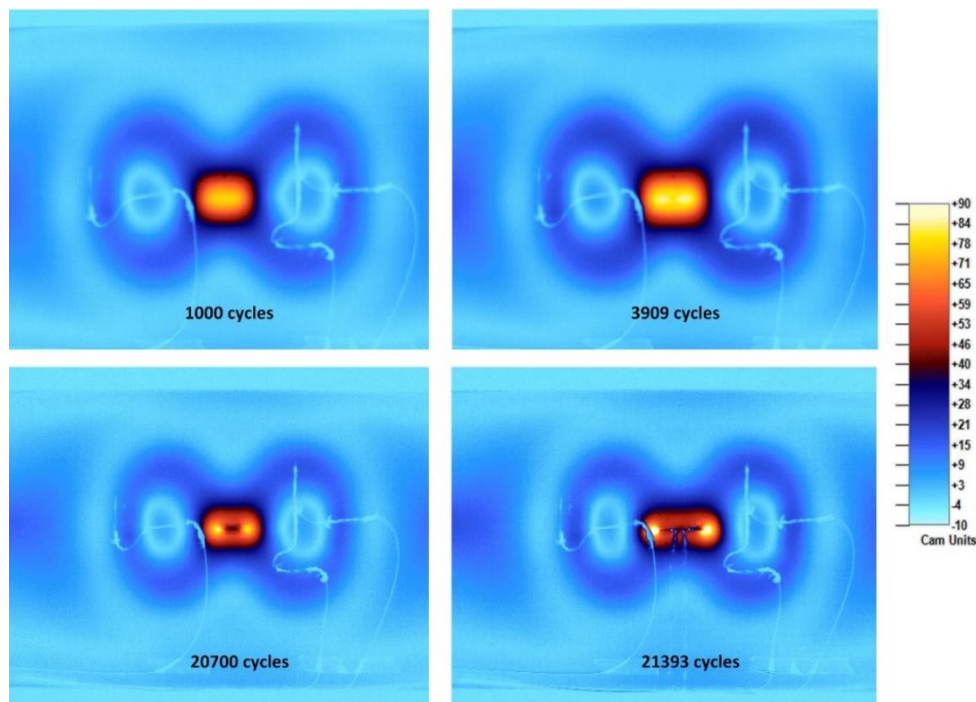


Figure 5.34: Dent 3 TSA magnitude of the dented area taken at specific number of cycles showing crack development (after 3909 cycles) and through crack (after 21393 cycles).

Similarly, Figure 5.35 shows the development of a fatigue crack in the stress concentration region of the Dent 6 specimen. At 4000 cycles a decrease in the stress level can be noticed (marked with an arrow), but the crack only becomes easily visible after 5600 cycles.

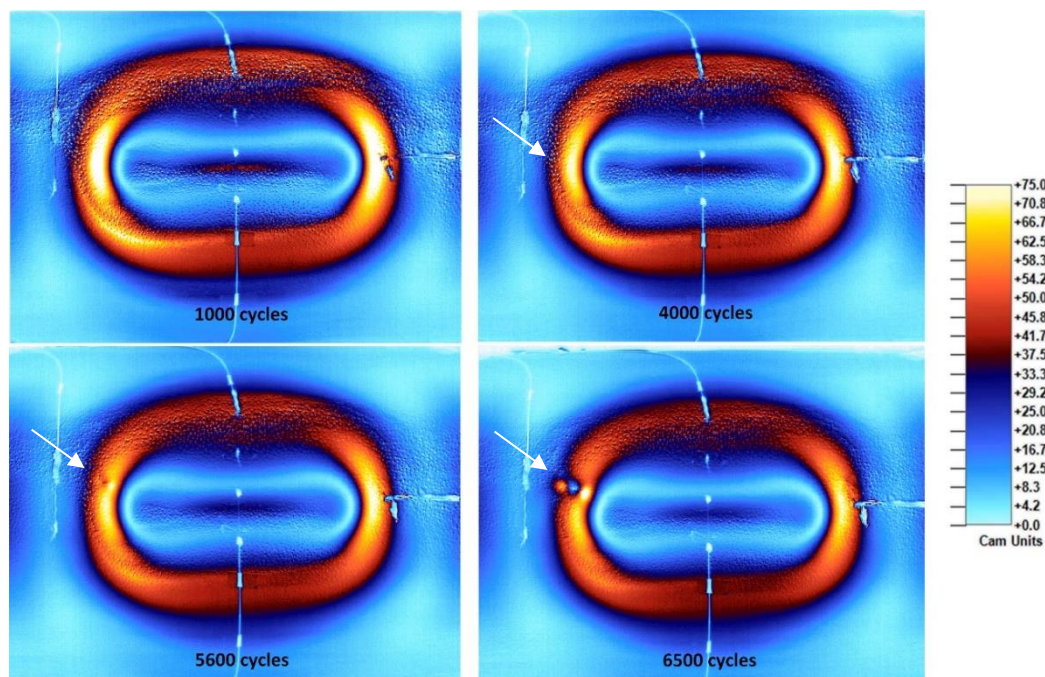


Figure 5.35: Dent 6 TSA magnitude of the dented area taken at specific number of cycles showing crack development (after 4000 cycles) and through crack (after 6500 cycles).

The stress concentration of the crack tips becomes more evident as it grows, meaning an increase in the crack stress intensity factor. The failure of all the specimens tested had the characteristic of leaking before break, due to the small thought cracks geometry, by the fatigue process and because of the material high toughness.

Analyzing TSA stress response of specimens Dent 3 and Dent 6 over the time in a line which passes through the center of the cracks, it can be observed the influence of the crack propagation during the performance of the tests.

Figure 5.36 shows the influence of the crack size evolution on the TSA specimens' response. This comparison was made until some cycles before leaking. It can be seen that, at the beginning of crack growth, a slight stress relief occurs at the position of the stress concentration, while the regions at the edge of the crack experience a stress increase.

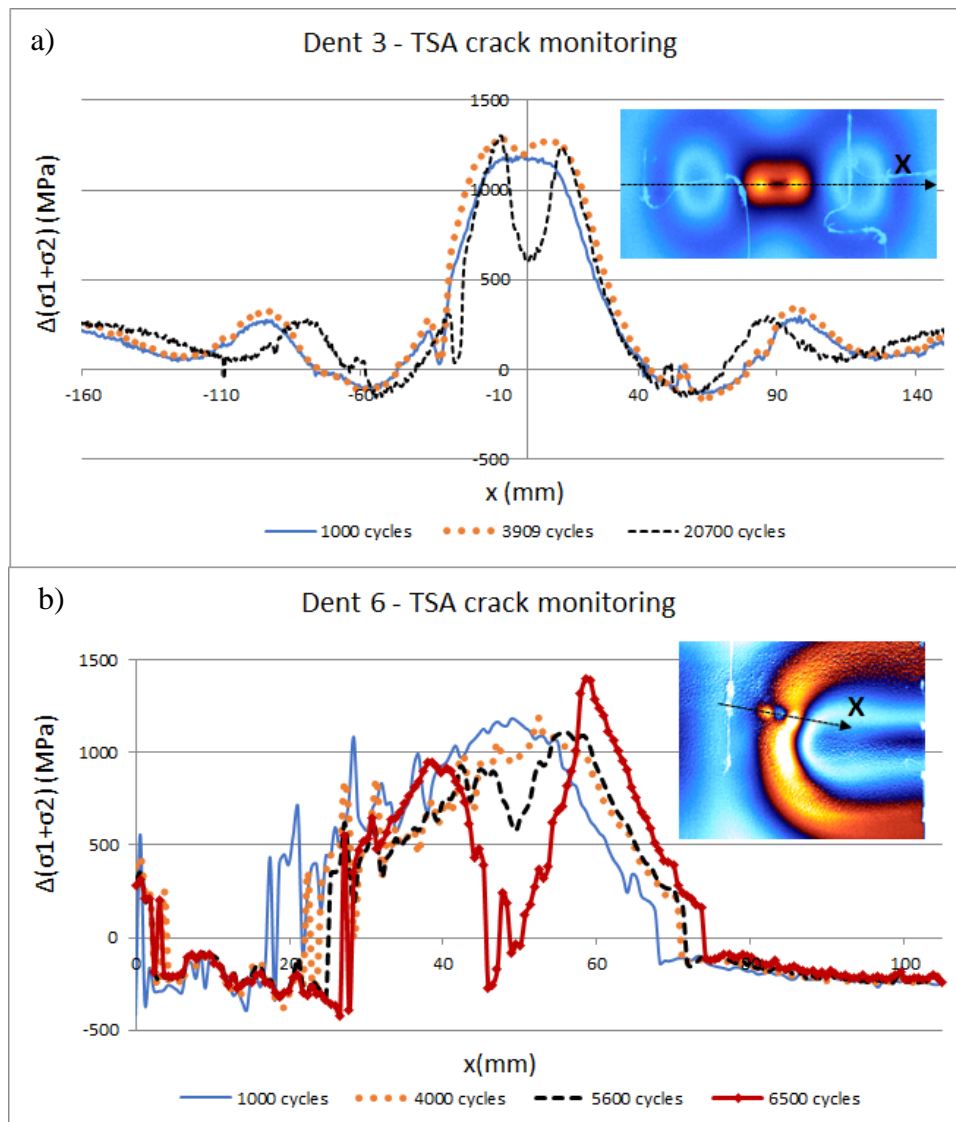


Figure 5.36: TSA magnitude (converted in sum of principal stress ranges) measurements along the symmetry line inside the dent area showing the influence of crack propagation during the number of cycles.

5.4 Fatigue monitoring using IR thermography

IR thermography can be used as a powerful tool to predict and monitor fatigue crack initiation and growth.

There are two distinct approaches; one based on the thermal response of the specimen, where the Quasi - Static method for fatigue limit measurement is employed (section 2.4.1.2), and the other based on the comparison of the thermoelastic response measured using the TSA (presented in section 5.3.6).

5.4.1

Assessment of fatigue hot spots by temperature measurements when the specimen is loaded in quasi-static conditions

This type of assessment uses the quasi-static methodology for the fatigue limit measurement, introduced at section 2.4.1.2, to provide valuable by determining the critical hot spot locations in complex shaped structures.

The concept behind this approach is that the critical points on the sample surface, when loaded, will undergo plastic deformation accumulating a certain amount of damage; this will be related with the fatigue limit measurement. The most critical positions will reach the fatigue limit value at a number of cycles lower than the less critical ones.

Determining the temperature for each surface point under quasi-static loading makes possible to determine their order of importance and select the spot that will suffer fatigue first.

Some sites of interest were pre-selected to be analyzed, as shown by Figure 5.37. Instead of analyzing all the points on the surface, only the positions capable of causing fatigue were analyzed. Sites that presented compressive stress magnitudes during the first stage of the assessment were not considered in the evaluation.

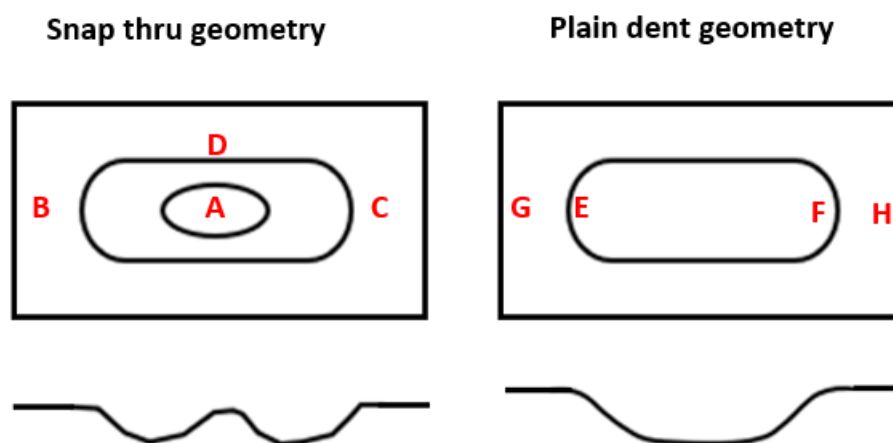


Figure 5.37: Pre-selected interest positions for both specimen geometry.

For each dented specimen, and in the first block of pressure loading, the hydrostatic pressure was increased gradually (0.2 MPa/s) while IR temperature measurements were made. Curves pressure vs. time and temperature vs. time were plotted as presented in Figure 5.38 for specimen Dent 6. The von Mises equivalent stress for each point was determined from the second type of FE models with the correspondent applied pressure.

Figure 5.38 shows the application of an extended quasi-static method IR method for the determination of the full alternated (in this case) biaxial fatigue limit of point E of the Dent 6 specimen. The temperature variation was curve fitted to minimize temperature measurement noise. This slope deviation point is related with the fully alternate fatigue strength, and it was found to be equal to $\sigma_{von_Mises} = S_{e_Dent_6-E} = 235.5$ MPa.

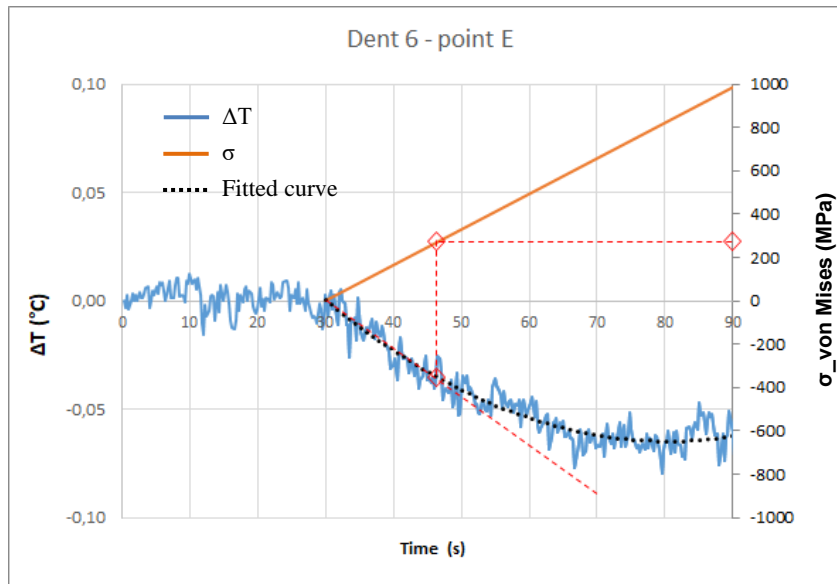


Figure 5.38: Quasi-static IR method applied to Dent 6 point E.

Figure 5.39 compares the thermal response of all Dent 6 analyzed points when the specimen is loaded, each point reaching the fatigue limit at a different time, the most critical (point E) in a shorter time (lower hydrostatic pressure) than the others. The time axis is only used to relate the temperature measured with the pressure applied and then with the stress/strain acting at the observed point.

Off course, for each applied pressure, different values of the von Mises equivalent stress occur due to the more or less severity of the stress state that actuates in the analyzed point. This, consequently, implies different deviations of the initial straight line for each temperature curve. The point to be made here is that all deviations points must lead to the same value of $\sigma_{von Mises}$ that represents the material uniaxial fatigue limit.

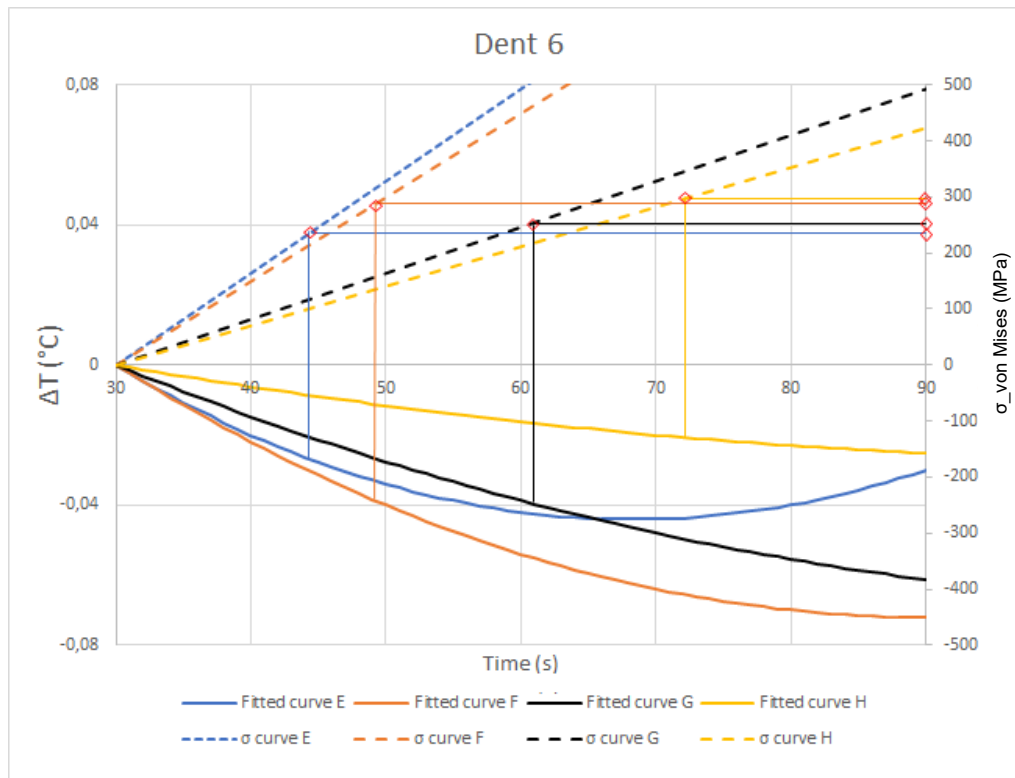


Figure 5.39: Quasi-static IR method applied to all Dent 6 points.

Although slightly different values of $\sigma_{von Mises}$ are seen in Figure 5.38 (this difference possibly caused by method uncertainty), all points represent the uniaxial fatigue limit of the material in terms of its von Mises equivalent stress.

The results of all assessed points of all specimens are presented in Table 11. The average fatigue strength determined for each point of the dents in this way was equal to 228.7 MPa with standard deviation of ± 32.8 MPa. This value is similar to the average value 245.0 MPa with standard deviation of ± 24.0 MPa that measured for the dog bone specimens at Chapter 3.

This is a very important finding because it is the first time biaxial stress states are used to predict the fatigue limit using a quasi-static method.

Table 11: Measured IR response for each dented specimen.

Specimen	A		B		C		D		E		F		G		H	
	S_e (MPa)	time (s)	S_e (MPa)	time (s)	S_e (MPa)	time (s)	S_e (MPa)	time (s)	S_e (MPa)	time (s)	S_e (MPa)	time (s)	S_e (MPa)	time (s)	S_e (MPa)	time (s)
Dent 1	-	-	-	-	-	-	-	-	234.5	54.0	189.0	57.0	208.3	102.5	162.0	108.0
Dent 2	238.3	64.5	224.8	76.8	237.8	81.8	268.3	75.0	-	-	-	-	-	-	-	-
Dent 3 ¹⁸	-	-	-	-	-	-	-	-	-	-	-	-	-	-	-	-
Dent 4	308.9	51.8	237.1	81.0	202.3	83.5	241.5	80.0	-	-	-	-	-	-	-	-
Dent 5	-	-	-	-	-	-	-	-	242.4	56.5	196.2	42.5	194.5	57.5	206.8	57.5
Dent 6	-	-	-	-	-	-	-	-	235.5	45.7	287.8	49.2	251.9	60.7	295.9	72.0
Dent 7	-	-	-	-	-	-	-	-	220.2	61.5	217.6	56.8	208.0	80.0	201.8	96.0
Dent 8	-	-	-	-	-	-	-	-	197.2	54.0	203.9	61.5	211.2	66.8	209.1	72.2
Dent 9	-	-	-	-	-	-	-	-	242.6	57.3	221.3	55.5	205.9	81.8	238.8	71.0

5.4.2

TSA Monitoring Tool Algorithm to Detect Fatigue Crack Initiation

As presented in section 5.3.6, TSA imagens taken at different moments in the loading history (number of cycles) help to monitor fatigue crack initiation and its growth. The stress state around a fatigue crack is identified by the change of pattern in the measured TSA signal. A typical signal will show larger temperature at the crack tip (stress concentration) and lower temperature at the crack face (stress relief).

This proposed methodology is based on a simple algorithm that evaluates the difference between two measured TSA images, checking their similarities and their differences. The algorithm, shown in Figure 5.40, uses two similar approaches: the first analyses the TSA stress data considering if it is in compression or in tension the and the second approach analyses only the TSA magnitude signal output. The TSA stress data is obtained from the magnitude signal output coupled with the phase angle information. This approach is called magnitude with signal, referring to the tensile or compressive stress signal given by the phase angle information.

¹⁸ Specimen Dent 3 was not subjected to this type of analysis due to schedule problems.

The TSA magnitude output is called magnitude without signal, because uses the raw magnitude output signal.

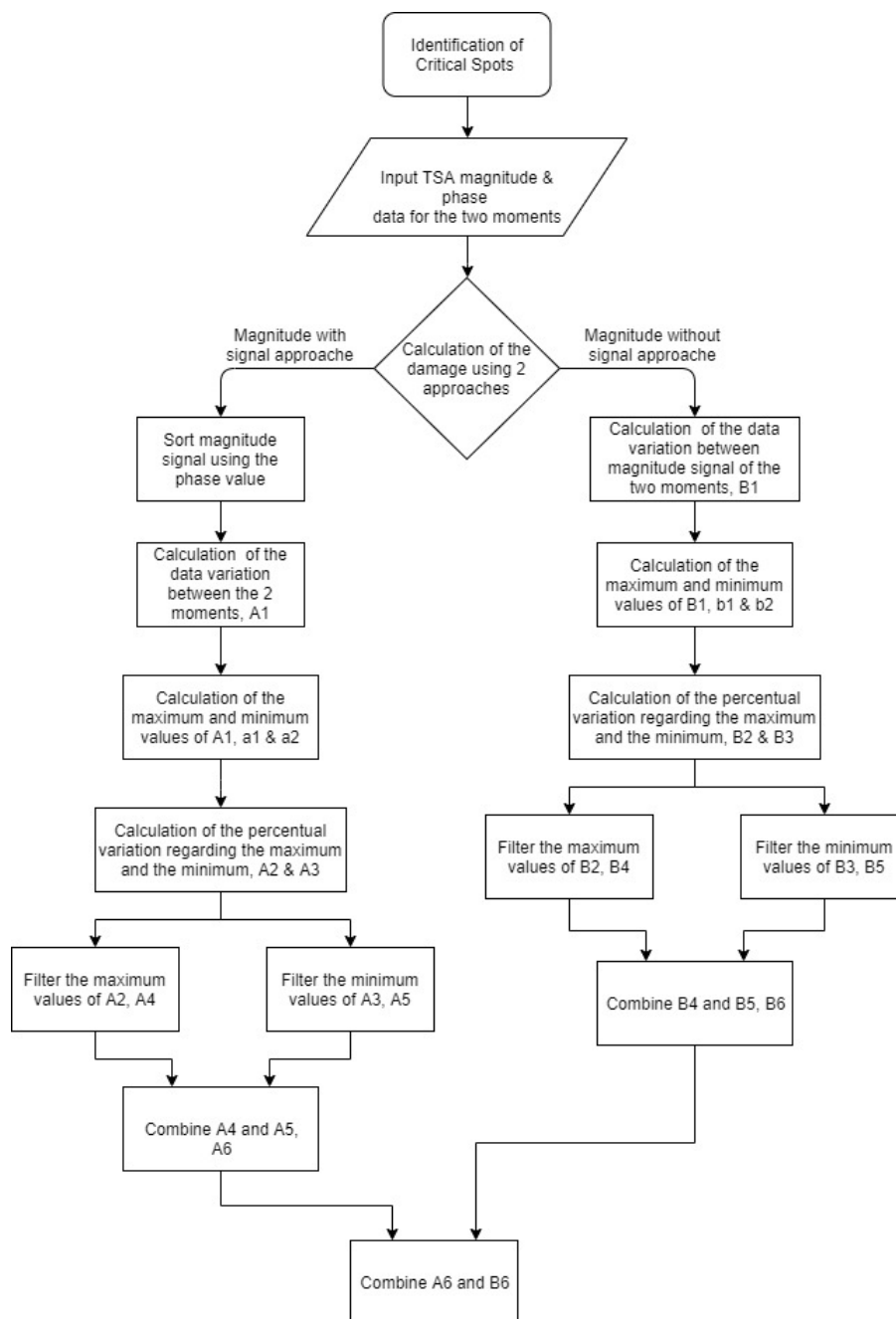


Figure 5.40: TSA monitoring tool algorithm.

In order to illustrate the use of the algorithm proposed, Figure 5.41 present its application to the data of Dent 6 specimen presented in Figure 5.36b for 1000 and 6500 cycles. As for both approaches the results turned to be very similar, only the magnitude with signal results are presented.

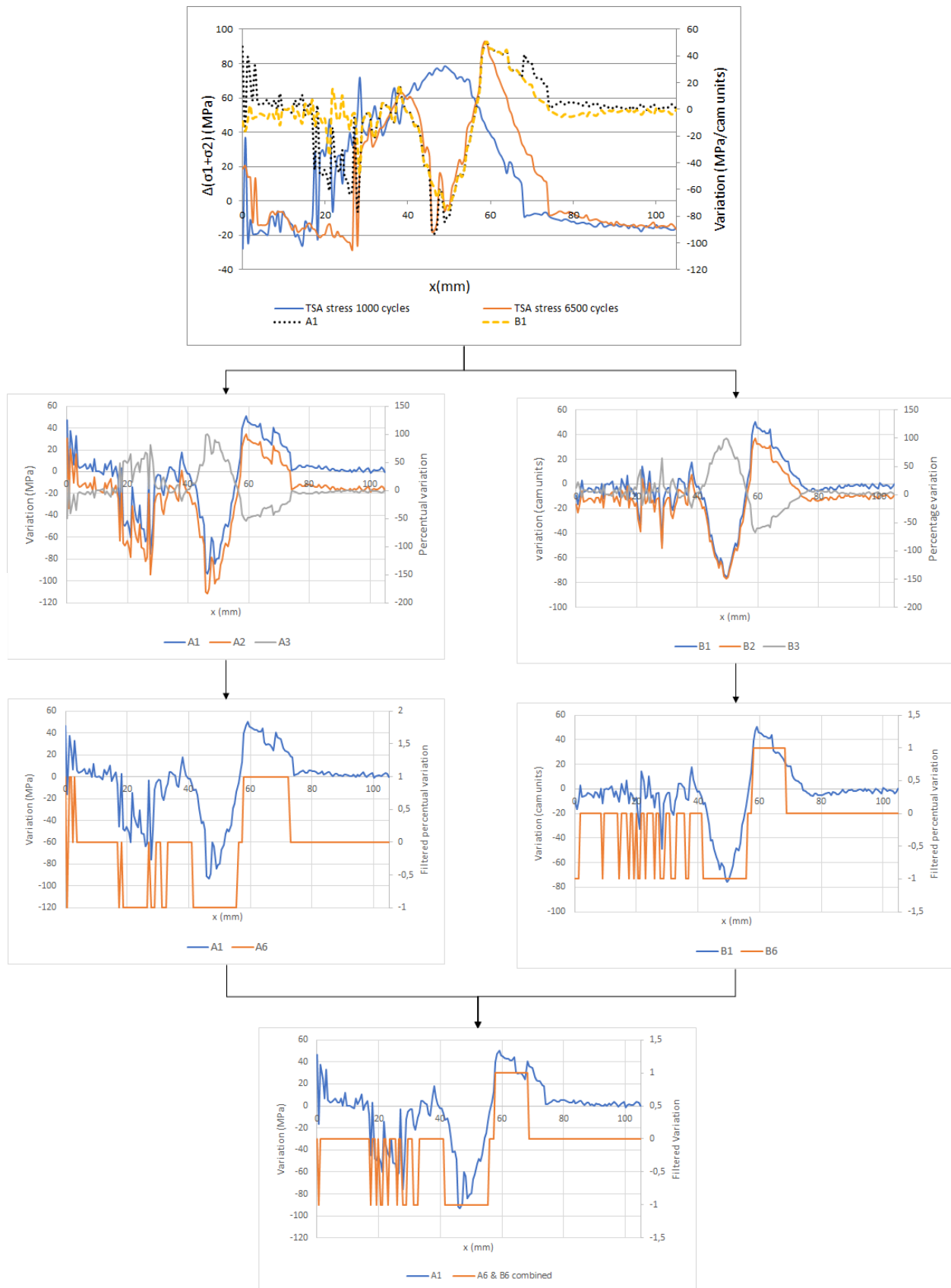


Figure 5.41: Dent 6 specimen TSA data for 1000 and 6500 cycles analyzed using the TSA monitoring algorithm proposed.

The automation of the algorithm was made by implementing the code in MATLAB®. This is a post processing tool as all analyzes are performed after the tests are completed. In future applications the development of a real time evaluation is planned. Figures 5.42 to 5.44 show the application of this TSA monitoring tool to specimens Dent 3, Dent 6 and Dent 7, respectively.

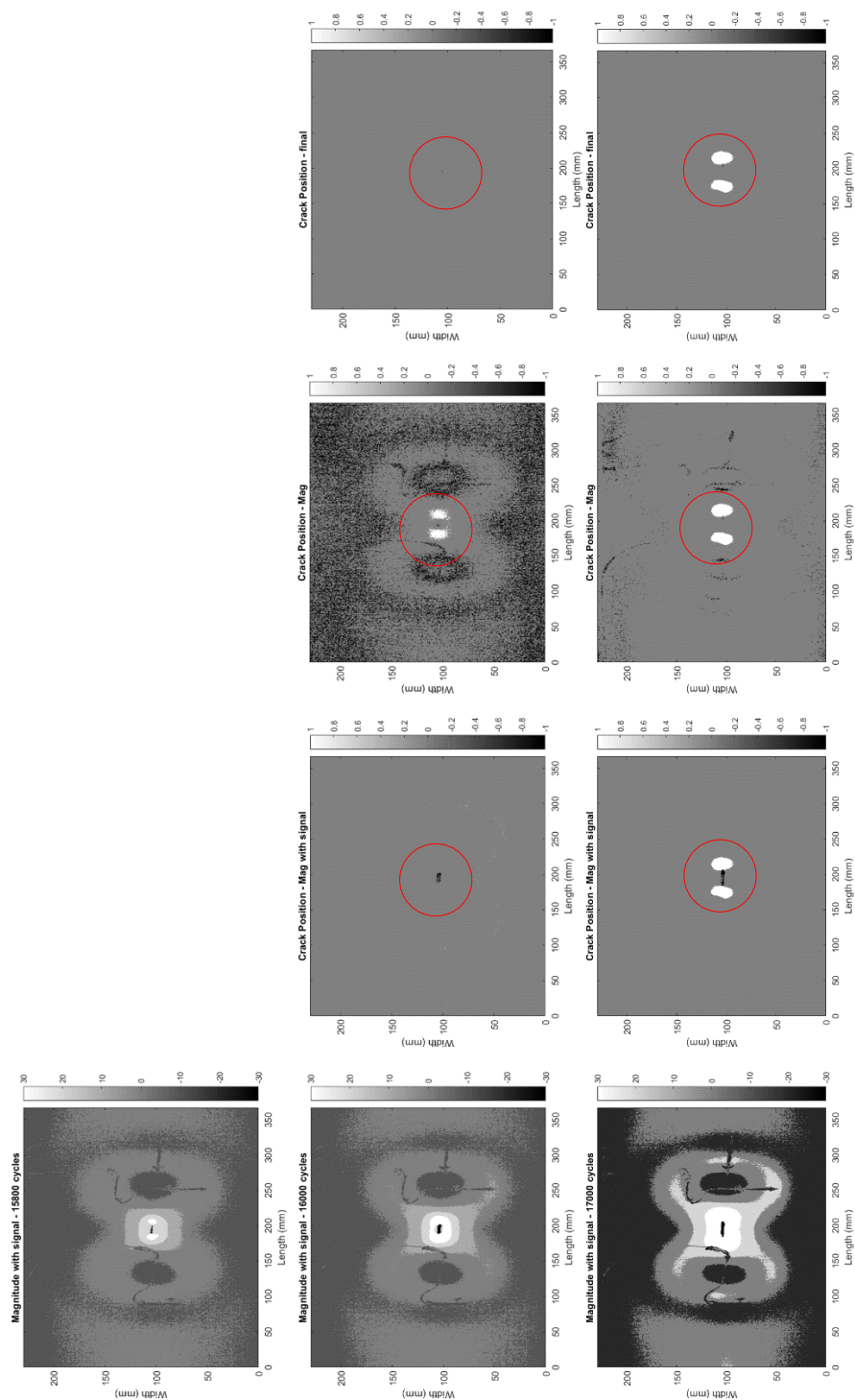


Figure 5.42: Dent 3 TSA crack monitoring.

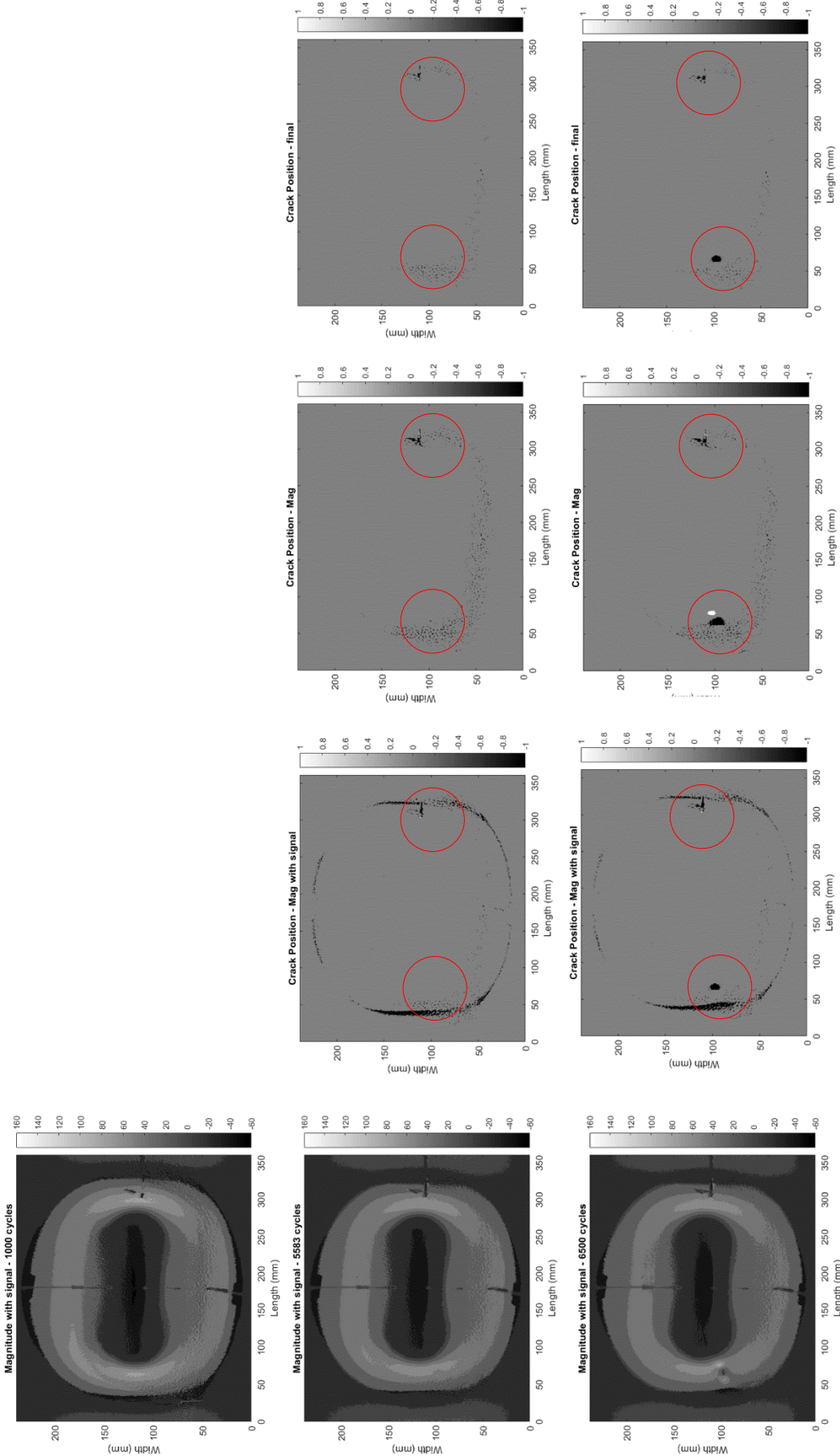


Figure 5.43: Dent 6 TSA crack monitoring.

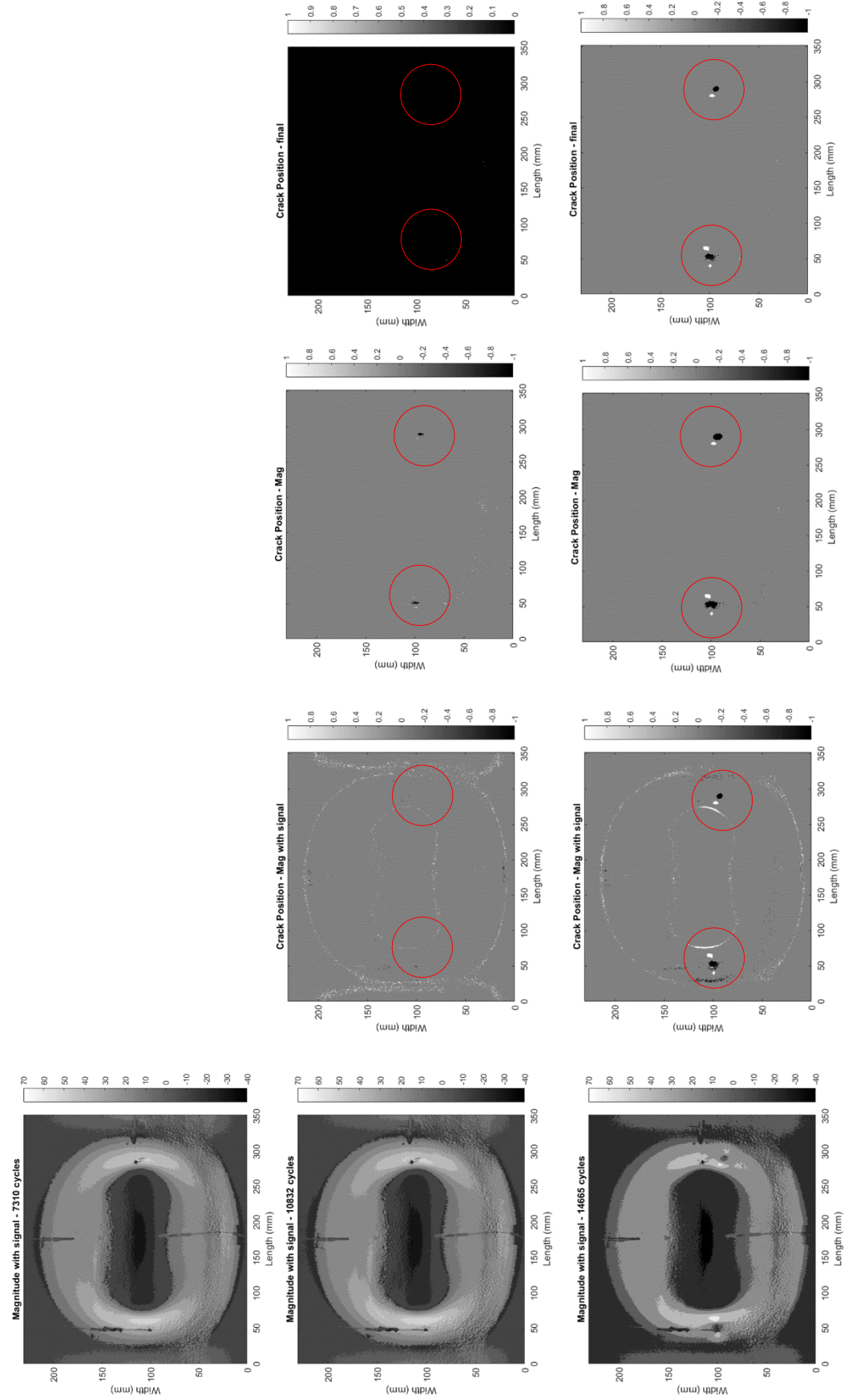


Figure 5.44: Dent 7 TSA crack monitoring.

Analyzing the results from the TSA crack monitoring above, the tensile areas are represented by white color while the areas under compression by black. At the same time, the stress relief caused by the nucleation of a crack is much easier noticeable than the crack tips for similar cycles.

5.5

Fatigue life estimation

This section uses the fatigue strength estimations, which were presented in Chapter 4, to assess the fatigue behavior of the tested dented specimens.

Initially, based on the experience of the literature, stress-life methodologies were adopted to evaluate the behavior of dented specimens, being measured the material fatigue limit and SN curves for different load ratios. The results obtained from the dents mechanical behavior assessment shown that the specimens were subjected to high levels of strain, which would suggest the use of the strain-life fatigue approach.

Although not as accurate for this application, the SN method is still a good analysis methodology due to its conservatism. Hence, because of the high strains, a more robust approach was required to correctly evaluate the hot spot of the dented regions. As a consequence, the Coffin-Manson strain-life methodology was employed. When necessary, due to different pressure ranges applied during a test (case of specimen Dent 3), the Miner's fatigue damage rule was also employed, as presented in section 5.5.6.

5.5.1

API-579 Part 12 and PDAM Approaches

Both the API-579 Part 12 and the PDAM approaches are based on the dent depth and on the pipe geometry (diameter and thickness). The influence of the dent is taken into account by assigning a stress concentration value. Although relatively similar, these approaches differ in their level of conservatism, being the API-579 Part 12 a little more conservative. Table 12 presents the minimum and maximum pressures, the calculated alternate stress used in both methods and the ratio H/D for each dented specimen.

Figures 5.45 and 5.46 show the API-579 Part 12 and the PDAM fatigue curves for both studied dent geometries, plain longitudinal dent ($H/D=0.15$) and humped

dent ($H/D=0.06$), plotted against the measured real life (number of cycles to loss of containment).

Table 12: Minimum and maximum pressures, the calculated alternate stress used in both methods and the ratio H/D for each dented specimen.

Dented Specimen	P_{\min} (MPa)	P_{\max} (MPa)	σ_a (MPa)	H/D
1	0.4	4.4	51.0	0.12^{19}
2	0.3	6.3	76.5	0.06
3 ²⁰	-	-	-	-
4	0.2	4.2	51.0	0.06
5	0.2	3.2	38.3	0.15
6	0.2	6.2	76.5	0.16
7	2.2	6.2	51.0	0.15
8	3.3	6.3	38.3	0.16
9	0.2	4.2	51.0	0.15

The analyses took as reference the ratio of the dent depth by the pipe specimen diameter (H/D). The level of conservatism increases from left to right, although both approaches provide conservative approaches to the fatigue life of the tested specimens.

¹⁹ Specimen Dent 1 was analyzed considering the interval $H/D = 0.15$.

²⁰ Specimen Dent 3 data was analyzed separately, due to the need of application of Miner's fatigue damage rule to evaluate the different loads that the specimen was subjected to.

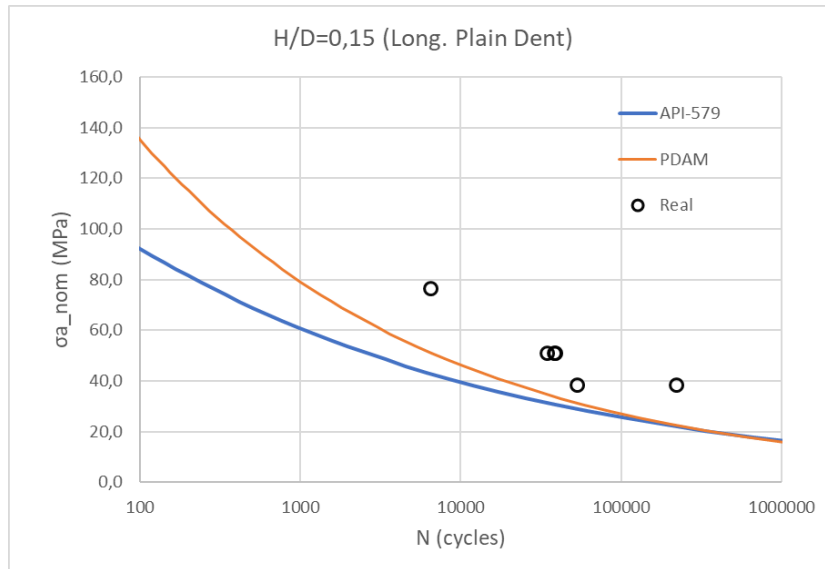


Figure 5.45: API-579 Part 12 and PDAM fatigue curves for the longitudinal plain dent geometry plotted against the measured life of the specimens.

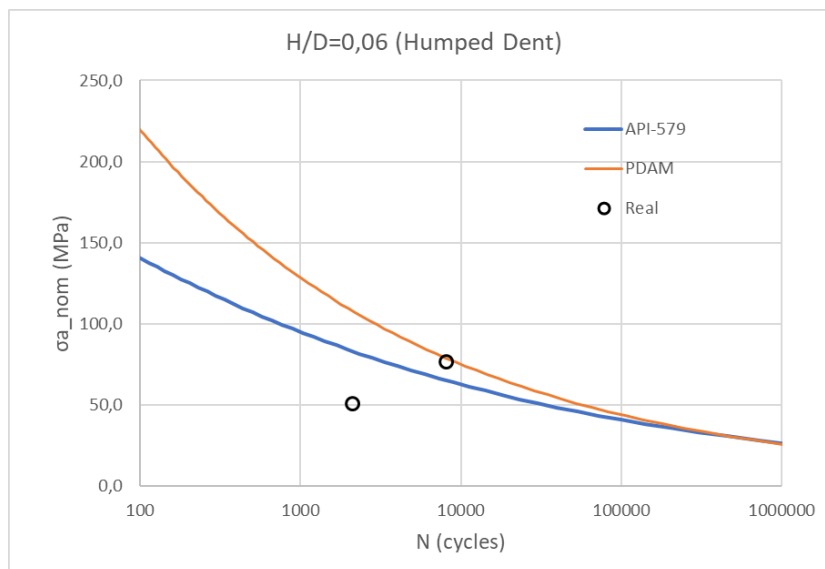


Figure 5.46: API-579 and PDAM fatigue curves for the humped dent geometry plotted against the measured life of the specimens.

5.5.2 Mean Stress Approach

The Mean Stress approach uses the results determined for each specimen using the second type of FEM coupled with a Gerber curve to evaluate the effect of the mean stress in the fatigue life. The used values of the true ultimate strength (S_u) and fatigue (S_L) were obtained from Chapter 3, being equal to 500 and 245 MPa, respectively. The finishing ($k_a=0.85$), size ($k_b=1$) and load ($k_c=1$) factors were obtained using Castro et al. [126], and the elastic stress concentration factors from the FE analysis of dents that were presented in Tables 10 and 13.

In the fatigue curves, for the plain dent specimen's analysis it was used an average stress concentration factor equal to 8.9, and for the humped dent analysis it was used 12.6. Table 13 show the nominal stresses obtain with the linear elastic FEM employed in this analysis.

Figures 5.47 and 5.48 show the Mean Stress fatigue curves for both studied dent geometries, several values of mean stress were studied in order to evaluate its influence.

Table 13: Stresses used in the fatigue analysis.

Dented Specimen	$\sigma_{a_{nominal}}$	$\sigma_{m_{nominal}}$	S_N^{21}	$K_{\sigma VM}$ (from FEM results of Table 10)
1	51.0	61.2	51.8	8.50
2	76.5	84.15	78.7	7.43
3 ²²	-	-	-	-
4	51.0	56.1	51.7	18.33
5	38.3	43.4	38.5	9.03
6	76.5	81.6	78.6	9.04
7	51.0	107.1	53.5	8.95
8	38.3	122.4	40.7	8.22
9	51.0	56.1	51.7	9.63

²¹ It was used the Gerber parabola in this calculation ($m=2$).

²² The values of specimen Dent 3 are not shown here because a more specific analysis will be presented later in section 5.5.6.

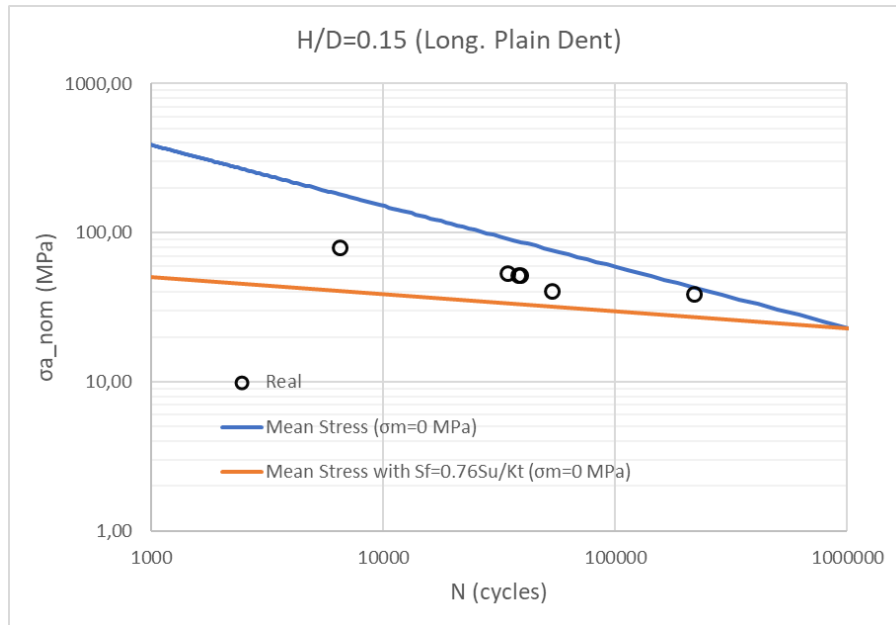


Figure 5.47: Mean Stress fatigue curves for the longitudinal plain dent geometry plotted against the measured life of the specimens.

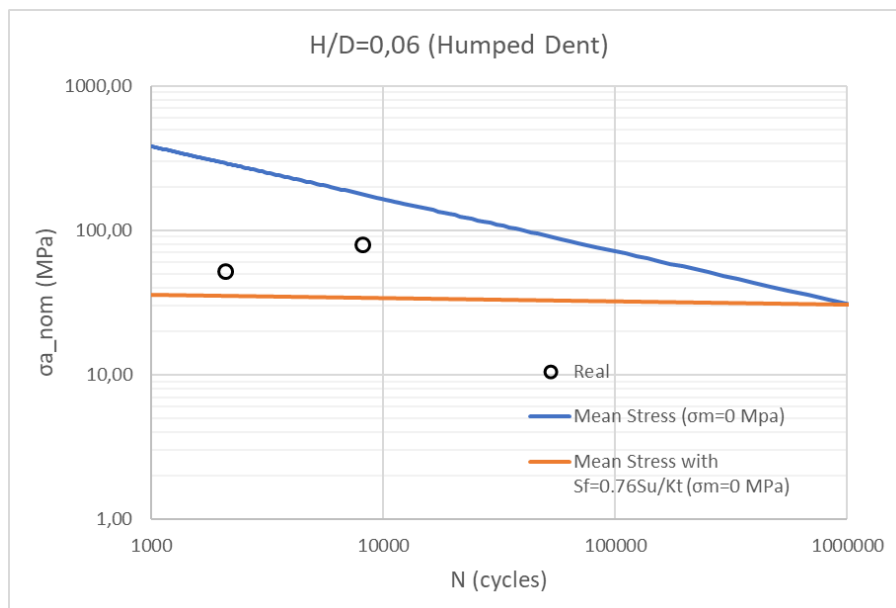


Figure 5.48: Mean Stress fatigue curves for the humped dent geometry plotted against the measured life of the specimens.

The Mean Stress approach provides a non-conservative set of results considering the curve with S_f without the influence of K_t . Otherwise, considering the curve with S_f influenced by the K_t the results are conservatives.

Figures 5.49 and 5.50, below, compares all SN fatigue methodologies for the analyzed dent defects. It becomes clear that the API-579 standard and the PDAM provide conservative and safe predictions, while the Mean Stress method depending on how S_f is calculated can provide conservative or non-conservative predictions.

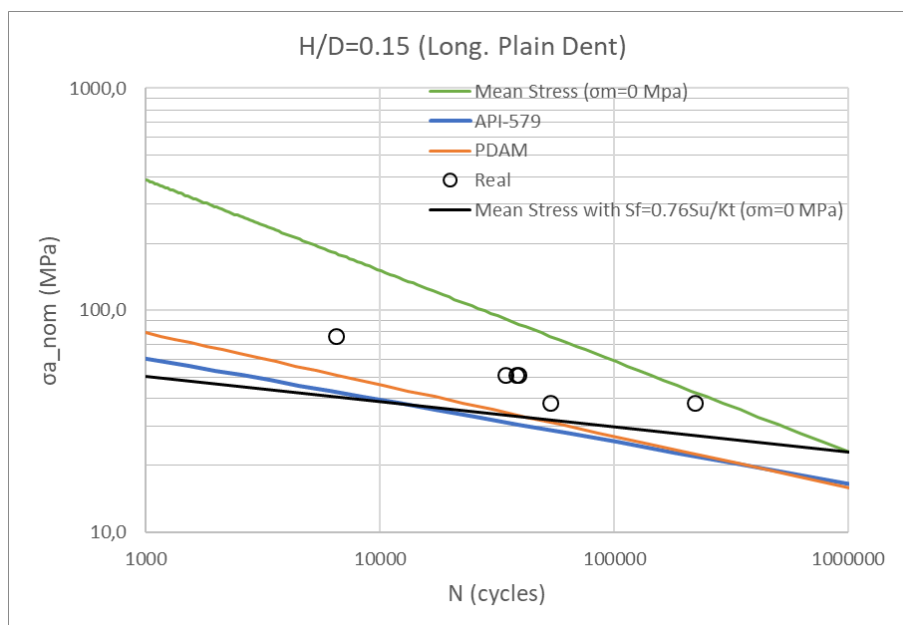


Figure 5.49: Comparison of the SN approaches for the longitudinal plain dent.

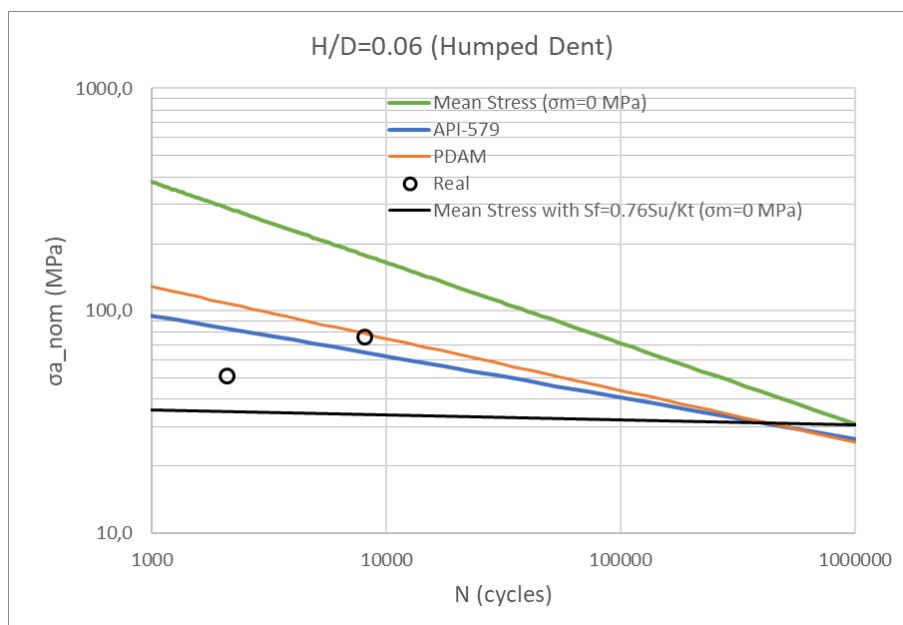


Figure 5.50: Comparison of the SN approaches for the longitudinal plain dent geometry.

5.5.3 Strain-Life (Coffin- Manson) Approaches

Switching from the SN to the ϵN approach, results presented in Figure 5.51 show a good agreement when the plotted points are compared with the curve that takes in consideration the mean stress equal to zero. In fact, it is not possible, at the present stage, to consider reliable and accurate values of the mean stress actuating in each hot spot of each specimen. Two sets of variables can be used to explain this impossibility. One set is related to the imposed mean stress or strain that are known or, at least, may be rationally guessed. Another set is related to the absence of knowledge of some key variables.

The first set includes: the knowledge of the mean imposed pressure and so the mean imposed nominal stress; the resulting mean strain per cycle that can be evaluated under elastic or elastic-plastic conditions; the total mean strain imposed to each hot spot that was not fully recorded but could be guessed from the initial DIC (first loading block) and from the near to the hotspots located fiber glass strain gauge (second block), including here the ratcheting behavior.

The second set includes unknown variables: the accumulated strain history behavior of strains induced in the hot spots due to steel plate fabrication, pipe fabrication, dent indentation and dent rerounding and, moreover, the resulting residual stress state induced by all those loading steps that anteceded the fatigue tests. Figures 5.10, 5.11, 5.12, 5.13 and 5.14 show examples of the stress-strain and pressure-strain behavior and residual stresses actuating in the hot spots caused by the indentation and dent rerounding phases. While these phases were simulated numerically and presented in those Figures, the plate and pipe fabrication phases were not considered in the numerical analyses. Moreover, Figures 5.10 (Dent 3 and Dent 6) shows that the mean stress actuating in the hot spots resulted to be near zero. Therefore, at the present stage, the agreement of the plotted points with the zero mean stress curve may be considered not being a surprise. Of course, for conservativeness to be used in design predictions, the use of a reasonably positive value of mean stress would be justifiable. This value could be, for example, the conservative mean stress value caused by the cyclic pressure loading and calculated from the nominal circumferential mean stress multiplied by the elastic-stress

concentration factor; or by the yield strength of the material, whichever stress value would be the minimum resulting from these calculations.

Table 14 presents the strains simulated with FEM and calculated with the two analytical methods for strain estimation used in the strain approaches.

Table 14: Strains used in the fatigue analysis.

Dented Specimen	ΔP (MPa)	FE ²³ $\Delta \epsilon$ ($\mu\epsilon$)	FE ϵ_a ($\mu\epsilon$)	$\Delta \epsilon$ Alternative Method 1 ($\mu\epsilon$)	ϵ_a Alternative Method 1 ($\mu\epsilon$)	$\Delta \epsilon$ Alternative Method 2 ($\mu\epsilon$)	ϵ_a Alternative Method 2 ($\mu\epsilon$)
1	4	4205	2102	8015	4007	5458	2729
2	6	5525	2762	12647	6324	9423	4712
3 ²⁴	-	-	-	-	-	-	-
4	4	8692	4346	27338	13669	23323	11661
5	3	3262	1631	5313	2656	3838	1919
6	6	6751	3375	17747	8873	14070	7035
7	4	4416	2208	8690	4345	6020	3010
8	3	3028	1514	4726	2363	3562	1781
9	4	4760	2380	9852	4926	6998	3499

Figure 5.51 plots the Coffin-Manson method for different mean stress levels and the results for the three different methodologies (Table 14) for estimating strain (discussed in section 4.1.4) the horizontal axis coordinates are given by the actual measured fatigue life of each specimens. These methodologies aside de dent geometry shape and considering only the strain magnitude that each dent causes. In this analysis the data called “Real” uses the actual number of cycles to failure plotted against the strain simulated with FEM, which is very similar to the experimental strains measured by DIC.

²³ The strain results came from the linear elastic FEM (second type of FE model).

²⁴ The values of specimen Dent 3 are not shown here because a more specific analysis will be presented later in section 5.5.6.

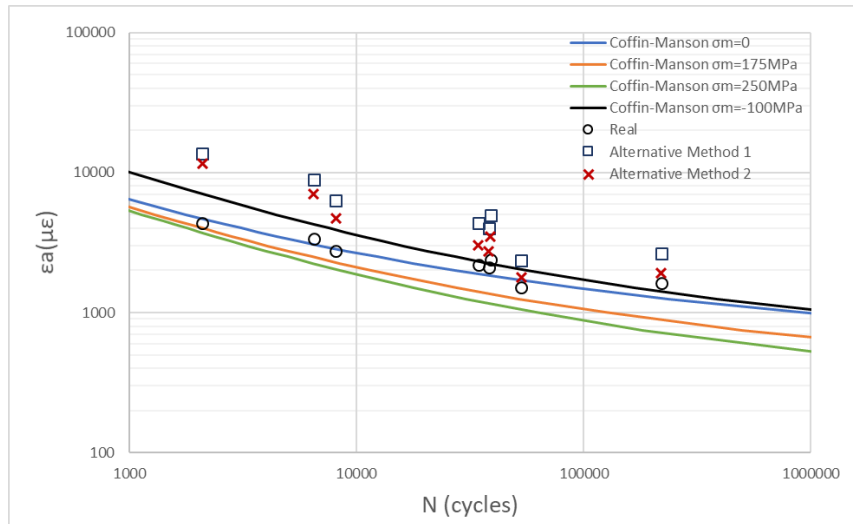


Figure 5.51: Coffin-Manson fatigue curves all dent geometries plotted against the measured life of the specimens.

An overall better agreement between measured fatigue life and the estimated results was obtained with the Coffin-Manson method without mean stress ($\sigma_m=0$), showing the efficiency of the methodology when applied to specimens subjected to large deformations.

The results obtained using the two alternative analytical methods were also satisfactory. Besides being a little more conservative, they estimate the total strain levels in a simpler manner to be coupled to a strain-life curve to be adopted by the user to determine the number of cycles to failure.

5.5.4

API-579 Part 14 or ASME Sec VIII div. 2 Part 5 Approaches

Figure 5.52 compares the similarity between the best-fit curve for carbon steel presented by the ASME Sec VIII div. 2 Part 5 [79], obtained with Eq. (69), with two Coffin-Manson curves, obtained with Eq. (50), one that uses the same parameters of the ASME standard [129] ($S_u=551$ MPa, $\epsilon_{cf}=1.16$ and $E=200$ GPa) and the Coffin-Manson without mean stress curve presented in Figure 5.51 ($S_u=500$ MPa, $\epsilon_{cf}=0.36$ and $E=182$ GPa), that was proposed based on the specimens material properties.

It can be seen that the SN curve proposed by the ASME standard [79] (blue curve) can be approximated without any major problem by a Coffin-Manson curve with the same parameters (green curve).

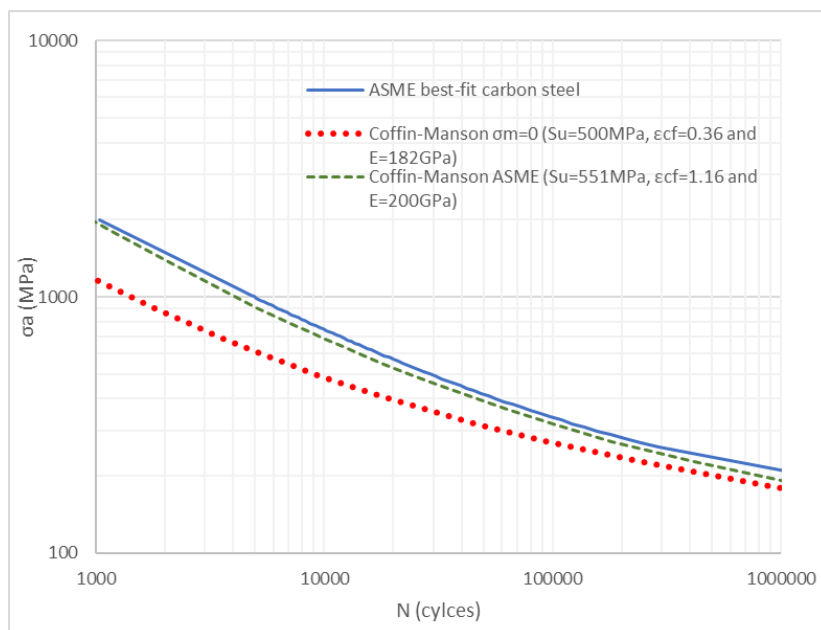


Figure 5.52: Comparison between the ASME SN carbon steel best-fit curve with an ϵN approach.

Figure 5.53 show the results of the analysis using the API 579-1/ASME FFS-1 - 2016 Part 14 methods A and B [66]. These methods were presented in section 4.1.5.

Table 15 presents the alternate stress calculated with the two methods present in the API 579-1/ASME FFS-1 - 2016 Part 14 and the elastic stress calculated using the material Young modulus (182 GPa) and the strain results from the linear elastic the second type of FEM.

Table 15: Alternate stress calculate with API 579-1/ASME FFS-1 - 2016 Part 14 and with FEM.

Dent	σ_a (MPa)			N (cycles)		
	API-579 Part 14 L2 Method A	API-579 Part 14 L2 Method B	Real (FEM)	API-579 Part 14 L2 Method A	API-579 Part 14 L2 Method B	Real (FEM)
1	374	374	396	70702	70702	38300
2	1844	551	524	1241	22051	8120
3	-	-	-	-	-	-
4	4017	828	935	238	7725	2100
5	322	322	308	119370	119370	220000
6	512	512	656	27061	27061	6500
7	444	444	414	41001	41001	34400
8	302	302	281	152591	152591	53300
9	481	481	448	32244	32244	38900

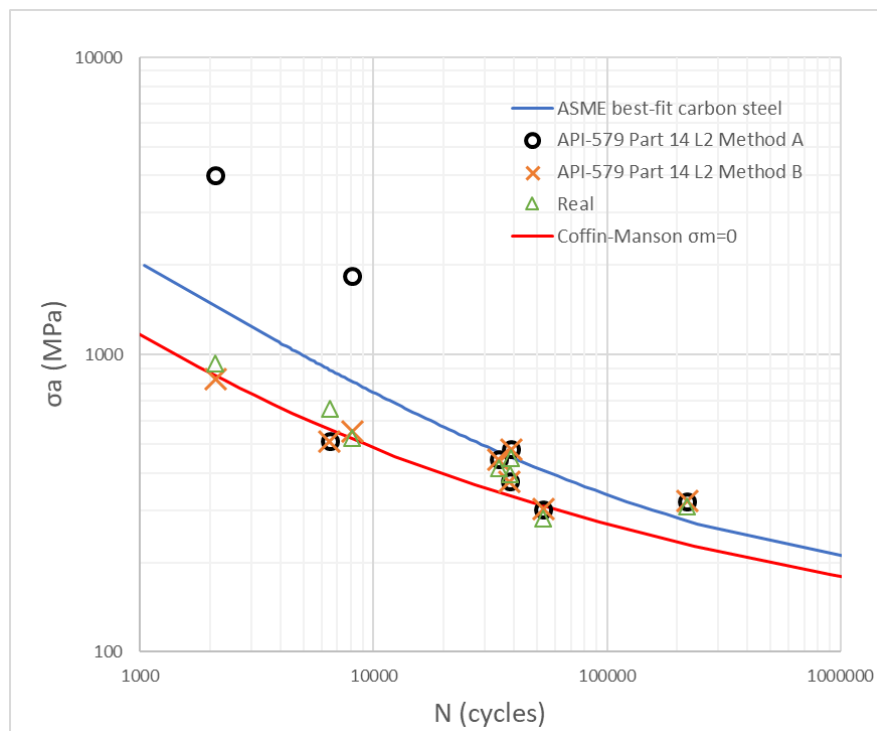


Figure 5.53: Coffin-Manson and the ASME fatigue curves plotted against the estimated life using the API 579-1/ASME FFS-1 - 2016 Part 14 methods A and B [66].

The API 579-1/ASME FFS-1 - 2016 Part 14 methods used in its calculation the results from the second type of finite element models, which provide an elastic approach. Thus, to use method B it was necessary to hypothesize that all strains could be considered linear elastic and the plastic portions could be considered equal to zero. This assumption is corroborated based on the behavior shown by Figures 5.23 and 5.24. Therefore, with the exception of the results of specimens Dent 2 and Dent 4, both with hump, both methods A and B provide the same results because of the absence of a plastic strains²⁵.

A more detailed analysis of the procedure used in this section will be presented in Appendix F.

²⁵ The ASME best-fit it is not a design-oriented curve so it does not have a built-in safety factor. The design-oriented standard curve has a safety factor equal to 2 in the stress portion and equal to 20 in the life, Eq. (69).

Figure 5.54 analyses only Dent 6 specimen, using the results from the first type of finite element model (elastic-plastic) and the results from the second type of model (linear elastic). The life estimated by the Method B of the first type of model is very similar to the actual life of the specimen.

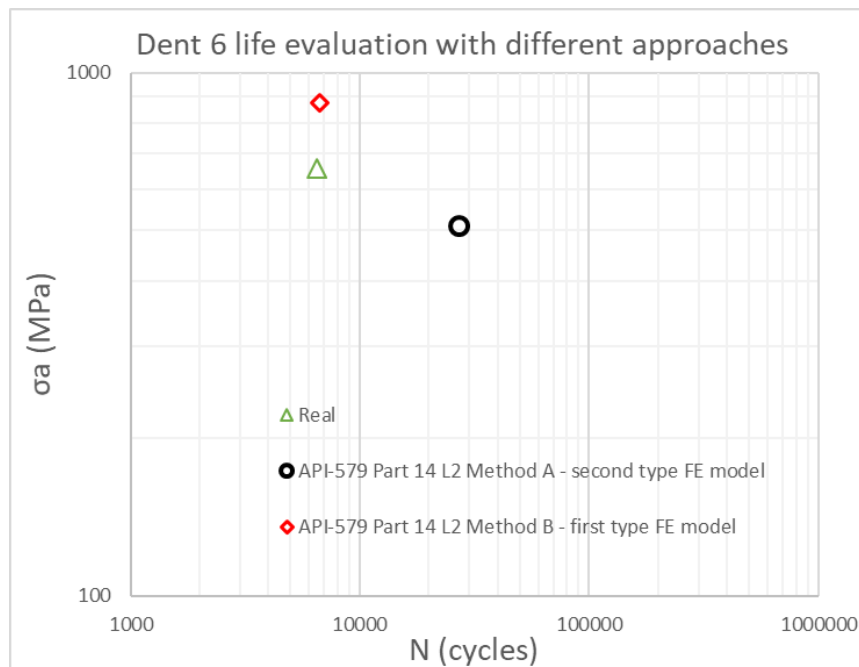


Figure 5.54: Dent 6 specimen results applying API 579-1/ASME FFS-1 - 2016 Part 14 [66] and different finite element models.

5.5.5 Comparison Between All Approaches

Figure 5.55 compares all methodologies, including the equation PDAM_95 [73], which considers an uncertainty factor corresponding to a 95% tail interval. The data were plotted considering the predictions for each specimen made with each approach and the real fatigue life determined in the tests. The 45° line represents best the estimation. The other two parallel lines represent the actual test determined lives a multiplied or divided by 10.

Table 16 presents the data points formed by the estimated life and the actual life of the specimens using all methodologies.

Table 16: Estimated life and the actual life of the specimens.

Dent	API-579 Part 12	PDAM	PDAM_95	Mean Stress	Coffin-Manson	Mean Stress	API-579 Part 14 Method A	API-579 Part 14 Method B	Actual
1	4681	10162	764	69265	22688	138276	70702	70702	38300
2	3662	10002	752	13714	8984	76740	1241	22051	8120
3	-	-	-	-	-	-	-	-	-
4	25200	43666	3285	7881	2516	245033	238	7725	2100
5	11864	22159	1667	49774	63496	285076	119370	119370	220000
6	264	1083	81	39529	4954	49735	27061	27061	6500
7	2249	5255	395	105013	18988	128224	41001	41001	34400
8	8668	14674	1104	183650	89312	250932	152591	152591	53300
9	2856	7034	529	45817	14601	139461	32244	32244	38900

The Coffin-Manson results presented the best agreement with the 45° line. As expected, PDAM_95 equation presented the most conservative results followed by the API-579 Part 12 and the PDAM equations. In the figure conservatism increases from the bottom up. The results of the API-579 Part 14 were close to the Coffin-Manson results.

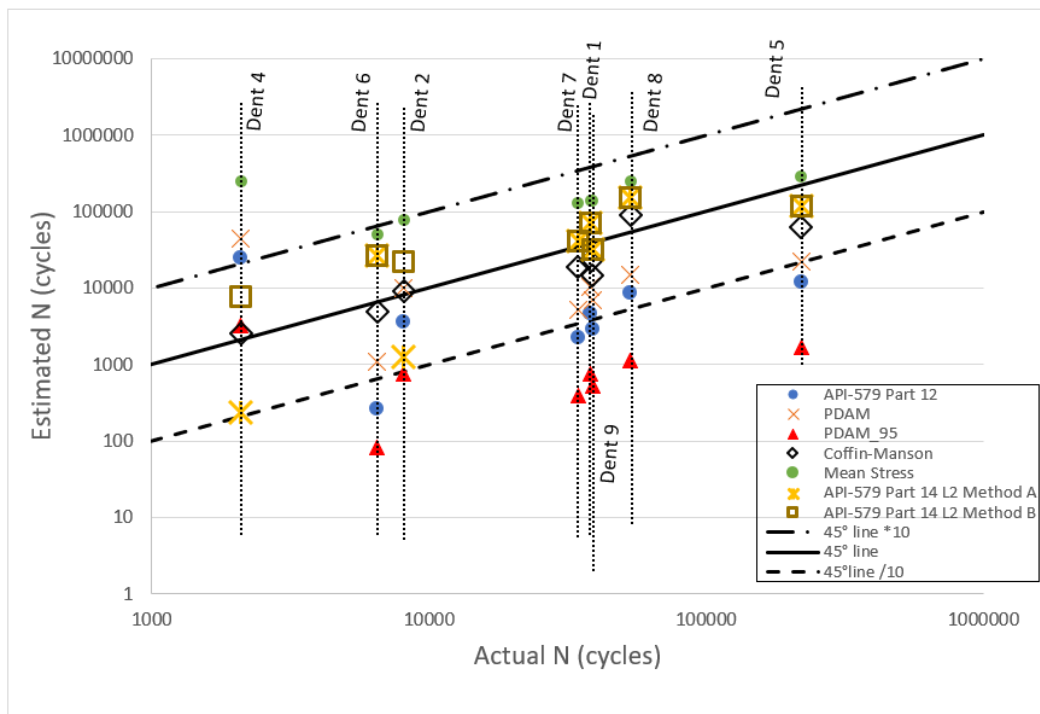


Figure 5.55: Comparison of all methodologies results with the actual fatigue life.

5.5.6 Dent 3 Fatigue Assessment

Specimen Dent 3 was analyzed separately because its range-variable pressure-loading history given in Figure 5.15a and in Table 17.

Strains presented in Figure 5.55 were associated with the applied pressure using the curve from interpolated DIC results for the last cycle of the first block of pressurization, presented in Figure 5.23. Using this relationship, the fatigue damage evolution was calculated and results are presented in Figure 5.56. In this case, total damage (up to initial leakage) was calculated to be 0.93. A different result is determined if the circumferential strain is associated to the applied pressure using the FE coupling curve (in this case a straight line) given in Figure 5.22.

Table 17: Specimen Dent 3 pressure-loading history.

Time interval (cycles)	Pressure Range (MPa)	Time interval (cycles)	Pressure Range (MPa)	Time interval (cycles)	Pressure Range (MPa)
1-138	2.00-2.25	2957-3242	1.00-3.25	18947-18988	0.75-1.50
139-281	1.75-2.50	3243-3290	0.75-1.00	18989-19198	0.75-1.75
282-491	1.50-2.50	3291-3573	0.00-0.00	19199-19388	0.75-2.00
492-1001	1.25-2.50	3574-3642	0.75-1.00	19389-19540	1.00-2.25
1002-1090	1.00-2.75	3643-3765	0.00-0.00	19541-19764	1.25-2.50
1091-1776	0.75-3.00	3766-3900	0.75-1.00	19765-19865	1.00-2.75
1777-2328	0.75-3.25	3901-4432	0.00-0.00	19866-19874	0.75-3.00
2329-2404	2.00-2.25	4433-7060	0.75-1.00	19875-20023	0.75-3.25
2405-2537	1.75-2.50	7061-8764	0.50-1.00	20024-20042	0.75-3.50
2538-2709	1.50-2.75	8765-18798	0.50-1.25	20043-20079	0.75-3.75
2710-2956	1.25-3.00	18799-18946	0.50-1.50	20080-21387	0.75-3.5

Figure 5.57 presents the damage evolution calculated using this relationship. Although the shape of Figures 5.57 and 5.58 are similar, total damage at leakage is found to be 1.29 if the FE pressure-strain curve is used. Considering all the uncertainties associate with fatigue calculations these two results can be considered satisfactory once both are relatively close to unity.

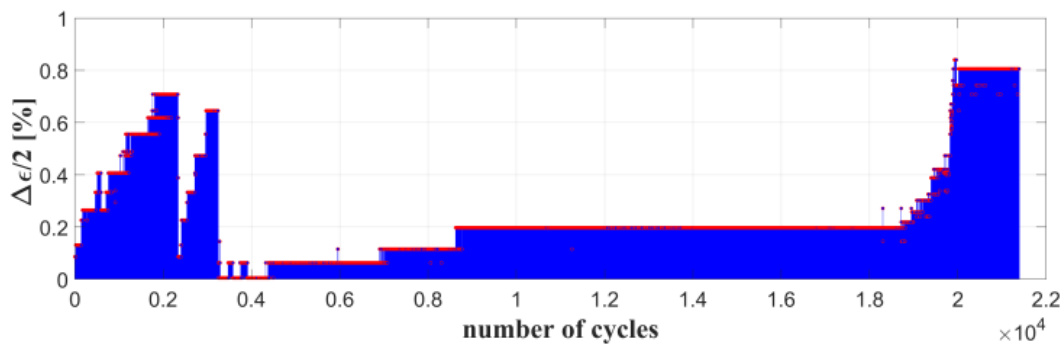


Figure 5.56: Circumferential strain amplitudes calculated from the relationship between pressure and strain given by the DIC curve of Figure 5.23.

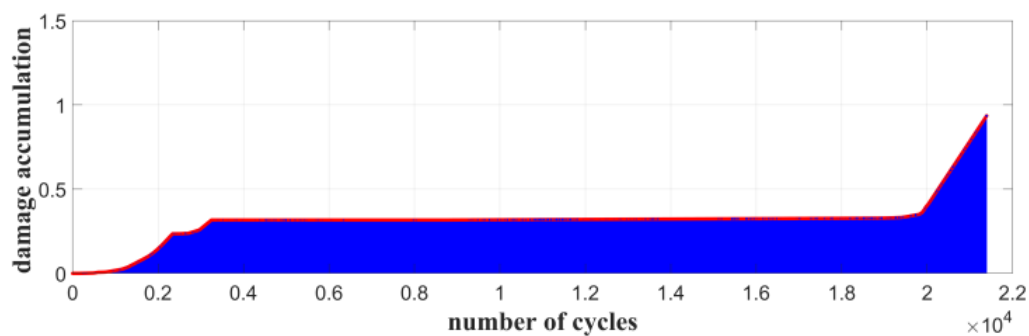


Figure 5.57: Fatigue damage accumulation calculated from strain-cycle history presented in Figure 5.55.

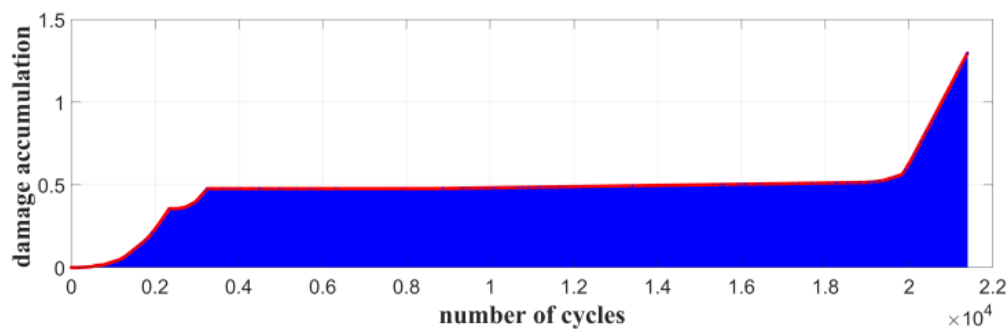


Figure 5.58: Fatigue damage accumulation calculated from strain-cycle history determined from the relation between applied pressure and strains calculated from finite elements given in Figure 5.22.

6. Conclusions and Future Work

6.1 Conclusions

This thesis used modern experimental techniques with emphasis on IR thermography to assess the fatigue behavior and the structural integrity of real scale specimens with complex shaped anomalies. The specimens were 3m long and had 323 mm external diameter and 6.35 mm wall thickness. They were made of pipeline tubes API 5L Gr. B and containing dent defects. Overall, this thesis can be divided into two parts. The first one consists of an investigation about the characteristics and behavior of the employed test material. The second part is a broad study about pipelines containing dents that are subjected to cyclic internal pressure loads. The final objective is to assess the fatigue resistance of pipelines with dents by using a combination of analytical, experimental and numerical methods.

6.1.1 Material Behavior

In order to fully understand the material behavior, a series of static and dynamic tests were performed.

6.1.1.1 Uniaxial Fatigue Behavior

Dog bone specimens were monotonic and cyclic tested under uniaxial loading conditions. Thermographic fatigue strength estimation methods were employed to analyze the temperature increase on the external surface during load application, identifying the transition from a conservative to a non-damaging state of energy to a dissipative and damaging one.

During the cyclic tests the temperature underwent a significant increase when it was submitted to elevated stress levels, above the fatigue limit. Plotting the stabilized temperatures against their corresponding stress amplitude levels it was possible to determine the fatigue limit for R several load ratios. Furthermore, because of the stress gradient present in a dog bone specimen geometry, all stress levels above the fatigue limit of the cyclic tests were analyzed as individual tests using only one specimen. This method was named the “ultra-rapid method”. The obtained results were very similar to those measured with the cyclic (rapid) methodology.

A couple of specimens were also tested using the so-called quasi-static approach, which results are related with the material’s fully alternate fatigue strength. Each uniaxial dog bone specimen was subjected to different levels of incremental deformation to evaluate the influence of plastic deformation in the fatigue limit. Similar results were found, regardless of the accumulated strain.

From the results obtained with the different IR methodologies and different load ratios it was possible to acquire a relationship between data points formed by pairs of alternate stress amplitude and mean stress values, verifying the influence of the mean stress on the material’s fatigue strength. The data was adjusted by a parabolic fitting equation presented in Eq. (18), the adjusting exponent m being equal to 1.4 and n equal to 1. These exponents fall between the exponents expected given by the Goodman and Gerber curves, respectively 1 and 1 and 1 and 2.0.

Moreover, having determined the values of a parameter ϕ for all the specimens that were cyclic tested, the SN fatigue curves were determined for each stress ratio R and compared with the SN curve determined from push-pull traditional tests. The estimated SN curves encompass data fitted to the interval 10^3 to 10^6 cycles.

6.1.1.2 TSA Calibration Constant

In the process of investigating the material behavior, it was also performed a TSA gain calibration to correlate the elastic cyclic stress range with the measured temperature variation induced by cyclic deformations. A linear calibration

relationship between the camera response, S^* , and the measured stress range was obtained through using uniaxial tensile specimens of low carbon steel, Eq. (19).

6.1.2 Fatigue Dent Assessment

The fatigue assessment of the dented specimen started with the definition of its final geometry; it was chosen the one with longitudinal shape without gouge, known as plain longitudinal dent. The next step was the creation of real size specimens through a process that consisted of five consecutive steps, starting with indentation, dent rerounding, and fatigue tests at predefined loading pressure ranges.

6.1.2.1 Shapes of the Dents

Although under very similar pos-indentation shapes and rerounding test conditions, some dents presented small variations in its depth and other suffered snap-thru buckling in the dent region, presenting humped shapes at its center portion. These results were confirmed by the numerical simulation that was able to reproduce the snap-thru buckling. Because of the slender geometry of the dented specimens, they can be defined as thin walled shell structures, prone to snap thru buckling as a result.

After snap thru occurred for some specimens at pressures lower than the one initially defined, the rerounding pressure was reduced to a safer level to maintain the desired smooth dent geometry for the majority of the tested specimens.

6.1.2.2 Finite Element Modeling

The dented specimens were subjected to cyclic internal pressure ranges to simulate as close as possible to the actual field operation conditions. Preliminary

pressure cycles, around two to three cycles, were executed in order to study the behavior of the dented region using different assessment techniques.

Two distinct types of FE models were developed to analyze the influence of dent shapes, and consequently of the generated dent stresses and strains in the dent fatigue behavior. The first FE modelling type aimed to simulate the hole process of creating the dents, from the pipe positioning in the press machine to the first cycles of cyclic pressure loading, considering the geometric, material and contact nonlinearities. The second type of FE model focussed only on the pipeline cyclic operation loading. It used the “exact” dent shape measured by the DIC technique to build the model geometry and only employed a linear elastic material behavior.

Good qualitative agreement between the results from the first type of numerical model and the experimental results were obtained, although some small deviations between the simulated and measured shape were observed. The deviations are credited to natural sources of testing uncertainty conditions as well as to the difference between the real material and the inputted material behavior, which is representative of the average measure stress-strain curve.

6.1.2.3

3-DIC technique and Stress/Strain Concentrations at the Dent Regions

Both types of FE element model identified the stress concentration positions in both worked dent geometries (smooth and snap-thru).

The 3D-DIC technique applied to the first loading cycles for all tested specimens provided the exact dent shapes used in second type of FE models. The DIC measured shapes accurately reproduced the actual shape of the samples, which was corroborated by measurements using the caliper. Besides that, among the variety of data that the DIC can provide, the circumferential strain may be one of the most relevant, being representative of the general behavior of the specimens.

The regions of stress concentration or hot spots were easily identified by the DIC technique. They were located at the hump regions and at the edges of the plain dents, those hotspots being the potential places for the development of fatigue cracks. In the present cases, for a given pressure loading, the maximum strains at

the hot spots of humped dents are much higher than those that occur at the hot spots of the specimens with plain dents.

The highest stress concentration was located on the outer surface of the specimens for both types of geometry, and fatigue cracking started from the outside surfaces. This conclusion was corroborated from the test results.

6.1.2.4

Comparison of Numerical and Experimental DIC and FBSG Results

The results of displacements and strains of the second type of FE model compared with the DIC and FBSG at the critical points presented very similar values. The FBSGs were used as a monitoring tool during the pressurization, providing information about the condition of the specimens along the realization of the tests.

6.1.2.5

TSA Monitoring and Results

The TSA technique was applied to determine and evaluate hot-spots, their importance in terms of stress ranges, crack initiation detection, assessment and monitor of crack propagation.

At the locations of stress concentration and when compared with other techniques, such as FE and DIC, it should be emphasized that some plasticity is occurring, and therefore the TSA results obtained at these locations must be interpreted as linear qualitative results.

TSA response shown that initiation and evolution of fatigue cracks were accompanied by a local stress relief, which were perceived as a decrease in the stress levels when compared to earlier stages. Initial and fatigue growth cracks could be identified. A crack initiated in the specimen could be identified by the stress concentration originated at its tips.

An analysis tool was developed, based on comparing TSA images obtained at different times, to monitor the initiation and growth of fatigue cracks. Changes in the pattern of stress distributions were identified to predict the location of a crack, which in some cases was not possible by simply analyzing the TSA signal.

Fatigue initiation in the dented specimens was also evaluated using the IR quasi-static methodology for the fatigue limit measurement. Predetermined specific positions were evaluated with the focus not on determining the fatigue limit itself, but focusing to know which positions reached this limit before the others, in other words, which were the most critical positions at which a crack would develop.

The stress concentration spots proved to be the most critical, being located at the hump and in the edges for the dent formats. The measured fatigue limit values for different positions at the dented specimens were extremely similar to those measured using dog bone specimen during the uniaxial tensile tests.

6.1.3 Fatigue Life Predictions

The fatigue life prediction methodologies available in the literature based on the SN and ϵ N criteria were used to estimate the fatigue life of the dented specimens. A certain level of conservatism was observed in each one of the methodologies used. The Coffin-Manson criterion with zero mean stress presented the best agreement with the real measured life, while the PDAM_95 shown the most conservative results followed by the API-579 Part 12 and PDAM predictions. The methodology proposed by the API-579 Part 14 Level 2 was seen to provide a reasonable alternative to predict fatigue life of specimens.

6.1.5 Final Comments

This work confirms that rapid fatigue damage assessment methods are practical and efficient tools that can provide a reliable, non-destructive and faster way to determine the fatigue behavior of materials using few specimens. More specifically, the results furnished fatigue data for the API 5L Gr. B steel. Moreover, the influence of the stress ratio R was evaluated for this material and an equation

showing the influence of the mean applied stress on the fatigue limit was given, which can be useful for design purpose.

The entire methodology for evaluating the fatigue is based on identifying, through the analysis of the temperature variation, the transition from a stage where the applied load does not induce damage and when it does. The dispersion between properties measured by traditional techniques and those by IR is generally around 15%.

The obtained results were, in some cases, compared with FEM simulations, DIC strain fields and FBSG measurements to corroborate the findings, showing good agreement between them.

The TSA technique, using relatively low cost IR camera and software, can also be used to determine hot-spots, their importance, measure fatigue crack initiation, and monitor its propagation. The present findings can be applied to other structures that may present dents such as tanks and pressure vessels.

6.2 Recommendation for Future Works

For future work better results, like a more precise shape, could be obtained through the refinement of numerical models. A stress-strain curve whose ratcheting effect was considered could be used. Instead of using the material average curve, the actual specimen curve would make the simulation as close as possible to reality. Another improvement could be the sensitivity of the specimen to snap thru, in this case a broad study is required on how the various factors, such as: geometry, loading, material, act in concurrence for occurrence of the buckling.

The analysis of temperature data could be improved by its automation, instead of each test depending on a individual interpretation a series of criteria could be established in conjunction with mathematical algorithms to standardize the results.

The TSA compare algorithm used to detect early development of fatigue cracks could be upgraded to analyze multiple photos together providing a larger number of results. Furthermore, a number of mathematical functions could also be used to improve the comparison methodology.

New developments in the thermocamera technology made it possible for cheaper models to emerge, one of these models is the FLIR Lepton 3.5. The quality of the results is proportional to the investment in the sensor, the low cost affordable approach yields useful results and offers the potential for TSA to be used in structural health monitoring.

7. References

1. Duga, J.J., Fisher, W.H., Buxbaum, R.W., Rosenfield, A.R., Burh, A.R., Honton, E.J., and McMillan, S.C. (1983) The Economic Effects of Fracture in the United States. NBS Special Publication 647-2, U.S. Department of Commerce, Washington, DC.
2. Sirca, G.F.; Adeli, H. (2018) Infrared thermography for detecting defects in concrete structures. *J. Civ. Eng. Manag.* Vol 24, pp508–515.
3. N.P. Avdelidis, B.C. Hawtin, D.P. Almond (2003) Transient thermography in the assessment of defects of aircraft composites, *NDT & E International*, Volume 36, Issue 6.
4. N Rajic, Principal component thermography for flaw contrast enhancement and flaw depth characterization in composite structures (2002), *Composite Structures*, Volume 58, Issue 4, pp521-528.
5. T. Sakagami, T. Komiyama (1998) Thermographic nondestructive testing for concrete structures, *Journal of JSNDI* 47-10, pp723–727.
6. T. Sakagami, S. Kubo (1999) Development of a new crack identification method based on singular current field using differential thermography, *SPIE Proceedings Series 3700* pp369–376.
7. T. Sakagami, S. Kubo, Y. Teshima (1999) Fatigue crack identification using near-tip singular temperature field measured by lock-in thermography, *Proceedings of SPIE - The International Society for Optical Engineering*
8. Sakagami, T., Nishimura, T., Kubo, S. (2005) Development of a self-reference lock-in thermography and its application to crack monitoring. *Proc. SPIE* 5782, pp379–387.
9. Sakagami, T., (2015) Remote nondestructive evaluation technique using infrared thermography for fatigue cracks in steel bridges. *Fatigue & Fracture of Engineering Materials & Structures*, 38, pp755-779.

10. Sakagami, T., Mizokami, Y., Shiozawa, D., Fujimoto, T., Izumi, Y., Hanai, T., Moriyama, A., (2017) Verification of the repair effect for fatigue cracks in members of steel bridges based on thermoelastic stress measurement. *Engineering Fracture Mechanics*, Vol 183, pp1-12.
11. Freire, J. L. F.; (2009) *Engenharia de dutos*. Rio de Janeiro. ABCM.
12. US Department of Transportation (2010) The state of the national pipeline infrastructure.
13. Rosenfeld, M. (2001) Proposed New Guidelines for ASME B31.8 on Assessment of Dents and Mechanical Damage. Topical Report GRI-01/0084. Des Plaines, IL: GRI.
14. Eiber, B. (2001) Report Overview Assessment of the 16 Inch Diameter Olympic Pipeline Integrity, Robert J. Eiber, Consultant Inc.
15. Barenblatt, G. I. Entov, V.M., Salganik, R.L. (1968) On the Influence of Vibrational Heating on the Fracture Propagation in Polymeric Materials, IUTAM Symposium on Thermoelasticity, East Kilbride.
16. Attermo, R., Ostberg, G. (1971) Measurements of the temperature rise ahead a fatigue crack. *Int. J. Fract. Mech.* 7, 122–124.
17. Charles, J.A., Appl, F.J., Francis, J.E. (1975) Using the scanning infrared camera in experimental fatigue studies”, *Experimental Mechanics*, Vol. 15, pp. 133–138.
18. Delorme, J.F., Sinicki, G, P. Gobin (1968) *J. Phys. D: Appl. Phys.* 1 1737.
19. Dengel, D., Harig, H. (1980) *Fatigue Fract. Eng. Mater. Struct.*, 3 113.
20. Kaleta, J., Blotny, R., Harig, H. (1990) *J. Test Eval.*, 19 326.
21. Catalbiano, T., Geraci, A., Orlando, M. (1984) *Il Progettista Industriale*, 2.
22. Geraci, A., La Rosa, G., Risitano, A. (1984) In: CRES Symposium, Catania Italy, ATA Ingegneria Automotoristica, 38, p1-8.
23. Geraci, A., La Rosa, G., Risitano, A. (1992) Influence of frequency and cumulative damage on the determination of fatigue limit of materials using the thermal infrared methodology, *Proceedings of the 15th Polish National Symposium on Experimental Mechanics of Solids*.
24. Curti, G., La Rosa, G., Orlando, M., Risitano, A., In: 14th AIAS Italian National Conference, Catania, Italy, (1986) 211.

25. Curti, G., Geraci, A., Risitano, A. (1989) Un nuovo metodo per la determinazione rapida del limite di fatica, *ATA Ingegneria Automotoristica*.10, 634.
26. La Rosa, G., Risitano, A., (2000) Thermographic methodology for rapid determination of the fatigue limit of materials and mechanical components, *International Journal of Fatigue*, Vol. 22(1), pp. 65-73.
27. Blarasin, A., Fracchia, R., Pozzati, M., (1988) *ATA – Ingegneria Automotoristica*, 51(5) 255.
28. Luong, M. P. (1988) Fatigue limit evaluation of metals using an infrared thermographic technique, *Mech Mater* 28 , pp. 155–163.
29. Luong, M. P. (1992). Infrared thermographic observations of rock failure. In *Comprehensive rock engineering principles* (ed. J. A.Hudson), vol. 4, pp. 715–730. Oxford, UK: Pergamon Press.
30. Luong, M. P., K Dang-Van (1993) Metal fatigue limit using infrared thermography *Atti della fondazione G. Ronchi*, anno IL.
31. Luong, M.P., (1995) Infrared thermographic scanning of fatigue in metals, *Nuclear Engineering and Design*, Vol. 158, pp. 363-376.
32. Fargione, G., Geraci, A., La Rosa, G., Risitano, A., (2002) Rapid determination of the fatigue curve by the thermographic method, *Int. J. Fatigue*, Vol. 24(1), pp. 11–19.
33. Cura, F., Curti, G., Sesana, R., (2005) A new iteration method for the thermographic determination of fatigue limit in steels, *International Journal of Fatigue*, Vol. 27, pp. 453–459.
34. Clienti, C., Fargione, G., La Rosa, G., Risitano, A., Risitano, G. (2010) A first approach to the analysis of fatigue parameters by thermal variations in static tests on plastics. Elsevier.
35. Risitano, A., Risitano, G., Clienti, C. (2010) Fatigue limit by thermal analysis of specimen surface in mono axial traction test. *EDP Sciences*.
36. Risitano, A., Risitano, G., Clienti, C. (2011) Determination of the fatigue limit by semi static tests.” *Convegno Nazionale IGF XXI*, Cassino (FR), Italia.
37. Colombo, C., Vergani, L., Burman, M., (2011) Static and fatigue characterization of new basalt fiber reinforced composites. Elsevier, 2011.

38. Crupi, V., Guglielmino, E., Risitano, G., Tavilla, F. (2015) Experimental analyses of SFRP material under static and fatigue loading by means of thermographic and DIC techniques, Elsevier, 2015.
39. Stanley, P. and Chan, W.K. (1986) SPATE stress studies of plates and rings under in-plane loading”, *Experimental Mechanics*, 26, 360–370.
40. Pitarresi, G., Patterson, E. A. (2003). A review of the general theory of thermoelastic stress analysis. *The Journal of Strain Analysis for Engineering Design*, 38(5), 405–417.
41. Weber, W. (1830) Über die spezifische Wärme fester Körper insbesondere der Metalle, *Ann. Phys . Chem* 96, 177-213.
42. Belgen, M.H. (1967) Structural stress measurements with an infrared radiometer. *ISA Trans.* 6: 49-53.
43. Belgen, M.H. (1967) Infrared Radiometric Stress Instrumentation: Application Range Study, NASA CR-1067.
44. Bakis, C., Yih, H., Stinchcomb, W., Reifsnider, K., (1989) Damage Initiation and Growth in Notched Laminates Under Reversed Cyclic Loading, in *Composite Materials: Fatigue and Fracture, Second Volume*, ed. P. Lagace (West Conshohocken, PA: ASTM International), 66-83.
45. Bakis, C., Simonds, R., Vick, L., Stinchcomb, W., (1990) Matrix Toughness, Long-Term Behavior, and Damage Tolerance of Notched Graphite Fiber-Reinforced Composite Materials, in *Composite Materials: Testing and Design (Ninth Volume)*, ed. S. Garbo, West Conshohocken, PA: ASTM International, pp349-370.
46. Lesniak, J. R., Boyce, B. R. (1995) Differential thermography applied to structural integrity assessment", *Proc. SPIE* 2473, Thermosense XVII: An International Conference on Thermal Sensing and Imaging Diagnostic Applications.
47. Sharpe, W.N. (2008) *Springer Handbook of Experimental Solid Mechanics*; Ed. Springer; 1st edition.
48. Khaja, A. A., & Rowlands, R. E. (2011). TSA Analysis of Vertically-and Incline-loaded Plates containing Neighboring Holes. In *Thermomechanics and Infra-Red Imaging, Volume 7* (pp. 117-122). Springer, New York, NY.

49. Stanley P., Chan W. K., (1986) The determination of stress intensity factors and crack tip velocities from thermoelastic infra-red emissions, In: Proceedings of International Conference of Fatigue of Engineering Materials and Structures, c262, IMechE, Sheffield, UK, pp. 105–114.
50. Stanley P., Dulieu-Smith J. M., (1993) Progress in the thermoelastic evaluation of mixed mode stress intensity factors, In: Proceedings of the SEM Spring Conference on Experimental Mechanics, Dearborn, pp. 617–626.
51. Lesniak J. R., Bazile D. J., Boyce B. R., Zickel M. J., Cramer K. E., Welch, C. S., (1997) Stress intensity measurement via infrared focal plane array, Non-Traditional Methods of Sensing Stress, Strain, and Damage in Materials and Structures. ASTM STP 1318, Philadelphia.
52. Lin S.T., Feng Z., Rowlands R.E., (1997) Thermoelastic determination of stress intensity factors in orthotropic composites using the J-integral”, Engineering Fracture Mechanics, Vol. 56 (4), pp. 579-592.
53. Tomlinson R.A., Nurse A.D., Patterson E.A, (1997) On determining stress intensity factors for mixed-mode cracks from thermoelastic data, Fatigue and Fracture of Engineering Materials and Structures, Vol. 20 (2), pp. 217-226.
54. Díaz F. A., Yates J. R., Tomlinson R. A., Patterson E. A., (2002) Some observation on the application of thermoelasticity to fatigue cracks”, In: Proceedings of SEM Conference, Milwaukee, USA.
55. Díaz F. A., Patterson E. A., Tomlinson R. A., Yates J. R., (2004) Measuring stress intensity factors during fatigue crack growth using thermoelasticity”, Fatigue and Fracture of Engineering Materials and Structures, Vol. 27, pp. 571-583.
56. Tomlinson R.A., Olden E.J., (1999) Thermoelasticity for the analysis of crack tip stress fields – A review, Strain, Vol. 35 (2), pp. 49-55.
57. Vieira, R.B., Gonzáles, G. L. G., Freire, J. L. F. (2018) Thermography Applied to the Study of Fatigue Crack Propagation in Polycarbonate, Experimental Mechanics, Volume 58, Issue 2, pp 269–282.

58. Paiva, V. E. L.; Freire, J. L., Etchebehere, R. C. (2018) Assessment of Chain Links Using Infrared Thermography. In: CONAEND&IEV2018 - 378, Congresso Nacional de Ensaios Não Destrutivos e Inspeção, 21^a IEV Conferência Internacional sobre Evaluación de Integridad y Extensión de Vida de Equipos Industriales ABENDI, 2018, São Paulo. Anais do Conaend&IEV2018, pp1-17.
59. Paiva, V. Maneschy, R. J., Freire, J. L., Gonzáles, G. L. G., Vieira, R. D., Vieira, R. B. (2018) Fatigue monitoring of a dented piping specimen using infrared thermography. In: PVP 2018, Paper No. PVP 2018-84597, ASME Pressure Vessels & Piping Conference, 2018, Praga, Czech Republic. Proceedings of the PVP 2018, Paper No. PVP 2018-84597, ASME Pressure Vessels & Piping Conference, p. 1-7.
60. Paiva, V., Maneschy, R. J., Freire, J. L., Gonzáles, G. L. G. Vieira, R. D. Ribeiro, A.S., Almeida, A.L.F.S. (2019) Fatigue assessment and monitoring of a dented pipeline specimen, In: PVP 2019, Paper No. PVP 2019-93663, ASME Pressure Vessels & Piping Conference, 2019, San Antonio, TX, USA. Proceedings of the PVP 2019, Paper No. PVP 2019-93663, ASME Pressure Vessels & Piping Conference, p. 1-8.
61. Paiva, V., Maneschy, R. J., Freire, J. L., Gonzáles, G. L. G. Vieira, R. D. Ribeiro, A.S., Almeida, A.L.F.S., Diniz, J. L. C., (2019) Fatigue Monitoring of a Dented Pipeline Specimen Using Infrared Thermography, DIC and Fiber Optic Strain Gages, SEM Conference and Exposition on Experimental and Applied Mechanics, 2019, Reno NV. Proceedings of the SEM Conference and Exposition on Experimental and Applied Mechanics, v. 1. p. 1-10.
62. Paiva, V. E., Vieira, R. D., Freire, J. L.F. (2018) Fatigue Properties Assessment of API 5L Gr. B Pipeline Steel using Infrared Thermography. In: SEM Conference and Exposition on Experimental and Applied Mechanics, 2018, Greenville SC. Proceedings of the SEM Conference and Exposition on Experimental and Applied Mechanics. v. 1. p. 1-7.

63. Paiva, V. E., Rego, L, Castro, J. T. P., Freire, J. L.F, (2017) Fatigue characterization of the c36000 copper alloy using the thermographic method. in: 24th ABCM international congress of mechanical engineering, 2017, Curitiba. proceedings of the 24th abcm international congress of mechanical engineering.
64. Paiva, V. E., Rego, L, Castro, J. T. P., Freire, J. L.F, (20187) Fatigue characterization of the 6351-t6 aluminium alloy using thermography. in: conaend&iev2018 - 388, congresso nacional de ensaios não destrutivos e inspeção, 21^a iev conferência internacional sobre evaluación de integridad y extensión de vida de equipos industriales abendi.
65. Boyce. B. R. (1999) Steps to Modern Thermoelastic Stress Analysis. ATM Conference. Ube, Japan. Stress Photonics, p. 1-2.
66. API (2016) 579-1/ASME FFS-1, Fitness-For-Service.
67. B31.8 (2018) - Gas Transmission and Distribution Piping Systems, ASME International.
68. B31.4 (2016) - Pipeline Transportation Systems for Liquids and Slurries, ASME Code for Pressure Piping, ASME International.
69. Kiefner, J.F. and Alexander, C.R. (1999) API 1156 - Effects of Smooth and Rock Dents on Liquid Petroleum Pipelines (Phase II)”, American Petroleum Institute, Addendum to API Publication 1156.
70. Zarea, M. F., Toumbas, D.N., Philibert, C.E., Deo, I. (1996) Numerical Models for Static Denting and Dynamic Puncture of Gas Transmission Linepipe and Their Validation, International Pipeline Conference, Volume 2, ASME.
71. DIN 2413 (2011) Seamless steel tubes for oil- and water-hydraulic systems - Calculation rules for pipes and elbows for dynamic loads, Deutsches Institut für Normung.
72. Bood, R.J., Galli, M.R., Marewski, U., Roovers, P., Steiner, M., Zaream, M. (1999) EPRG Methods for Assessing the Tolerance and Resistance of Pipelines to External Damage Part 1+2, International.
73. Cosham, A., Hopkins, P. (2002) The Pipeline Defect Assessment Manual, Proceedings of 4th International Pipeline Conference, Calgary, AB, The American Society of Mechanical Engineers, New York, NY, pp 1565-1581.

74. BS 7910 (2007) Guide to methods for assessing the acceptability of flaws in metallic structures, BSI.
75. Fowler, J. R., Alexander, C.R., Kovach, P.J., Connelly, L.M. (1994) Cyclic Pressure Fatigue Life of Pipelines with Plain Dents, Dents with Gouges, and Dents with Welds, Report PR-201-927 and PR-201-9324, American Gas Association.
76. Alexander, C.R., Kiefner, J.F. (1997) Effects of Smooth and Rock Dents on Liquid Petroleum Pipelines, American Petroleum Institute, API Publication 1156.
77. Rosenfeld, M.J. (1997) Development of a Model for Fatigue Rating Shallow Unrestrained Dents”, Final Report for Contract PR-281-9405, American Gas Association, Arlington, VA.
78. Rosenfeld, M.J. (1999) Guidelines for the Assessment of Dents on Welds”, Final Report for Contract PR-218-9822, Pipeline Research Council International, Catalog Number L51810.
79. ASME. (2010) Boilers and pressure vessels code: section VIII – division 2, NY, New York.
80. Pinheiro, B. C. (2006) Avaliação da fadiga de dutos de transporte de hidrocarbonetos submetidos a danos mecânicos. F133. Dissertação (Mestrado em Ciências em Engenharia Oceânica) -Universidade Federal do Rio de Janeiro/ COPPE/ Rio de Janeiro.
81. Pinheiro, B. C., Pasqualino, I. P., Cunha, S. B. (2008) Fatigue life analysis of steel pipelines with plain dents under cyclic: internal pressure. In: International Pipeline Conference, 7, Canada. Proceedings, Canada: ASME, pp. 1-10.
82. Pinheiro, B.C.; Pasqualino, I. P. (2009) Fatigue analysis of damaged steel pipelines under cyclic internal pressure, International Journal of Fatigue, v. 31, n. 5, p. 962–973.
83. Cunha, S. B., Pasqualino, I. P., Pinheiro, B. C. (2009) Stress-life fatigue assessment of pipelines with plain dents, Fatigue Fracture Engineering Materials & Structures, England, v. 32, n. 12, p. 961– 974.

84. Ávila, M. A. V. (2007) Análise de integridade estrutural de dutos com mossas simples”. 2007. 196 f. Dissertação (Mestrado em Engenharia Mecânica) -Pontifícia Universidade Católica do Rio de Janeiro, Rio de Janeiro.
85. Silva, B. F., Freire, J. L. F. (2012) Tensões cíclicas causadas por carregamento de pressão em um duto com mocha. In: Congresso Nacional de Ensaios Não Destrutivos e Inspeção, 30. São Paulo. Anais... São Paulo: Abendi, p. 420-433.
86. Silva, B. F (2012) Fadiga em Dutos com Mossas Solicitados por Ciclos de Pressão Interna, Master's Thesis, PUC-Rio.
87. Ong, L., Soh, A., Ong, J. (1992) Experimental and Finite Element Investigation of a Local Dent on a Pressurized Pipe, The Journal of Strain Analysis for Engineering Design 27 (3), pp.177–185.
88. Keating, P., and Hoffmann, R. (1997) Fatigue Behavior of Dented Petroleum Pipelines, Technical Report DTRS56-95-C-0003. Texas A&M University: Office of Pipeline Safety.
89. Rosenfeld, M, Porter, P., and Cox, J. (1998) Strain Estimation Using Vetco Deformation Tool Data, In International Pipeline Conference, (1) pp.389–397.
90. Lukasiewicz, S., Czyz, J., Sun, C., and Adeeb, S. 2006. “Calculation of Strains in Dents Based on High Resolution In-Line Caliper Survey” (January 1): 129–134. doi:10.1115/IPC2006-10101.
91. Noronha, D., Martins, R., Jacob, B., and De Souza, E. (2010) Procedures for the Strain Based Assessment of Pipeline Dents, International Journal of Pressure Vessels and Piping 87 (5) pp.254–265.
92. Gonzáles G L G, Paiva V E L, Vieira R D, Ribeiro A S, d'Almeida A L F S, Piovesan L M, Freire J L F. (2019). Correlação de Imagem Digital aplicada ao estudo do comportamento de tubulações com defeitos tipo mocha. COTEQ 2019 Conferencia sobre tecnologia de equipamentos, Rio de Janeiro, Brasil.
93. Gonzáles G L G, Paiva V E L, Vieira R D, Ribeiro A S, d'Almeida A L F S, Piovesan L M, Freire J L F. (2019) Strain measurements in dented pipelines under cyclic internal pressure using Digital Image Correlation. Rio Pipeline 2019 Conference & Exhibition, Rio de Janeiro, Brasil.

94. Jajo, J. O., (2014) Dent behavior of steel pipes under pressure load, Electronic Theses and Dissertations, University of Windsor.
95. Vollmer, M., Möllmann, K. P. (2010) Infrared Thermal Imaging: fundamentals, research and applications, Second Edition, Wiley-VCH.
96. Incropera, F.P. and DeWitt, D.P. (1996) Fundamentals of Heat and Mass Transfer, 4th edn, JohnWiley & Sons, Inc., New York.
97. De Witt, D.P. and Nutter, G.D. (1988) Theory and Practice of Radiation Thermometry, JohnWiley & Sons, Inc.
98. Radiation Curves, HyperPhysics, Department pf Physics and Astronomy, Available at: < <http://hyperphysics.phy-astr.gsu.edu/hbase/wien.html>> Viewed in 20/05/2019.
99. Rohsenow, W. M., Hartnett, J. P., Cho, Y.I. (1998) Handbook of heat transfer. Vol. 3. New York: McGraw-Hill.
100. Flir, The ultimate infrared handbook for R&D professionals. FLIR AB, Boston.
101. Vieira RB (2016) Thermography Applied to the Study of Fatigue in Polycarbonate, Master's Thesis, PUC-Rio.
102. Grinzato, E., (2012) Thermal Non-Destructive Testing and Evaluation, 18th World Conference on Non-Destructive Testing, Durban, África do Sul.
103. Grosso, M., Souza, M.P.V., Rebello, J.M.A., Margarit-Mattos, I.C.P., Pereira, G.P., Soares, S.D. (2012) Avaliação de falhas em revestimentos anticorrosivos via termografia ativa, Intercorr, Salvador, Bahia, Brasil, pp.14-18.
104. Maldague, X. (2001) Theory and Practice of Infrared Technology for Nondestructive Testing. New York, John Wiley & Sons, Inc.
105. Quinn, S., Dulieu-Barton, J. M., & Langlands, J. M. (2004). Progress in thermoelastic residual stress measurement. Strain, 40(3), 127-133.
106. Diaz. F. A.; Patterson. E. A.; Yates. J. R. (2013) Application of thermoelastic stress analysis for the experimental evaluation of the effective stress intensity factor”. Article. Frattura ed Integrità Strutturale, 25.
107. Harwood, N., Cummings, W. M. (1991) Thermoelastic Stress Analysis CRC Press; 1 edition.
108. Barton, J. M., Stanley, P., (1997) Reproducibility and reliability of the response from four SPATE systems, Experimental Mechanics 37 440-444.

109. Dulieu-Smith, S.M., (1995) Alternative calibration techniques for quantitative thermoelastic stress analysis", *Strain*, pp. 9-16.
110. Quinn, S., Shiang-Jiun, L., McCabe, J., Rowlands, R. (2006) Determining Orthotropic Coefficients From, and Thermoelastic Stress Analysis of Diametrally Loaded Composite Disk, Conference: ASME 2006 International Mechanical Engineering Congress and Exposition.
111. Wei. B. (2008) Thermoelastic Stress Analysis Techniques for Mixed Mode Fracture and Stochastic Fatigue of Composite Materials, p. 1-127. Dissertation, Doctor of Philosophy in the School of Civil and Environmental Engineering - Georgia Institute of Technology.
112. Meade, M. L. (1983) Lock-in amplifiers: Principles and applications, IEE Electrical Measurement Series, London: P. Peregrinus.
113. Ryall, T. G., Wong, A. K. (1988) Determining stress components from thermoelastic data – a theoretical study, *Mechanics of Materials*, Volume 7, Issue 3.
114. Huang, Y.M., AbdelMohsen, H.H., Rowlands, R.E. (1990) Determination of individual stresses thermoelastically, *Experimental Mechanics* 30: 88.
115. Huang, Y.M., Rowlands, R.E. & Lesniak, J.R. (1990) Simultaneous stress separation, smoothing of measured thermoelastic information, and enhanced boundary, *Experimental Mechanics* 30: 398.
116. Harwood, N., Cummings, W. M., (1989) Calibration of the thermoelastic stress analysis technique under sinusoidal and random loading conditions, *Strain*, Volume 25, Issue 3, pp.101-108.
117. Lin, S. J., Matthys, D. R., & Rowlands, R. E. (2005). Individual stresses in perforated plates by thermoelasticity and Airy function. In SEM Annual Conference and Exposition on Experimental and Applied Mechanics, Portland, Oregon (pp. 186-194).
118. Greene, R. J., & Patterson, E. A. (2006). An integrated approach to the separation of principal surface stresses using combined thermo-photoelasticity. *Experimental mechanics*, 46(1), 19-29.
119. Sakagami, T., Kubo, S., Fujinami, Y., & Kojima, Y. (2004). Experimental stress separation technique using thermoelasticity and photoelasticity and its application to fracture mechanics. *JSME International Journal Series A Solid Mechanics and Material Engineering*, 47(3), 298-304.

120. ASTM E 466-07 - Standard Practice for Conducting Force Controlled Constant Amplitude Axial Fatigue Tests of Metallic Materials
121. Rosenfeld, M.J. (1998) Investigations of Dent Rerounding Behavior. IPC1998-2036, pp. 299-307.
122. Stress Photonics Inc., (2016) DeltaTherm 2 Manual, v6.
123. Relatório de tração gr. B (2014) Report Ensaios de tração nos materiais base de nove tubos usados na confecção dos espécimes tubulares, PUC-Rio 2014.
124. ISO 3183 (2nd ed.) /API Spec 5L 44th (2019) Petroleum and natural gas industries — Steel pipe for pipeline transportation systems.
125. Relatório de fadiga gr. B (2014) Report Ensaios de fadiga no material base de um dos tubos usados na confecção dos espécimes tubulares, PUC-Rio 2014.
126. Castro JT, Meggiolaro MA (2009) Fadiga - Técnicas e Práticas de Dimensionamento Estrutural sob Cargas Reais de Serviço: Volume I & II, 2nd ed. CreateSpace.
127. Shigley J. (2011) Mechanical Engineering Design. New York: McGraw-Hill.
128. Sutton M.A., Orteu J.J., Schreier H. (2009) Image correlation for shape, motion and deformation measurements: basic concepts, theory and applications, Springer Science & Business Media.
129. O'Donnell, W. J. (2006) Code Design and Evaluation for Cyclic Loading – Sections III and VIII”, Chapter 39, ASME Companion Guide to the Boiler and Pressure Vessel Code, Vol. 2, K.R. Rao, Editor, Third Edition.
130. ANSYS (2007) ANSYS advanced analysis techniques guide, Ansys Help.
131. ANSYS (2010) Mechanical ANSYS Mechanical Structural Nonlinearities - Lecture 3, Introduction to Contact.
132. Crisfield, M.A. (1980) A Fast Incremental Iterative Solution Procedure that Handles Snap-Through, Computer and Structures, Vol.13 pp.55-62.
133. Corona, E. (2007) Mechanics of Offshore Pipelines: Buckling and Collapse, Vol. I, Elsevier Science; 1 edition.
134. Karman, V.T., dan Kerr, A.D. (1962) Instability of Spherical Shells Subjected to External Pressure, National Aeronautics and Space Administration, Washington.

135. Hühner, C., Zimmermann, R., Rolfes, R., Rolfes, B. (2002) Sensitivities to Geometrical and Loading Imperfections on Buckling of Composite Cylindrical Shells, European Conference on Spacecraft.
136. Potter, R. T., Greaves, L. J. (1987) The Application of Thermoelastic Stress Analysis Techniques To Fiber Composites, Proceedings Volume 0817, Optomechanical Systems Engineering.
137. Saad , M. A., Thermodynamics for Engineers, Prentice Hall Inc., 1966.

Appendix A.

A.1

IR Thermography Physical Principles

All matter, whether solid, liquid or gaseous, being at a temperature above absolute zero (0K) emits radiation. The emission can be attributed to changes in the electron configurations of the atoms or molecules constituting the materials [95].

Blackbodies are idealizations, and no real object can emit the maximum thermal radiation at a given temperature. The real emission of thermal radiation from any object can, however, be easily computed by multiplying the blackbody radiation by a quantity that describes the influence of the object under study, the emissivity ε . The emissivity of an object is the ratio between the amount of radiation emitted from the surface and the emitted by an idealize blackbody at the same temperature, as shown at Eq. (A.1):

$$\varepsilon = \frac{\phi_{obj}}{\phi_{bb}} \quad (A.1)$$

where ϕ_{obj} and ϕ_{bb} are respectively the total radiant energy emitted by an object and by a blackbody at the same temperature.

From the definition of emissivity, it is noticeable that $0 \leq \varepsilon \leq 1$, as blackbodies are just idealizations real objects, called grey-bodies, have smaller emissivity that are proportional to a blackbody, once they can't emit all the radiation.

The emissivity can be presumed from Kirchhoff's law [95-97], which states that the amount of radiation absorbed (α) by any object is equal to the amount of radiation that is emitted (ε) by this object, described by Eq. (A.2):

$$\alpha = \varepsilon \quad (A.2)$$

Energy conservation requires that any radiation incident on any object (ϕ_{obj}) must be reflected (ϕ_r) (whether it is directed according to the law of reflection or diffusely scattered from rough surfaces), transmitted (ϕ_t) through the object, or absorbed (ϕ_a) within the object:

$$\phi_{obj} = \phi_{\rho} + \phi_{\tau} + \phi_{\alpha} \quad (\text{A.3})$$

Considering the fraction of the incident radiation the sum of the parcels must be equal to 1, this law can be rewrite as the Total Radiation Law:

$$1 = \phi_{\rho} + \phi_{\tau} + \phi_{\alpha} \quad (\text{A.4})$$

Each object will have a different set of energy parcels depending on its own properties, for example, a perfect blackbody would have $\phi_{\rho} = \phi_{\tau} = 0$ and $\phi_{\alpha} = 1$, since, by definition, it absorbs all the incident radiation ($\alpha_{bb} = \varepsilon_{bb} = 1$).

Planck's Law describes the amplitude of radiation emitted (i.e., spectral radiance) by a blackbody as a function of its temperature (T) and of the wavelength of emission (λ):

$$\phi_{bb}(\lambda, T) = \frac{2\pi c^2 h}{\lambda^5 \left(e^{\frac{ch}{k\lambda T}} - 1 \right)} \quad (\text{A.5})$$

where c is the speed of light, h is the Planck's constant ($6.6260 \cdot 10^{-34} m^2 kg s^{-1}$) and k is the Boltzmann constant ($1.381 \cdot 10^{-23} m^2 kg s^{-2} K^{-1}$).

Figure A.1, below, shows the plot of Plank's Law for various temperature ranges.

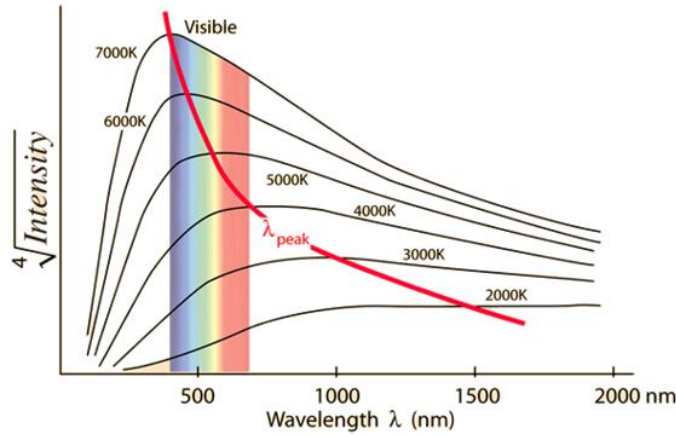


Figure A.1: Plot of Planck's Law for various temperature ranges and wavelength [98].

Through the integration of the Plank's Law, it is obtained the Stefan–Boltzmann Law, which describes the power radiated from a blackbody in terms of its temperature, stating that the total energy radiated per unit surface area of a blackbody across all wavelengths per unit time (also known as the blackbody

radiant emittance) is directly proportional to the fourth power of the black body's thermodynamic temperature T , as presented in Eq. (A.6) :

$$\phi_{bb} = \int_{\lambda} \phi_{bb}(\lambda, T) = BT^4 \quad (\text{A.6})$$

where B is the Stefan-Boltzmann constant ($5.670 \cdot 10^{-8} \text{Wm}^{-2}\text{K}^{-4}$) and T is the temperature of the blackbody.

For real objects, which has emissivity lower than 1, Stefan–Boltzmann Law can be rewrite in terms of the emissivity of each material to describe the amount of energy radiated from the grey bodies:

$$\phi_{obj} = \varepsilon(\lambda)BT^4 \quad (\text{A.7})$$

A grey body is defined as a body with constant emissivity over all wavelengths and temperatures. Such an ideal body does not exist in practice, but the assumption is a good approximation for many objects, for most practical applications in thermography, ε is independent of wavelength resembling a grey body [99].

A.1.1 Radiation in IR Thermography Applications

In applications related to IR Thermography, the radiation measured is attenuated by the environment, where the measure takes place due to absorption by gases and scattering by particles [100].

Between the surface, which the temperature is being measured, and the IR sensor usually is the atmosphere. The atmosphere of the environment interacts with radiation like any other object absorbing, transmitting and reflecting a portion of the energy [98]. Because of that, the total radiation that reaches the sensor is the sum of three portions:

$$\phi_{measured} = \underbrace{\tau_{env}\phi_{obj}}_{(1)} + \underbrace{\rho_{obj}\tau_{env}\phi_{env}}_{(2)} + \underbrace{\varepsilon_{env}\phi_{env}}_{(3)} \quad (\text{A.8})$$

where the parcel (1) is the energy radiated by the object, ϕ_{obj} , after being attenuated by the environment transmittance, τ_{env} . The parcel (2) is the energy radiated by the

environment, ϕ_{env} , after being reflected by the object, ρ_{obj} , and then attenuated by the environment transmittance, τ_{env} . The parcel (3) is the energy radiated by the environment itself.

To IR wavelength assuming that the object is opaque ($\tau_{obj} = 0$) and that the environment does not reflect radiation ($\rho_{env} = 0$), Eq. (A.8) can be rewrite in terms of the Total Radiation Law (Eq. (A.4)):

$$\phi_{measured} = \underbrace{\tau_{env}\phi_{obj}}_{(1)} + \underbrace{(1 - \varepsilon_{obj})\tau_{env}\phi_{env}}_{(2)} + \underbrace{(1 - \tau_{env})\phi_{env}}_{(3)} \quad (A.9)$$

Through the maximization of both the environment transmittance and the object's emissivity it is possible to reduce the noise and amplify the energy measured by the IR camera. For that IR sensors use the so-called “atmospheric windows”, specific wavelength intervals that are almost not absorbed by the environment. Figure A.2 shows the IR atmospheric transmittance and the two typical “windows” used by commercial cameras (3-5 μm and 8-14 μm):

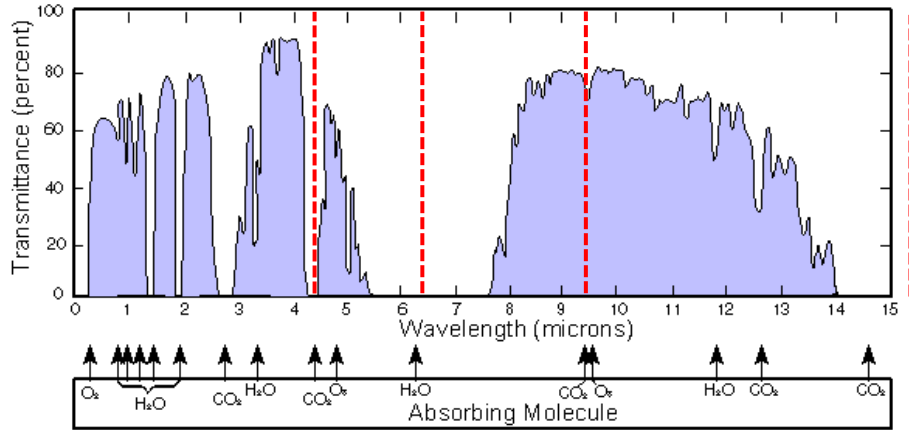


Figure A.2: Atmospheric windows used in IR thermography [100].

The IR camera used in this thesis was a FLIR A655sc, its operation is based on the non-quantum principle and works in the spectral range from 7.5 to 14 μm . More information about it will be given in Section A.2.

A.2 IR Sensors

IR sensors can be divided into two categories: quantum and non-quantum or cooled and non-cooled. Each type of sensor, depending on its constitution and operation, will be suitable for one of the "atmospheric windows" described in Section A.1.

The quantum type detector works similar to most digital cameras, being the only difference the constituent materials and the need of a cryocooler, which lowers the sensor temperature to cryogenic temperatures. This reduction in sensor temperature is necessary to reduce thermally-induced noise to a level below that of the signal from the scene being imaged, turning the sensor very expensive not only to produce but also to operate, since the cooling process requires a long time to start working and it's more delicate.

This kind of sensor measures the variation of conductivity caused by change of energy of an atom jumping to a higher energy state when a photo hits the semiconductor and is absorbed. Having higher sensitivity and greater magnification capabilities than the uncooled cameras, quantum detectors are much more expensive and are able to work in both atmospheric windows (3-5 and 8-14 μm), depending on the construction of the sensor. Until recently, photon detectors were the only viable choice for practical thermography applications.

With the demilitarization of micro-bolometer technology, a new and cheaper type of thermal camera has emerged. The non-quantum or non-cooled sensor absorbs the IR radiation causing its temperature to rise and induces a change of its resistance, which is later quantified by an electric circuit.

Uncooled IR sensors can be stabilized to an operating temperature to reduce image noise, not needing to be cooled and not requiring expensive coolers. This makes IR cameras smaller and less expensive. However, their resolution and image quality tend to be lower than cooled ones, with restriction to the higher wavelength atmospheric window (8-14 μm). This is due to differences in their fabrication processes. An uncooled thermal camera also needs to deal with its own heat signature. It was not until recent advancements that these sensors became viable for thermography use.

Appendix B.

The analytical foundations of the TSA have been discussed previously by Potter et al. [136] and are developed from classic mechanics [137].

The first law of thermodynamics states that for a closed system undergoing a reversible process:

$$dU = \Delta W + \Delta Q \quad (\text{B.1})$$

where dU is the increase in internal energy, ΔW is the work done on the system and ΔQ is the heat transferred from the environment to the system.

Since the internal energy variation is independent of the process, its infinitesimal change can be mathematically described by the exact differential d , while heat and work are process dependent quantities and their changes are signified by Δ (the symbology d denotes exact and Δ other variations). It is convenient to rewrite Eq. (B.1) as:

$$du = \Delta w + \Delta q \quad (\text{B.2})$$

with lower case letters u , w and q representing the corresponding quantities per unit volume.

The mechanical work done by external loading into the system is absorbed as strain energy stored inside the deformed body. Based on unit volume, the work performed can be expressed as the strain energy density:

$$dw = \sigma_{ij} d\varepsilon_{ij} \quad i, j = 1, 2, 3, \dots \quad (\text{B.3})$$

where σ_{ij} and ε_{ij} are components of the stress and strain tensors, respectively.

Thermodynamics defines entropy per unit of volume, s , as:

$$dq = Tds \quad (\text{B.4})$$

with T being the absolute temperature in Kelvin.

The entropic quantity s is considered as a thermodynamic parameter (a state variable). Combining Eq. (B.2) and Eq. (B.4) produces:

$$du = du(\varepsilon_{ij}, s) = \sigma_{ij}d\varepsilon_{ij} + Tds \quad i, j = 1, 2, 3, \dots \quad (\text{B.5})$$

where ε_{ij} is another thermodynamic state variable that defines u independently of the process. This means that the internal energy u is a function of these two variables, but not of the process that leads to changes in ε and s .

With elastic solids, one prefers a different set of state variables, ie, σ_{ij} and T , in which it requires the introduction of Gibbs free energy as a thermodynamic potential. The free energy of Gibbs per unit volume g is defined as:

$$g = u - Ts - \sigma_{ij}\varepsilon_{ij} \quad (\text{B.6})$$

Differentiating Eq. (A.6) becomes:

$$dg = du - Tds - \sigma_{ij}d\varepsilon_{ij} - \varepsilon_{ij}d\sigma_{ij} \quad (\text{B.7})$$

Combining Eq. (B.5) and (B.7) gives:

$$dg = -sdT - \varepsilon_{ij}d\sigma_{ij} \quad (\text{B.8})$$

Eq. (B.8) shows that the Gibbs free energy g depends on temperature and stress so may be write as:

$$g = g(T, \sigma_{ij}) \quad (\text{B.9})$$

whose differential form is

$$dg = \frac{\partial g}{\partial T}dT + \frac{\partial g}{\partial \sigma_{ij}}d\sigma_{ij} \quad (\text{B.10})$$

Comparing the Eq. (B.8) and (B.10) with respect to temperature and stress, respectively, it is observed the following relations:

$$\frac{\partial g}{\partial T} = -s \quad (\text{B.11})$$

$$\frac{\partial g}{\partial \sigma_{ij}} = -\varepsilon_{ij} \quad (\text{B.12})$$

Since entropy is a thermodynamic property, it can be described as a function of two independent (state) variables, in this case, temperature and stress. Thus:

$$s = s(T, \sigma_{ij}) \quad (\text{B.13})$$

Applying the differentiation, it is obtained:

$$ds = \frac{\partial s}{\partial T} dT + \frac{\partial s}{\partial \sigma_{ij}} d\sigma_{ij} \quad (\text{B.14})$$

Eq. (B.9) and (B.13) indicate that both the Gibbs free energy g and entropy s are functions of temperature and stress, combining both Eq. (B.11) and (B.14):

$$-\left(\frac{\partial s}{\partial T} dT + \frac{\partial s}{\partial \sigma_{ij}} d\sigma_{ij}\right) = \frac{\partial^2 g}{\partial T^2} dT + \frac{\partial^2 g}{\partial T \partial \sigma_{ij}} d\sigma_{ij} \quad (\text{B.15})$$

Simplifying Eq. (B.15) using Eq. (B.12) and (B.14) leads to:

$$-ds = \frac{\partial^2 g}{\partial T^2} dT - \frac{\partial \varepsilon_{ij}}{\partial T} d\sigma_{ij} \quad (\text{B.16})$$

Thermodynamics, in general, it defines specific heat (per unit mass) at a constant pressure or pressure C_σ as:

$$\rho C_\sigma = \left(\frac{\partial q}{\partial T}\right)_\sigma \quad (\text{B.17})$$

where ρ is the density. Note that the density is not constant since $\Delta\rho/\rho = -\varepsilon_{ij}$ and at least for isotropic materials this first strain invariant change is proportional to the first stress invariant change, in which the TSA measures.

Substituting Eq. (B.16) into Eq. (B.17) and noting Eq. (B.18), gives:

$$\rho C_\sigma = \left(\frac{T \partial s}{\partial T}\right)_\sigma = \left(\frac{\partial s(T, \sigma_{ij})}{\partial T}\right)_\sigma \quad (\text{B.18})$$

Partially differentiating Eq. (B.18) with respect to T :

$$\frac{\partial^2 g}{\partial T^2} = -\frac{\partial s}{\partial T} \quad (\text{B.19})$$

and substituting Eq. (B.18) into Eq. (B.19) results in:

$$\rho C_\sigma = -T \frac{\partial^2 g}{\partial T^2} \quad (\text{B.20})$$

Combining Eqs. (B.4), (B.16) and (B.20) produces:

$$\frac{dq}{T} = \rho C_\sigma \frac{dT}{T} + \frac{\partial \varepsilon_{ij}}{\partial T} d\sigma_{ij} \quad (\text{B.21})$$

For an adiabatic process, $dq = 0$, so under these conditions Eq. (B.21) can be simplified to:

$$\rho C_\sigma \frac{dT}{T} = -\frac{\partial \varepsilon_{ij}}{\partial T} d\sigma_{ij} \quad (\text{B.22})$$

Moreover, assuming thermal expansion coefficient, $\alpha_{ij}(\alpha)$, are defined for isotropic media as:

$$\frac{\partial \varepsilon_{ij}}{\partial T} = \alpha \delta_{ij} \quad (\text{B.23})$$

Substituting Eq. (B.23) into Eq. (B.22):

$$\rho C_\sigma \frac{dT}{T} = -\alpha \delta_{ij} d\sigma_{ij} = -\alpha d\sigma_{kk} \quad (\text{B.24})$$

Integrating Eq. (B.24) between two equilibrium states, 0 and 1:

$$\rho C_\sigma \int_0^1 \frac{dT}{T} = -\alpha \int_{(\sigma_{kk})_0}^{(\sigma_{kk})_1} d\sigma_{kk} \quad (\text{B.25})$$

gives

$$\rho C_\sigma \ln \left(\frac{T_1}{T_0} \right) = -\alpha [(\sigma_{kk})_1 - (\sigma_{kk})_2] \quad (\text{B.26})$$

or

$$\rho C_\sigma \ln \left(1 + \frac{\Delta T}{T_0} \right) = -\alpha \Delta \sigma_{kk} = \alpha (\Delta \sigma_1 + \Delta \sigma_2 + \Delta \sigma_3) \quad k = 1, 2 \text{ and } 3 \quad (\text{B.27})$$

where σ_{kk} is the first stress invariant, σ_1 , σ_2 and σ_3 are the principal stresses, and ΔT is the temperature variation between two equilibrium states associated with the change of stress.

Expanding the natural logarithm term of Eq. (B.27) in terms of power series yields:

$$\rho C_\sigma \left[\frac{\Delta T}{T_0} - \frac{1}{2} \left(\frac{\Delta T}{T_0} \right)^2 + \frac{1}{3} \left(\frac{\Delta T}{T_0} \right)^3 - \dots \right] = -\alpha \Delta \sigma_{kk} \quad (\text{B.28})$$

During TSA tests ΔT associated with the cyclic stresses is very small (of the order of 0.001°C) compared with the environmental temperature, T_0 , so the higher order terms of the above power series can be neglected. Therefore:

$$\rho C_\sigma \frac{\Delta T}{T_0} = -\alpha \Delta \sigma_{kk} \quad (\text{B.29})$$

or

$$\Delta T = -T_0 \frac{\alpha}{\rho C_\sigma} \Delta \sigma_{kk} \quad (\text{B.30})$$

Assuming $K_m = \alpha C_\sigma$ as the thermomechanical coefficient, or gain, rewriting Eq. (B.30) as:

$$\Delta T = -T_0 K_m \Delta \sigma_{kk} \quad (\text{B.31})$$

Under plane-stress isotropic, TSA equation can be written as:

$$S^* = K(\Delta \sigma_1 + \Delta \sigma_2) \quad (\text{B.32})$$

where S^* is the signal output from the thermal sensor and K is the thermomechanical coefficient.

Appendix C.

The shape of the dent depends greatly on the format of the indenter. As previously mentioned, several different indenters were modeled, totalizing 16 different formats, but only 2 were fabricated and tested. Figures C.1 to C.3 show the formats of the simulated indenter and of its produced dents after rerounding. The sixteenth indenter was selected to create the dents in this study, its format and results were reported along this thesis.

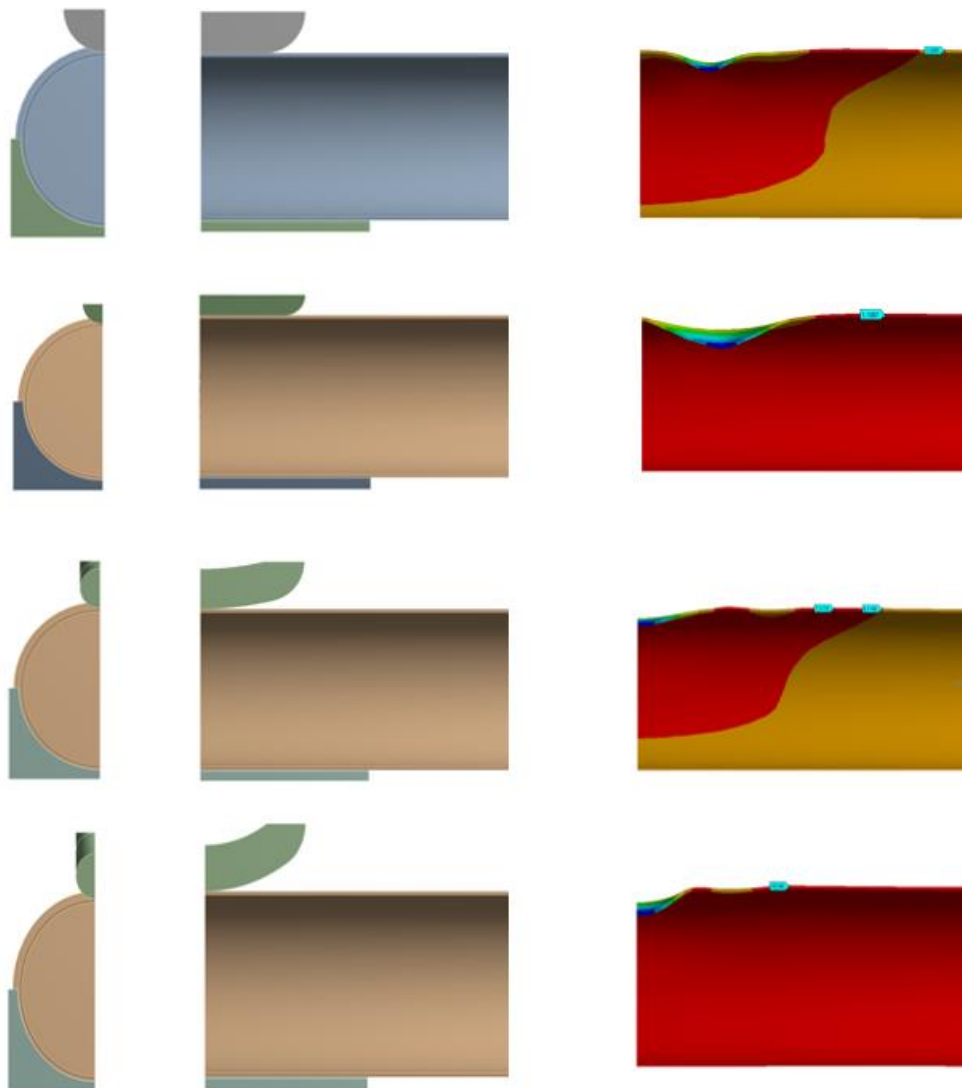


Figure C.1 Indenters 1 to 4 and results.

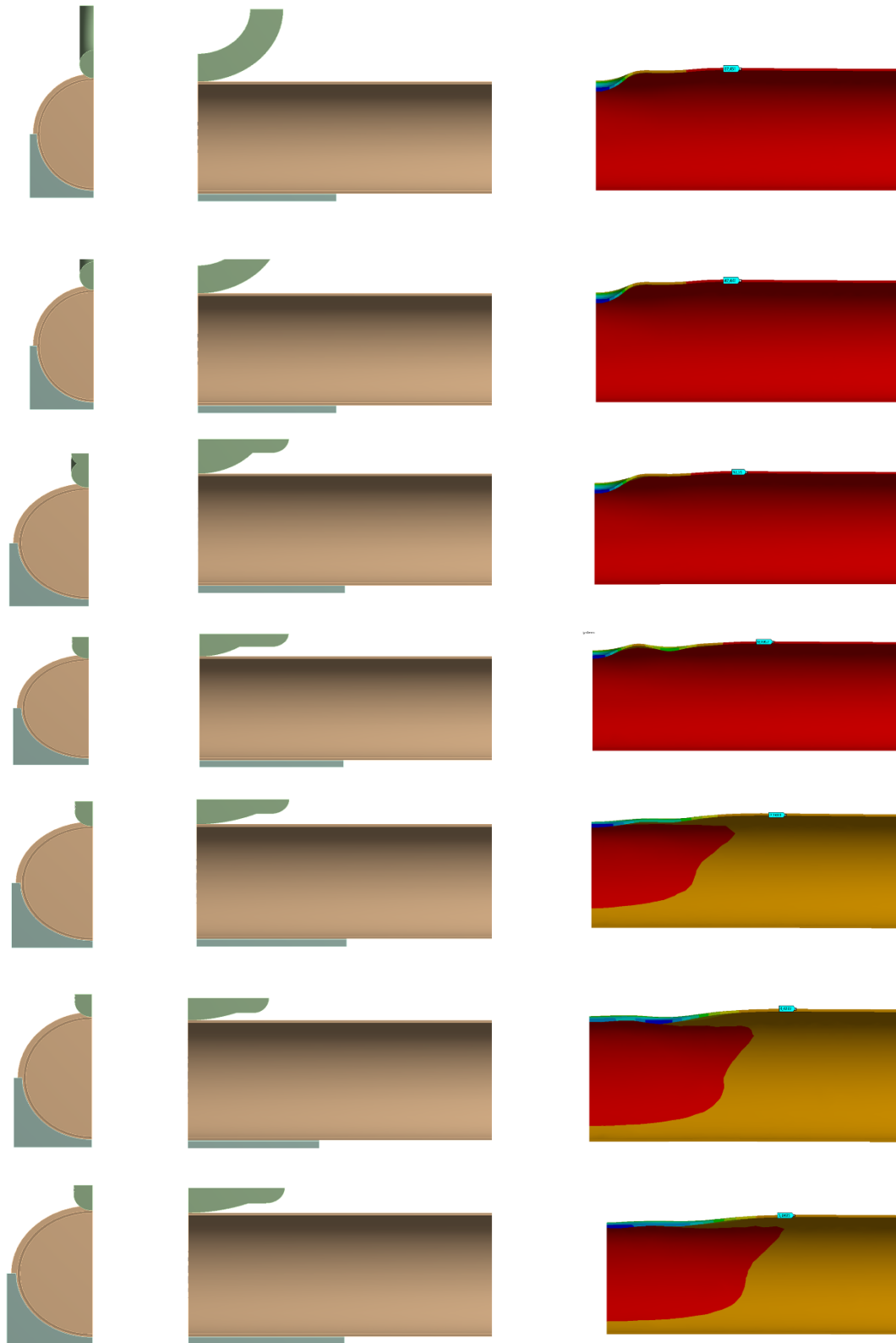


Figure C.2: Indenters 5 to 11 and results.

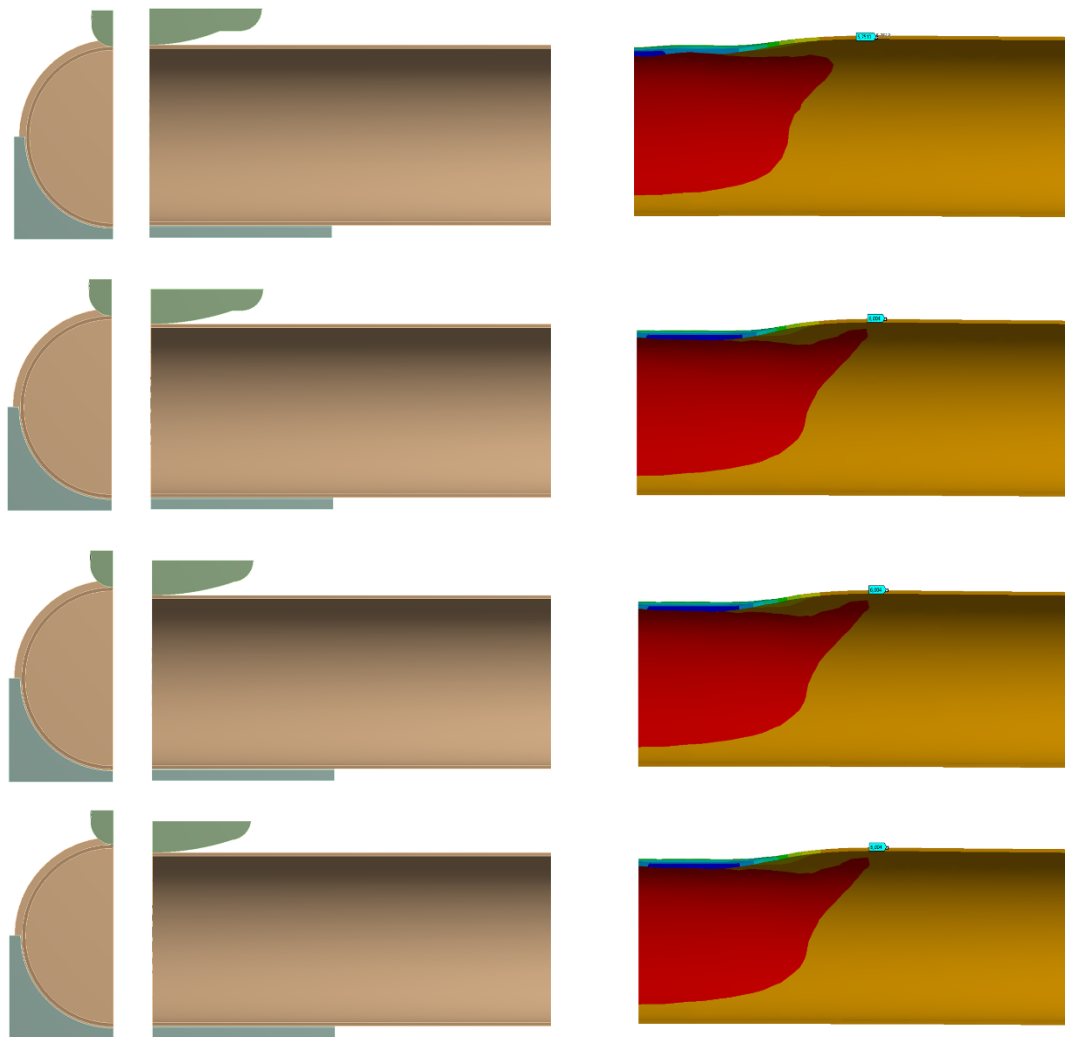


Figure C.3: Indenters 12 to 15 and results.

Appendix D.

Here is presented a case similar to the dent studied in this work. It was developed a plane stress model of a plate containing a hole using FEM. The plate geometry is shown in Figure D.1.

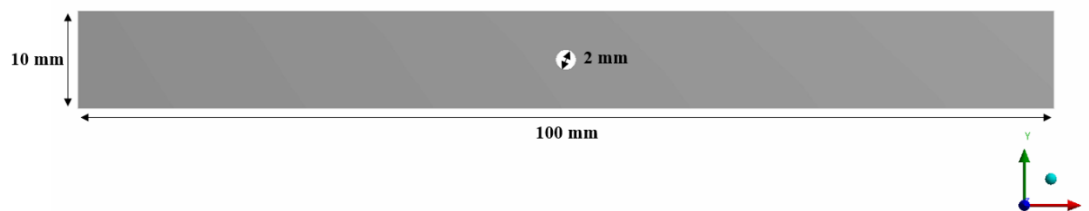


Figure D.1: Geometry of the plane stress plate with a hole model.

This model uses the same material studied in this thesis, the API 5L Gr. B pipeline steel, the used stress-strain curve was shown in Figure 4.7.

Appropriate boundary conditions were applied, a fixed support condition was applied to the right end of the plate and a cyclic pressure loading to the right end, as shown in Figure D.2. The models mesh consisted of 15757 elements, being constituted by the elements SOLID186, CONTA174 and TARGE170, and a total of 48163 nodes.

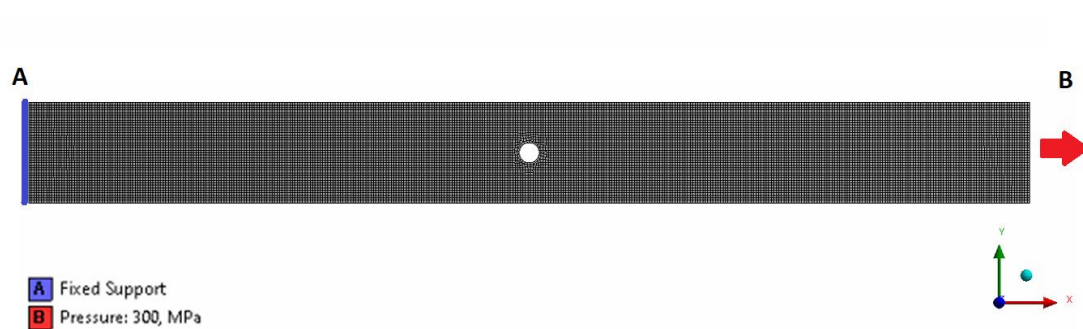


Figure D.2: Model mesh and boundary conditions.

The plate was subjected to three load cycles, the applied load ranged from 300 MPa to -300MPa. Figures D.3 to D.5 show results of the two analyzed arbitrary positions, one located at the edge of the hole and one located at the nominal section of the plate.

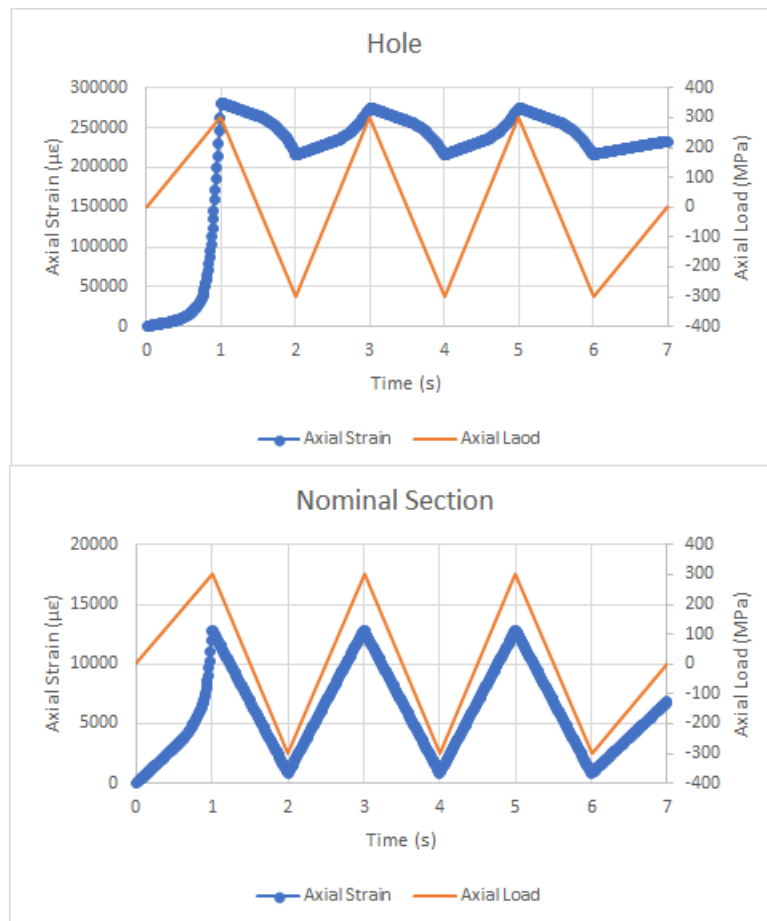


Figure D.3: Axial strain at the analyzed position and axial load the was applied in the plate for both interest points.

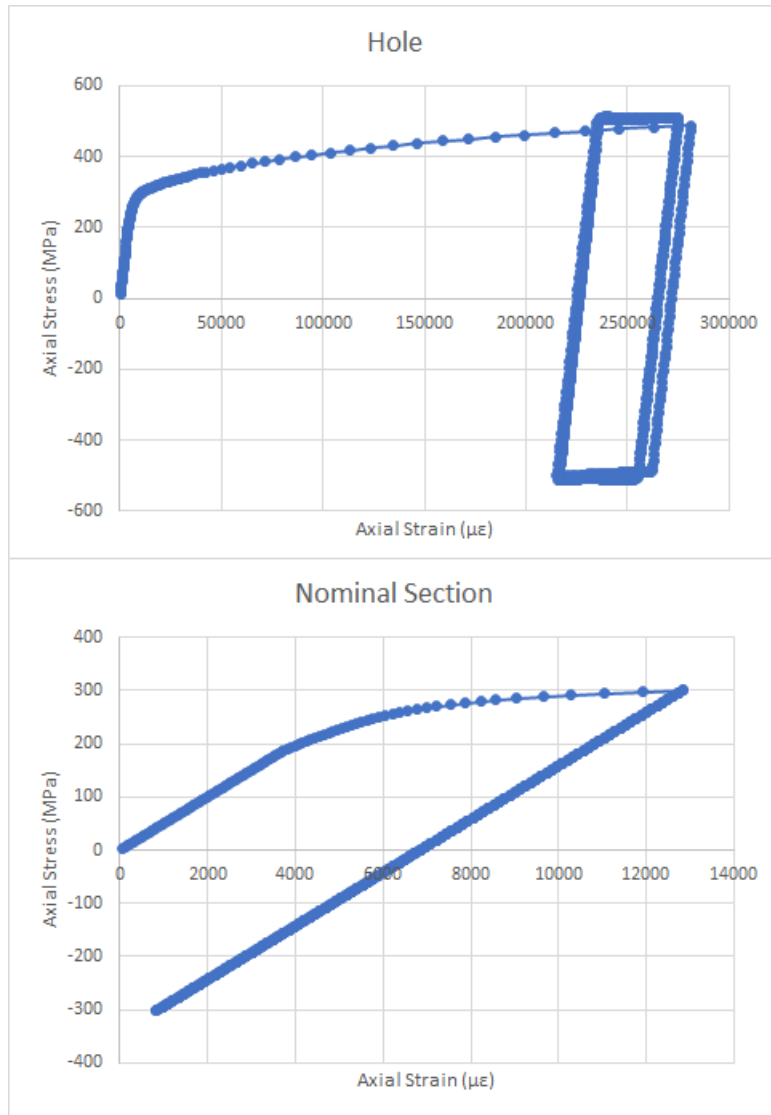


Figure D.4: Stress-Strain history developed during the application of the cyclic load for both interest points.

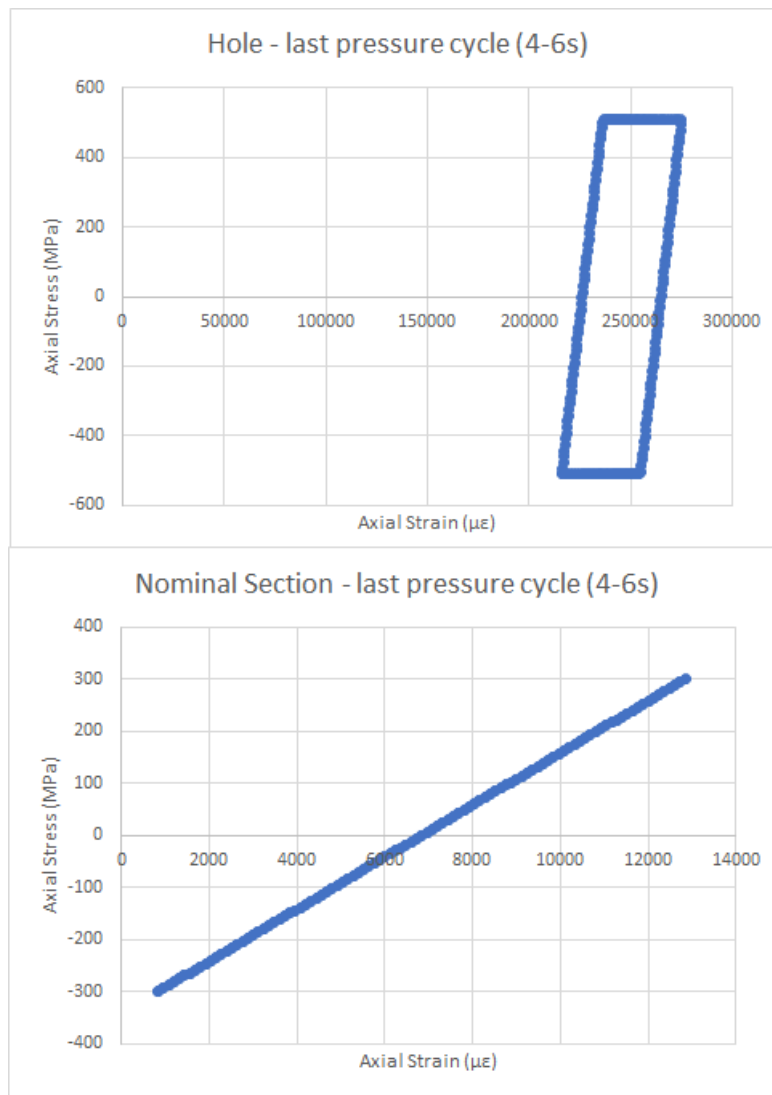


Figure D.5: Stress-Strain history developed during the last load cycle for both interest points.

Appendix E.

Here is presented the values use for the calculation of stress/strain concentration generated by the dent biaxial strain/stress state in the pipe specimens measured and estimated with the experimental and numerical techniques are shown in Tables E.1 to E.5.

Table E.1: TSA data.

Dent	ΔP (MPa)	Measured		Analytical		
		S^* (<i>cam units</i>)	$\sigma_1 + \sigma_2$ (MPa)	σ_1 (MPa)	σ_2 (MPa)	$\sigma_1 + \sigma_2$ (MPa)
1	4	55.2	829	102	51	153
2	6	66.5	999	153	76.5	229.5
3	1.5	81.6	1226	38.25	19.125	57.375
4	4	106.2	1595	102	51	153
5	3	54.6	820	76.5	38.25	114.75
6	6	91.4	1373	153	76.5	229.5
7	4	55.3	830	102	51	153
8	3	47.1	707	76.5	38.25	114.75
9	4	57.8	868	102	51	153

Table E.2: FE data.

Dent	ΔP (MPa)	ϵ_c ($\mu\epsilon$)	ϵ_l ($\mu\epsilon$)	σ_c (MPa)	σ_l (MPa)	$\sigma_{\text{von Mises}}$ (MPa)	$\sigma_1 + \sigma_2$ (MPa)
1	6	6307	-1204	1189	138	1127	1327
2	6	5525	-941	1049	143	985	1192
3	6	19128	2570	3980	1662	3462	5641
4	4	8692	2189	1870	959	1619	2829
5	4	4350	-1447	783	-28	798	755
6	6	6751	-622	1313	281	1197	1594
7	6	6624	-1402	1241	117	1186	1358
8	6	6056	-1451	1124	73	1089	1197
9	6	7142	-1386	1345	151	1276	1497

Table E.3: DIC data.

Dent	ΔP (MPa)	ε_{c_end} ($\mu\varepsilon$)	$\varepsilon_{c_beginning}$ ($\mu\varepsilon$)	ε_{l_end} ($\mu\varepsilon$)	$\varepsilon_{l_beginning}$ ($\mu\varepsilon$)	$\Delta\varepsilon_c$ ($\mu\varepsilon$)	$\Delta\varepsilon_l$ ($\mu\varepsilon$)	$\Delta\sigma_c$ (MPa)	$\Delta\sigma_l$ (MPa)	$\Delta\sigma_{von\ Mises}$ (MPa)	$\Delta\sigma_{1+\sigma_2}$ (MPa)
1	6	7645	1450	-395	1114	6195	-1509	1148	70	1115	1218
2	6	5890	66	-1822	-191	5824	-1631	1067	23	1056	1090
3	6	20750	988	2827	704	19762	2123	4080	1610	3559	5690
4	4	9119	211	1753	189	8908	1564	1875	847	1627	2723
5	4	4327	48	1024	479	4279	545	889	366	773	1254
6	6	8356	1727	-391	1275	6629	-1666	1226	65	1195	1290
7	6	8064	1927	-633	-118	6137	-515	1197	265	1088	1462
8	6	9531	3475	-704	-182	6056	-522	1180	259	1074	1439
9	6	9279	2173	171	-489	7106	660	1461	558	1277	2019

Table E.4: Nominal data.

Dent	ΔP (MPa)	σ_c (MPa)	σ_l (MPa)	$\sigma_{von\ Mises}$ (MPa)	ε_c ($\mu\varepsilon$)	ε_l ($\mu\varepsilon$)	$\sigma_{1+\sigma_2}$ (MPa)
1	6	153	77	133	714	168	230
2	6	153	77	133	714	168	230
3	6	153	77	133	714	168	230
4	4	102	51	88	476	112	153
5	4	102	51	88	476	112	153
6	6	153	77	133	714	168	230
7	6	153	77	133	714	168	230
8	6	153	77	133	714	168	230
9	6	153	77	133	714	168	230

Table E.5: FBSG data.

Dent	ΔP (MPa)	ε_c ($\mu\varepsilon$)	$\varepsilon_{c_nominal}$ ($\mu\varepsilon$) ²⁶
1	5	4183	659
2	6	4910	841
3 ²⁷	-	-	-
4	3	5273	350
5	4	2794	560
6	6	5482	841
7	4	4008	560
8	6	3260	841
9	6	6493	841

²⁶ The nominal circumferential strain in this casa was calculated assuming an uniaxial stress state.

²⁷ No sensor was positioned in the critical position.

Appendix F.

In Figures F.1 to F.8 the procedure used in the implementation of methods A and B proposed by the API 579-1/ASME FFS-1 - 2016 Part 14 is presented. The stress/strains were obtained from the second type of finite element models. Point A represent the most critical point.

Critical Section																																																																																																																																																																																																																																																																																																																																																																																																																																																																																																																																																																																																																																																																																																																																																																																																																																																																																																																																																																																																																																																																																																																																																																																																																																																																																																																																																																																																																																																																																																																																																																																																																																		
------------------	--	--	--	--	--	--	--	--	--	--	--	--	--	--	--	--	--	--	--	--	--	--	--	--	--	--	--	--	--	--	--	--	--	--	--	--	--	--	--	--	--	--	--	--	--	--	--	--	--	--	--	--	--	--	--	--	--	--	--	--	--	--	--	--	--	--	--	--	--	--	--	--	--	--	--	--	--	--	--	--	--	--	--	--	--	--	--	--	--	--	--	--	--	--	--	--	--	--	--	--	--	--	--	--	--	--	--	--	--	--	--	--	--	--	--	--	--	--	--	--	--	--	--	--	--	--	--	--	--	--	--	--	--	--	--	--	--	--	--	--	--	--	--	--	--	--	--	--	--	--	--	--	--	--	--	--	--	--	--	--	--	--	--	--	--	--	--	--	--	--	--	--	--	--	--	--	--	--	--	--	--	--	--	--	--	--	--	--	--	--	--	--	--	--	--	--	--	--	--	--	--	--	--	--	--	--	--	--	--	--	--	--	--	--	--	--	--	--	--	--	--	--	--	--	--	--	--	--	--	--	--	--	--	--	--	--	--	--	--	--	--	--	--	--	--	--	--	--	--	--	--	--	--	--	--	--	--	--	--	--	--	--	--	--	--	--	--	--	--	--	--	--	--	--	--	--	--	--	--	--	--	--	--	--	--	--	--	--	--	--	--	--	--	--	--	--	--	--	--	--	--	--	--	--	--	--	--	--	--	--	--	--	--	--	--	--	--	--	--	--	--	--	--	--	--	--	--	--	--	--	--	--	--	--	--	--	--	--	--	--	--	--	--	--	--	--	--	--	--	--	--	--	--	--	--	--	--	--	--	--	--	--	--	--	--	--	--	--	--	--	--	--	--	--	--	--	--	--	--	--	--	--	--	--	--	--	--	--	--	--	--	--	--	--	--	--	--	--	--	--	--	--	--	--	--	--	--	--	--	--	--	--	--	--	--	--	--	--	--	--	--	--	--	--	--	--	--	--	--	--	--	--	--	--	--	--	--	--	--	--	--	--	--	--	--	--	--	--	--	--	--	--	--	--	--	--	--	--	--	--	--	--	--	--	--	--	--	--	--	--	--	--	--	--	--	--	--	--	--	--	--	--	--	--	--	--	--	--	--	--	--	--	--	--	--	--	--	--	--	--	--	--	--	--	--	--	--	--	--	--	--	--	--	--	--	--	--	--	--	--	--	--	--	--	--	--	--	--	--	--	--	--	--	--	--	--	--	--	--	--	--	--	--	--	--	--	--	--	--	--	--	--	--	--	--	--	--	--	--	--	--	--	--	--	--	--	--	--	--	--	--	--	--	--	--	--	--	--	--	--	--	--	--	--	--	--	--	--	--	--	--	--	--	--	--	--	--	--	--	--	--	--	--	--	--	--	--	--	--	--	--	--	--	--	--	--	--	--	--	--	--	--	--	--	--	--	--	--	--	--	--	--	--	--	--	--	--	--	--	--	--	--	--	--	--	--	--	--	--	--	--	--	--	--	--	--	--	--	--	--	--	--	--	--	--	--	--	--	--	--	--	--	--	--	--	--	--	--	--	--	--	--	--	--	--	--	--	--	--	--	--	--	--	--	--	--	--	--	--	--	--	--	--	--	--	--	--	--	--	--	--	--	--	--	--	--	--	--	--	--	--	--	--	--	--	--	--	--	--	--	--	--	--	--	--	--	--	--	--	--	--	--	--	--	--	--	--	--	--	--	--	--	--	--	--	--	--	--	--	--	--	--	--	--	--	--	--	--	--	--	--	--	--	--	--	--	--	--	--	--	--	--	--	--	--	--	--	--	--	--	--	--	--	--	--	--	--	--	--	--	--	--	--	--	--	--	--	--	--	--	--	--	--	--	--	--	--	--	--	--	--	--	--	--	--	--	--	--	--	--	--	--	--	--	--	--	--	--	--	--	--	--	--	--	--	--	--	--	--	--	--	--	--	--	--	--	--	--	--	--	--	--	--	--	--	--	--	--	--	--	--	--	--	--	--	--	--	--	--	--	--	--	--	--	--	--	--	--	--	--	--	--	--	--	--	--	--	--	--	--	--	--	--	--	--	--	--	--	--	--	--	--	--	--	--	--	--	--	--	--	--	--	--	--	--	--	--	--	--	--	--	--	--	--	--	--	--	--	--	--	--	--	--	--	--	--	--	--	--	--	--	--	--	--	--	--	--	--	--	--	--	--	--	--	--	--	--	--	--	--	--	--	--	--	--	--	--	--	--	--	--	--	--	--	--	--	--	--	--	--	--	--	--	--	--	--	--	--	--	--	--	--	--	--	--	--	--	--	--	--	--	--	--	--	--	--	--	--	--	--	--	--	--	--	--	--	--	--	--	--	--	--	--	--	--	--	--	--	--	--	--	--	--	--	--	--	--	--	--	--	--	--	--	--	--	--	--	--	--	--	--	--	--	--	--	--	--	--	--	--	--	--	--	--	--	--	--	--	--	--	--	--	--	--	--	--	--	--	--	--	--	--	--	--	--	--	--	--	--	--	--	--	--	--	--	--	--	--	--	--	--	--	--	--	--	--	--	--	--	--	--	--	--	--	--	--	--	--	--	--	--	--	--	--	--	--	--	--	--	--	--	--	--	--	--	--	--	--	--	--	--	--	--	--	--	--	--	--	--	--	--	--	--	--	--	--	--	--	--	--	--	--	--	--	--	--	--	--	--	--	--	--	--	--	--	--	--	--	--	--	--	--	--	--	--	--	--	--	--	--	--	--	--	--	--	--	--	--	--	--	--	--	--	--	--	--	--	--	--	--	--	--	--	--	--	--	--	--	--	--	--	--	--	--	--	--	--	--	--	--	--	--	--	--	--	--	--	--	--	--	--	--	--	--	--	--	--	--	--	--	--	--	--	--	--	--	--	--	--	--	--	--	--	--	--	--	--	--	--	--	--	--	--	--	--	--	--	--	--	--	--	--	--	--	--	--	--	--	--	--	--	--	--	--	--	--	--	--	--	--	--	--	--	--	--	--	--	--	--	--	--	--	--	--	--	--	--	--	--	--	--	--	--	--	--	--	--	--	--	--	--	--	--	--	--	--	--	--	--	--	--	--	--	--	--	--	--	--	--	--	--	--	--	--	--	--	--	--	--	--	--	--	--	--	--	--	--	--	--	--	--	--	--	--	--	--	--	--	--	--	--	--	--	--	--	--	--	--	--	--	--	--	--	--	--	--	--	--	--	--	--	--	--	--	--	--	--	--	--	--	--	--	--	--	--	--	--	--	--	--	--	--	--	--	--	--	--	--	--	--	--	--	--	--	--	--	--	--	--	--	--	--	--	--	--	--	--	--	--	--	--	--	--	--	--	--	--	--	--	--	--	--	--	--	--	--	--	--	--	--	--	--	--	--	--	--	--	--	--	--	--	--	--	--	--	--	--	--	--	--	--	--	--	--	--	--	--	--	--	--	--	--	--	--	--	--	--	--	--	--	--	--	--	--	--	--	--	--	--	--	--	--	--	--	--	--	--	--	--	--	--	--	--	--	--	--	--	--	--	--	--	--	--	--	--	--	--	--	--	--	--	--	--	--	--	--	--	--	--	--

Figure F.1: Specimen Dent 1 procedure.

Figure F.2: Specimen Dent 2 procedure.

Figure F.3: Specimen Dent 4 procedure.

Critical Section													
Point	Radial length (mm)	sx (MPa)	sy (MPa)	sz (MPa)	txy (MPa)	tyz (MPa)	txz (MPa)	ex (ε)	ey (ε)	ez (ε)	exy (ε)	eyz (ε)	exz (ε)
1	0	103,9567	-125,946	14,82285	21,3451	-86,366	97,475	-1,60E-04	7,54E-04	-8,88E-04	1,18E-04	3,05E-04	-1,23E-03
2	1,7725	286,7269	21,5697	96,92596	20,5324	-55,3952	115,353	-5,90E-04	1,38E-03	-5,14E-04	2,44E-05	2,93E-04	-7,91E-04
3	3,5449	448,9682	118,7082	163,0026	21,1253	-27,4638	145,789	-8,75E-04	2,00E-03	-3,57E-04	-4,01E-05	3,02E-04	-3,92E-04
4	5,3174	594,4192	171,5898	215,3663	22,7514	0,82579	183,561	-1,03E-03	2,63E-03	-3,92E-04	-7,93E-05	3,25E-04	1,18E-05
5	7,0899	727,0223	186,4151	256,4686	25,032	32,6802	224,056	-1,09E-03	3,26E-03	-5,97E-04	-9,65E-05	3,58E-04	4,67E-04
Stress Linearization													
sm_x		sm_y	sm_z	sm_xy	sm_yz	sm_xz							
437,7916667		89,21033	153,8721	21,81358	-27,24092	150,7304							
sb_x		sb_y	sb_z	sb_xy	sb_yz	sb_xz							
-309,61259		-153,1	-119,632	-2,03123	-57,872045	-65,7493							
seqm (Pm)	418,2856353							-159,84	754,36	-887,80	117,69	304,93	-1233,80
								-590,33	1380,10	-513,88	24,38	293,32	-791,36
								-874,55	2002,50	-356,50	-40,11	301,79	-392,34
								-1033,20	2628,20	-392,01	-79,32	325,02	11,80
								-1087,90	3264,60	-596,88	-96,50	357,60	466,86
sm+sb x=0	128,1790767	-63,89	34,24052	19,78235	-85,112965	84,98117							
sm+sb x=t	747,4042567	242,3106	273,5037	23,8448	30,631125	216,4797							
seqm x=0	268,78												
seqm x=t	620,84												
API 579 part 14													
Method A													
Point	ΔSp,k	Kf (SCF já)	Ke,k	Salt,k (MP	Salt,k (psi)	N (ASME)	$K_{c,d} = 1.0$	$(for S_{c,d} \leq S_{PS})$					
A	644,1888558	1	1	322,0944	46716	119370,5	$K_{c,d} = 1.0 + \frac{(1-n)}{n(m-1)} \left(\frac{\Delta S_{c,d}}{S_{PS}} - 1 \right)$	$(for S_{PS} < \Delta S_{c,d} < mS_{PS})$					
B	304,2303369	1	1	152,1152	22062	4,31E+08	$K_{c,d} = \frac{1}{n}$	$(for \Delta S_{c,d} \geq mS_{PS})$					
Ke,k procedure													
Point	ΔSn,k (Pl+Pm+Q)	Sn,k	SY	S (B31.1)	Sm (ASME II p	SU	SMYS/SM	Sps	m	n	Ke,k		
A (x=t)	620,84	310,4223	316	103,42	147	500	0,632	500	3	0,2	1		
B (x=0)	268,78	134,3915	316	103,42	147	500	0,632	500	3	0,2	1		
Method B													
Point	Δεseq,k	Δεe,k	Δεeff,k	Eya,k	Salt,k (MPa)	Salt,k (psi)	N (ASME)						
A	0	3539,499	3539,499	182000	322,09	46716	119370,5						
B	0	1671,595	1671,595	182000	152,12	22062	4,31E+08						

Figure F.4: Specimen Dent 5 procedure.

Critical Section														
Point	Radial length (mm)	sx (MPa)	sy (MPa)	sz (MPa)	txy (MPa)	tyz (MPa)	txz (MPa)	ex (ε)	ey (ε)	ez (ε)	exy (ε)	eyz (ε)	exz (ε)	
1	0	-226,199	-528,52	-222,828	-0,581448	268,751	0	3,03E-04	-4,37E-06	-2,16E-03	1,97E-05	-8,31E-06	3,84E-03	
2	1,7593	242,4698	-155,704	27,72892	0,0126483	167,314	0	-5,92E-04	1,54E-03	-1,30E-03	9,34E-06	1,81E-07	2,39E-03	
3	3,5186	687,5075	146,0967	251,8243	0,412307	72,359	0	-1,30E-03	3,12E-03	-7,46E-04	9,58E-06	5,89E-06	1,03E-03	
4	5,2778	1128,464	380,8671	452,9072	-0,145593	-27,4841	0	-1,87E-03	4,83E-03	-5,14E-04	5,92E-07	-2,08E-06	-3,93E-04	
5	7,0371	1584,865	552,5622	634,4104	-2,42417	-143,605	0	-2,34E-03	6,75E-03	-6,22E-04	-3,75E-05	-3,46E-05	-2,05E-03	
Stress Linearization														
sm_x		sm_y	sm_z	sm_xy	sm_yz	sm_xz								
684,7847553		101,4073	236,4813	-0,22607	69,09863333	0								
sb_x		sb_y	sb_z	sb_xy	sb_yz	sb_xz								
-895,7632297		-538,556	-426,899	0,539801	200,48805	0								
seqm (Pm)	542,3090903													
sm+sb x=0		-210,9784744	-437,149	-190,418	0,313736	269,5866833	0							
sm+sb x=t		1580,547985	639,9634	663,3801	-0,76587	-131,3894167	0							
seqm x=0		523,70												
seqm x=t		956,56												
API 579 part 14														
Method A														
Point	ΔSp,k	Kf (SCF já)	Ke,k	Salt,k (MPa)	Salt,k (psi)	N (ASME)	$K_{s,d} = 1.0$ (for $S_{s,d} \leq S_{PS}$)							
A	1024,568443	1	1	512,2842	74301	27061,18	$K_{s,d} = 1.0 + \frac{(1-n)}{n(m-1)} \left(\frac{\Delta S_{s,d}}{S_{PS}} - 1 \right)$ (for $S_{PS} < \Delta S_{s,d} < mS_{PS}$)							
B	555,9771053	1	1	277,9886	40319	215163,3	$K_{s,d} = \frac{1}{n}$ (for $\Delta S_{s,d} \geq mS_{PS}$)							
Ke,k procedure														
Point	ΔSn,k (Pl+Pm+Q)	Sn,k	SY	S (B31.1)	Sm (ASME II p)	SU	SMYS/SM	Sps	m	n	Ke,k			
A (x=t)	956,5634242	478,2817	316	103,42	147	500	0,632	500	3	0,2	1			
B (x=0)	523,6958094	261,8479	316	103,42	147	500	0,632	500	3	0,2	1			
Method B														
Point	Δεpeq,k	Δεe,k	Δεeff,k	Eya,k	Salt,k (MPa)	Salt,k (psi)	N (ASME)							
A	0	5629,497	5629,497	182000	512,28	74301	27061,18							
B	0	3054,819	3054,819	182000	277,99	40319	215163,3							

Figure F.5: Specimen Dent 6 procedure.

Figure F.6: Specimen Dent 7 procedure.

Critical Section							
Point	Radial length (mm)	sx (MPa)	sy (MPa)	sz (MPa)	txy (MPa)	tyz (MPa)	txz (MPa)
1	0	85,26735	-79,6905	1,88055	-0,248381	44,3177	62,692
2	1,7168	253,8329	33,64373	86,58936	-0,018858	37,002	93,499
3	3,4337	401,0008	102,7518	151,6242	0,086996	26,5622	128,156
4	5,1505	535,1608	135,3754	201,23	-0,0261884	10,9305	166,698
5	6,8674	664,7909	139,2939	239,6892	-0,453796	-11,9609	209,139
Stress Linearization							
sm_x	sm_y	sm_z	sm_xy	sm_yz	sm_xz		
392,3362426	78,43198	141,3413	-0,05903	23,10093333	130,7443		
sb_x	sb_y	sb_z	sb_xy	sb_yz	sb_xz		
-285,5448468	-105,612	-116,772	0,055019	27,1054	-73,2113		
seqm (Pm)	368,2785809						
sm+sb x=0	106,7913957	-27,18	24,56882	-0,00401	50,20633333	57,533	
sm+sb x=t	677,8810894	184,0439	258,1138	-0,11405	-4,004466667	203,9555	
seqm x=0	176,59						
seqm x=t	581,05						

ex (ε)	ey (ε)	ez (ε)	exy (ε)	eyz (ε)	exz (ε)
-1,09E-04	5,97E-04	-5,82E-04	1,14E-06	-3,55E-06	6,33E-04
-4,91E-04	1,20E-03	-3,76E-04	1,90E-06	-2,69E-07	5,29E-04
-7,39E-04	1,78E-03	-3,46E-04	2,74E-06	1,24E-06	3,79E-04
-8,87E-04	2,39E-03	-4,70E-04	3,80E-07	-3,74E-07	1,56E-04
-9,69E-04	3,03E-03	-7,26E-04	-8,44E-06	-6,48E-06	-1,71E-04
ex (με)	ey (με)	ez (με)	exy (με)	eyz (με)	exz (με)
-109,28	596,76	-581,51	1,14	-3,55	633,11
-491,19	1196,50	-376,28	1,90	-0,27	528,60
-738,99	1784,00	-346,35	2,74	1,24	379,46
-886,93	2385,60	-470,01	0,38	-0,37	156,15
-969,26	3028,00	-725,55	-8,44	-6,48	-170,87

API 579 part 14											
Method A											
Point	ΔSp,k	Kf (SCF já)	Ke,k	Salt,k (MPa)	Salt,k (psi)	N (ASME)	$K_{s,d} = 1.0$ $K_{s,d} = 1.0 + \frac{(1-n)}{n(m-1)} \left(\frac{\Delta S_{s,d}}{S_{PS}} - 1 \right)$ $K_{s,d} = \frac{1}{n}$ (for $S_{s,d} \leq S_{PS}$) (for $S_{PS} < \Delta S_{s,d} < mS_{PS}$) (for $\Delta S_{s,d} \geq mS_{PS}$)				
A	604,24835	1	1	302,1242	43819	152591,7					
B	195,172622	1	1	97,58631	14154	1336966					
Ke,k procedure											
Point	ΔSn,k (Pl+Pm+Q)	Sn,k	SY	S (B31.1)	Sm (ASME II p)	SU	SMYS/SM	Sps	m	n	Ke,k
A (x=t)	581,0548411	290,5274	316	103,42	147	500	0,632	500	3	0,2	1
B (x=0)	176,5943774	88,29719	316	103,42	147	500	0,632	500	3	0,2	1
Method B											
Point	Δεseq,k	Δεe,k	Δεeff,k	Eya,k	Salt,k (MPa)	Salt,k (psi)	N (ASME)				
A	0	3320,046	3320,046	182000	302,12	43819	152591,7				
B	0	1072,377	1072,377	182000	97,59	14154	1336966				

Figure F.7: Specimen Dent 8 procedure.

Critical Section							
Point	Radial length (mm)	sx (MPa)	sy (MPa)	sz (MPa)	txy (MPa)	tyz (MPa)	txz (MPa)
1	0	336,3745	-1,4035	442,5785	-0,535941	131,572	142,968
2	1,7598	529,9056	138,1744	410,2336	-0,0383474	80,696	167,188
3	3,5196	704,1489	218,2215	378,8295	0,17955	39,2763	209,139
4	5,2794	861,0015	240,3927	330,2244	-0,00276472	-0,07457	263,802
5	7,0393	1002,35	206,3299	246,2551	-0,70581	-44,7496	326,172
Linearização							
sm_x	sm_y	sm_z	sm_xy	sm_yz	sm_xz		
692,5542645	179,6365	367,3604	-0,08726	40,65505967	217,6148		
sb_x	sb_y	sb_z	sb_xy	sb_yz	sb_xz		
-332,0419218	-103,043	89,08545	0,024676	84,4656855	-94,108		
seqm (Pm)	590,8173558						
sm+sb x=0	360,5123428	76,59398	456,4458	-0,06258	125,1207452	123,5068	
sm+sb x=t	1024,596186	282,679	278,2749	-0,11193	-43,81062583	311,7228	
seqm x=0	458,01						
seqm x=t	922,50						

ex (ε)	ey (ε)	ez (ε)	exy (ε)	eyz (ε)	exz (ε)
-2,70E-04	1,12E-03	-1,29E-03	1,88E-03	-7,66E-06	1,88E-03
-8,50E-04	2,01E-03	-7,90E-04	1,15E-03	-5,48E-07	1,15E-03
-1,23E-03	2,88E-03	-5,86E-04	5,61E-04	2,57E-06	5,61E-04
-1,45E-03	3,79E-03	-6,43E-04	-1,07E-06	-3,95E-08	-1,07E-06
-1,57E-03	4,76E-03	-9,24E-04	-6,39E-04	-1,01E-05	-6,39E-04
ex (με)	ey (με)	ez (με)	exy (με)	eyz (με)	exz (με)
-269,65	1121,00	-1291,70	1879,60	-7,66	1879,60
-850,37	2007,60	-790,48	1152,80	-0,55	1152,80
-1228,10	2884,80	-586,11	561,09	2,57	561,09
-1450,60	3790,20	-642,72	-1,07	-0,04	-1,07
-1565,60	4761,40	-924,46	-639,28	-10,08	-639,28

API 579 part 14												
Method A												
Point	ΔSp,k	Kf (SCF já)	Ke,k	Salt,k (MP Salt,k (psi)	N (ASME)	$K_{s,d} = 1.0$	$(for S_{s,d} \leq S_{PS})$					
A	963,6570036	1	1	481,8285	69883	32244,13	$K_{s,d} = 1.0 + \frac{(1-n)}{n(m-1)} \left(\frac{\Delta S_{s,d}}{S_{PS}} - 1 \right)$	$(for S_{PS} < \Delta S_{s,d} < mS_{PS})$				
B	523,9280713	1	1	261,964	37995	280683,5	$K_{s,d} = \frac{1}{n}$	$(for \Delta S_{s,d} \geq mS_{PS})$				
Ke,k procedure												
Point	ΔSn,k (Pl+Pm+Q)	Sn,k	SY	S (B31.1)	Sm (ASME II p)	SU	SMYS/SM	Sps	m	n	Ke,k	
A (x=t)	922,4963248	461,2482	316	103,42	147	500	0,632	500	3	0,2	1	
B (x=0)	458,0148266	229,0074	316	103,42	147	500	0,632	500	3	0,2	1	
Method B												
Point	Δεseq,k	Δεe,k	Δεeff,k	Eya,k	Salt,k (MPa)	Salt,k (psi)	N (ASME)					
A	0	5294,819	5294,819	182000	481,83	69883	32244,13					
B	0	2878,726	2878,726	182000	261,96	37995	280683,5					

Figure F.8: Specimen Dent 9 procedure.